UNIVERSITY OF MISKOLC

MIKOVINY SÁMUEL DOCTORAL SCHOOL OF EARTH SCIENCES

Head of the Doctoral School:
Prof. Dr. Péter Szűcs

INTEGRATION OF FLOW MODELLING, GEOCHEMISTRY AND ISOTOPIC TRACERS FOR SUSTAINABLE MANAGEMENT OF GROUNDWATER IN SIWA OASIS, WESTERN DESERT, EGYPT

Ph.D. THESIS

AUTHOR:
Mohamed Hamdy Eid Hemida

SCIENTIFIC SUPERVISORS:
Prof. Dr. Péter Szűcs
Dr. Attila Kovács

Institute of Water Resources and Environmental Management
Department of Hydrogeology and Engineering Geology

Miskolc-Hungary
2025

DEDICATION

With heartfelt gratitude, I dedicate this work to my beloved mother, whose unwavering support and pure love guided me throughout my life. From the moment I was born until the day she passed; she worked tirelessly to ensure my success. Although you left this world before witnessing my graduation, your teachings and sacrifices inspire me every day.
I promise to honor your legacy by helping others, just as you taught me to do. Every achievement in my life is a testament to your love and guidance. Rest in peace, dearest mother, until we meet again at the end of life. You will always be my greatest love, my strength, and my everything.

With love and gratitude,
Mohamed

ADVISOR'S FOREWORD

for the (PhD thesis)

"INTEGRATION OF FLOW MODELLING, GEOCHEMISTRY AND ISOTOPIC TRACERS FOR SUSTAINABLE MANAGEMENT OF GROUNDWATER IN SIWA OASIS, WESTERN DESERT, EGYPT"

by Mohamed Hamdy Eid Hemida

The topic of the Candidate's thesis, integrated hydrogeological modeling for sustainable groundwater management in arid regions, is at the forefront of international research. The development introduced to the hydrogeological modeling workflow by the Candidate in this thesis pertains to the comprehensive characterization of complex, multi-layered aquifer systems, as applied in the case study of the Siwa Oasis in the Western Desert of Egypt. The suggested integrated application of advanced machine learning techniques, high-resolution geophysical data, multi-isotopic tracers, and numerical flow modeling enables an accurate and holistic understanding of groundwater systems characterized by high heterogeneity, structural complexity, and critical sustainability challenges. This approach is highly relevant in contemporary hydrogeological practice and represents a significant contribution to water resource management in arid ecosystems globally.

The author explores innovative opportunities for the use of geophysical well-log data in combination with Self-Organizing Maps (SOM) and K-means clustering for high-resolution hydrostratigraphic characterization. The 3D geological modeling is based on the integration of machine learning-derived lithofacies classification with aeromagnetic and gravity data to map fault systems controlling hydraulic connectivity between the deep Nubian Sandstone Aquifer (NSSA) and the shallow Tertiary Carbonate Aquifer (TCA). This assumption is grounded on the demonstrated correlation between geological structure, hydraulic properties, and groundwater flow patterns in the aquifer system. The proposed methodology significantly enhances the 3D high-resolution interpretation of heterogeneous aquifer systems at regional scales, particularly in data-scarce arid regions where traditional methods are cost-prohibitive.

An essential aspect of this thesis is the integration of geochemical and multi-isotopic tracers ($\delta^{2}H$, $\delta^{18}O$, ^{13}C, ^{14}C, $^{87}Sr/^{86}Sr$) with advanced statistical techniques and inverse mixing models (NETPATH, Faure) to quantitatively delineate recharge sources, estimate groundwater residence times, and validate fault-controlled recharge pathways. The Candidate successfully demonstrated that the TCA receives 63-87% of its recharge from upward leakage from the fresh NSSA through fault conduits, while hypersaline lakes contribute 0.6-4% through downward seepage. These empirical findings were then integrated into a predictive numerical flow model (FEFLOW) to simulate long-term aquifer behavior under current extraction rates, revealing critical drawdown patterns and predicting

water levels will drop to 30-70 m by 2100. The optimization of the model geometry and hydraulic parameter assignment in accordance with the established hydrostratigraphic framework and structural controls has been proven to be an effective approach in calibrating aquifer properties. The final model provides actionable information for decision-making regarding sustainable management and can be updated with new hydrogeological data.

Furthermore, the Candidate's research addresses the practical challenges of water quality degradation and soil salinization through multiple innovative contributions. The quantitative linkage between 270% agricultural expansion and 168% increase in hypersaline lake area, established through multi-temporal remote sensing analysis, provides critical insights into the drivers of environmental degradation. The development of an Integrated weight Water Quality Index (IWQI) and probabilistic health risk assessment using Monte Carlo simulation demonstrates the Candidate's ability to translate scientific findings into public health protection strategies. Most notably, the development and successful testing of a novel zeolite/geopolymer membrane from natural kaolinite and diatomite, achieving 99.5% salt rejection and 7.05 kg/m²/h water flux, represents a significant technological innovation with direct applicability to desalination challenges in arid regions.

The Candidate's continuous efforts towards scientific research, creativity, and the comprehensive results presented in this thesis demonstrate exceptional scientific knowledge and suitability for independent research. In our opinion, the Candidate's results, particularly those related to integrated hydrogeological modeling, multi-isotopic tracer applications, numerical flow modeling, and innovative desalination technology, merit publication in highly ranked international journals of hydrogeology, water resources management, and groundwater sustainability. We certify that this dissertation contains only valid data, and the presented results represent the Candidate's own work. In our opinion, it meets the scope and quality requirements set by the Mikoviny Sámuel Doctoral School of Earth Sciences. Based on the above, we fully support and recommend the public defense of the thesis and the award of the Ph.D. title.

16/10/2025

Supervisor
Prof. Dr. Péter Szűcs
University full professor

Co-supervisor
Dr. Attila Kovács
Ph.D. University of Miskolc

CONTENTS

List of Abbreviations

TCA	Tertiary carbonate aquifer
NSSA	Nubian Sandstone aquifer
GR	Gamma ray
Rd	Deep resistivity
SP	Spontaneous potential
Rw	Resistivity of water
Ø	Total porosity
$Ø_{eff}$	Effective porosity
V_{sh}	Volume of shale
Q	Discharge rate
Δs	Average drawdown
T	Transmissivity
K	Hydraulic conductivity
SGS	Sequential Gaussian Simulation
LU/LC	land use/land cover
SVM	Support vector machine
FCCs	False color composites
PCA	Principal component analysis
SOM	Self-Organizing map
TAHG	Tilt angle of horizontal gradient
FVD	First Vertical Derivative
SVD	Second Vertical Derivative
TH	Total hardness
SI	Minerals saturation index
LMWL	Local meteoric line
GMWL	Global meteoric water line
d-excess	deuterium excess
IWQI	Integrated weight water quality index
FFBP-NN	Feed forward back propagation neural network
CDI	Chronic daily intake
IR	Ingestion rate reflects
EF	Exposure frequency
ED	Exposure duration
BW	Body weight
SA	Skin surface area
Kp	Permeability constant
CF	Conversion factor
RfD	Reference dose

ABS	Digestive coefficient of the gastrointestinal tract
CSF	Conversion slope factor of metals.
HQ	Hazard quotient index
HI	Total hazard index
CR	Carcinogenic risk index
D/K	Diatomite-Kaolinite
Z/GP	Zeolite geopolymer
Rj	Salt rejection
XRD	X-ray diffraction
HRTEM	Transmission Electron Microscopy
FTIR	FTIR: Fourier Transform Infrared spectrometer
ICP	Inductively Coupled Plasma

List of figures

pressure regulation on both the retentate and permeate sides to optimize performance during the desalination process. The schematic illustration depicts the arrangement of zeolite phases within the Z/GP membrane and the mechanism by which cations are adsorbed.

Figure 15. The three extracted clusters of subsurface lithofacies in NSSA with plotting Rd vs GR in all logs to represent the complete system of the aquifer.

Figure 16. Self-Organizing Map (SOM) component planes used for clustering with color gradient demonstrate lithological changes in NSSA

Figure 17. K-means clusters of subsurface lithology in NSSA with plotting Rd vs GR (a) and Silhouette score (b).

Figure 18. (a) Visualization of the well logs in Sharqia borehole in 1D with two types of clusters validated with lithological log where black color is the aquifer layer. Yellow color is shale layer, and red color is shaly sand layer supported with (b) the error and accuracy of each method

Figure 19. Fence diagram demonstrates the interpolation of SOM clusters (a), k-means clusters (b) and lithology (c) in 3D showing the heterogeneity of the NSSA with upper cretaceous shale. The lithological interpolation results comparing SOM, k-means, and actual lithology logs using HB Kriging (d), and Sensitivity analysis using systematic noise injection methodology (e)

Figure 20. Vertical panel shows the response of well logs, Vsh, Ø, $Ø_{eff}$, K, and lithological clusters

Figure 21. Distribution map of the average hydraulic conductivity and effective porosity from well logs in Siwa Oasis

Figure 22. Interpolation of the lithology, hydraulic conductivity, effective porosity, and shale volume in 2D showing the hydrostratigraphic units and fault plane along A-Ä cross section.

Figure 23. The relationship between drawdown and time for long duration pumping test (a) and recovery test (b) and calibration curve of hydraulic conductivity estimated from well logs vs pumping test

Figure 24. Bouguer anomaly distribution map in Siwa Oasis

Figure 25. Gravity Upward continued to height of 1000m to image sources buried at and below 500m depth (a) and to height of 7000m to image sources buried at and below 3500m (b), Residual anomaly map after the anomaly sources deeper than 0.5km (upward continued 1km) (c), and 3.5km (upward continued 7km) (d) are removed which is characterized by negative and positive gravity values.

Figure 26. Structural pattern maps and extracted lineaments from following filters, **(a) FVD, (b)** THD, (c) SVD, (d) TA, (e) AS and (f) TAHG, applied on the residual anomaly (upward continued 1km), (g) Rose diagrams illustrate lineament orientations filtered by the gravity datasets revealing predominant trends that align closely with the orientations of major structures in the study area, and (h) Combined Lineament map from different edge filtering techniques applied on the residual (upward 1 km).

Figure 27. Structural pattern maps and extracted lineaments from following filters, (a) FVD, (b) THD, (c) SVD, (d) TA, (e) AS and (f) TAHG, applied on the residual anomaly (upward continued 7 km), (g) Combined Lineament map from different edge filtering techniques applied on the residual (upward 7 km), and (h) rose diagram showing predominantly NE-SW, NW-SE

Fig 28. Inversion Results Gravity Model for 0.5 km including (a) Observed gravity anomalies, (b) Computed gravity anomalies from the inverted interface, (c) Error and gravity difference, and (d) Estimated depths from inversion. inversion results gravity model for 3.5 km including (e) Observed gravity anomalies, (f) Computed

gravity anomalies from the inverted interface, (f) Error and gravity difference, and (g) Estimated depths from inversion, (h)

Figure 29. (a, b) 3D model of estimated depth, (c, d) RMS for 0.5 and 3.5 km, respectively in the study area.

Figure 30. FCC 7-4-2 in RGB respectively for Landsat TM a) 1990, c) 2000, e) 2010, g) OLI 2020 and their corresponding resultant thematic map using SVM (b, d, f, and h respectively).

Figure 31. Field observation of the water logging and soil salinization (dry sabkha)

Figure 32. Graphical representation of Piper (a), Gibbs (b), and Durov (c) diagrams

Figure 33. Minerals saturation index extracted from PHREEQC model.

Figure 34. The ionic ratio between the major ions in the different water resources of Siwa Oasis.

Figure 35. Spearman correlation matrix of the measured parameters.

Figure 36. Distribution map of $\delta^{18}O$ (a), Plotting graph of $\delta^{2}H$ and $\delta^{18}O$ (b), EC of the TCA from 1998 to 2022(c), and plot of EC vs $\delta^{18}O$ (d)

Figure 37. 3D scatter plot (a) and 2D scatter plot between TDS and $\delta^{18}O$ (b) of the 3 clusters extracted from K-means cluster analysis

Figure 38. scatter plot of $\delta^{18}O$ vs D-excess showing the effect of evaporation on isotopic signature

Figure 39. Groundwater flow direction (a), and TDS with the mixing line between the endmembers (b)

Figure 40. linear graph between $\delta^{2}H$ and $\delta^{18}O$ including lakes and TCA (cluster 3,2) as two end members (a), linear graph between $\delta^{2}H$ and $\delta^{18}O$ including NSSA and TCA (cluster 1) as two end members (b), and calibration curve between the calculated mixing percentage from $\delta^{18}O$ and the computed from the geochemical reaction (C)

Figure 41. Conceptual model based on geological boundary illustrate the contribution percentage from hyper saline lake to the karst aquifer (TCA) supported with shallow depth lineaments in karst aquifer and deep faults in NSSA

Figure 42. The distribution maps of the 18O, 87/86Sr, TDS, Sr, and groundwater flow direction in NSSA and TCA

Figure 43. The relationship between salinity vs $^{87/86}Sr$ and Sr vs $^{87/86}Sr$ supported with mixing line based on Faure model

Figure 44. The relationship between $\delta^{18}O$ vs $^{87/86}Sr$ and Sr vs $\delta^{18}O$

Figure 45. The relationship between depth vs $^{87/86}Sr$ and $\delta^{2}H$ vs $\delta^{18}O$

Figure 46. The spatial comparison between NETPATH model and Faure model in estimation of contribution % from NSSA to TCA along the fault plane and calibration curve between NETPATH model and Faure model.

Figure 47. The distribution map of the corrected age in Siwa Oasis and the relationship between age and depth of water samples

Figure 48. The calibration curve and maps showing the observed and computed initial head in NSSA and springs water level (TCA) in steady state condition.

Figure 49. The transient state calibration curve for NSSA and TCA and boreholes distribution map used for calibration of NSSA.

Figure 50. The changes in the water level in the NSSA from 1960 (initial head) to the current state (2025) and predicted water level in 2100.

Figure 51. The changes in the discharge rate and hydraulic head of the springs (TCA) from 1960 to 2100 based on the transient model

Figure 52. Reverse particle tracking from wells in 2D and 3D showing the recharge area in east of Siwa Oasis and recharge of TCA from NSSA through faults and fracture system based on the pathlines.

Figure 53. Ploting of samples with the values of IWQI (a) and distribution map of IWQI in NSSA (b) and TCA (c)

Figure 54. The relationships between the true values and predicted values of the water quality

Figure 55. The interval values of HQ in different age group with different exposure routes represented by Box plot graph.

Figure 56. Distripution maps of Hazard index ina adult and child through oral and dermal contact

Figure 57. Box plot of the carcinogenic risk (CR) in adult and child through oral (a and b) and dermal (c and d) contact.

Figure 58. The predicted HQ dermal in old age group (adult) (a), $HQ_{predicted}$ dermal in young age group (child) (b), $HQ_{predicted}$ oral for adult (c), and $HQ_{predicted}$ oral for child.

Figure 59. Predicted carcinogenic risk (CR) in adult (a, b and c) and child (d, e and f) through oral contact for Cd, Cr, and Pb respectively

Figure 60. Predicted carcinogenic risk (CR) in adult (a, b and c) and child (d, e and f) through dermal contact for Cd, Cr, and Pb respectively

Figure 61. XRD patterns of raw kaolinite (A), metakolinite (B), synthetic D/K geopolymer (C), and the synthetic Z/GP membrane (D).

Figure 62. (A) SEM image showing the D/K geopolymer substrate, (B) SEM image illustrating the oriented pores within the D/K geopolymer, (C) SEM image of the Z/GP membrane highlighting its crystalline morphology, (D) SEM image depicting the porous matrix structure of the Z/GP membrane, (E) HRTEM image of the D/K geopolymer revealing its agglomerated particles and porous matrix, and (F) HRTEM image of the Z/GP membrane emphasizing its nanostructured porous material.

Figure 63. The FT-IR spectra of the synthetic D/K geopolymer (A), and the studied Z/GP membrane and The N_2 adsorption/desorption isotherm curve of the synthetic Z/ GP membrane.

Figure 64. (A) Shows the influence of Z/GP membrane thickness on desalination performance, (B) the impact of feed temperature on the performance of the membrane, (C) the stability of the Z/GP membrane during a 130-hour desalination process, and (D) the recyclability of the prepared Z/GP membrane for reuse in desalination processes of Siwa brackish groundwater.

Figure 65. Schematic diagram of the recommended solutions in Siwa Oasis for sustainable development.

Figure 1s. Lineament extracted from (a) FVD; (b) SVD, (c) TA, and (d) TAHG with edge detection applied on residual 0.5km

Figure 2s. Lineament extracted from (a) FVD; (b) SVD, (c) TA, and (d) TAHG with edge detection applied on residual 3.5km

Figure 3s. Combined Lineament map of the gravity and magnetic from different edge filtering techniques with 0.5km (a), 3.5km (b), and the resultant rose diagram showing predominantly NE-SW, NW-SE and E-W trend (c, d).

Figure 4s. Distribution maps of physicochemical parameters for the NSSA, springs, and drains

List of tables

Summary

This PhD thesis presents a comprehensive, multi-disciplinary investigation of the Siwa Oasis hydrogeological system, integrating geophysical data (well logs, gravity, magnetics), machine learning algorithms (SOM, K-means), multi-temporal remote sensing (Landsat with SVM), geochemical and isotopic tracers (δ^2H, $\delta^{18}O$, ^{13}C, ^{14}C, $^{87}Sr/^{86}Sr$), numerical flow modeling (FEFLOW), water quality assessment (IWQI, health risk analysis), and innovative desalination technology (zeolite/geopolymer membrane). This integrated approach provides a quantitative, predictive foundation for sustainable groundwater management in this critical arid ecosystem.

Key Findings

1. 3D Geological and Structural Architecture: The 3D geological model revealed fault systems controlling hydraulic connectivity between the deep Nubian Sandstone Aquifer (NSSA) and shallow Tertiary Carbonate Aquifer (TCA). SOM outperformed K-means in lithological delineation, with hydraulic conductivity ranging from 1.2-6.6 m/d. Gravity and magnetic analysis identified dominant NE-SW, NW-SE, and E-W structural trends, with basement depths of 2.5-4.5 km. Deep faults act as conduits for upward NSSA-to-TCA recharge, while shallow fractures facilitate surface leakage.

2. Land-Use Change and Salinization: The remote sensing analysis quantified a 270% agricultural expansion over 30 years, causing a 168% increase in hypersaline lake area, the primary driver of soil and water salinization. NSSA contains freshwater (Mixed Ca-Mg-Cl-SO_4), while TCA and springs are brackish-saline, and lakes are hypersaline (Na-Cl, Ca-Mg-SO_4). Geochemical modeling identified mineral supersaturation (montmorillonite, calcite, dolomite) reducing soil permeability and increasing waterlogging.

3. Dual-Source Mixing Model: The stable isotope analysis confirmed TCA receives paleo-meteoric water from both NSSA (depleted $\delta^{18}O$) and saline lakes (enriched $\delta^{18}O$). NETPATH modeling quantified hypersaline lake contributions at 0.6-4% (highest from Zeitun Lake) and NSSA contributions at 63-87% through upward flow.

4. Groundwater Age and Recharge Pathways: The Faure mixing model demonstrated 80-90% NSSA contribution in low-salinity zones (1000-2000 mg/L) along faults, 50-80% in intermediate zones (2000-5000 mg/L), and 0-40% in high-salinity northern regions (5000-9000 mg/L). Radiocarbon dating revealed TCA ages of 640-13,551 years and NSSA ages of 4,296-14,184 years, with youngest ages near Siwa Lake indicating active mixing. Older groundwater (>10,000 years) near faults preserves paleowater from the African Humid Period.

5. Numerical Flow Modeling and Future Predictions: The flow model demonstrated critical drawdown from 1960-2025: western areas declined from 175m to 75m, eastern areas from 142m to 128m. Under current extraction rates (330,000 m^3/day), water levels will drop to 30-70m by 2100. Reverse particle tracking validated NSSA-to-TCA recharge along fault pathways and confirmed downward leakage from salt lakes to TCA.

6. Water Quality and Health Risk Assessment: The Integrated weight Water Quality Index (IWQI) identified extremely poor water quality in TCA due to high salinity. Feed-Forward Back-Propagation Neural Networks (FFBP-NN) predicted water quality with high accuracy. Health risk assessment revealed significant non-carcinogenic and carcinogenic risks, especially for children, from cadmium, chromium, and lead exposure, necessitating targeted mitigation strategies.

7. Innovative Desalination Technology: A geopolymer-based zeolite membrane from natural kaolinite and diatomite achieved 99.5% salt rejection and 7.05 kg/m²/h water flux at 75°C, with excellent thermal stability and durability over multiple reuse cycles. This eco-friendly, cost-effective technology provides a sustainable solution for groundwater salinization in arid regions.

This research moves beyond descriptive analysis to create a scientifically robust, predictive framework for sustainable groundwater management in Siwa Oasis. The integration of advanced geological, geochemical, isotopic, numerical, and technological approaches provides actionable insights for water resource management in similar arid ecosystems globally.

1. Introduction

The global water crisis, marked by declining water supply and quality, is particularly acute in arid, populated regions like Egypt [2]. This crisis threatens agriculture, a sector highly vulnerable to water scarcity and the associated challenge of soil salinization [3]. In groundwater-dependent ecosystems such as Siwa Oasis, sustainable agriculture requires integrated management of soil, water, and crops to maintain a delicate water-salt balance [4], especially under the pressures of human development and climate change [5]. Egypt has recently prioritized expanding cultivated projects using groundwater as a main resource in the desert regions, including Siwa area in the western desert [6]. Siwa Oasis, which relies entirely on groundwater for all purposes, faces significant challenges such as waterlogging, rapid groundwater and soil salinization. Waterlogging, caused by poor irrigation practices, inadequate drainage, and over-irrigation, has led to rising water tables, increased soil salinity, and the expansion of salt lakes, rendering some water unsuitable for irrigation [7,8]. In 1963, there were less than 200 wells of any use with depth about 12 m below the ground level. From 1981 to 1996, farmers began to drill thousands of wells in the fractured limestone aquifer with poor design which produced excess of water and formed the lakes in low land of Siwa depression and continuous deterioration of agricultural land. During this period, all wells were drilled in the shallow aquifers (carbonate aquifer) with no controlling valves and no casing [9]. The total discharge from these wells reached to 400000m^3/d where only 60% were used for irrigation and excess water discharged into lakes [10]. From 1996 to 2001, different actions occurred. One of them aimed at the rehabilitation of poorly designed wells (400 wells), while 665 wells were still with low priority. Continuous drilling of new wells made the problem worse with time [5].

To address these issues, surface investigations are essential for understanding subsurface conditions. Integrating satellite imagery, spatial data systems, and artificial intelligence provides an efficient and robust method for tracking soil salinity in vulnerable environments such as Siwa Oasis [8]. Effective monitoring of surface conditions, including land use/land cover changes, is crucial for evaluating environmental concerns such as soil salinity, waterlogging, groundwater deterioration with salinity, and changes in surface area of different salt lakes [11].

Geological heterogeneity is widely acknowledged as a key factor shaping groundwater flow patterns. Its spatial distribution plays a critical role in creating preferential flow pathways and controlling the movement and transport processes within subsurface systems [12]. The significance of geological geometry stems from how variations in these properties impact numerical modeling efforts, including model calibration, recharge estimation, and the dispersion of contaminant plumes. These factors ultimately influence sustainability management strategies and the overall understanding of aquifer hydraulics [13]. Understanding heterogeneous groundwater systems, characterized by significant variations in lithology and hydraulic properties, remains a major challenge in hydrogeological research [13]. Traditional methods like borehole correlation often fail to accurately capture this

heterogeneity, leading to incorrect predictions of groundwater flow and contaminant movement. In contrast, geophysical logs data has proven more effective in addressing these challenges. By utilizing various logs sensitive to lithology and water saturation, well logging provides continuous subsurface data, enabling a more detailed exploration of lithological variations [14]. Machine learning techniques, such as Self-Organizing Maps (SOMs) and k-means clustering analysis (CA), have revolutionized aquifer characterization by uncovering hidden patterns in complex datasets [15]. These methods have gained traction in rock typing, particularly in characterizing petroleum and gas formations, and have been integrated with core drilling data to improve subsurface understanding [15–17].

Aeromagnetic techniques are essential for mineral exploration, subsurface mapping, geothermal studies, archaeology, and engineering [18]. These methods detect magnetic field variations caused by differences in magnetic susceptibility within geological formations like folds and faults [18].

Comprehending the chemical properties of water, primary drivers, and origins of groundwater contamination is essential for the sustainable stewardship of aquatic and groundwater resources [19–22]. The chemical composition of groundwater is influenced by natural mechanisms such as the dissolution and precipitation of minerals, the geological makeup of aquifers, the duration of water retention underground, and the exchange of ions [7,13,23]. Nonetheless, human actions, including the release of industrial waste, farming techniques, and the encroachment of salt water, have profoundly impacted the quality of groundwater [19,24–27]. Hydrochemical and stable isotope techniques are widely used to study groundwater recharge, trace solute sources, and model contaminant transport [28]. Methods like Piper diagrams, Gibbs diagrams, ion ratios, cluster analysis, principal component analysis (PCA), and NETPATH simulations are commonly employed to analyze hydrogeochemical processes [13,19,21,26].

Sustainable management of complex aquifers, such as the Nubian Sandstone Aquifer (NSSA) and Tertiary Carbonate Aquifer (TCA), requires a detailed understanding of recharge processes and groundwater mean transit times. Environmental isotopes provide valuable insights into recharge conditions, such as infiltration temperatures and water ages, which are crucial for identifying recharge areas, estimating flow rates, understanding mixing processes, and calibrating groundwater flow models [7,29]. Recent research emphasizes the widespread presence of toxic metals like lead, iron, manganese, cadmium, copper, and chromium in groundwater and surface water systems worldwide [19,20,22,24,30,31]. These toxic metals present a significant threat due to its extreme toxicity and tendency to accumulate in biological tissues, even at minimal levels. These metals are enduring environmental pollutants with profound health consequences, including damage to vital organs, neurological conditions, respiratory and cardiovascular ailments, and cancer. Evaluating water quality and pinpointing contamination sources are essential measures for protection both environmental integrity and public health. Techniques such as hazard quotient (HQ), hazard index

(HI), and carcinogenic risk (CR), alongside Monte Carlo simulation, provide robust tools for assessing these risks effectively[19,20,26,30,32,33].

Desalination approaches (membrane distillation, reverse osmosis, and pervaporation) are highly dependent on the membrane material employed [34]. Synthetic inorganic membranes made from natural aluminosilicate resources, like zeolite, have been explored as alternatives to traditional polymeric membranes are favored for their exceptional thermal and chemical resilience, nano-porous architecture, and economical production costs. Geopolymer membranes, with their significant porosity, thermal stability, chemical resistance, and mechanical strength, offer a viable alternative [35]. This study aims to address the critical challenges of water scarcity, soil salinization, and groundwater contamination in Siwa Oasis through an integrated approach combining advanced monitoring techniques, machine learning, and innovative desalination technologies. By developing accurate conceptual and numerical models and sustainable management strategies, this research contributes to the broader goal of ensuring water security and agricultural productivity in arid regions.

2. Problem statement and research aim

Siwa Oasis, a unique and ecologically sensitive region in Egypt's Western Desert, is confronting a severe and multifaceted water crisis that threatens its long-term sustainability. The Oasis is entirely dependent on groundwater resources, drawing from two principal aquifers: the shallow Tertiary Carbonate Aquifer (TCA), which is the primary source for agricultural irrigation, and the deep Nubian Sandstone Aquifer (NSSA), which provides essential fresh water for drinking and domestic use. However, decades of unsustainable water management practices, including over-extraction and inefficient flood irrigation, have precipitated a cascade of interconnected environmental problems. These include widespread waterlogging and soil salinization, which have led to a significant decline in agricultural productivity. Concurrently, the intensive exploitation of both aquifers has resulted in declining water levels and a marked deterioration in water quality. The TCA is experiencing increasing salinity. The NSSA is also showing signs of stress, with falling water levels and instances of localized contamination. Furthermore, recent investigations have revealed the presence of toxic metals in both soil and water, posing a considerable risk to human health and the delicate ecosystem of the Oasis. These anthropogenic pressures are compounded by the complex geological and hydrogeological setting of the Oasis, which is characterized by a network of faults and fractures that govern groundwater flow and facilitate mixing between the TCA and NSSA. The region's extreme aridity, with high evaporation rates and negligible rainfall, further exacerbates the challenges of water scarcity and salinization. To address these pressing issues, a holistic and integrated research approach is essential.

This PhD thesis presents a holistic and multi-disciplinary investigation into the complex hydrogeological system of the Siwa Oasis, Egypt. Faced with escalating water scarcity, soil salinization, and water quality degradation, this research aims to provide a comprehensive scientific

basis for the sustainable management of the oasis's vital groundwater resources. To achieve this overarching goal, the study is structured around seven interconnected research objectives:

1. **To Develop a High-Resolution 3D Hydrogeological Model:** To pioneer a novel, cost-effective workflow integrating machine learning (SOM, K-means) with geophysical data (well logs, gravity, magnetics) to accurately characterize the subsurface architecture, delineate aquifer and aquitard layers, and map the structural fault systems that control groundwater flow and inter-aquifer connectivity.
2. **To Diagnose the Drivers of Soil Salinization and Water Quality Degradation:** To utilize multi-temporal remote sensing (Landsat) and machine learning (SVM) to quantify the spatio-temporal dynamics of land use change, lake expansion, and soil salinization over a 30-year period, and to link these changes to the underlying hydrogeochemical processes through detailed water chemistry analysis.
3. **To Identify Groundwater Recharge Sources and Quantify Mixing Ratios:** To employ a multi-isotope approach ($\delta^{2}H$, $\delta^{18}O$) combined with advanced statistical analysis (PCA, K-means) and inverse geochemical modeling (NETPATH) to definitively identify the sources of recharge to the shallow aquifer (TCA) causing groundwater salinization and to quantify the mixing ratios between fresh, deep groundwater and saline surface water (salt lakes).
4. **To Determine Groundwater Residence Times and Validate Recharge Pathways:** To apply a suite of isotopic tracers (including $^{87}Sr/^{86}Sr$ and ^{14}C) and a dual-model approach including forward and inverse mixing models (Faure and NETPATH) to estimate the age of the groundwater, validate the recharge pathways identified in the previous aim, and provide a quantitative understanding of the temporal dynamics of the aquifer system.
5. **To Develop a Predictive Numerical Flow Model for Sustainable Management:** To construct and calibrate a fully integrated, three-dimensional numerical flow model (FEFLOW) that can simulate the long-term impacts of groundwater abstraction, predict future water level declines, and use reverse particle tracking to visually validate the conceptual model of inter-aquifer flow and recharge.
6. **To Assess Water Quality Suitability and Associated Human Health Risks:** To develop and apply a novel Integrated Weighted Water Quality Index (IWQI), FFBP-NN prediction model, and a probabilistic health risk assessment (Monte Carlo simulation) to evaluate the suitability of the groundwater for drinking purposes and to quantify the carcinogenic and non-carcinogenic health risks associated with exposure to potential toxic elements.
7. **Develop Innovative, Low-Cost Desalination Technology:** To synthesize, characterize, and test a novel zeolite/geopolymer (Z/GP) membrane derived from abundant, natural materials as a sustainable and economically viable solution for the desalination of brackish groundwater, thereby offering a practical technological intervention to mitigate water scarcity in the region.

By systematically addressing these seven aims, this thesis provides an unprecedentedly detailed and integrated understanding of the Siwa Oasis hydrogeological system, offering critical scientific insights and practical tools to guide its sustainable management and ensure its long-term viability.

Potential Challenges and Limitations

The successful achievement of this study's comprehensive objectives is subject to several potential challenges and limitations. The accuracy of the 3D geological model, for instance, is highly dependent on the quality and spatial distribution of the available well log data. A scarcity of data in certain areas of the Siwa Oasis may introduce a degree of uncertainty into the model. Similarly, the interpretation of gravity and magnetic data can be inherently ambiguous, and the structural features identified through these methods will require careful validation against other geological and hydrogeological data. The application of isotopic and geochemical tracers also carries its own set of uncertainties. The interpretation of groundwater age and mixing processes relies on a number of assumptions within the NETPATH and Faure models, which may not fully capture the intricate complexities of the aquifer system.

Furthermore, the development of the proposed zeolite/geopolymer membrane is an experimental process, and challenges related to material synthesis, scalability, and long-term performance under real-world field conditions are anticipated. To mitigate these potential challenges, a number of strategies will be employed. These include the cross-validation of results obtained from different methods, such as using the groundwater flow model to validate the findings of the multi-isotopic tracer mixing model. Pumping tests will be conducted to validate the hydraulic conductivity values calculated from well logs. The interpretation of gravity and magnetic data will be supported by inversion methods to validate the structural controls on groundwater flow paths. Lithological logs will be used to validate the results of the cluster analyses, and backward particle tracking will be applied to the available well and spring data to further refine the understanding of groundwater flow paths.

3. Study area description

3.1. Geographical location

Siwa Oasis is an isolated closed depression located in the northwestern desert of Egypt (**Fig 1**). It is surrounded by the Mediterranean Sea to the north (approximately 330 km away), the Libya-Egypt border to the west (70 km), and Cairo to the east (560 km). The depression lies between latitudes 29.12°N and longitudes 25.43°E. Siwa Oasis is characterized by three major economic activities: agriculture, industry, and tourism. Agriculture primarily involves the cultivation of palm trees, olives, fruits, and vegetables. The industrial sector includes mineral water bottling and olive oil extraction, while tourism focuses on medical treatment. The oasis has an elongated shape, stretching approximately 82 km in an east-west direction, with a width ranging from 2 to 20 km. Its total area is about 1,050 km² (250,000 feddans), and as of 2010, the population was approximately 23,546 residents[5].

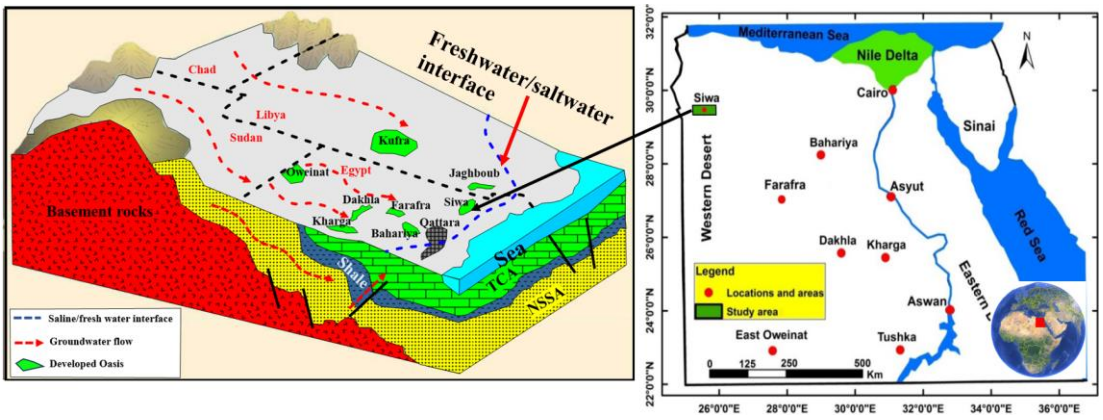

Figure 1. Location map and regional scale of the aquifer systems in Egypt

3.2. Geomorphology

The topography of Siwa Oasis is diverse, with elevations ranging from 19 meters below sea level to 154 meters above sea level (Fig 2a). The area comprises several distinct geomorphological units. Mobile sand dunes dominate the southern part of the depression, while a steep escarpment of limestone plateau is found in the northern region. The central part of the oasis features a flat depression that includes agricultural land, salt lakes, and playas. Major lakes in this depression, such as Zeitoun, Aghourmy, Siwa, and Maraqi lakes (Fig 2a, b), are fed by drainage water from agricultural lands. These lakes play a significant role in the local ecosystem and hydrology, although their salinity has increased over time due to high evaporation rates and agricultural runoff [7].

3.3. Geology and depositional environment of the study area

The geology of Siwa Oasis is characterized by a complex stratigraphic sequence that includes both surface and subsurface formations (Fig 2b, c). The stratigraphy of the Siwa Oasis spans above basements (granite), from the Lower Carboniferous to the Quaternary, reflecting a dynamic interplay between marine transgressions, fluvial sedimentation, and tectonic deformation [36]. This region is part of the broader Western Desert Basin, which includes sedimentary sequences influenced by Tethyan marine incursions and subsequent continental processes [36,37]. Fig 3a is a lithological cross-section that provides a detailed view of the distribution of carbonates, sands, shales, and Quaternary deposits in the study area. The stratigraphic framework of the Siwa Oasis consists of several distinct lithological units (Fig 3a). The oldest unit is the Lower Carboniferous Formation, composed of shales and sandstones deposited in shallow marine environments.

These sediments reflect a phase of marine transgression and subsidence, which facilitated the accumulation of fine-grained deposits in low-energy settings [38]. Overlying the Carboniferous shales are the lower and Upper Cretaceous deposits, which include fluvial-deltaic sandstones and shales. The Bahariya Formation and Alam El Bueib Formation are key components of this sequence, representing deposition in dynamic fluvial and deltaic environments influenced by tectonic uplift and erosion of nearby highlands [36,39]. These formations were deposited during periods of alternating sea-level rise and fall, which controlled sediment supply and accommodation space. The Tertiary

period is marked by the deposition of extensive carbonate platforms, represented by the Marmarica Formation. This formation consists of lagoonal, transitional, and fully marine carbonates, reflecting deposition in warm, shallow marine environments under relatively stable tectonic conditions [38]. The carbonates include lime mudstones, wackestones, and packstones, indicating variations in water depth and energy levels. The uppermost part of the stratigraphic column consists of Quaternary deposits, composed of unconsolidated sands, gravels, and clays. These sediments were deposited in fluvial, alluvial, and aeolian environments, reflecting the modern arid climatic conditions of the region [40].

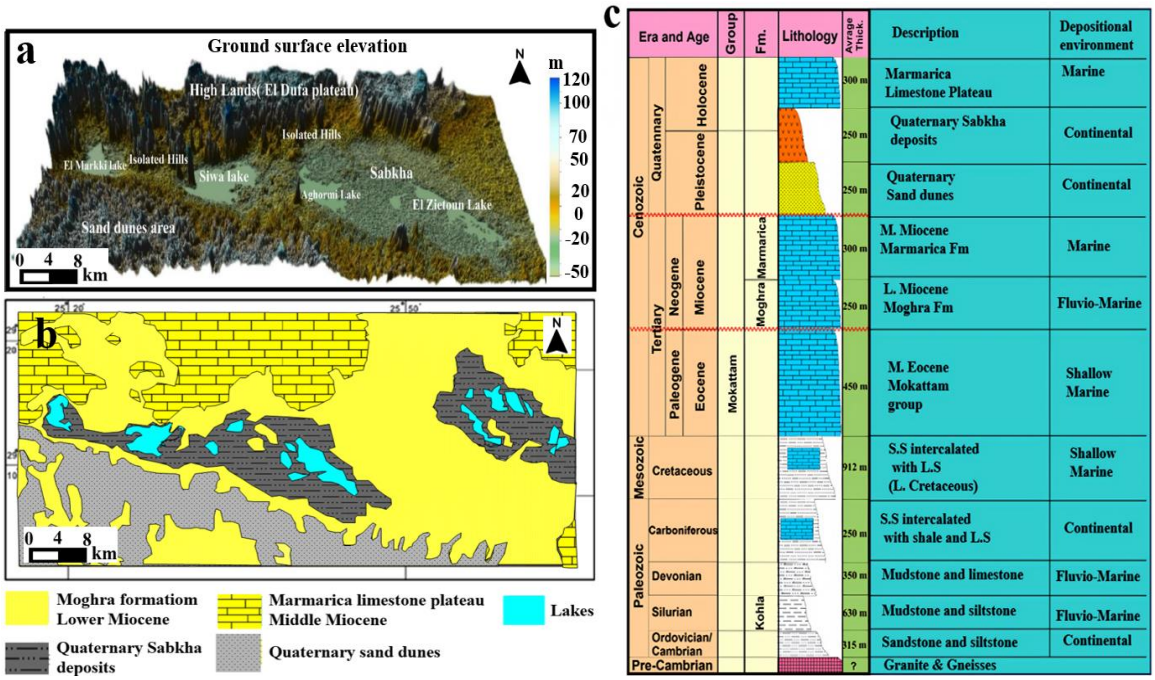

Figure 2. Geomorphological map including the most important features (a) and surface geological map (b), and subsurface geological column (c) of Siwa Oasis.

3.4. Climate

Siwa Oasis experiences an extreme arid climate, characterized by cold winters and hot, dry summers. The average annual air temperature ranges from 14.12°C to 29.32°C. Soil temperatures at a depth of 5 cm can reach up to 32.8°C. Wind patterns in the oasis are dominated by three primary directions: SE, NW, and NE, with frequencies of 12.4%, 24.4%, and 18.2%, respectively. These winds contribute to erosion and deflation, particularly in April, when they transport salt particles and loose sand, depositing them in lowland areas. Based on 20 years of meteorological data (**Table 1**), the Oasis experiences hot summers and mild winters, with an annual mean temperature of 21.3°C. The hottest months are June, July, and August, with mean temperatures reaching up to 29.25°C, while the coldest month is January, with a mean temperature of 11.7°C. Rainfall is exceptionally scarce, with a total annual average of only 9.6 mm [5]. The summer months (June, July, August, and September) are virtually rainless. The relative humidity is low, averaging 45% annually, and drops to as low as 33% in May. Conversely, the potential evapotranspiration (ETo) is extremely high, with a total annual

value of 2265 mm, far exceeding the annual rainfall. This significant water deficit, driven by high temperatures and low humidity, underscores the region's dependency on groundwater and highlights the hydrogeological challenges posed by the arid climatic conditions.

Table 1: Climatological data from Siwa meteorological station based on monthly mean of 20 years monitoring.

Month	Mean Temp. °C	Rainfall mm/month	Relative Humidity %	EP mm/Month	ETo (mm/day)
January	11.7	0.8	55	62	3.2
February	13.4	2	45	101	3.9
March	16.4	0.7	44	175	5.6
April	20.85	0.9	37	229	7.4
May	25.55	1.5	33	274	8.7
June	28.2	0	35	276	9.3
July	29.25	0	37	283	9.2
August	29	0	40	255	8.4
September	26.55	0	46	192	6.7
October	23.2	0.3	50	151	5.3
November	18.15	0.6	53	100	3.8
December	13.3	2.8	60	67	2.9
Annual mean	21.3	-	45	188.75	74.4
Annual total	-	9.6	-	2265	-

3.5. Water Resources and hydrogeology

Siwa Oasis relies heavily on both surface water and groundwater resources. Historically, the presence of four major lakes attracted settlers to the area. However, increasing salinity caused by high evaporation rates and agricultural drainage has rendered these lakes unsuitable for domestic use [8]. The hydrogeology of Siwa Oasis is dominated by two main aquifer systems: the deep NSSA and the shallower TCA. These aquifers are part of a thick sedimentary sequence (approximately 3400 m) that ranges in age from the Paleozoic to the Recent. The cross section of the aquifer systems (**Fig 3a**) from west to east showed that Nubian aquifer consists of multi layers affected by fault system and isolated from the TCA by aquiclude layer (upper cretaceous shale) modified after Elsheikh [1].

The geological structure of the Oasis is complex, with a network of normal faults trending in N-S, E-W, NE-SW, and NW-SE directions [41]. These faults play a critical role in controlling the lithofacies variations, the thickness of the geological formations, and the occurrence of natural springs [40]. The NSSA is a vast, non-renewable fossil aquifer that underlies a large part of North Africa. In the Siwa Oasis, the NSSA is the primary source of fresh water, with a total dissolved solids (TDS) content of less than 256 mg/l [40]. The aquifer is composed of sandstone with intercalations of shale and clay. The water in the NSSA is over pressure (artesian). The recharge to the NSSA is believed to have occurred during the pluvial periods of the late Pleistocene and early Holocene, and there is limited evidence of significant modern recharge [42]. The groundwater flow from the south east and south west to the north and central Siwa Oasis (**Fig 3b**).

The TCA overlies the NSSA and is the primary source of water for irrigation in the Siwa Oasis. It is a semi-confined aquifer composed of Eocene-Miocene limestone and dolomite, with intercalations of shale, siltstone, sandstone, and evaporite deposits. The average thickness of the TCA is approximately 550 m [40]. The discharge from the TCA occurs through a large number of wells and natural springs, with a total discharge rate of approximately 442,000 m³/day [40]. The water quality of the TCA is highly variable, with salinity ranging from fresh to brackish and even saline in some areas. The TDS content can be as high as 8000 mg/l [40]. The groundwater flow from south west to the north east and north west in shallow tertiary carbonate aquifer (TCA).

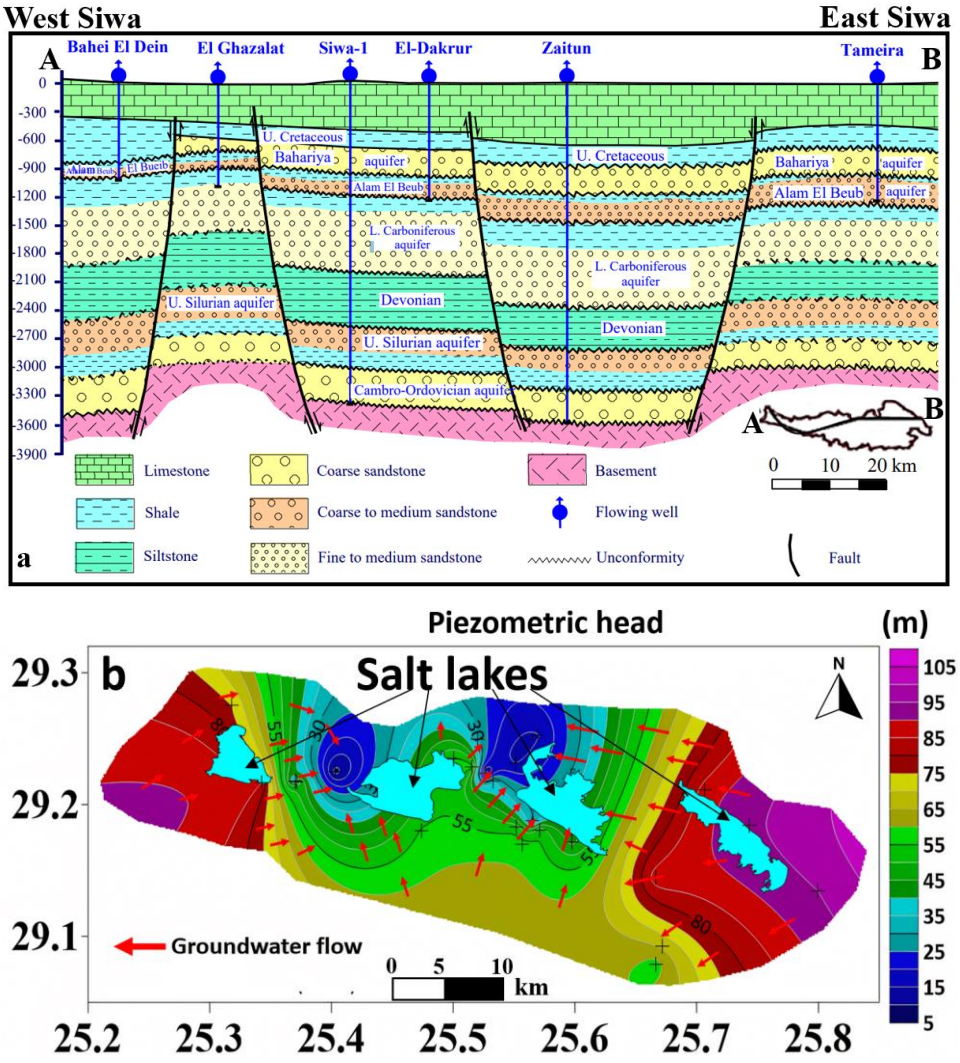

Figure 3. East-west cross section of the subsurface geology of Siwa Oasis modified after Elsheikh [1] (a), groundwater flow direction (b).

Based on previous studies and literatures, **Table 2** shows the comparison between NSSA and TCA in depth, geology, geochemistry, and uses of water in each aquifer.

Table 2. Comparison between NSSA and TCA based on literatures and previous studies

Feature	TCA	NSSA	References
Depth	Shallow, 10-510 m	700 - 3240 m	[40]
Geology	Fractured limestone, Miocene age	Paleozoic and Mesozoic (Pre-Upper Cenomanian).	[1,40]

		Fine to coarse sandstone with shal e layers.	
Geochemistry	Highly variable, from fresh to saline (1500 - 8100 ppm)	Generally fresh, with salinity incr easing westward (190 - 365 ppm i n upper parts)	[43]
Use	Agricultural and domestic purposes	Main source of freshwater, used for bottling drinking water	[44]
Hydraulic Conductivity (K) (m/day)	0.1 - 10	0.41 - 6	[10,45]
Transmissivity (T) (m^2/day)	10 - 1000	69 - 73	[10,45]
specific yield	0.21-0.24	0.19	[10,45]
specific storage (m^{-1})	0.000036-0.000047	0.000069	[10,45]
Aquifer Type	Confined to semi-confined, highly fractured	Confined	[43]
Sub-aquifers	Five distinct zones based on d epth and lithology	Bahariya, Alam El Bueib, Lower Cretaceous, Upper Silurian, Camb ro-Ordovician	[43]
Porosity	Secondary porosity	20 - 30% (Bahariya Formation)	[43]
Piezometric Head	Variable, generally lower than NSSA	High, decreases westward	[43]

4. Material and methods

To determine all the challenges in Siwa Oasis regarding water quality and quantity and find optimum solutions for these challenges, integrated approaches were applied with different materials and datasets as follow (**Fig 4**):

A) understand the aquifer systems from the geological and hydrogeological point of view to determine the lithofacies, aquifer and aquitard layers, heterogeneity, and build the geometry of the aquifers system. To achieve this, well logs including GR, SP, R, and lithological logs were used as well as applying two types of cluster analysis (K-means and SOM) to predict the lithofacies for the wells that lack the lithological logs

B) To determine the fracture and fault system that control the groundwater flow and location where different water resources could mix between different aquifers and surface water, aeromagnetic data with edge filtering were used and validated with 2D and 3D inversion and well logs correlation.

C) To determine petrophysical and hydraulic parameters that are very important factors needed in the Numerical flow model, pumping test data and well logs data were used based on cooper Jacob and Kozeny Karmen methods.

D) The remote sensing data and SVM were used to detect the changes in the surface area of the salt lakes and water logging in the soil that increased the soil salinization and reduced plant production.

E) The physicochemical parameters, heavy metal, stable isotopes, and radiocarbon were used for several aims including 1) type of salts and minerals could accumulate in the soil using

PHREEQC geochemical model, 2) determine the recharge source, salinity origin, residence time, and mechanism controlling water chemistry in the aquifer system based on different mixing models, 3) The suitability of water resources for drinking purposes and health risk of toxic metals using ANN and Monte Carlo simulation.

F) Integration of multiple data and results from previous findings of using well logs, aeromagnetic data, pumping test, remote sensing, stable isotopes and radiocarbon to build numerical flow model and estimate the sustainability of the groundwater in the aquifer systems and predict the future risk from drawdown in the water level. The model also aimed to validate the findings of the multi-isotopic data regarding groundwater salinization and recharge source.

G) Examination of innovative solution to decrease groundwater and soil salinization using raw material such as Diatomite and Kaolinite to create effective Zeolite geopolymer in salt rejection.

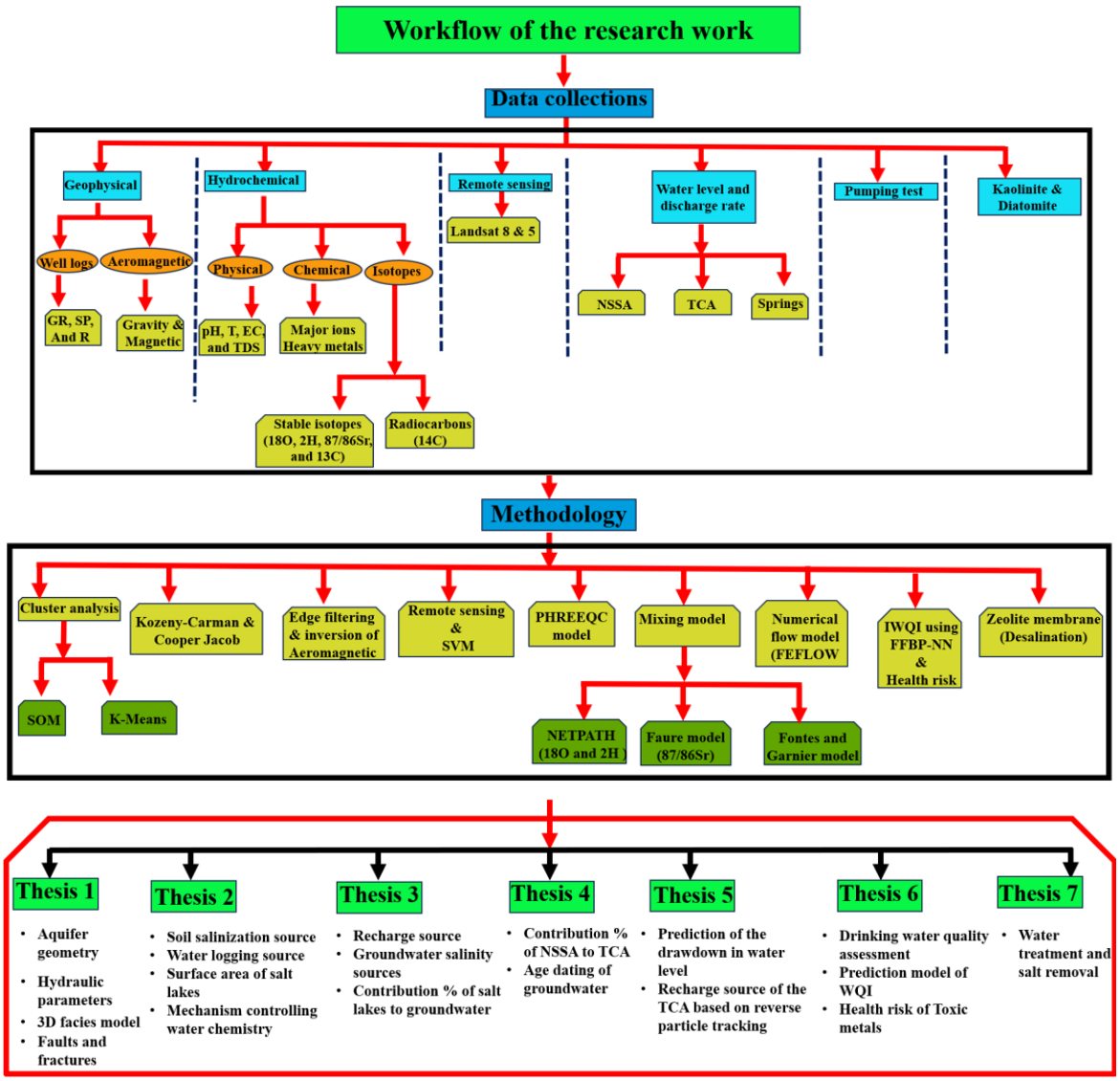

Figure 4. The research framework showing the datasets used, methodology, and results

4.1.Aquifer characterization and structure system delineation

Well logging is a vital technique employed for characterizing aquifers and understanding environmental deposition processes [46]. In this study, well logs including Gamma Ray (GR), Spontaneous Potential (SP), shallow and deep resistivity logs, along with water resistivity measurements were analyzed to delineate lithological boundaries and identify aquifer zones. GR logs were employed to distinguish between sand and shale formations, providing valuable insights into depositional environments. SP logs were used to detect permeable zones and lithological transitions, while resistivity logs provided essential data for evaluating porosity, water saturation, and the hydraulic properties of the aquifer system. Additionally, pumping test data were utilized to calculate key hydrogeological parameters, such as hydraulic conductivity and transmissivity. Together, these datasets enabled the identification of aquifer layers and their hydraulic connectivity, contributing to a comprehensive understanding of the subsurface environment. Furthermore, this study presents a significant methodological advance by integrating high-resolution aeromagnetic and gravity data to map the deep structural framework controlling the aquifer system. The current study relied on 15 wells penetrating the aquifer systems and **Fig 5** shows the distribution of the wells

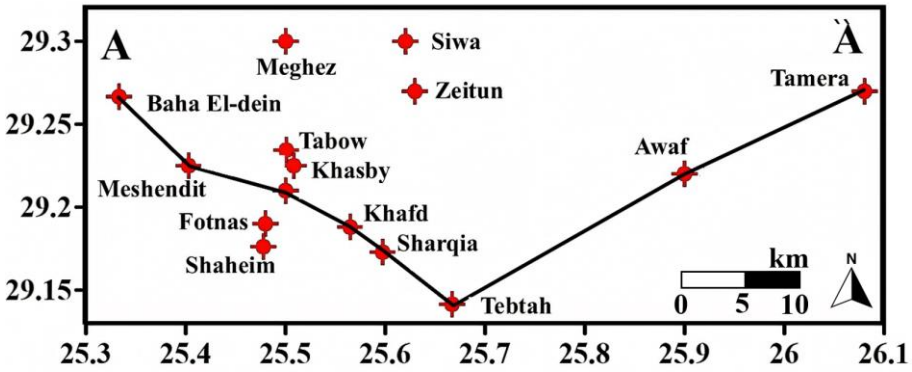

Figure 5. The distribution of the wells in Siwa Oasis penetrating the aquifer systems

4.1.1. Aquifer and aquitard layers detection based on cluster analysis

Cluster analysis is a powerful method used to differentiate aquifer layers based on well log data [15–17]. In this study, GR, SP, and resistivity data of formation and water content (R_t and R_w) were utilized to perform clustering, enabling the distinction between various lithologies, such as shale and sand. By applying advanced clustering techniques, including Self-Organizing Maps (SOM) and k-means, distinct clusters were generated to represent aquifer layers and evaluate their key properties, such as porosity and hydraulic conductivity. This approach facilitated the identification of boundaries between aquifer zones and provided a more accurate characterization of the subsurface lithofacies.

4.1.2. Self-organizing map (SOM)

In this study, SOM was utilized to classify subsurface lithologies and delineate aquifer layers based on well logs data. SOM, also referred to as Kohonen maps [47], are a type of artificial neural network commonly employed for unsupervised learning and dimensionality reduction. They are particularly effective for clustering and visualizing high-dimensional data in a lower-dimensional space while

preserving the topological relationships among data points [17]. This unique capability enables a detailed and continuous interpretation of subsurface lithological variations, making SOM an invaluable tool for identifying aquifer heterogeneities and lithological boundaries [48].

The SOM inputs included GR, SP, deep resistivity (R_d), and resistivity of water (R_w) key parameters that reflect lithological and hydrogeological variations. The SOM was implemented using the SOM Toolbox in MATLAB. This process maps multi-dimensional data into a two-dimensional grid while maintaining the spatial relationships of the original dataset. To ensure optimal configuration of the SOM, Vesanto's rule was applied to determine the appropriate number of output neurons. This rule provides a formula (Eq 1) to estimate the number of neurons based on the complexity and size of the dataset (Fig 6), ensuring the SOM is well-suited to handle the input data effectively [49].

$$N = 5\sqrt{s} \qquad (1)$$

N is optimal number of output neurons and s is the total number of samples in the dataset. The factor 5 ensures sufficient neurons to adequately represent the dataset's variability, while the square root of the sample size balances the complexity of the SOM, avoiding oversimplification or overfitting. After determining N, it was distributed across a two-dimensional grid (e.g., m×n, where m×n≈N) to create a visually interpretable layout.

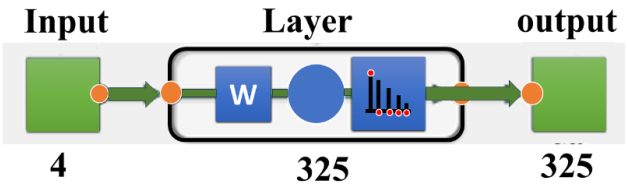

Figure 6. The structure of the SOM showing the number of input parameters and neurons used for clustering.

The process began with data normalization to standardize the input variables, ensuring that each parameter contributed equally to the clustering process. Subsequently, SOM training was performed using a competitive learning algorithm, where input data vectors were mapped to neurons in the output layer based on similarity. The Best Matching Unit (BMU) was identified for each input vector (x), and the weight vectors of neighboring neurons (Wj) were adjusted iteratively to refine the clustering. The training process begins with the initialization of variables, including the weight vectors (Wj), the winner constraint, and the learning rate (η(t)). The weight vectors are randomly initialized within the range of the input data, while the learning rate and neighborhood size start with large values that decrease progressively during training. The BMU was calculated using a distance metric such as the Euclidean distance. The weight vectors of the BMU and its neighboring neurons are then updated to move closer to the input vector (Eq 2) and the neighborhood function, typically a Gaussian function, ensures that the BMU and its surrounding nodes are updated, but nodes farther away are updated less (Eq 3).

$$\mathbf{W_i(t+1) = W_i(t) + \eta(t) \cdot h_{i,BMU}(t) \cdot \left(X - W_i(t)\right)} \qquad (2)$$

$$\mathbf{h_{i,BMU}(t) = \exp\left(-\frac{\|r_i - r_{i,BMU}\|^2}{2\sigma^2(t)}\right)} \qquad (3)$$

hj,BMU(t) is the neighborhood function, typically Gaussian with r_i representing the position of neuron i in the SOM grid and σ(t) denoting the neighborhood radius, which decreases over time. The learning rate (η(t)) and neighborhood radius are gradually reduced as the training progresses, allowing for finer adjustments to the weight vectors in the later stages of learning. As training continues, the neurons' weight vectors separate from each other, forming distinct categories or clusters that represent the input data. The process stops when a predefined stopping criterion, such as a maximum number of iterations or minimal change in weights, is reached. The resulting 2D map provides an intuitive and visual representation of the clusters and their relationships, making it a powerful tool for exploratory data analysis.

The number of clusters was predetermined using two approaches: (1) analysis of lithological logs to identify distinct stratigraphic units and (2) computation of the silhouette score to optimize the clustering structure. This combination ensured that the SOM accurately captured the geological characteristics of the subsurface and differentiated between various lithologies and aquifer layers effectively.

4.1.3. K-mean cluster analysis

k-means clustering analysis was applied to identify lithological units and aquifer zones within the groundwater system using well log data (GR, SP, Rd, and Rw). The selected logs, which include key indicators of lithology, were used as input features for the clustering process. K-means clustering works by partitioning the dataset into a predefined number of clusters, minimizing intra-cluster distances while maximizing the separation between clusters. The similarity between data points was measured using the Euclidean distance. The Euclidean distance (D_E) between two points in an n-dimensional space, represented as x = (x1, x2, …, xn) and y = (y1, y2, …, yn), is calculated based on the following formula (Eq 4):

$$D_E = \sqrt{\sum_{i=1}^{n}(x_i - y_i)^2} \qquad (4)$$

To determine the optimal number of clusters, the silhouette score was utilized. A higher silhouette score indicates a better-defined clustering structure, ensuring that the selected number of clusters effectively represents the lithological variations.

4.1.4. Petrophysical parameters estimation

The petrophysical parameters were derived from geophysical logging data, specifically GR and Rt logs, tortuosity (a) and cementation factor (m). The key parameters estimated include formation factor, total and effective porosity, and shale volume. The formation factor (F), introduced by Archie [50] through empirical testing, is defined as the ratio of the resistivity of a clean, water-saturated aquifer (Rt) to the resistivity of the pore water (Rw) (Eq 5). In this study, Rw values were determined through the chemical analysis of groundwater samples which was corrected based on the water temperature.

$$F = (Rt / Rw) \qquad (5)$$

Archie proposed a method to relate factor of formation and total voids or porosity in sediments (Eq 6). However, a key limitation of this formula is its sensitivity to shale content, often leading to overestimation of porosity in formations with significant shale. Despite this limitation, the formula remains valuable for formation mainly composed of sand grains and low percentage of shale.

$$F = a*(Ø)^{-m} \qquad (6)$$

Where (a) represent tortuosity factor and (m) is the cementation factor. From the literature the (a) and (m) were estimated to be 1 and 2 respectively [51]. Total porosity (Øt) accounts for all pore spaces within the rock, while effective porosity ($Ø_{eff}$) represents only the interconnected pores, excluding the contribution of shale volume (V_{sh}). In this approach of study, effective porosity is estimated based on standard formula (Eq 7).

$$Ø_{eff} = Ø_{total} * (1-V_{sh}) \qquad (7)$$

Estimating shale volume (V_{sh}) is essential because it significantly influences key petrophysical parameters, including two types of porosity (total and effective porosity). In this study, V_{sh} is calculated using a non-linear relationship [52] (Eq 8). This formula was developed to minimize the overestimation of V_{sh} by incorporating the gamma-ray index (Iγ) of the targeted formation.

$$V_{sh}=0.33(2^{2*I\gamma}-1) \qquad (8)$$

The gamma-ray index (I_γ) is determined using a linear equation (Eq 9) introduced by Schlumberger (1984). This formulation establishes a relationship between the natural GR_{log}, the GR for clean sand (GR_{min}), and the gamma-ray reading for shaly layers (GR_{max}).

$$I_\gamma = (GR_{log}-GR_{min})/(GR_{max}-GR_{min}) \qquad (9)$$

4.1.5. Hydraulic conductivity using well logs

In this study, a set of geophysical logs was conducted in a 15 deep well and the depth of well logs could reach 1200 m below sea level. One of the most recognized derivations of permeability based on the medium's characteristics was introduced by Kozeny [53] and later refined by Carman [54]. Consequently, it is commonly referred to as the Kozeny-Carman equation in the literature. Over time, the equation has been presented in various forms, one of which was provided by Bear (Eq 10) [55].

$$k = \left(\frac{\delta w g}{\mu}\right) \cdot \left(\frac{d^2}{180}\right) \cdot \left(\frac{\emptyset^3}{(1-\emptyset)^2}\right) \qquad (10)$$

In this equation, *K* represents the hydraulic conductivity, *d* is the grain size diameter (cm), δw is the fluid density (0.9982 g/cm³ at 20°C), μ is the dynamic viscosity (0.019 g/cm·sec at 20°C), and *g* is the acceleration due to gravity (980 cm/sec²). This equation calculates the saturated hydraulic conductivity based on grain size distribution [55,56] and has been shown to reliably predict the saturated hydraulic conductivity of most soils [57]. To apply the Kozeny-Carman equation, the grain size diameter is required. For the Nubian sandstone, the grain size diameter is 0.5 mm based on literature and grain size analysis [58].

4.1.6. Hydraulic conductivity using pumping test

Pumping tests serve as crucial field experiments aimed at collecting information on groundwater extraction rates and hydraulic characteristics. In this research, data from pumping tests conducted at seven groundwater wells are examined to assess aquifer properties, such as transmissivity (T) and hydraulic conductivity (K). The hydraulic parameters derived from geophysical well logging was cross-checked with those obtained from pumping tests to confirm the accuracy of the geophysical approach. The duration of each test spanned up to 24 hours, with T and K calculated using the Cooper and Jacob [59] technique, specifically tailored for leaky confined aquifers experiencing transient flow conditions (NSSA). This approach involves plotting the elapsed time since pumping began against the observed drawdown on a semi-logarithmic scale and fitting a straight line to the data. The slope of this line over one logarithmic cycle yields the average drawdown (Δs) and transmissivity (Eq 11).

$$\Delta s = 2.3Q/4\pi T \qquad (11)$$

Since hydraulic conductivity (K) represents the rate of flow per unit width of the aquifer, and transmissivity (T) defines the rate of flow over the entire thickness (b) of the aquifer, Equation 12 is used for the calculation of K from the T

$$T = K * b \qquad (12)$$

4.1.7. Fracture and fault systems delineation

Delineation of the fracture and fault system in Siwa oasis is crucial where the connection between the different aquifers is controlled with these elements. This study relies on three main datasets to explore the subsurface characteristics of Siwa Oasis: airborne gravity data and magnetic data, and Digital Elevation Model (DEM) topography data. These datasets work together to provide a detailed understanding of the region's structural and geological features. The gravity data, sourced from the Getech Group, consist of a 10 km (5-minute) grid of Bouguer anomaly recorded at 600 meters above ground. The magnetic data, also provided by Getech, include a consolidated 1000-meter grid of total magnetic intensity (TMI). This grid was created using aeromagnetic data, along with Magsat data, at an average terrain clearance of 1000 meters, with 10 nT contour intervals and 3000-meter line spacing.

4.1.7.1.Lineament Extraction

To extract lineaments from the gravity data, several advanced filtering techniques were applied to the Bouguer Anomaly. These techniques include the upward continuation, the Second Vertical Derivative (SVD), Horizontal Gradient (HG), Analytic Signal (AS), Tilt Angle (TA), and the Tilt Angle of the Horizontal Gradient (TAHG). Each filter plays a unique role in enhancing the visibility of geological structures, helping to identify both shallow and deep-seated contacts within the study area [18,37,60–62]. By combining these filters, subtle variations in gravity data are amplified, allowing for precise mapping of structural features that are critical for geological assessment.

4.1.7.2.Regional and residual separation

The upward continuation technique was used to project gravity data to higher elevations. This process smooths out short-wavelength anomalies linked to shallow structures, making deeper geological features more visible [63]. This method is particularly effective for mapping density variations in the subsurface, providing valuable insights into the region's geology [64]. In lineament extraction, upward continuation is often paired with techniques like the Total Horizontal Derivative (THD) to better define fault orientations [63,65]. The Bouguer gravity field, reflecting sources at various depths, is decomposed using upward continuation to separate shallow and deep anomalies. Upward continuation to heights of 1000 m and 7500 m chosen based on literature to target specific lineaments reduces the influence of shallow features as height increases. Jacobsen [66] notes that upward continuation to height z maps sources at or below z/2. The study focused on shallow carbonates (up to 0.5 km) to identify shallow lineaments. The deeper structures of NSSA included depth intervals were selected based on literature indicating basement depths of 3 to 3.5 km in the region [67].

4.1.7.3.Filtering Techniques

First Vertical Derivative (FVD)

The First Vertical Derivative (FVD) is a powerful tool for detecting geological edges by amplifying rapid changes in potential field data. Mathematically (Eq 13), it is expressed as:

$$\frac{\partial P}{\partial z} \qquad (13)$$

where P is the amount of the gridded gravity or magnetic anomaly reduced to the pole and z is the vertical direction. The FVD highlights the edges of geological structures, making it particularly useful for lineament mapping [68]. It is often combined with edge detection methods like the Total Horizontal Derivative (THD) to improve the accuracy of structural interpretations [69].
Applications of the FVD include identifying tectonic faults and mapping hydro-structural features that influence groundwater flow [70].

Second Vertical Derivative (SVD)

The Second Vertical Derivative (SVD) is widely used in potential field data interpretation to enhance sensitivity to shallow subsurface structures. Mathematically (Eq 14), it is expressed as:

$$\left\{\frac{\partial^2 P}{\partial z^2}\right\} = k_x^2 f\{P\} + k_y^2 f\{P\} = \left(k_x^2 + k_y^2\right) f\{P\} = |k|^2 f\{P\} \qquad (14)$$

where $f\{\,\}$ is the Fourier transform operator, so $f\{P\}$ is the Fourier transform of the potential field g or the total magnetic field T, k_x , k_y denote the wavenumbers in the x- and y-direction and $|k|$ is the modulus of the wavenumbers. The SVD acts as a high-pass filter, amplifying high-frequency components and enhancing shallow features like faults and lithological boundaries [71]. However, it also amplifies noise, so preprocessing steps such as low-pass filtering or upward continuation are often necessary [72].

Total Horizontal Gradient (THG)

The Total Horizontal Gradient (THG), also known as the Total Horizontal Derivative (THD), is calculated (Eq 15) as:

$$THG = \sqrt{\left(\frac{\partial P}{\partial x}\right)^2 + \left(\frac{\partial P}{\partial y}\right)^2} \qquad (15)$$

where P is the amount of the gridded gravity or magnetic anomaly reduced to the pole, $\frac{\partial P}{\partial x}$ and $\frac{\partial P}{\partial y}$ are the horizontal derivatives in the X and Y directions, respectively. The THG highlights abrupt changes in subsurface density, effectively outlining geological boundaries [72,73]. It is often integrated with the FVD and SVD to delineate the structural framework of the study area.

Analytical Signal (AS)

The Analytical Signal (AS) method enhances edge detection by utilizing the gradients of the potential field in the x, y, and z directions (Eq 16). The AS is calculated as:

$$AS = \sqrt{\left(\frac{\partial P}{\partial x}\right)^2 + \left(\frac{\partial P}{\partial y}\right)^2 + \left(\frac{\partial P}{\partial z}\right)^2} \qquad (16)$$

Where $\frac{\partial P}{\partial z}$ represents the vertical gradient of the gravity anomaly or reduced to the pole magnetic anomaly. (AS) is the amplitude of the analytic signal at (x, y), and (∂P/∂x, ∂P/∂y and ∂P/∂z) are the two horizontal and vertical derivatives of the gravity field respectively. The AS peaks over regions of significant density variation, delineating structural discontinuities [74].

Tilt Angle (TA)

The Tilt Angle (TA) method, introduced by Miller and Singh [75], is defined in Equation 17:

$$TA = tan^{-1}\left[\frac{\frac{\partial P}{\partial z}}{\sqrt{\left(\frac{\partial P}{\partial x}\right)^2 + \left(\frac{\partial P}{\partial y}\right)^2}}\right] \qquad (17)$$

The TA filter normalizes the vertical gradient of the potential field with respect to its horizontal gradient, providing a quantitative measure of the field's inclination. It is relatively insensitive to noise and is effective for detecting structural edges[76].

Tilt Angle of the Horizontal Gradient (TAHG)

The Tilt Angle of the Horizontal Gradient (TAHG), introduced by Ferreira[77], is calculated from Equation 18.

$$TAHG = tan^{-1}\left(\frac{\frac{\partial HG}{\partial z}}{\sqrt{\left(\frac{\partial HG}{\partial x}\right)^2 + \left(\frac{\partial HG}{\partial y}\right)^2}}\right) \qquad (18)$$

This method identifies the horizontal boundaries of buried geological structures by locating the maximum values of the TAHG.

Enhanced Horizontal Gradient Amplitude (EHGA)

The Enhanced Horizontal Gradient Amplitude (EHGA) method refines the edges of potential field data, enhancing the detection of both shallow and deep geological structures. It is calculated from Eq 19.

$$EHGA = R\left(asin\left(P\left(\frac{\frac{\partial HG}{\partial z}}{\sqrt{(\frac{\partial HG}{\partial x})^2+(\frac{\partial HG}{\partial y})^2+(\frac{\partial HG}{\partial z})^2}}-1\right)+1\right)\right) \quad (19)$$

Where R is the real part of the function and P is a positive number ≥2. The EHGA ranges from -$\pi/2$ to + $\pi/2$ when the peaks are directly located over the edges.

4.1.7.4.3D Density Interface Modeling using iterative Gravity Inversion

Geophysical inversion has advanced significantly due to improved data collection, visualization, and computational power. Gravity inversion, using linear and nonlinear methods, is crucial for mapping density distributions and geometries [78]. The flow diagram of the Grav3D code for estimating the 3D geometry of a horizontal density interface is illustrated in **Fig 7** [79]**.**

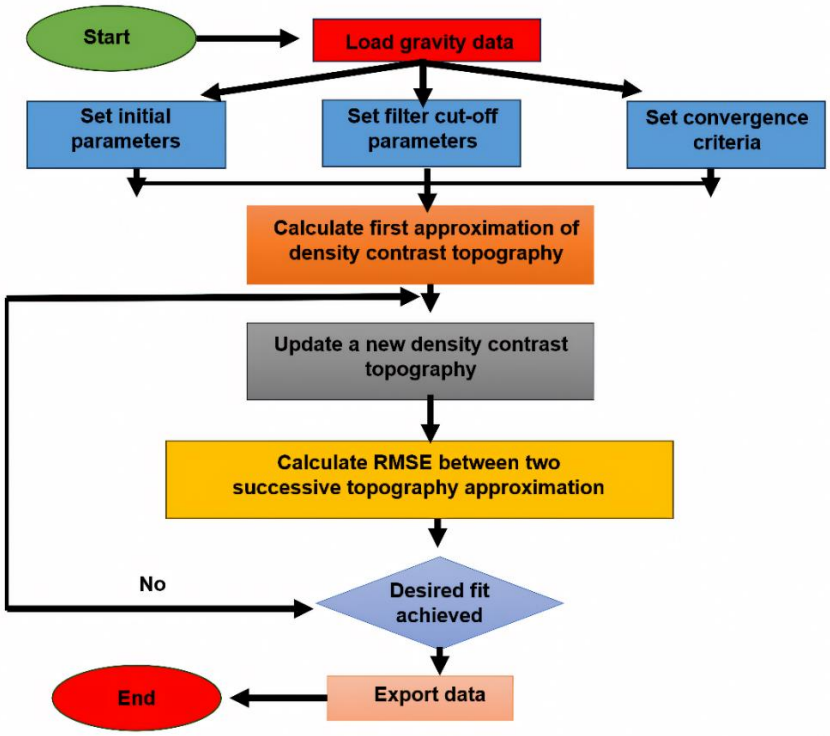

Figure 7. The flow diagram of the Grav3D code for estimating the 3D geometry of a horizontal density interface**.**

The iterative inversion process requires a low-pass filter for convergence. This study employs FFT-based inversion **(Eq 20),** combining Oldenburg's method with Xu's approach [80,81], to iteratively estimate perturbing body geometries from gravity anomalies, ensuring precise density interface reconstruction

$$\mathbf{h(x,y)} = \mathbf{F^{(-1)}}\left[-\frac{\mathbf{F[\Delta g(x,y)]e^{|k|z_0}}}{\mathbf{2\pi G\rho}} - \sum_{\mathbf{n=2}}^{\infty}\frac{\mathbf{|k|^{n-1}}}{\mathbf{n!}}\mathbf{F[h^n(x,y)]}\right] \quad (20)$$

h is the interface topography at coordinates (x,y), F and $F^{(-1)}$ denote the Fourier transform and its inverse, respectively, Δg is the gravity field, k is the radial wavenumber, z_0 is the average depth to the density interface, g is the gravitational constant, ρ is the density contrast. The iterative process begins by computing the Fourier transform of the first part of **Eq 20**, assuming z_0 =500 m, to obtain an initial approximation of the interface topography h. A new set of depth estimate is then calculated by using the **h** values from the previous step. The process continues until the convergence criteria are met hence the root mean square error (RMS) can be used to the measure the misfit between two successive depth estimates (**Eq 21**)

$$RMS = \sqrt{\frac{\sum_{i=1}^{M}\sum_{j=1}^{N}\left(h_{i,j}{}^{t+1} - h_{i,j}{}^{t}\right)^2}{M*N}} \quad (21)$$

where *M* and *N* are the numbers of grid size in north and east coordinates respectively, **t** is the iteration step. Using Grav3D software, input parameters include density contrast (Δρ), the mean depth of the density interface, the roll-off frequency parameters (SH and WH) for filtering, and the stopping criterion for the iterative process (default RMS threshold: 10^{-4}). This method requires careful specification of several user-defined hyperparameters that critically influence the inversion outcomes. Additionally, a major challenge in gravity inversion is the nonuniqueness of solutions, where multiple density distributions can reproduce the observed gravity anomalies equally well. To mitigate this, several a priori constraints were integrated into the inversion. For the shallow model (targeting 0 – 500 m depth), literature and previous studies on the area [82], as well as used well log data, indicated the presence of carbonate lithology and the average density of this upper layer was set at 2.2 g/cm³**.** This value was used as a fixed constraint in the initial model. The average depth to the carbonate unit was defined at 500 m, consistent with well log observations and the depth sensitivity of the filtering applied to the residual gravity map, which highlights features such as shallow faults, fractures, lithological boundaries within the sedimentary cover, and other sources located within the upper 500 m. For deeper structures, the underlying sedimentary rocks and basement units were assigned average densities of 2.6 g/cm³ and 2.7 g/cm³, respectively [82]. A similar approach constrained the mean depth to values around 3 to 3.5 km, consistent with prior geological and borehole data indicating the depth to the Precambrian basement. Furthermore, the inversion was validated by comparing estimated depth values with independent well log data from 14 wells distributed across the study area, improving confidence in the interpretation of the subsurface structural framework.

4.2.Detection of soil salinization source

The current study integrates remote sensing, machine learning (SVM), and hydrochemistry, to detect groundwater quality deterioration as well as soil salinization and water logging problem. A digital elevation model supported by machine learning was used to predict the change in the land cover

(surface Salt Lakes area, soil salinization area, vegetation cover, and water logging) and its effect on water quality deterioration.

4.2.1. Remote Sensing

To achieve consistent thematic mapping across a 30-year time series, four cloud-free Landsat scenes were collected for the same season in the years 1990, 2000, 2010, and 2020. The datasets include three Landsat 5 Thematic Mapper (TM) images (1990, 2000, and 2010) and one Landsat 8 Operational Land Imager (OLI) image (2020), all attained through US Geological Survey (USGS). The attributes of the TM and OLI sensors are outlined in Table 1s (Appendix 2). Given the significant changes within the study area, traditional land use/land cover (LU/LC) mapping methods proved inefficient. As a result, this study employed machine learning algorithms, particularly the support vector machine (SVM), for objective and consistent mapping. False color composites (FCCs) served as critical data inputs, allowing for optimal feature discrimination. For consistency, FCCs of the identical spectral intervals were utilized for all scenes. Specifically, FCC 7,4, and 2 with respect to Short-wave Infrared, Near Infrared, and Green in RGB were used for Landsat TM data, while FCC 7, 5, and 2 with respect to Short-wave Infrared, Near Infrared, and, and Blue were applied for Landsat OLI data. These FCCs were employed as reference maps for visual interpretation and extracting training and testing data. Six LU/LC classes lake water, wet sabkha, marshes or dry sabkha, vegetation cover, sand dunes, and Moghra formation were delineated based on visual overlay analysis and georeferenced maps. Training and testing data were maintained spatially constant across all scenes to ensure unbiased classification. Consistent with recommendations in prior studies [53–55], training data constituted 70 – 80% of the dataset, while testing data accounted for 20 – 30% (**Table 2s and 3s. Appendix 2**). These training pixels were used to train the classifier across the full band sets of Landsat TM and OLI sensors.

4.2.2. Machine Learning Model

The support vector machine (SVM) is a supervised learning model that separates classes by fitting a hyperplane in a multidimensional feature space, optimizing class separation by maximizing the margin between classes [83]. The hyperplane is formed exclusively by support vectors, which are a select group of training data points, guaranteeing a broad margin and reducing classification inaccuracies. This study adopted the radial basis function (RBF) kernel, as its efficacy has been demonstrated in similar remote sensing studies [84,85]. The kernel efficiently maps the input space to a higher-dimensional feature space, facilitating non-linear separability. A penalty parameter (C = 100) was included to address potential misclassifications during training, balancing margin width and misclassification tolerance. The SVM classifier, trained on the FCC inputs, effectively distinguished the six LU/LC classes. By leveraging the RBF kernel and spatially consistent training data, the model delivered robust and reliable classifications across the 30-year dataset.

4.2.3. Hydrogeochemical evaluation

4.2.3.1.Data collection and analysis

In 2022, a detailed hydrogeochemical assessment was performed to examine the groundwater and surface water quality in Siwa Oasis, involving the gathering of water samples (153 samples) from various resources **(Fig 8).** These included 19 samples from clastic aquifer (deep NSSA), 114 from the carbonate aquifer (shallow TCA), 8 from natural springs, 5 from saline lakes, and 7 from drainage channels that feed the lakes.

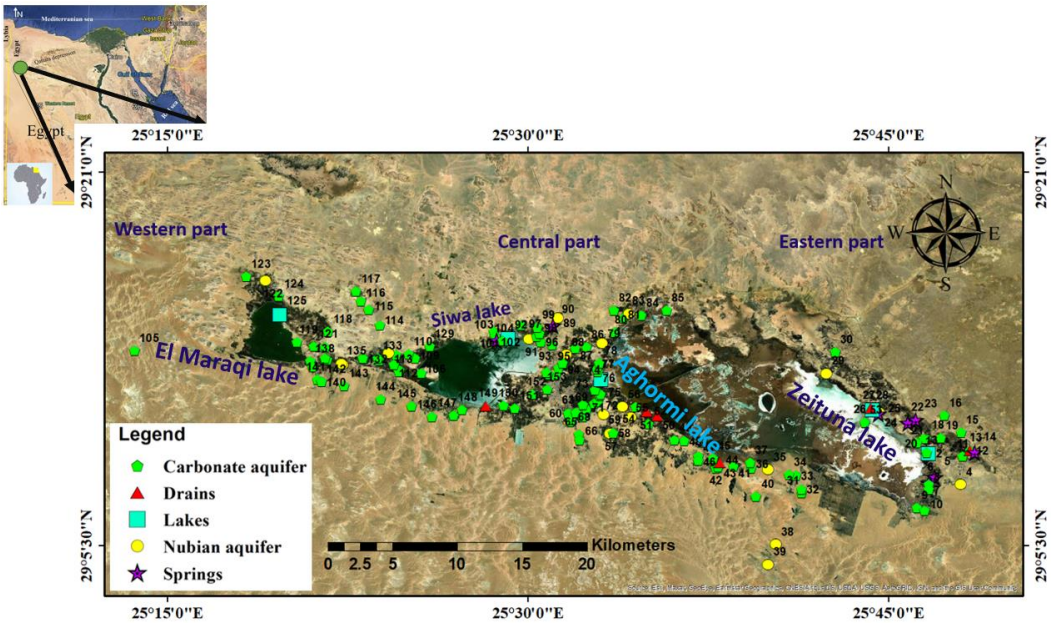

Figure 8. The coordinates of the investigated area (Siwa Oasis) showing the sampling points location and salt lakes distribution.

Field measurements for pH and EC were taken using portable instruments; a WTW model LF 538 pH meter was used for pH, and a YSI model 35 conductivity meter for EC. The major ions and metals were conducted in the laboratory of the desert research center, Matarya, Egypt. The metals were measured with ICP. The flame photometer was utilized for Na^+ and K^+ measurements. The titration with standard EDTA methods were performed to analyze total hardness and volumetric method for Alkalinity (CO_3^{2-} and HCO_3^-) measurements. Magnesium ions (Mg^{2+}) were derived from TH and calcium ions (Ca^{2+}) concentrations. Chloride levels (Cl^-) were determined through titration using silver nitrate ($AgNO_3$). Sulfate (SO_4^{2-}) concentrations were measured using a turbidimetric approach. Measurement accuracy, evaluated via ionic balance error (IBE), was assessed for ion concentrations in milliequivalents per liter (meq/L). IBE values remained within a ±5% range. Ionic balance (IB), which quantifies the percentage disparity between the total positive and negative ions in water **(Eq 22)**.

$$IBE = [(C - A) / (C + A)] \times 100 \qquad (22)$$

Where C = total cations and A = total anions. The toxic metals were examined using ICP. All measured parameters are reported in **Table 4s (Appendix 2)**

4.2.3.2.Mechanism controlling water chemistry

The geochemical modeling program PHREEQC [86] was employed to calculate the Saturation Index (SI) for various mineral phases in the collected water samples. This calculation was a critical step for two primary reasons: 1) to assess the potential for mineral precipitation from irrigation water, which can lead to soil salinization and reduced soil permeability, and 2) to provide essential constraints for the NETPATH inverse mixing models by defining the geochemical state of the end-member and mixed water samples.

The water's saturation level relative to different minerals was assessed using the following equation (Eq 23):

$$SI = Log\ (IAP / K) \qquad (23)$$

where SI represents the saturation index, IAP is the ion activity product, and K is the solubility constant. An SI value of zero indicates equilibrium, a positive value indicates supersaturation (potential for precipitation), and a negative value indicates undersaturation (potential for dissolution).

Input Parameters and Model Limitations

The calculation of the SI in PHREEQC was based on a comprehensive set of field and laboratory measurements. Input parameters included:

1) **Physical Parameters:** pH, EC, DO, T°c, and TDS
2) **Chemical Parameters:** Major ions (Ca^{2+}, Mg^{2+}, K^{+}, Na^{+}, Cl^{-}, SO_4^{2-}, HCO_3^{-}, CO_3^{2-}), nutrients (NO_3^{-}, NH_3), silica (SiO_2), and trace metals (Fe^{2+}, Fe^{3+}, Mn^{2+}, Ni^{2+}, Zn^{2+}, Cu^{2+}, Cd^{2+}, Cr, Pb, Ba, Sr).

Several measures were taken to ensure the reliability of the model and address its limitations. The potential for overestimation of mineral precipitation was acknowledged, particularly given the hot and arid climate of Siwa Oasis where evaporation can drive minerals out of solution. To mitigate uncertainties associated with field measurements, redox-sensitive species (Fe^{2+}/Fe^{3+}, Mn^{2+}/Mn^{4+}) and DO levels were carefully measured. All water sample temperatures were below 50°C, and the ionic balance for all samples was confirmed to be within an acceptable error margin of ±5%. The specific water samples used as end-members and mixed samples for the subsequent NETPATH analysis are detailed in the mixing model's section.

For further hydrogeochemical assessment, ionic ratios and various graphical methods, including Piper plot [87], Durov plot [88], and Gibbs graph [89], were generated using specific software called DIAGRAMMES. These tools facilitated the evaluation and interpretation of the geochemical reactions governing evolution of different water resources in the study area

4.3.Recharge source and salinity origin

In this chapter, the recharge sources of the aquifers were determined using stable isotope signatures (δ^2H and $\delta^{18}O$) measured in all water samples, providing critical insights into whether shallow and deep aquifers in the current semi-arid region receive significant recent recharge. This approach also elucidated the effects of water-rock interaction and climatic factors on the isotopic composition of

groundwater, offering a deeper understanding of the hydrogeochemical processes governing the aquifer system. To further investigate the sources of salinity and the high spatial variability in groundwater salinity within the TCA, the NETPATH mixing model was developed and supported by Principal Component Analysis (PCA) and K-means cluster analysis. These mixing models supported with multivariate statistical techniques were employed to select appropriate end members, quantify the contribution of salt lakes and deep NSSA to the salinity of the shallow TCA, and identify the primary factors driving the observed spatial heterogeneity in groundwater salinity. The δ^2H and $\delta^{18}O$ values are reported as deviations in per mil (‰) from the $^2H/^1H$ and $^{18}O/^{16}O$ ratios in a reference standard called the Vienna Standard Mean Ocean Water (VSMOW), which has defined δ^2H and $\delta^{18}O$ values of 0‰. Stable isotope measurements were conducted using a Liquid-Water Isotope Analyser-24d produced by Los Gatos Research. This device employs off-axis integrated cavity ring-down spectroscopy to determine the absolute concentrations of $^2H^1H^{16}O$, $^1H^1H^{18}O$, and $^1H^1H^{16}O$ through laser absorption measurements. laboratory standards were calibrated to international standards (δ^2H = –9.0‰; –74.9‰; –147.7‰; $\delta^{18}O$ = –0.53‰; –10.41‰; –19.95‰ for BWS1, BWS2, BWS3, respectively [90]. The precisions are better than 1.0‰ and 0.15‰ for d^2H and $d^{18}O$, respectively.

4.3.1. Groundwater salinity source based on mixing model

NETPATH software were used to create a mixing model between surface water (salt lakes) and groundwater (TCA and NSSA) to detect the detect the reason for the large variations in the groundwater salinity of the shallow TCA. The model was performed with assumption that beside the water rock interaction and mineral or salt dissolution in the carbonate aquifer (TCA), there is leakage downward of salt water from the hyper saline lakes through the fracture system causing increase in the groundwater salinization. This assumption is based on previous investigation of the surface area of salt lakes that increased rapidly within the last 30 years except Zeitun lake in east Siwa using change detection of the remote sensing data. The second assumption is the overpressure of the deep fresh water in deep NSSA could flow upward through the fault system causing dilution of the saline water in the TCA. According to these assumptions, 7 models were applied using the following steps;

1) Using input parameters such as major ions (Ca^{2+}, Mg^{2+}, K^+, Na^+, Cl^-, SO_4^{2-}, HCO_3^-, CO_3^{2-}, NO_3^-, SiO_2, physical parameters (pH, EC, T°c), and TDS and trace metals (Fe^{2+}, Fe^{3+}, Mn^{2+}, Ni^{2+}, Zn^{2+}, Cu^{2+}, Cd^{2+}, Cr, Pb, Sr).
2) Using mineral phases based on the geological composition of the aquifer system (dolomite, chalcedony, gypsum, illite, calcite, halite, montmorillonite, and exchange phases).
3) Select the end members (initial and final water) based on groundwater flow direction, the extracted clusters from k-means, and the lowest and highest value of $\delta^{18}O$, δ^2H, and TDS. The first scenario for salt water leakage from the lakes, the first endmembers were selected from TCA (sample 9, 10, 144, 117 and 7) with low $\delta^{18}O$, δ^2H, and TDS values and the second endmember from the salt lakes (sample 27 and 92) with high $\delta^{18}O$, δ^2H, and TDS values. The final water (mixed samples) was selected from the TCA with intermediate $\delta^{18}O$, δ^2H, and TDS values

(samples 20, 21, 93, and 87). The second scenario of upward flow of fresh water from the NSSA to TCA, the first end members were selected from TCA (sample 21 and 87) with high $\delta^{18}O$, $\delta^{2}H$, and TDS values and second endmember from NSSA (sample 4 and 56) with low $\delta^{18}O$, $\delta^{2}H$, and TDS and final water from TCA (sample 15 and 68) with intermediate $\delta^{18}O$, $\delta^{2}H$, and TDS.

4) Selecting the reaction type (precipitation/dissolution) based on the mineral saturation index value.
5) The output of the models included the contribution % of each endmember and the evaporation factor
6) Validation of the results of the NETPATH with mixing model based on stable isotope signature only (**Eq 24**). The mixing percentage or contribution was calculated using $\delta^{18}O$

$$\mathbf{Cm = C_1}f \mathbf{+ C_2(1 - }f\mathbf{)} \qquad \mathbf{(24)}$$

Cm represents the concentration of the mixed sample (final water), C1 denotes the stable isotope concentration in initial water (endmember 1), C2 signifies the stable isotope concentration in initial water (endmember 2), f indicates the percentage contribution of endmember 1 to the mixture, and $1 - f$ represents the percentage contribution of endmember 2 to the mixture.

4.3.2. Principal Component Analysis

Principal Component Analysis (PCA) is a statistical technique used to reduce the dimensionality of extensive datasets while retaining critical information. It transforms original variables into uncorrelated principal components, with the primary component capturing the maximum variance and subsequent components explaining the remaining variability [91]. PCA was applied to all measured attributes or parameters (physical parameters, major ions, metals, and isotopes). The aim was to identify the key hydrochemical processes influencing water chemistry and determine critical parameters for k-means cluster analysis. Components were chosen based on two criteria: a cumulative explained variance of more than 50% and Eigenvalues greater than 1 (**Fig 9** a, b), with varimax rotation applied to enhance interpretability. The analysis involved standardizing variables to ensure equal contributions, selecting components based on explained variance and Eigenvalue criteria, and performing PCA transformation to generate uncorrelated components.

4.3.3. K-means clustering

K-means cluster analysis is a unsupervised statistical method designed to categorize objects in a multivariate dataset by grouping them according to their similarities, measured using a distance metric [92,93]. In this research, the technique was employed to classify 153 water samples collected from the surface water and groundwater. The dataset comprised Fe, Mn, SiO_2, TDS, K^+, Mg^{2+}, Ca^{2+}, Cl^-, SO_4^{2-}, HCO_3^-, NO_3, NH_3, δ^2H, and $\delta^{18}O$, which reflect the composition and properties of the water samples. The analysis began with standardizing the data using the StandardScaler tool from Scikit Learn, ensuring all variables were scaled uniformly to prevent features with larger magnitudes from disproportionately influencing the results. Exploratory data analysis, such as generating boxplots and histograms, was conducted to assess the distribution of variables and detect outliers.

Outliers were subsequently eliminated using the interquartile range (IQR) method, improving the robustness of the clustering process by minimizing the impact of extreme data points. The optimal number of clusters was determined using the Elbow and Silhouette methods (Fig 9), which involve plotting the Within-Cluster-Sum-of-Squares (WCSS) and Silhouette Score (Fig 9c, d) against various cluster counts (Eq 25 and 26).

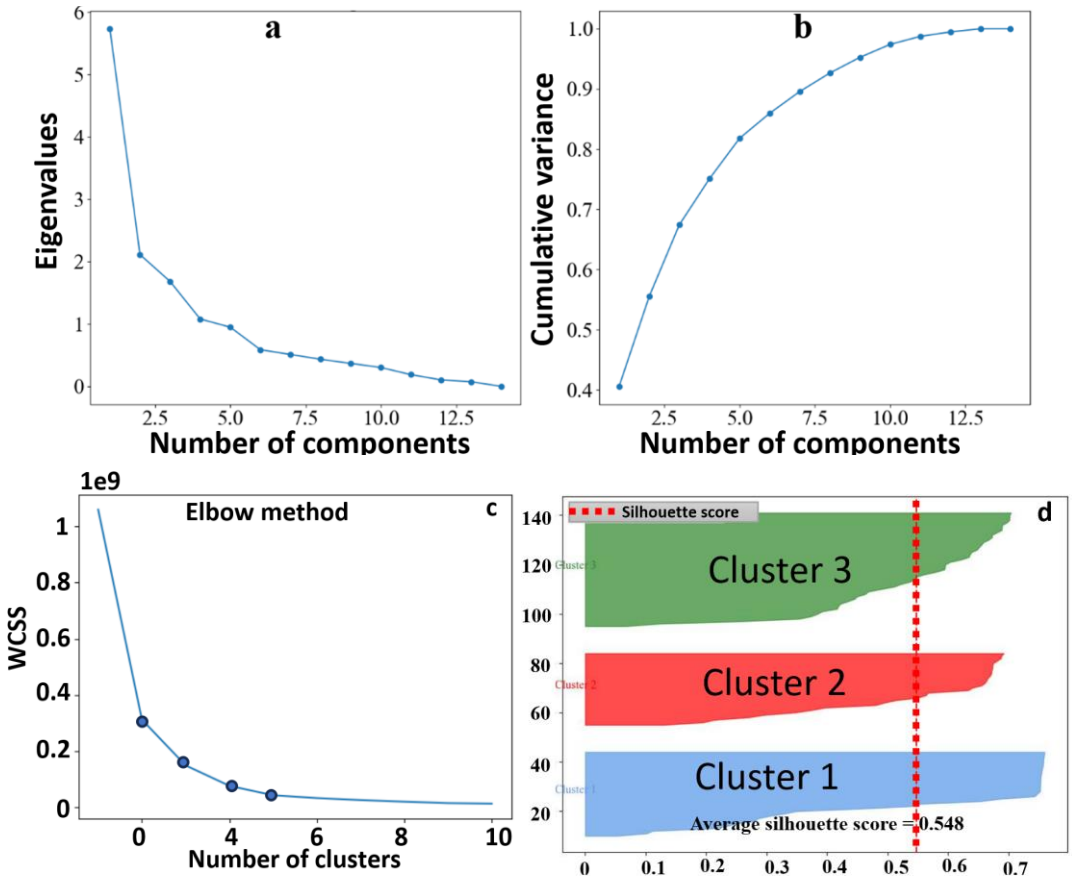

Figure 9. The scree plot of Eigenvalues for extracting optimum number of components (a), cumulative explained variance (b), Elbow curve showing the optimum number of clusters and WCSS (c), and average silhouette score of the three extracted clusters (d)

The "elbow" point, where the rate of WCSS decrease slows significantly, indicated the ideal number of clusters for the analysis.

$$\mathbf{WCSS} = \sum_{i=1}^{k} \sum_{j=1}^{n} \left\| x_j^{(i)} - c_i \right\|^2 \qquad (25)$$

Where k is the number of clusters, n is the number of data points. $x_j^{(i)}$ is the j-th data point in the i-th cluster. c_i is the centroid of the i-th cluster [93].

The Silhouette Score were computed for a range of cluster numbers which provide a quantitative measure of cluster cohesion and separation, ensuring the validity and reliability of the clustering results (Eq 26).

$$\mathbf{Silhouette\ Score} = \frac{1}{n} \sum_{i=1}^{n} (bi - ai)/\max(ai, bi) \qquad (26)$$

Where n represents the total number of data points, a_i is the average distance between the i-th data point and all other data points within the same cluster, and b_i is the smallest average distance between the i-th data point and data points in a different cluster. To assess the significance of the identified clusters, statistical tests such as ANOVA and the Kruskal-Wallis's test were applied. These tests help determine whether the clustering solution is statistically meaningful and whether significant differences exist in the water quality parameters across the clusters.

4.4.Recharge source and residence time of the aquifer systems

In this chapter, additional analysis including ^{14}C, $\delta^{13}C$, $^{87}Sr/^{86}Sr$ were measured in 45 water samples to investigate groundwater dynamics and residence times. The samples were treated with phosphoric acid under vacuum conditions to release dissolved inorganic carbon (DIC) as carbon dioxide (CO_2). The extracted CO_2 was purified using a vacuum line to remove impurities and other gases, after which it was converted into graphite for analysis. The $^{14}C/^{12}C$ ratio was measured using a MICADAS-type Accelerator Mass Spectrometer (AMS) at the Debrecen AMS facility. Stable isotope analyses of water and DIC were conducted using an automated GASBENCH II system coupled with a Thermo Finnigan DeltaPLUS XP mass spectrometer. Additionally, $^{87}Sr/^{86}Sr$ ratios were determined using thermal ionization mass spectrometry (TIMS), achieving an analytical precision of ±0.0001. The primary objective of this research was to integrate multi-isotopic tracers (^{14}C, $\delta^{13}C$, $^{87}Sr/^{86}Sr$) with the previous measured major ion and heavy metal data to develop forward and inverse mixing models (Faure and NETPATH). These models were used to identify the locations where the NSSA recharges the TCA, quantify the contribution percentages at each location and determine the most promising sites for future well-drilling plans. Furthermore, groundwater residence times were estimated using the Fontes and Garnier model, which incorporates age corrections to account for factors such as the downward leakage of salt lakes or irrigation return back into the shallow TCA through the fracture system, which can alter the isotopic signature and apparent age of the groundwater.

4.4.1. Inverse geochemical and mixing model

NETPATH inverse model was employed to simulate observed changes in groundwater chemistry and flow between initial and final water states, providing insights into key processes such as water–rock interactions, mixing, and evaporation. The accuracy of the model's outputs relies heavily on the availability of comprehensive mineralogical, chemical, and isotopic data, particularly $\delta^{13}C$ and ^{14}C [94]. For the mixing model, the NETPATH inverse approach identified two end members based on $^{87}Sr/^{86}Sr$ versus Sr concentrations, with mixed water samples plotted between these end members. This model was used to quantify the contribution percentages and determine recharge locations for the shallow TCA from the deep NSSA. The mixing model was calibrated using the Faur model, which is typically represented by a line or curve connecting the two end members and intersecting the mixed samples, thereby illustrating the contribution percentage from each end member. The contribution percentages were calculated using the following equations (**Eq 27-28**) [95]:

$C_1/ (C_{mix} \times M_1) + C_2 (C_{mix}*M_2)$ in the vertical axis (27)

$C_{mix}=C_1 f + C_2 (1-f)$ in the horizontal axis (28)

Here, C_1 represent the first parameter concentration in the first end member (TDS and Sr), C_2 represent the first parameter concentration in the second end member (TDS and Sr), M_1 represent the second parameter concentration in the first end member (^{18}O and $^{78/68}Sr$), M_2 represent the second parameter concentration in the second end member (TDS and Sr). This approach not only quantifies the contributions of each end member but also provides a robust framework for understanding recharge dynamics and mixing processes in the aquifer system, offering valuable insights for groundwater resource management.

4.4.2. Groundwater residence time estimation

The measurement and correction of ^{14}C ages using ^{13}C play a crucial role in understanding groundwater flow systems [96,97]. Groundwater age is determined using dissolved inorganic carbon (DIC) as a tracer, calculating the difference in ^{14}C content between the present and the recharge period based on its half-life. The calculation is expressed as follows (**Eq 29**):

$$\mathbf{t = -8267 * \ln (A_{sample} / A_0)} \quad \mathbf{(29)}$$

Here, t represents the groundwater age (in years), A_{sample} is the measured ^{14}C content of DIC, and A_0 is the initial ^{14}C content in recharge water. Although the modern carbon standard (A_0) is 100 pMC, the actual initial ^{14}C content in groundwater is often lower due to chemical reactions during groundwater evolution. These include processes such as carbonate dissolution, precipitation, cation exchange, and isotopic exchange reactions, which alter the ^{14}C concentration and require correction for accurate age determination. Numerous methods have been developed to correct ^{14}C ages based on $\delta^{13}C$ values of dissolved inorganic carbon (DIC) [98–103] and geochemical mass transport models like NETPATH [86,104]. Some correction approaches account for both open- and closed-system calcite dissolution [98].

Radiocarbon (^{14}C) dating is commonly used to date DIC in groundwater, particularly for recharged water on a time scale of approximately 1–30 thousand years before present. Over the past 50 years, various adjustment models have been developed to account for isotope dilution and isotopic exchange processes that occur in carbonate groundwater systems. Early models, such as those proposed by Fontes and Garnier [98] and Plummer and Glynn [105], provided foundational frameworks for correcting ^{14}C ages. Studies by Plummer [105] and Han [106] have shown that even with a constant assumption of ^{14}C content in soil CO_2, adjustments to the initial ^{14}C content ($^{14}C_0$) are necessary for the complex geochemical reactions, such as mineral precipitation/dissolution and/or ion exchange, which impact the isotopic composition of DIC. These advancements ensure more accurate and nuanced age estimations in groundwater studies, particularly for systems influenced by a variety of interacting processes. The dissolution of carbonate minerals is a key process influencing the ^{14}C content of DIC in groundwater. During this process, dissolved carbon, primarily in the form of bicarbonate (HCO_3), is generated from a mixture of soil CO_2 and inorganic carbon sources, as described by the following reaction (**Eq 30**):

$$CO2(g) \overset{+xH2O}{\rightarrow} CO2(aq) \overset{+H2O}{\rightarrow} H2CO3(aq) \rightarrow [H\,(aq) + HCO3\,(aq)] + [Me\,(aq) + CO3\,(aq)] \rightarrow 2HCO3(aq) + Me(aq) \rightarrow MeCO3(s) \quad \textbf{(30)}$$

where *Me* represents typically Ca or Mg, and the subscripts g, s, and aq denote gaseous, solid, and dissolved states, respectively. Since the amount of CO_2 involved in these reactions is finite, the dissolution reaction is considered largely irreversible. This process leads to the dilution of the ^{14}C content derived from soil CO_2, as the bicarbonate produced incorporates carbon from both soil CO_2 and inorganic sources, effectively lowering the initial ^{14}C concentration. In addition to the dilution of the ^{14}C content in soil CO_2 caused by the dissolution of carbonate minerals (**Eq 31**), isotopic exchange can occur between different carbon-bearing species, including gas, water, and mineral phases. This exchange is reversible, meaning that carbon isotopes can move between these phases, further impacting the ^{14}C content of the DIC. As a result, the isotopic composition of the DIC becomes influenced by a combination of soil CO_2, inorganic carbon, and the isotopic equilibrium established through these exchanges, complicating the interpretation of groundwater age and the original ^{14}C content.

$$CO2(g) \overset{xH2O}{\leftrightarrows} CO2(aq) \overset{H2O}{\leftrightarrows} H2CO3(aq) \leftrightarrow [H\,(aq) + HCO3\,(aq)] \overset{Me-2H}{\leftrightarrows} [Me\,(aq) + CO3\,(aq)] \rightarrow 2HCO3(aq) + Me(aq) \overset{precipitation/dissolution}{\leftrightarrows} MeCO3(s) \quad \textbf{(31)}$$

In groundwater systems, two extreme situations involving isotopic exchange can occur:

a) Isotopic Exchange Controlled by Gaseous CO_2

Under open-system conditions, where DIC is under-saturated with respect to calcite, isotopic exchange predominantly occurs between gaseous CO_2 and dissolved HCO_3^-. In this scenario, the carbon isotopic composition of CO_2(g) remains unchanged, and the exchange process is controlled by gaseous soil CO_2 (**Eq 32**). This situation reflects minimal influence from solid carbonate phases, meaning that isotopic composition depends primarily on processes involving gaseous and dissolved carbon species.

$$CO2(g) \overset{xH2O\,/-xH2O}{\leftrightarrows} CO2(aq) \overset{H2O}{\leftrightarrows} H2CO3(aq) \leftrightarrow [H\,(aq) + HCO3\,(aq)] \overset{Me-2H\ or-Me+2H}{\leftrightarrows} [Me\,(aq) + CO3\,(aq)] \Rightarrow 2HCO3(aq) + Me(aq) \quad \textbf{(32)}$$

b) Isotopic Exchange Controlled by Solid Carbonate Minerals

In contrast, under closed-system conditions, where calcite continuously dissolves and re-precipitates, isotopic exchange occurs between HCO_3^- and solid carbonate phases (**Eq 33**).

$$CO2(aq) \overset{H2O}{\leftrightarrows} H2CO3(aq) \leftrightarrow [H\,(aq) + HCO3\,(aq)] \overset{Me-2H\ or-Me+2H}{\leftrightarrows} [Me\,(aq) + CO3\,(aq)] \Rightarrow 2HCO3(aq) + Me(aq) \overset{precipitation/dissolution}{\leftrightarrows} MeCO3(s) \quad \textbf{(33)}$$

Proton transfer reactions facilitate the reversible exchange between bicarbonate and carbonate ions, resulting in ^{14}C exchange between HCO_3^- and solid carbonate minerals like calcite [107]. In this case, the isotopic composition of DIC depends on processes involving solid carbonate dissolution, re-precipitation, and proton exchange. Since the mass of solid carbonate is significantly larger than the

DIC, changes in isotopic composition of the minerals may be less apparent. Thus, the exchange is controlled by solid carbonate minerals (indicated by thick arrows).

In the current study, Age correction was performed using the approaches of Fontes and Garnier, where the initial water was defined as soil water prior to its downward leakage into the aquifers, and the final water was represented by samples from the TCA and NSSA. The NETPATH modeling incorporated known mineral phases within the aquifer matrix and the major ion concentrations of groundwater. In the NSSA, observed mineral phases, particularly in the upper Cretaceous shale and lower Cretaceous sand, included halite, gypsum, and silica, which were integrated into the model. For the TCA, which is dominated by carbonate rocks, calcite and dolomite phases were included. Additionally, clay minerals such as montmorillonite and illite, present in the sedimentary layers, were incorporated into the simulation. The cation exchange process involving calcium and sodium within these clay minerals was also considered during the modeling process.

4.5.Groundwater flow modeling

In this chapter, a three-dimensional numerical model was developed using the FEFLOW finite element software to simulate the groundwater flow system in Siwa Oasis. The primary objectives of the model were to investigate the hydraulic interaction between the NSSA and the TCA, validate recharge mechanisms identified in the previous chapter through isotopic analysis, and predict future drawdown in groundwater levels and sustainability of the limited water resources. The following chart shows the framework of building the numerical flow model (Fig 10).

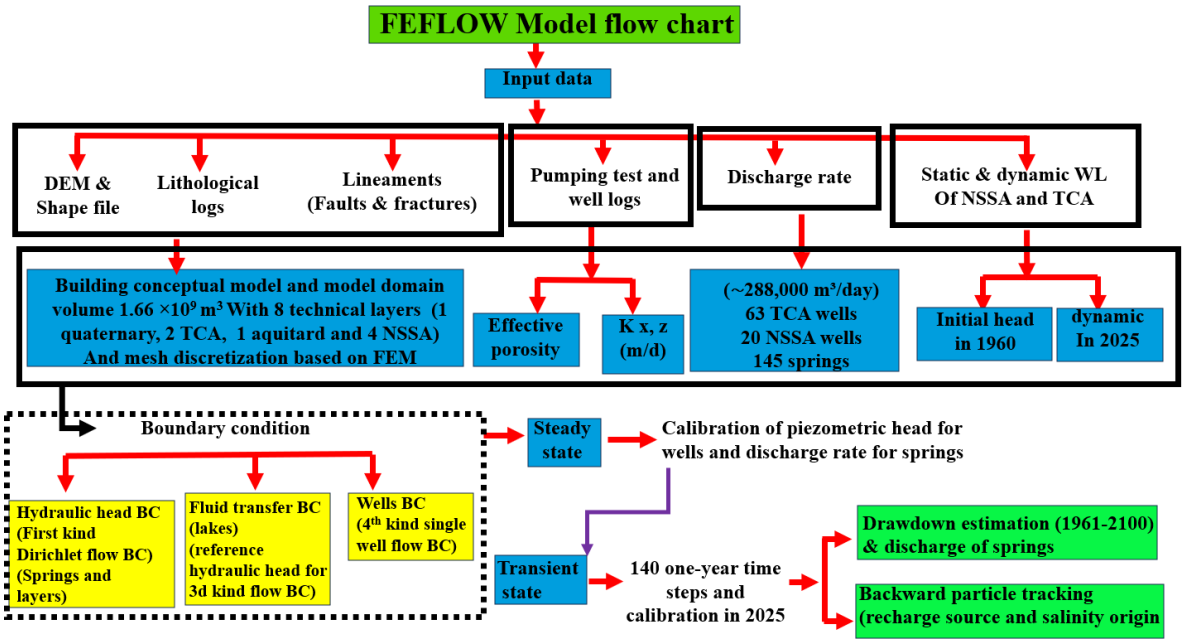

Figure 10. The framework used to build the numerical flow model

4.5.1. Underlying Assumptions and Conceptual Model

The development of the conceptual model was based on several key assumptions derived from the regional hydrogeological context:

a) **Regional Flow System:** The local flow system of Siwa Oasis is considered an integral part of the vast regional NSSA flow system. Therefore, the model boundaries, particularly for the deep NSSA, are assumed to have minimal water level fluctuations.

b) **Constant Head Boundaries:** The presence of high-flow artesian wells and springs with relatively stable discharge rates (approximately 288,000 m^3/day) suggests a steady influx of water into the system. This, along with the stabilizing effect of the freshwater-saltwater interface to the north, justifies the use of specified head boundaries, allowing water to move across the boundaries based on hydraulic gradients and aquifer properties.

c) **Negligible Direct Recharge:** Given the hyper-arid climate, with high evaporation and extremely low precipitation, direct recharge to the shallow aquifer from rainfall is considered negligible. However, recharge from agricultural irrigation return flow was incorporated, with infiltration rates estimated between 0.0000058 and 0.00005 m/day.

d) **Faults as Conduits:** Major faults systems are assumed to act as primary vertical conduits facilitating hydraulic connection and water transfer between the NSSA and the TCA.

Based on these assumptions, a conceptual model was constructed. The model domain, covering a total volume of 1.66 x 10^9 m^3, was discretized into an unstructured finite element mesh with 2,790,928 triangular prism elements and 1,574,100 nodes. The mesh was refined around faults and wells to capture steep hydraulic gradients accurately. The hydrostratigraphy was represented by eight technical layers: a Quaternary soil layer, two layers for the fractured TCA, an impermeable Upper Cretaceous shale layer acting as an aquitard, and four layers representing the NSSA (**Fig 11**).

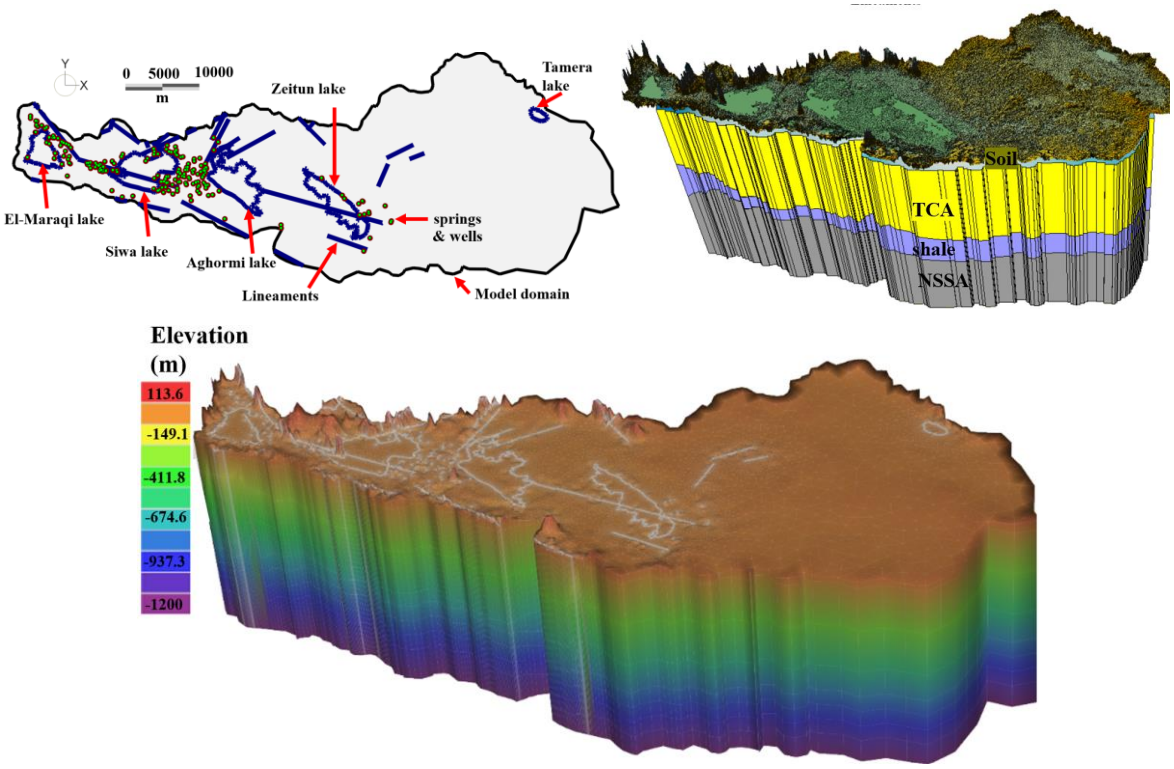

Figure 11. The model boundary including structure lineaments and lakes boundary, 3D geometry of the study area constructed based on well log correlations with 3D discretization using FEM

4.5.2. Input Data and Parameterization

The model was built with data from various sources:

a) Geospatial Data: A Digital Elevation Model (DEM) and shapefiles (catchment area) were used to define the surface topography and the geometry of geological features, including the extent of the salt lakes.

b) **Geological Data:** Lithological logs from 15 wells provided the basis for constructing the 3D geological framework and defining the eight model layers. Lineament maps derived from remote sensing and aeromagnetic data analysis were used to incorporate major faults and fractures as discrete features in the model.

c) **Hydraulic Parameters:** Initial values for hydraulic conductivity (Kx, Ky, Kz) (Fig 12), effective porosity, and specific storage were assigned to each layer based on data from pumping tests (cooper Jacobe method), well logs (Kozeny carmen equation), and values reported in the literature. Fault zones were modeled as vertical conduits with an initial hydraulic conductivity of 0.001 m/s and a thickness of 50 m, which were later adjusted during calibration.

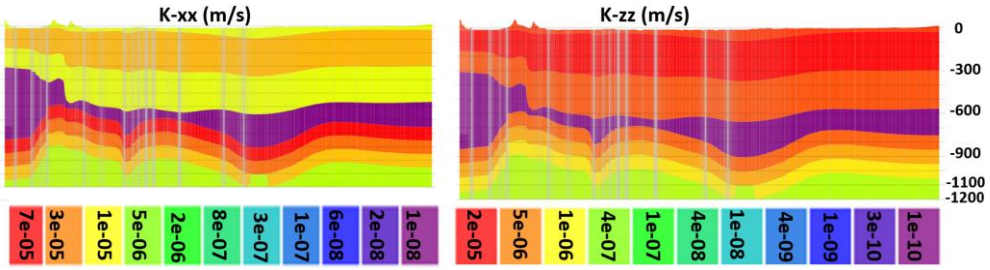

Figure 12. The final horizontal and vertical hydraulic conductivity used for the calibrated numerical flow model

d) **Hydrological Data:** The total discharge rate was set to approximately 288,000 m^3/day, distributed among 63 TCA wells, 20 NSSA wells, and 145 springs. Initial head conditions for the year 1960 were digitized from historical hydrogeological maps, while dynamic water levels for 2025 were used for transient calibration.

4.5.3. Boundary Conditions

Specific boundary conditions were assigned to represent the physical system:

a) **Hydraulic Head Boundary (First Kind - Dirichlet):** Applied to the lateral boundaries of the deep NSSA layers and to the springs, representing a specified, constant hydraulic head.

b) **Fluid Transfer Boundary (Third Kind):** Applied to the surface salt lakes to simulate leakage and fluid exchange between the lakes and the underlying shallow aquifer.

c) **Wells Boundary (Fourth Kind):** Applied to the abstraction wells, simulating a specified extraction rate from the respective aquifer layers.

4.5.3. Model Calibration and Simulation Scenarios

The model was calibrated in two stages:

a) **Steady-State Calibration:** The model was first calibrated under steady-state conditions, representing the pre-development state (1960). Hydraulic conductivity and recharge parameters were adjusted until a good match was achieved between simulated and observed initial heads for the NSSA (R^2=0.99) and the TCA (R^2=0.93).

b) **Transient-State Calibration:** The calibrated steady-state model was then used as the initial condition for a transient simulation from 1961 to 2025. The model was calibrated against measured water levels from 19 TCA wells and 10 NSSA wells. The transient calibration achieved a strong correlation, with R^2 values of 0.98 for the NSSA and 0.83 for the TCA, and a low RMSE of 0.66 m and 0.62 m, respectively, indicating a reliable model.

Following calibration, two main simulation scenarios were executed:

Future Drawdown Prediction (2025-2100): The model was run to predict future water level changes in both aquifers until the year 2100, assuming the current abstraction rate of 288,000 m^3/day continues. This scenario aimed to assess the long-term sustainability of the groundwater resources and identify areas vulnerable to significant drawdown.

Reverse Particle Tracking: This analysis was performed to trace the pathways of groundwater flow backward in time. This helped to validate the hypothesis that the NSSA is the primary source of recharge to the TCA via the fault systems and to investigate the origins of salinity in the shallow aquifer. The governing equation for groundwater flow in FEFLOW is the transient groundwater flow equation, derived from Darcy's Law and the continuity equation (**Eq 34**)

$$\boldsymbol{S_s \frac{\partial h}{\partial t} = \frac{\partial}{\partial x}\left(K_x \frac{\partial h}{\partial x}\right) + \frac{\partial}{\partial y}\left(K_y \frac{\partial h}{\partial y}\right) + \frac{\partial}{\partial z}\left(K_z \frac{\partial h}{\partial z}\right) - w} \qquad \textbf{(34)}$$

K_{xx}, K_{yy}, K_{zz} (m/d) is the Hydraulic conductivity along the x, y, and z directions, representing the ability of the aquifer to transmit water. h (m) is the Hydraulic head, which describes groundwater potential. The parameter *w* (m^3/d per unit volume) is the Source/sink term. Ss (1/m) is the Specific storage, which quantifies the volume of water released or taken up per unit volume of aquifer per unit head change. t (days) is the Time, making the equation applicable for transient (unsteady) flow conditions.

The reverse (backward) particle tracking was employed to investigate the sources that recharge the TCA. In FEFLOW, particle tracking corresponds to solving the Nd-dimensional Stochastic Differential Equation (SDE), which is theoretically consistent with the Fokker-Planck Equation (FPE) for the transition probability f (x, t). According to the Îto formulation, the SDE can be written as follow (**Eq 35, 36, and 37**)

$$\mathbf{X}_p(t+\Delta t) = \mathbf{X}_p(t) + \mathbf{A}\left(\mathbf{X}_p, t\right)\Delta t + \mathbf{B}\left(\mathbf{X}_p, t\right)\cdot \Delta \mathbf{w}(\Delta t) \qquad (35)$$

$$\mathbf{A} = \mathbf{v} + \nabla\cdot\mathbf{D} + \varepsilon^{-1}\mathbf{D}\cdot\nabla\varepsilon = \mathbf{v} + \nabla\cdot\mathbf{D} + \mathbf{D}\cdot\nabla \ln\varepsilon = \lim_{\Delta t\to 0}\frac{1}{\Delta t}\langle \mathbf{X}_p(t) - \mathbf{X}_p(t_0)\rangle \qquad (36)$$

$$\mathbf{2D} = \mathbf{B}\cdot\mathbf{B}^t = \lim_{\Delta t\to 0}\frac{1}{\Delta t}\langle\left[\mathbf{X}_p(t) - \mathbf{X}_p(t_0)\right]\left[\mathbf{X}_p(t) - \mathbf{X}_p(t_0)\right]^t\rangle \qquad (37)$$

The vector A is commonly called the drift vector. It is responsible for the advective (deterministic) movement of a particle, which is the sum of the fluid velocity and a velocity that originates from the spatial variation of dispersion tensor D and porosity ε. The term B.Δw is called the white-noise and corresponds to the non-deterministic part (or stochastic term) of the equation. The matrix B is a diffusion matrix, and Δw are increments of independent Wiener processes. FEFLOW supports several integration schemes for particle tracking, including Backward Îto. The Backward Îto scheme is the fastest, as it does not require evaluating the divergence of the dispersion tensor in the drift part (Eq 38, 39).

$$\mathbf{X}_p(t+\Delta t) = \mathbf{X}_p(t) + \mathbf{v}\big(\mathbf{X}_p, t\big)\Delta t + \mathbf{B}\big(\mathbf{X}_p + \mathbf{Y}_p(t), t\big)\cdot \boldsymbol{\xi}(t)\sqrt{\Delta t} \quad (38)$$

$$\mathbf{Y}_p(t) = \mathbf{B}\big(\mathbf{X}_p, t\big)\cdot \boldsymbol{\xi}(t)\sqrt{\Delta t} \quad (39)$$

4.6.Water quality and health risk assessment

This thesis pioneers a comprehensive framework for assessing the suitability of water resources for human consumption and quantifying the associated health risks in the Siwa Oasis. By integrating a novel Integrated Weighted Water Quality Index (IWQI) with advanced machine learning (FFBP-NN) and probabilistic risk assessment (Monte Carlo simulation), this study moves beyond deterministic water quality standards to provide a nuanced, risk-based evaluation of water safety.

4.6.1. Integrated weight water quality index

The IWQI was employed to assess water quality and its suitability for drinking purposes. IWQI is a ranking system that reflects the overall influence of physicochemical characteristics on water quality [108,109]. The approach of IWQI estimation involves 5 steps: applying entropy weight to quantify the contribution of each parameter, utilizing CRITIC-based weighting to account for the contrast and conflict among parameters, determining the integrated weights by combining both methods, calculating the IWQI, and finally based on WQI score the suitability of water for drinking could be evaluated.

4.6.1.1. Entropy weight

The entropy-weighted water quality index (EWQI) is a method used to evaluate water quality based on physicochemical and metals measured attributes, providing an overall entropy value for interpretation [110]. The calculation process comprises three phases:

Step 1 (Matrix Eigenvalues): The eigenvalues of the matrix X are estimated using Eq 40, where m and n represent the number of investigated samples and hydrochemical parameters, respectively.

$$\mathbf{x} = \begin{bmatrix} \mathbf{x_{11}} & \mathbf{x_{12}} & \mathbf{x_{1n}} \\ \mathbf{x_{21}} & \mathbf{x_{22}} & \mathbf{x_{2n}} \\ \mathbf{x_{m_1}} & \mathbf{x_{m_2}} & \mathbf{x_{mn}} \end{bmatrix} \quad \mathbf{(40)}$$

Step 2 (Standard Matrix Calculation): Eq 41 and 42 are applied to normalize the data and calculate the standard matrix Y, which is necessary due to large dimensional differences in chemical parameters. Normalization ensures consistent scaling, where $(Xij)_{max}$ is the maximum value and $(Xij)_{min}$ is the minimum value for each parameter.

$$Yij = \frac{Xij-(Xij)min}{(Xij)max-(Xij)min} \quad (41)$$

$$\mathbf{Y} = \begin{bmatrix} \mathbf{Y_{11}} & \mathbf{Y_{12}} & \mathbf{Y_{1n}} \\ \mathbf{Y_{21}} & \mathbf{Y_{22}} & \mathbf{Y_{2n}} \\ \mathbf{Y_{m_1}} & \mathbf{Y_{m_2}} & \mathbf{Y_{mn}} \end{bmatrix} \quad (42)$$

Step 3 (Entropy and Weight Calculation): Eq 43-45 calculate the information entropy (ej) and entropy weight (wj). Here, Pij is the normalized proportion of parameter j for sample i:

$$ej = \frac{1}{Lnm} + \sum_{i=1}^{m}(\mathbf{Pij} \times \mathbf{LnPij}) \quad (43)$$

$$Pij = \frac{Yij}{\sum_{i}^{m}(\mathrm{Yj})} \quad (44)$$

$$Wj1 = \frac{1-ej}{\sum_{i=1}^{n}(1-ej)} \quad (45)$$

4.6.1.2. CRITIC Method

The Criteria Importance Through Inter-criteria Correlation (CRITIC) technique was employed to calculate the objective weights of variables, addressing the limitations of traditional information entropy methods. The CRITIC method is a robust approach that combines the variability of each criterion and its correlation with other criteria to derive weights, ensuring an objective assessment of their relative importance. The objective weight could be achieved based on following equations (Eq 46-48):

$$r_{ij} = \frac{\sum(x_{ij}-\overline{x_{ij}})(y_{ij}-\overline{y_{ij}})}{\sqrt{\sum(x_{ij}-\overline{x_{ij}})^2 \Sigma(y_{ij}-\overline{y_{ij}})^2}} \quad (46)$$

$$Sj = \delta j \sum_{i=1}^{m}(1 - \mathrm{rij}) \quad (47)$$

$$Wj2 = \frac{Sj}{\sum_{j=1}^{m}(Sj)} \quad (48)$$

The wj_2, m, S_j, and δ_j indicators identifies the objective weight, total number of variables, quantity of information, and standard deviation, respectively.

4.6.1.3. Integrated-weight

The following equation is utilized to determine the integrated-weight Wj (Eq 49-51):

$$\mathrm{W}_j = pwj1 + (1-p)\, wj2 \quad (49)$$

$$p = \sum_{j=1}^{m}\left[\left(W_j - w_{j1}\right)^2\left(W_j - w_j2\right)^2\right] \quad (50)$$

$$Wj = \frac{wj1 \times wj2}{\sum_{j=1}^{m}(wj1 \times wj2)} \quad (51)$$

p is a preference coefficient, where p lies within the range of 0 to 1, i.e., pϵ [0,1].

4.6.1.4. Integrated Weight Water Quality Index (IWQI)

After determining wj_1 and twj_2, the IWQI is calculated using the following formulas (Eq 52, 53).

$$Qj = \frac{Cj-Cjp}{Sj-Cjp} \times 100 \quad (52)$$

$$IWQI = \sum_{j=1}^{m}(WjQj) \quad (53)$$

j is the experimental concentration of each attribute measured in mg/L, and Cjp reflects the standard value of the variable in pure drinking water. For all variables except pH, the standard value is zero;

for pH, the standard value is seven. The primary standard values (Sj) for each parameter are based on the WHO guidelines [111]. Based on IWQI scores, water quality is classified into five distinct categories. If the IWQI value is below 100, the water is categorized as "excellent to good," between 100 and 150 denotes "medium or intermediate quality," from 150 to above 200 indicate "poor" to "extremely poor" water quality [112].

4.6.2. FFBP-NN for IWQI prediction

The Neural Network (NN) library in MATLAB was utilized to perform feed-forward backpropagation neural network (FFBP-NN) modeling for predicting the IWQI. The input parameters for the model included EC, TDS, pH, TH, Na^+, K^+, Cl^-, HCO_3^-, Fe, Mn, NO_3^-, and SO_4^{2-}. Initially, all 14 parameters were considered, but after iterative testing and stepwise regression, Ca^{2+} and Mg^{2+} were removed to optimize the model's accuracy with few parameters. The modeling process was conducted using Levenberg-Marquardt algorithm employed for training. The FFBP-NN architecture featured two layers: one hidden layer with sigmoid activation functions and an output layer with linear activation neurons. The number of neurons in the hidden layer ranged from 2 to 14, and the optimal configuration was determined experimentally based on performance metrics such as MSE, MAE, RSE, RMSE, and R. A single hidden layer was chosen, as recommended by researchers for simpler datasets, while more complex models may benefit from multiple hidden layers [113]. The dataset was divided into three subsets, with 70% allocated for training and 15% each for validation and testing. This division was determined after testing various proportions, with the selected split yielding the best model performance. A schematic diagram of the initial FFBP-NN model is illustrated in Fig 13.

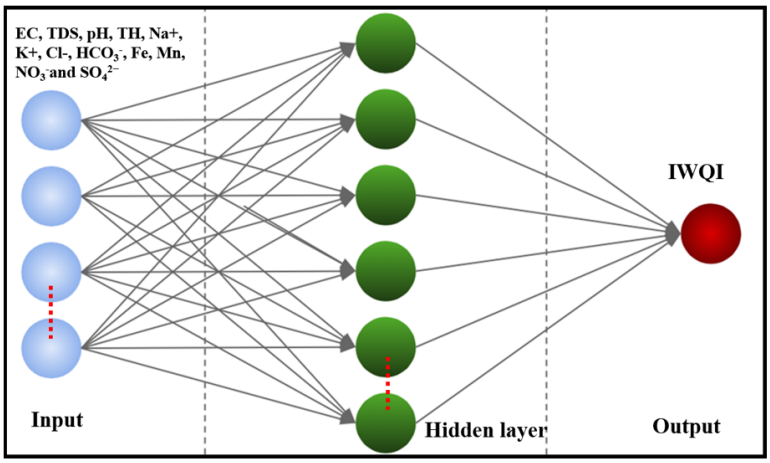

Figure 13: Schematic diagram of FFBP-NN showing the structure of NN, hidden layer, input and output parameters.

The network's performance was evaluated using metrics such as MSE (Eq 54), regression R-value (Eq 55), RMSE (Eq 56), MAE (Eq 57), and RSE (Eq 58), which provided a comprehensive assessment of the model's accuracy and reliability in predicting IWQI.

$$MSE = \frac{1}{n}\sum_{i=1}^{n}(y_i' - y_i^*)^2 \qquad (54)$$

The variable n denotes the total count of data points within a designated group. y'_i represents the empirical measurement of the IWQI corresponding to the i-th parameter, while y^*_i indicates the forecasted or computational outputs for the evaluative parameter (IWQI) linked to the i-th data entry.

$$R(y', y^*) = \frac{cov(y', y^*)}{\sigma_{y'}\sigma_{y^*}} \quad (55)$$

Here, $\sigma_{y'}$ denotes the standard deviation of benchmark data, while σ_y signifies the dispersion of forecasted outcomes. Superior model efficacy is reflected by a higher R coefficient and a reduced mean squared error (MSE).

$$RMSE = \sqrt{\text{MSE}} \quad (56)$$

$$MAE = \frac{1}{n}\sum_{i=1}^{n} | y'_i - y^*_i | \quad (57)$$

$$RSE = \sum(y'_i - y^*_i)^2 / \sum(y''_i - y'_i)^2 \quad (58)$$

The notation y" represents the arithmetic mean of the empirically observed target variable's data points.

4.6.3. Risk assessment of the potential toxic elements

The assessment of health risks in this study follows the model recommended by the USEPA [114,115]. Health risk assessment analyzes the potential impact of environmental pollutants on human health, categorized into two types: carcinogenic (CR) and non-carcinogenic (NCR) risks. Carcinogenic risks evaluate the probability of developing cancer due to prolonged exposure to one or more contaminants. Non-carcinogenic risks, on the other hand, assess the adverse effects of exposure, including genetic and teratogenic impacts. Heavy metals (HMs) in drinking water primarily enter the human body through ingestion and dermal absorption [19,26,31,32]. Consequently, this study evaluates health risks associated with direct drinking and skin contact exposure routes (**Eq 59 -64**).

$$\text{CDI}_{\text{oral}} = \frac{\text{C}_\text{w} \times \text{IR} \times \text{EF}}{\text{BW} \times \text{AT}} \times \text{ED} \quad (59)$$

$$\text{CDI}_{\text{dermal}} = \frac{\text{C}_{\text{ave}} \times \text{ET} \times \text{EF} \times \text{Kp} \times \text{SA} \times \text{CF}}{\text{BW} \times \text{AT}} \times \text{ED} \quad (60)$$

$$HQ_{dermal/oral} = \frac{\text{CDI}_{\text{dermal}}/\text{CDI}_{\text{oral}}}{\text{RfD}_{\text{dermal}}/\text{RfD}_{\text{oral}}} \quad (61)$$

$$RfD_{dermal} = RfD_{oral} \times ABS \quad (62)$$

$$HI = \sum HQ \quad (63)$$

$$\text{CR} = \text{CDI} \times \text{CSF} \quad (64)$$

CDI_{oral} quantifies the mean quantity of contaminants ingested daily through direct consumption, while $\text{CDI}_{\text{Dermal}}$ estimates the average per-day dose assimilated via cutaneous contact. C denotes the concentration of toxic metals in aqueous samples (mg/L), IR reflects the daily water consumption rate (L/day), EF indicates exposure regularity (days/year), ED represents the total duration of contact (years), BW corresponds to individual body mass (kg), SA defines the skin surface area exposed

(cm^2), Kp characterizes the dermal permeability constant (cm/hour), CF serves as a unit conversion factor, and ET specifies the time per exposure event (hours/day). HQ is the hazard quotient index, HI is the total hazard index, RfD is the reference dose, ABS is the digestive coefficient of the gastrointestinal tract, CR represent the carcinogenic risk index, and CSF represents the conversion slope factor of metals. These assessment variables are systematically detailed in **Table 11s (Appendix 2)**.

4.6.4. Monte Carlo simulation

Monte Carlo simulation is a robust technique employed in risk assessment to address uncertainties associated with metals concentrations and exposure parameters, enabling the prediction of carcinogenic and non-carcinogenic risks. This method facilitates the estimation of health risk values by generating multiple iterations to simulate variability and randomness in exposure data [22,26,31]. In this study, Python version 3.9.7 was utilized to implement the Monte Carlo simulation. The Python code was executed for 10,000 iterations to calculate the probability of both carcinogenic and non-carcinogenic risks of heavy metals, considering the exposure scenarios for adults and children.

4.7.Desalination of brackish water of the TCA

In this chapter, applicable solution for groundwater salinization was applied based on the previous investigation using zeolite/geopolymer (Z/GP) membrane created from abundant natural resources (kaolinite and diatomite). Given the significant role of the NSSA in reducing the salinity of the TCA through effective fault and fracture locations during the mixing process, it became essential to explore the efficiency of mixing water from these two aquifers in a controlled surface pipeline system. This method, supported by the addition of ecofriendly, low-cost inorganic materials, aims to prevent soil and groundwater salinization, ensuring sustainable development in a region. The treatment of mixed NSSA and TCA water using a dual approach of dilution and geopolymer-based desalination demonstrates considerable potential to address the salinity issues in Siwa Oasis.

4.7.1. Synthesis of Zeolite/Geopolymer Membrane

The main substances utilized for creating the compound were kaolinite and diatomaceous earth, both processed materials supplied by the Egyptian Center for Metallurgical Research. Sodium hydroxide (NaOH) granules, with 97% purity, acquired from El-Nasr Chemical Co., acted as the alkali catalyst in the production procedure. The geopolymer derived from diatomaceous earth and kaolin was fabricated using the approach outlined by Papa [116]. First, kaolin was heat-treated to generate reactive metakaolin by exposing it to 750°C for 5 hours. The metakaolin was then blended uniformly with diatomaceous earth, functioning as the silicon provider, in combination with an NaOH solution. This blend was agitated at 500 revolutions per minute for 8 hours, ensuring a silicon-to-aluminum molar proportion of 2:1, matching the poly (sialate-siloxo) geopolymer structure. The resulting paste was poured into tube-shaped casts and hardened at 50°C for 24 hours, producing the diatomaceous earth/kaolin (D/K) geopolymer. This geopolymer was later employed as the base material for

hydrothermal conversion into zeolite. For the hydrothermal step, the geopolymer tube was immersed in an NaOH solution inside a Teflon-coated steel reactor. The setup underwent hydrothermal processing at 100°C for 24 hours. Afterward, the zeolite-converted geopolymer was isolated from the leftover NaOH solution, rinsed extensively with purified water to eliminate any remaining contaminants, and dried at 70°C for 10 hours. The end product, the zeolite-modified geopolymer, was fashioned into thin, circular plates with a diameter of 2.5 cm using a precision cutting tool. The surfaces of these plates were refined using a dual-wheel polishing device to achieve even and consistent textures appropriate for salt removal uses.

4.7.2. Characterization Techniques

The structural and morphological properties of the Z/GP membrane and its raw materials were thoroughly analyzed using various advanced techniques. The crystal structures were examined through X-ray diffraction (XRD) analysis, performed with a PANalytical Empyrean X-ray diffractometer. The surface morphology of the membrane and the geopolymer substrate was characterized using Scanning Electron Microscopy (SEM) with a Gemini Zeiss-Ultra 55 microscopes. To investigate the internal structure, High-Resolution Transmission Electron Microscopy (HRTEM) was employed, utilizing a JEOL-JEM2100 Transmission Electron Microscope. The chemical composition was determined through X-ray Fluorescence (XRF) analysis using the Panalytical Axios Advanced system, while the structural chemical groups were identified using a Fourier Transform Infrared (FTIR) spectrometer (Shimadzu FTIR 8400S). Additionally, the surface area and pore size distribution of the membrane were measured using a Beckman Coulter SA3100 surface area analyzer, providing critical insights into its porosity and adsorption properties. A comprehensive chemical analysis of the combined or representative water sample from TCA and NSSA mixture revealed the presence of the following ions: calcium (Ca^{2+}) at 115.6 mg/L, magnesium (Mg^{2+}) at 113.5 mg/L, sodium (Na^{+}) at 874 mg/L, potassium (K^{+}) at 46 mg/L, bicarbonate (HCO_3^{-}) at 182 mg/L, carbonate (CO_3^{2-}) at 16.3 mg/L, chloride (Cl^{-}) at 1630 mg/L, and sulfate (SO_4^{2-}) at 276 mg/L.

4.7.3. Desalination Performance of Zeolite

The effectiveness of the Z/GP membrane in removing salt from brackish groundwater sourced from Siwa Oasis was assessed using a pervaporation apparatus (**Fig 14**). In this configuration, the membrane was firmly positioned inside a permeation chamber, which was sealed using silicone O-rings to ensure a tight fit. The pressure was kept at normal atmospheric levels on the side of the retentate, while it was lowered to less than 10 kPa on the side of the permeate. The permeate solutions were gathered at specific time intervals by condensing them in liquid nitrogen cooled to very low temperatures. Brackish groundwater was used in its natural state with a Total Dissolved Solids (TDS) concentration of 3205 mg/L. Tests were conducted across a temperature range of 30°C to 90°C. Continuous recirculation and stirring of the feed ensured consistent contact between the concentration polarization layer and the Z/GP membrane surface. Each test processed 1000 mL of

the water sample. Membrane performance was measured based on two parameters: total salt rejection (Rj) and water flux (F). Water flux, expressed in $kg \cdot m^2 \cdot h^{-1}$, was calculated using Eq 65.

$$F = W / (\Delta t \times A) \quad (65)$$

Here, W represents the mass of the permeate in kilograms, Δt the collection time in hours, and A is the membrane area in square meters. Salt rejection (Rj) was calculated using Eq 66.

$$Rj = [(S_{if} - S_{ip}) / S_{if}] \times 100\% \quad (66)$$

Where S_{if} and S_{ip} are the ionic conductivities of the feed and permeate, respectively. This comprehensive assessment highlights the Z/GP membrane's potential for effective desalination of brackish groundwater, providing a sustainable solution for addressing salinity issues in Siwa Oasis.

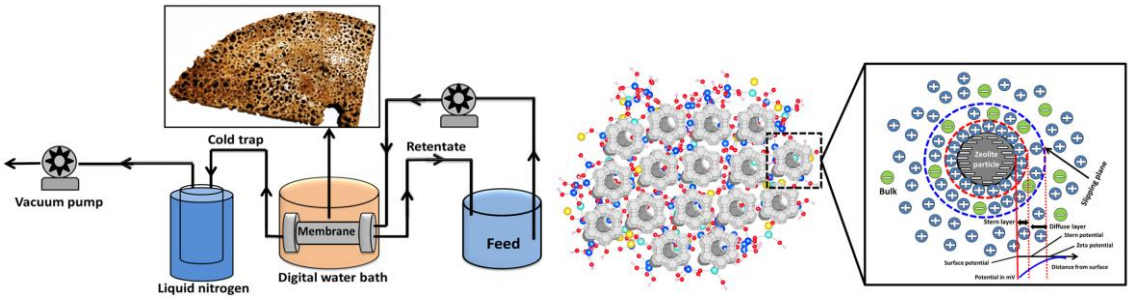

Figure 14. Schematic diagram of the pervaporation system used for desalination experiments with the synthetic Z/GP membrane. The system includes a sealed permeation module containing the membrane, a feed recirculation loop to maintain uniform contact between the brackish water and the membrane surface, and a permeate collection chamber where desalted water is condensed using liquid nitrogen. The setup also features pressure regulation on both the retentate and permeate sides to optimize performance during the desalination process. The schematic illustration depicts the arrangement of zeolite phases within the Z/GP membrane and the mechanism by which cations are adsorbed.

5. Results and discussion

5.1.Aquifer Characterization and 3D facies model

5.1.1. Self-Organizing Maps (SOM)

Self-Organizing Maps (SOM) effectively delineated three distinct hydrogeological units within the NSSA, grouped into three clusters based on silhouette score validation and validated by lithological logs. Cluster 1 represents high-permeability, coarse-grained lithofacies functioning as primary aquifer units, Cluster 2 corresponds to heterogeneous mixed-grain lithofacies with variable permeability serving as semi-confining units, and Cluster 3 identifies fine-grained, low-permeability lithofacies acting as aquitard/confining layers. The clustering analysis employed a dual-SOM methodology utilizing data points derived from well logs. The 13×25 grid configuration was optimized for detailed visualization of hydrogeological characteristics observed in the Sharqia borehole, while the 3×1 SOM provided targeted cluster extraction for validation against lithological logs. Fig 15 demonstrates the three extracted clusters with plotting deep resistivity vs gamma ray, clearly distinguishing the different lithofacies based on their petrophysical properties in all system. The inverse relationship between GR and Rd data effectively delineated the boundaries between the three clusters: Cluster 1 (Sand layer): Defined by low GR and high Rd values, reflecting coarse-

grained, clean sand. Cluster 2 (Shaly sand): Displayed intermediate GR and Rd values, indicating a mixed lithology of sand and shale.

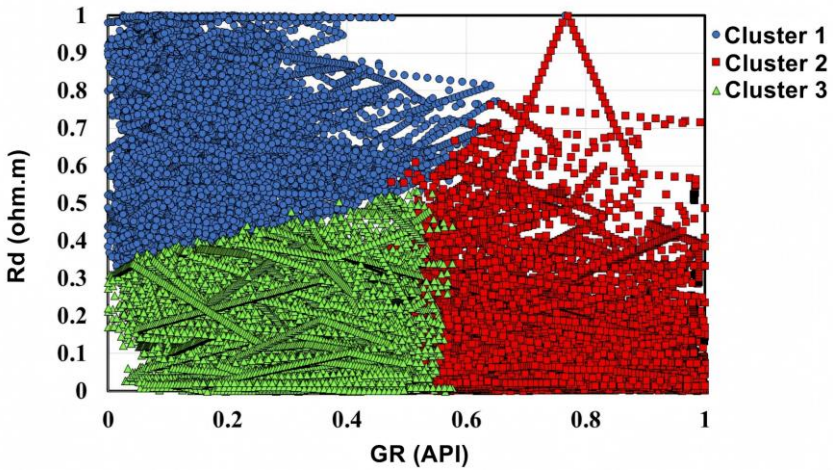

Figure 15. The three extracted clusters of subsurface lithofacies in NSSA with plotting Rd vs GR in all logs to represent the complete system of the aquifer.

Cluster 3 (Shale): Characterized by high GR and low Rd values, typical of fine-grained shale material. These clusters capture the grain size distribution within the aquifer system. High GR and low Rd values in Cluster 3 signify fine-grained shale, while low GR and high Rd values in Cluster 1 represent coarser-grained sand. Cluster 2, with its intermediate values, underscores the transitional nature of shaly sand, highlighting the lithological heterogeneity of the aquifer. This classification aligns seamlessly with the geological framework of the Nubian Sandstone Aquifer System (NSSA), where GR logs serve as a reliable indicator of shale content, and Rd values help distinguish grain sizes and lithologies.

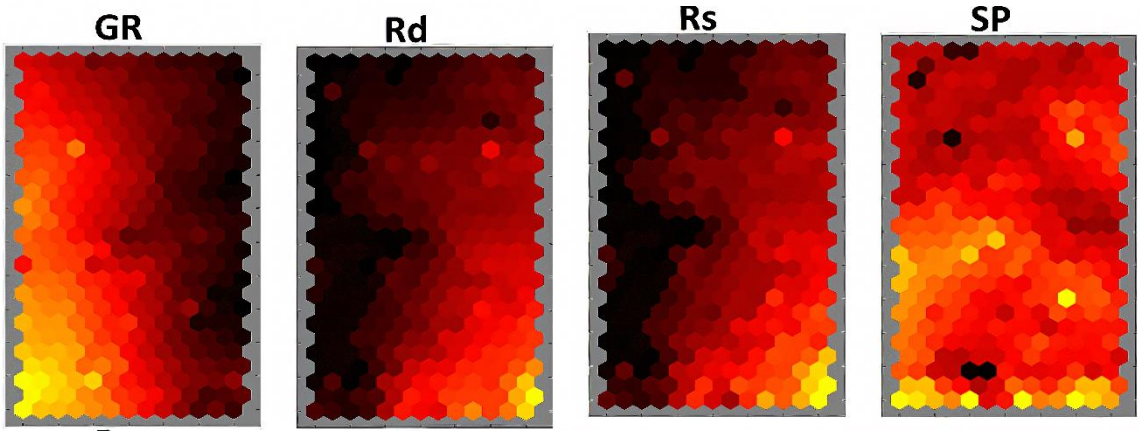

Figure 16. Self-Organizing Map (SOM) component planes used for clustering with color gradient demonstrate lithological changes in NSSA

The SOM component planes (Fig 16) illustrate how the four input parameters (GR, SP, Rd, and Rs) are distributed across the 2D grid, revealing the correlations and relationships between these well log responses in the Sharqia borehole dataset. The GR component plane displays a distinct spatial pattern, with colors transitioning from dark (low GR values) on the right side to yellow (high GR values) on the left side, with a red transitional zone in between. The resistivity component planes (Rd and Rs)

show remarkably similar spatial distributions, both displaying an inverse relationship to the GR plane. In both resistivity planes, colors transition from dark (low resistivity values) on the left to bright (high resistivity values) on the right. This inverse correlation between gamma ray and resistivity responses is consistent with expected petrophysical relationships, where higher GR signatures typically correspond to clay-rich intervals that exhibit lower resistivity due to increased conductivity from bound water in clay minerals. The SP (spontaneous potential) component plane shows a pattern that partially correlates with both the gamma ray and resistivity distributions, displaying intermediate characteristics that suggest its sensitivity to both clay content and formation water salinity effects. The strong inverse correlation observed between GR and resistivity parameters (Rd and Rs) across the SOM grid demonstrates the effectiveness of the SOM in capturing the fundamental petrophysical relationships present in the well log data. The similar responses of deep resistivity (Rd) and short resistivity (Rs) suggest consistent formation characteristics at both measurement depths in this particular dataset.

5.1.2. K-means cluster analysis

Choosing the right number of clusters is crucial in k-means clustering. Picking too many clusters might create artificial lithologies that do not exist, while too few could miss important rock layers, leading to unclear results [117]. In this study, the optimal number of clusters was determined using silhouette values and lithological logs. The process with the highest silhouette value of 0.59 (**Fig 17 a, b**) confirmed the optimum number of clusters are three clusters which agree with the lithological logs.

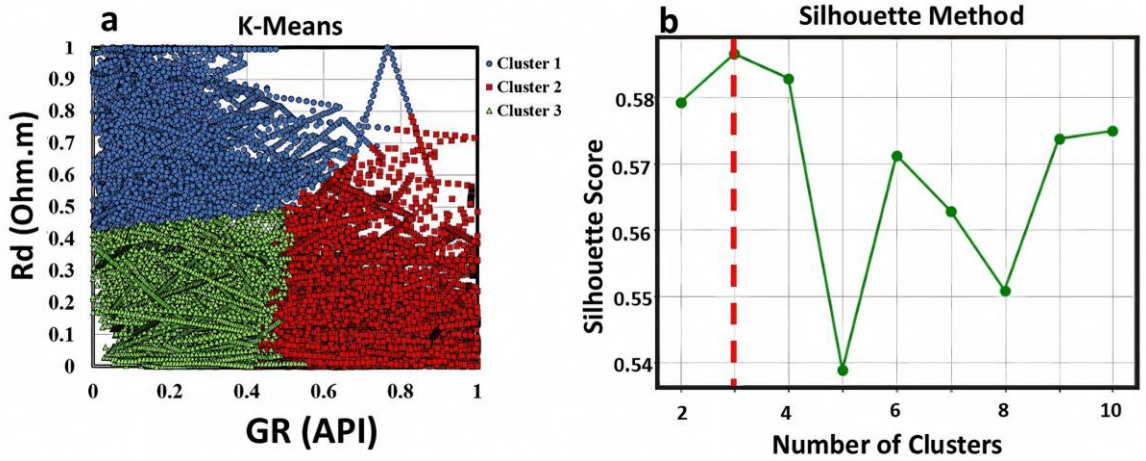

Figure 17. K-means clusters of subsurface lithology in NSSA with plotting Rd vs GR (a) and Silhouette score (b).

Cluster 1 demonstrated low GR values and high Rd responses, Cluster 2 showed intermediate GR and Rd values, and Cluster 3 displayed high GR values with low Rd responses. These clusters represent distinct lithofacies signatures that require independent validation through comparison with lithological logs before hydrogeological interpretations are made for the NSSA.

5.1.3. Validation of SOM and K-means clusters in 1D

The clusters identified through the SOM were validated using 1D and 2D lithological logs to confirm the method's reliability, especially in areas where such logs are missing or need higher resolution. Fig 18 shows the well logs from the Sharqia borehole, including GR, Rd, Rs, and SP, measured in API, ohm.m, ohm.m, and mV, respectively. Validating the three clusters (sand, shaly sand, and shale) was crucial to assess whether SOM could improve or even replace traditional lithological logs. Clusters based on GR, SP, and resistivity logs can provide higher petrophysical resolution than traditional lithological logs generated from cutting samples in specific scenarios where continuous measurement advantages outweigh discrete sampling limitations [118,119].

Such insights are vital for identifying the best zones for screen placement or groundwater extraction, making SOM and k-means clustering a valuable tool for aquifer characterization. In the Sharqia well, five distinct sand layers (Fig 18) were identified as potential targets for groundwater extraction at different depths, based on the lithological log and Cluster 1 (black color) in the SOM results. The agreement between the K-means clusters, SOM clusters, and lithological logs was clear, as all three methods consistently pinpointed the same five aquifer layers as suitable for screen placement. However, while the overall aquifer range was similar across the methods, there were notable differences in estimating the true thickness of the sand layers.

Both SOM and K-means clustering demonstrate method specific advantages for different aspects of lithofacies characterization in the NSSA. For aquifer layer (sand) thickness estimation, particularly in the depth range of 750 to 850 meters, SOM clustering provides more accurate delineation of permeable zones than k-means, which is crucial for evaluating groundwater resources and planning effective screen placements. The SOM's ability to preserve topological relationships and handle gradational boundaries appears particularly beneficial for identifying the true extent of aquifer units, helping to avoid overestimation of sand layer thickness that could impact well design and production optimization. Conversely, K-means clustering demonstrates superior performance in identifying and characterizing fine-grained lithofacies, particularly shale and shaly sand layers, showing clearer correspondence with lithological log descriptions for these confining units. K-means provides more consistent cluster assignments within homogeneous intervals and cleaner boundary definition for low-permeability zones, making it more effective for delineating aquitard units that control groundwater flow patterns. The K-means' assumption of distinct cluster centers provides robust identification of clearly differentiated lithological units.

Rather than viewing these methods as competing approaches, the optimal strategy for lithofacies analysis in complex aquifer systems involves leveraging their specific strengths: utilizing SOM for accurate aquifer characterization and thickness estimation, while employing K-means for reliable identification of confining units. Both clustering approaches provide valuable complementary information to traditional lithological logs, enhancing the resolution and continuity of subsurface characterization for hydrogeological applications. The integration of multiple clustering methods

with conventional geological data offers a more comprehensive understanding of aquifer architecture than any single approach alone. The analysis (Fig 18) reveals that SOM achieves superior overall performance with 95.0% accuracy compared to K-means' 94.1%, representing a 0.9% improvement with statistical significance confirmed by Cohen's kappa scores of 0.925 versus 0.911 respectively, both indicating almost perfect agreement well above chance levels. Error analysis by lithology type demonstrates method-specific advantages, with SOM showing particularly strong performance for Lithofacies 2 (sand) classification (6.2% versus 8.9% error rate), while both methods achieve perfect classification for Lithofacies 3 (shaly sand) (0.0% error rate).

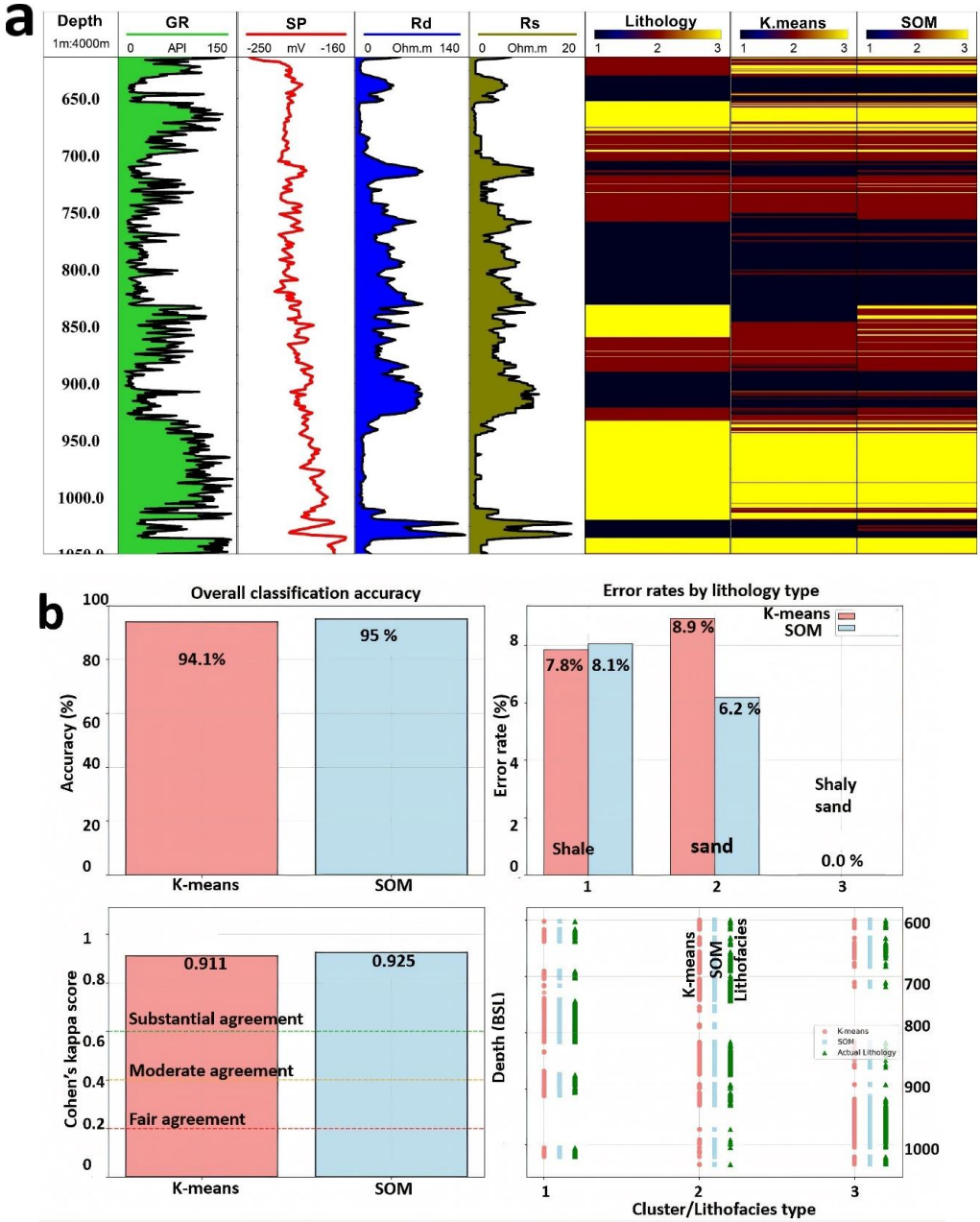

Figure 18. (a) Visualization of the well logs in Sharqia borehole in 1D with two types of clusters validated with lithological log where black color is the aquifer layer. Yellow color is shale layer, and red color is shaly sand layer supported with (b) the error and accuracy of each method

The 2.7% error reduction achieved by SOM for Lithofacies 2 classification is particularly significant for hydrogeological applications where accurate identification of mixed lithofacies is critical for flow modeling and aquifer characterization. The method-specific performance variations observed suggest that different lithology types may exhibit distinct clustering characteristics. K-means' slight advantage for Lithofacies 1 (shale) may reflect this lithology's homogeneous properties and well-defined boundaries, which align with K-means' spherical clustering assumptions. Conversely, SOM's superior performance for Lithofacies 2 demonstrates its enhanced capability for identifying complex transitional zones and mixed lithofacies, which are critical for accurate aquifer characterization. These results provide robust quantitative evidence supporting SOM's selection over K-means clustering, with both methods demonstrating exceptional performance (>94% accuracy) and statistical reliability (kappa >0.9) that validates the effectiveness of the clustering approach for automated lithological classification in groundwater system characterization.

While both clustering methods demonstrate excellent performance (>94% accuracy), several limitations warrant consideration for future enhancements. K-means clustering's assumption of spherical clusters may not fully capture the complex, irregular distributions of petrophysical parameters in geological formations, while its sensitivity to initialization and outliers can impact consistency. SOM, despite superior overall performance, requires careful parameter selection and higher computational complexity. Future improvements could include fuzzy clustering approaches to better handle gradational lithological boundaries, ensemble methods combining multiple clustering algorithms, integration of geological constraints such as stratigraphic relationships, and hybrid machine learning approaches incorporating deep learning for complex pattern recognition. Additionally, uncertainty quantification methods providing confidence measures for cluster assignments would enhance the reliability of automated lithological interpretation and support more informed decision-making in hydrogeological applications.

5.1.4. 3D lithological correlation based on cluster analysis

To convert the 1D cluster analysis into a continuous 2D and 3D model of the NSSA, the clusters were spatially interpolated using Horizontally-Biased (HB) Kriging (**Fig 19 a, b, c, d**). This geostatistical method was specifically chosen to preserve the lateral continuity of the thin, sub-horizontal layers that characterize the NSSA. The resulting 3D fence diagrams provided a clear visualization of the vertical and horizontal heterogeneity of the aquifer system.

A systematic comparison of the interpolated models revealed significant differences between the two clustering methods. The model based on K-means clustering tended to overestimate the thickness of the sand layers and underestimate the confining shale units. In contrast, the SOM-based model demonstrated superior robustness, accurately reconstructing the distinct lithological layers with greater fidelity to the original well logs. Sensitivity analysis (**Fig 19 e**) was conducted using systematic noise injection methodology to evaluate clustering robustness under varying data quality conditions. Gaussian noise was systematically added to the original parameters at amplitudes of 5%,

10%, 15%, and 20% to simulate measurement uncertainties and environmental effects commonly encountered in well log data.

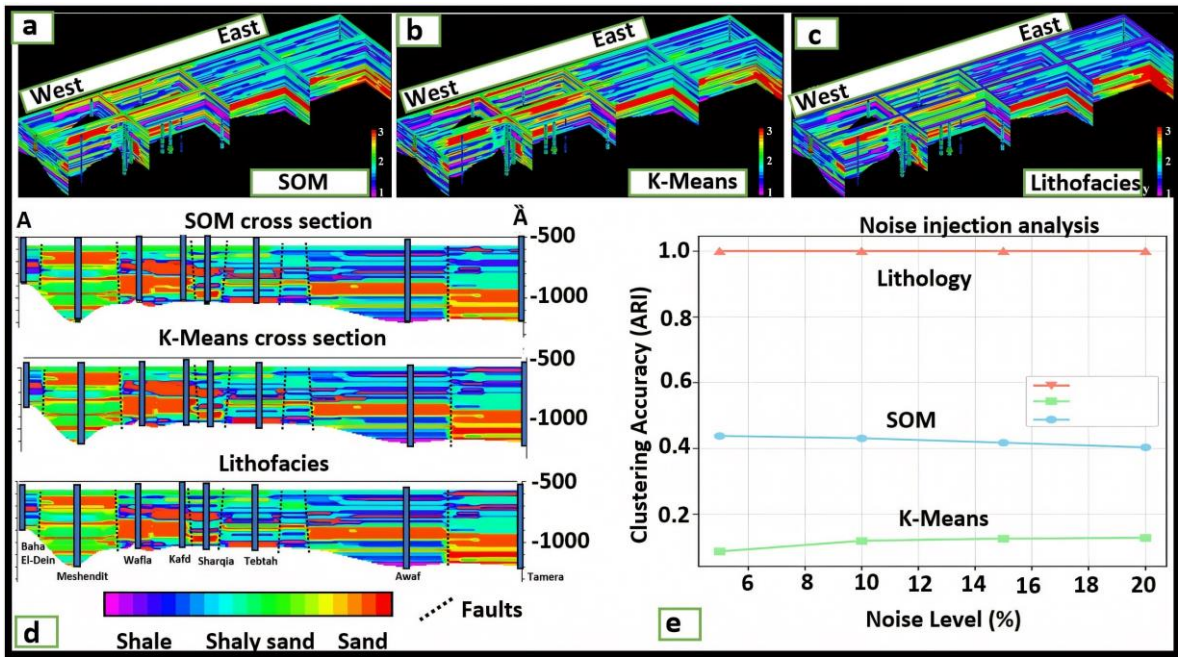

Figure 19. Fence diagram demonstrates the interpolation of SOM clusters (a), k-means clusters (b) and lithology (c) in 3D showing the heterogeneity of the NSSA with upper cretaceous shale. The lithological interpolation results comparing SOM, k-means, and actual lithology logs using HB Kriging (d), and Sensitivity analysis using systematic noise injection methodology (e)

The SOM maintained a high level of accuracy (Adjusted Rand Index = 0.4) even with significant data noise, proving to be four times more resistant to uncertainty than the K-means method (ARI = 0.1). The final validated 3D model, which leverages the superior performance of the SOM, provides critical insights for groundwater management. The model clearly shows that the eastern and central parts of Siwa Oasis contain thicker, more continuous sand layers with less interbedding of shale, making these the most promising locations for future well drilling and sustainable abstraction. Conversely, the western part of the oasis is characterized by a higher proportion of shale, which would likely lead to slower water level recovery after pumping. This slower recovery not only impacts well yield but also increases the risk of downward leakage of saline water from the overlying TCA, potentially compromising the long-term quality of the NSSA. Therefore, the 3D model serves as a crucial predictive tool, guiding future development away from vulnerable areas and towards the most resilient parts of the aquifer system.

5.1.5. Petrophysical and hydraulic parameters in 1D

The analysis incorporated multiple parameters, including shale volume (Vsh), total and effective porosity (Ø and $Ø_{eff}$), hydraulic conductivity (K (m/d)), and well-log responses. The cluster plot in Fig 20 shows a strong alignment with the measured parameters of shale volume, effective porosity, and hydraulic conductivity. For instance: The shale cluster (C3) matches with high shale volume (60–

100%) and low effective porosity (0–10%). The shaly sand cluster (C2) shows moderate shale content and effective porosity. The sand cluster (C1) is marked by low shale volume (0–11%) and high effective porosity (24–40%). This consistency between the clusters and measured parameters highlights the reliability of the clustering approach in capturing lithological variations. The clusters, which are consistently interbedded, confirm that the NSSA is composed of multiple layers. The lower Cretaceous layers are interspersed with moderately permeable shaly sand and very low-permeable shale layers (upper Cretaceous), which significantly influence groundwater flow and quality through water-rock interactions. The hydraulic conductivity values align well with the hydrostratigraphic units observed in the vertical logs of the Sharqia Well. High hydraulic conductivity is associated with sand layers sandwiched between shale boundaries, accurately pinpointing potential aquifer zones through cluster analysis and lithological logs. The hydraulic conductivity log also shows that SOM clusters offer higher-resolution identification of sand layers compared to traditional lithological logs. The mean hydraulic conductivity in the Sharqia Well was calculated to be 2.18 m/d. The spatial analysis of mean hydraulic conductivity and effective porosity across 15 wells shows that the central region of Siwa Oasis has the highest values (**Fig 21**). This highlights the area's potential as a key zone for groundwater resources within the aquifer system. This is likely due to the significant thickness of the sand layer and the limited presence or minimal interbedding of shale in this region. The best locations for future well drilling include Tabow, Khasby, Khafd, and Shahiem in central Siwa Oasis, as well as Tamera in the eastern part of the study area. The findings show that hydraulic conductivity ranges from 1.2 to 6.6 m/d. The lowest values are found in the northern and northwestern areas of the oasis, particularly near Zeitun, Siwa, and Meshendit, close to the Baha El-Dein boreholes. In contrast, the highest hydraulic conductivity values are observed in the central part of the oasis (Tabow, Khasby, Khafd, and Shahiem) and at Tamera in the easternmost section of the study area.

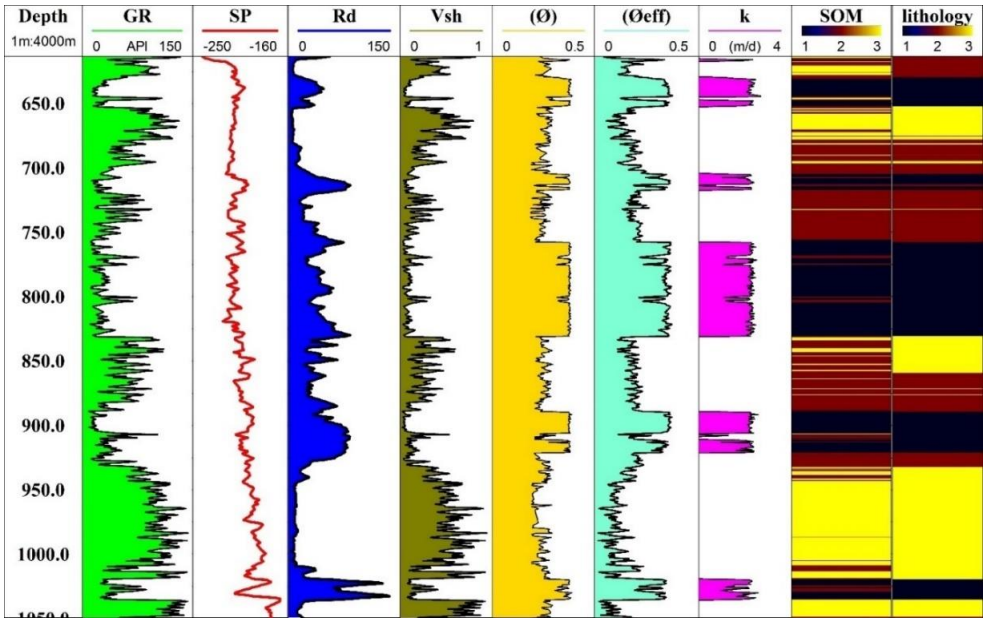

Figure 20. Vertical panel shows the response of well logs, Vsh, Ø, $Ø_{eff}$, K, and lithological clusters

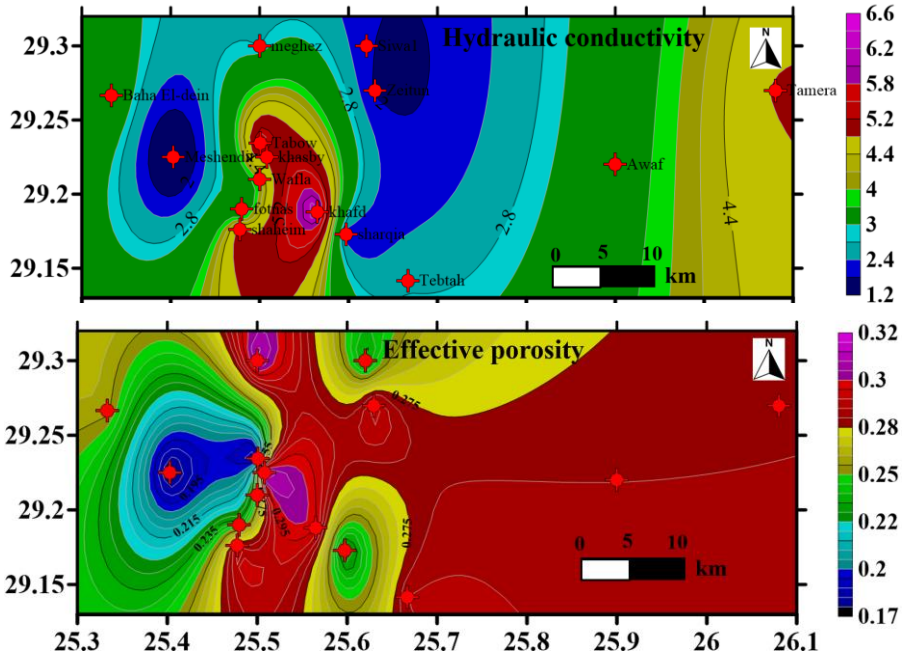

Figure 21. Distribution map of the average hydraulic conductivity and effective porosity from well logs in Siwa Oasis

5.1.6. Petrophysical and hydraulic parameters in 2D

In the initial phase, petrophysical and hydrogeological parameters were calculated for all boreholes (1D interpretation, Fig 20) and compiled into profiles for 2D analysis (Fig 22). The correlation of hydrostratigraphic units along profile A-Ȁ showed that the two main aquifer layers (Bahariya and Alam El-Buieb) vary in depth, shifting upward from east to west due to tectonic activity that formed several faults in the NSSA.

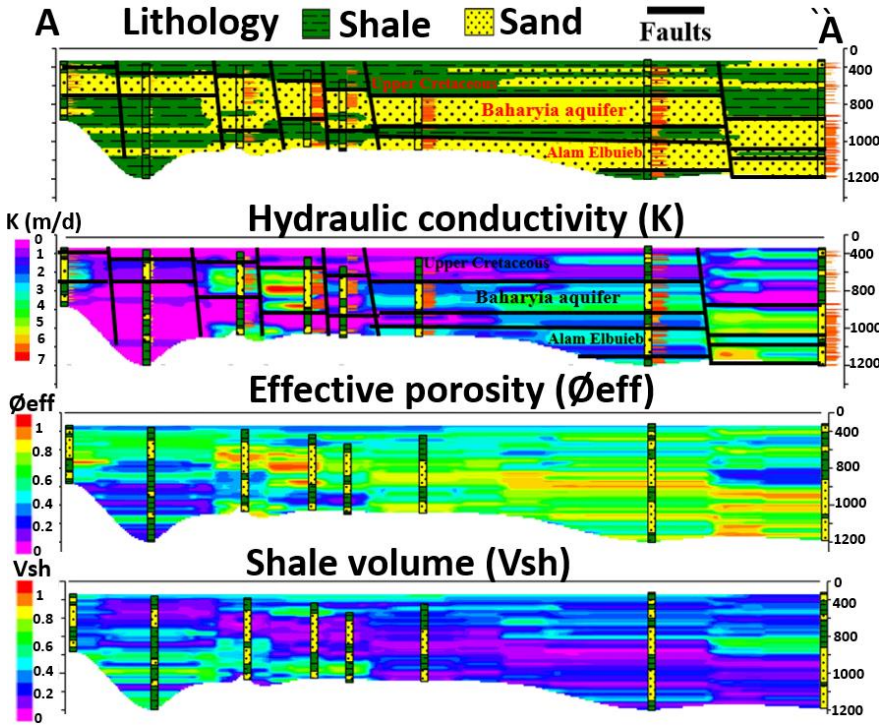

Figure 22. Interpolation of the lithology, hydraulic conductivity, effective porosity, and shale volume in 2D showing the hydrostratigraphic units and fault plane along A-Ä cross section.

These faults likely play a key role in the area, where the over pressured NSSA may recharge the overlying karst aquifer (TCA). The aquifer sand layer reaches its maximum thickness between the Khafd and Wafla wells in central Siwa Oasis. Hydraulic conductivity interpolation along profile A-Ä confirmed the east-to-west shift of the sand layer caused by faulting. A similar trend was observed for effective porosity and shale volume, with average porosity ranging from 0.18 in the west (Meshendit) to 0.35 in central Siwa (Khafd). Hydraulic conductivity peaked between Khafd and Wafla wells (4 m/d to 6.1 m/d), driven by the thick sand layer and minimal shale intercalation. Conversely, the lowest values (1.7 m/d to 3 m/d) were found in the western part of Siwa Oasis, from Meshendit to Baha El-Dein boreholes, due to the thick shale layer, as shown by shale volume interpolation. These findings indicate that over-extraction in the western Siwa Oasis could lead to a cone of depression in piezometric head and delay its recovery. Additionally, drawdown and recovery may affect water quality through water-rock interactions with the salt-bearing shale layer. For sustainable development, future drilling is recommended in the eastern and central parts of Siwa Oasis.

5.1.7. Validation of the hydraulic conductivity

The hydraulic conductivity of the aquifer was calculated using the Kozeny-Carman method using well logs and validated against results from the Cooper and Jacob method [59]. While the Kozeny-Carman method provides detailed estimates, the Cooper and Jacob method offers an approximation, focusing on saturated, and extensive sandy layers, screen intervals under equilibrium conditions [120]. The Cooper and Jacob method's results are highly influenced by the screen interval and discharge rate, with higher discharge rates leading to higher hydraulic conductivity values and vice versa (**Fig 23**). Optimizing the pumping rate can improve accuracy [121].

In this study, pumping rates varied significantly, ranging from 3456 m^3/day in Khashby to 7920 m^3/day in Khafd, which in some cases led to overestimated hydraulic conductivity. Despite the methodological differences, the hydraulic conductivity estimates from both approaches showed acceptable agreement with the Kozeny-Carman model. **Fig 23** illustrates the relationship between drawdown and time, showcasing an example of pumping data analysis using the Cooper and Jacob method for the Sharqia well. The analysis included a long-duration pumping (**Fig 23a**) and recovery test (**Fig 23b**). The recovery test revealed significant drawdown, attributed to the high intercalation of shale, which delayed water level recovery. Hydraulic conductivity values for the aquifer layer ranged from 0.8 m/day in the Meshendit well to 7.16 m/day in the Khafd well, consistent with findings from well logs. The highest conductivity was observed in central Siwa (Khafd well), while the lowest was in the western part of the study area (Meshendit well). **Fig 23c** presents the calibration curve comparing hydraulic conductivity values derived from pumping tests and well logs where the hydraulic conductivity was calculated using transmissivity divided by aquifer thickness (k=T/b). The

curve shows strong agreement between the two methods, with an R^2 value of 0.92, confirming the reliability of the results.

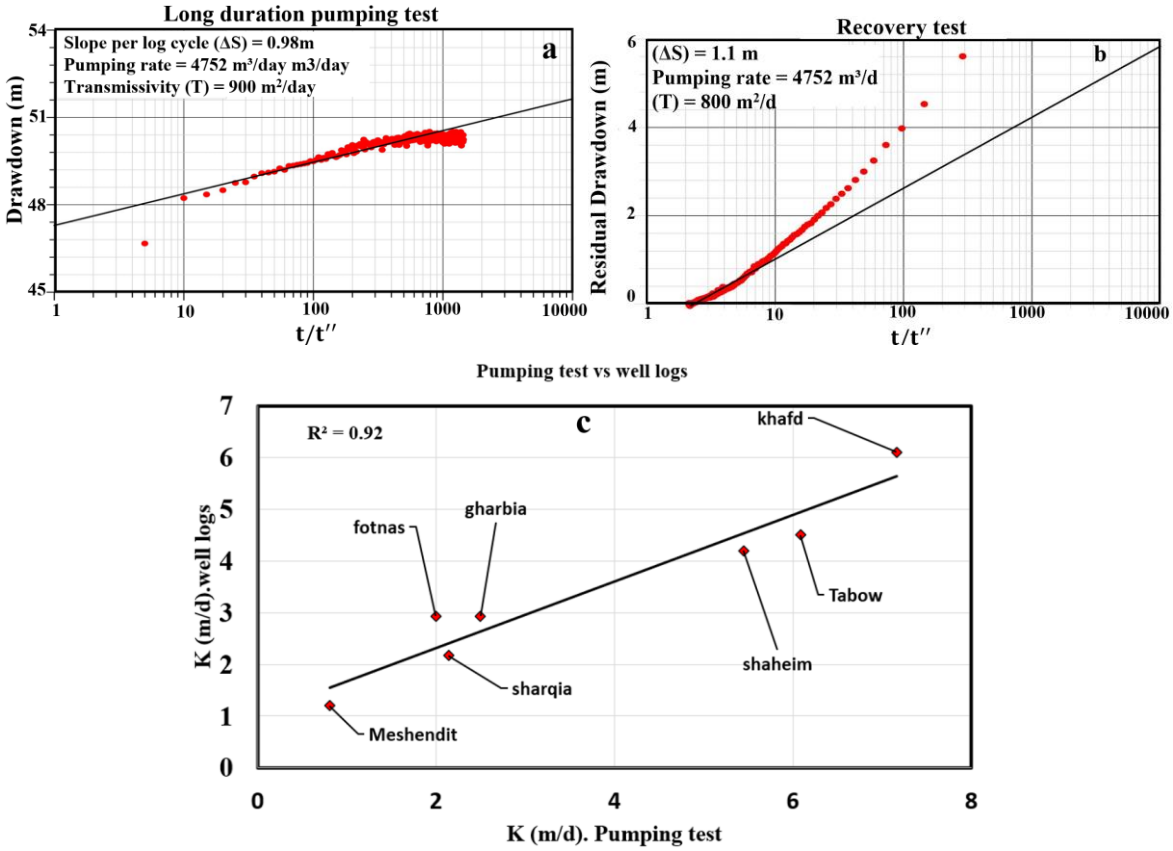

Figure 23. The relationship between drawdown and time for long duration pumping test (a) and recovery test (b) and calibration curve of hydraulic conductivity estimated from well logs vs pumping test

5.1.8. Fracture and fault systems controlling flow dynamics

The delineation of the fracture and fault systems in the study area is crucial to detect the main zones control the flow dynamics between the aquifer system and surface water. The fault system in the NSSA is the only pathway for the upward flow to recharge the TCA where the two aquifers are separated by impermeable shale layer. The fracture system in the shallow TCA is the only pathway for the salt lakes and agricultural drainage to leakage downward to the TCA causing water salinization and contamination. To differentiate between fractures and faults in the gravity data interpretation, a depth-based classification approach was employed based on the distinct hydrogeological characteristics of each aquifer system. Lineaments extracted from gravity anomalies corresponding to the TCA depth range (0 to 500 m below ground surface) are interpreted as fracture systems, which primarily control groundwater flow and permeability enhancement in the carbonate rocks. Conversely, lineaments corresponding to the deeper NSSA interval (500 to 3500 m depth) are classified as fault systems, reflecting the greater depth and confining pressure conditions that favor fault development with significant displacement. This depth-dependent distinction is well-supported by previous investigations in the Western Desert region, which have documented fracture-controlled

flow in shallow carbonate aquifers and fault-controlled architecture in the deeper NSSA [6,49,51,69,129,130]. To clarify the scale and nature of the detected subsurface features, the anomalies interpreted from the 1000 m and 7000 m upward continuation maps were evaluated in light of their respective depth sensitivities. Anomalies enhanced at the 1000 m level are attributed to shallower structures, likely representing small-scale fractures, cavities, or near-surface fault traces within the carbonate aquifer. In contrast, the broader anomalies evident in the 7000 m continuation are more indicative of deeper, regional fault systems possibly rooted in the basement. This distinction supports a multi-scale structural interpretation, where shallow and deep features may reflect interconnected deformation patterns governed by the same tectonic framework. The observed alignment and continuity of some shallow fractures with deeper trends further reinforces this structural linkage.

5.1.8.1. Lineaments extraction using gravity data

5.1.8.1.1. Regional and residual anomalies in gravity

The Bouguer anomaly map within the specific study area (Fig. 24), range between -12 and 16 mGal. Positive anomalies are concentrated in the NE and SW portions, potentially reflecting underlying structural features or denser subsurface materials. The Bouguer anomaly map (Fig. 24) shows a contour pattern that aligns with the main tectonic trends and surface features. Gravity values decrease toward the southeast, reaching about -12 mGal, and increase to the north. The gravity map shows a NE-SW and E-W and NW-SE trends.

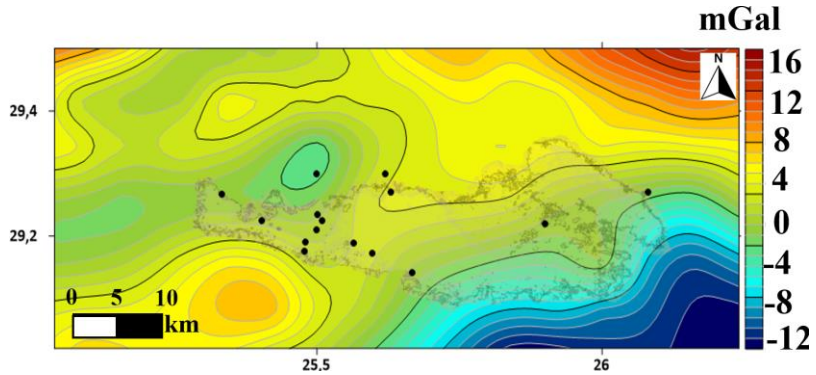

Figure 24. Bouguer anomaly distribution map in Siwa Oasis

To delineate the subsurface structural framework of the Siwa Oasis, the Bouguer gravity field was systematically decomposed using upward continuation and residual anomaly mapping (Fig 25 a, b, c, d). This spectral filtering technique allowed for the separation of gravity signals originating from different depths, providing a multi-scale view of the region's tectonic architecture. The gravity field upward continued to 1000 m (Fig 25a), along with its corresponding residual map, isolated anomalies originating from sources shallower than 500 m (Fig 25c). This analysis revealed a prominent set of NE-SW and NW-SE trending lineaments, which are interpreted as fracture systems within the shallow TCA. These fractures are critical as they represent potential pathways for the downward leakage of saline surface water into the aquifer, a key factor in the observed water quality

degradation. Conversely, the gravity field upward continued to 7000 m (Fig 25b) highlighted the deep-seated structures below 3.5 km (Fig 25d). This revealed a major positive anomaly in the northeast, indicative of a basement uplift, and significant negative anomalies in the southeast and west, corresponding to deep sedimentary basins. The persistence of these major structural trends at depth underscores the influence of regional tectonics on the overall basin geometry. The residual map that filtered out the deep signals effectively isolated the structures within the NSSA. This map revealed a series of synclinal and anticlinal features, with the identified faults interpreted as the primary conduits for upward recharge from the deep NSSA into the overlying TCA. The alignment of these intermediate-depth faults with the shallow fracture systems provides a clear, integrated model of inter aquifer hydraulic connectivity.

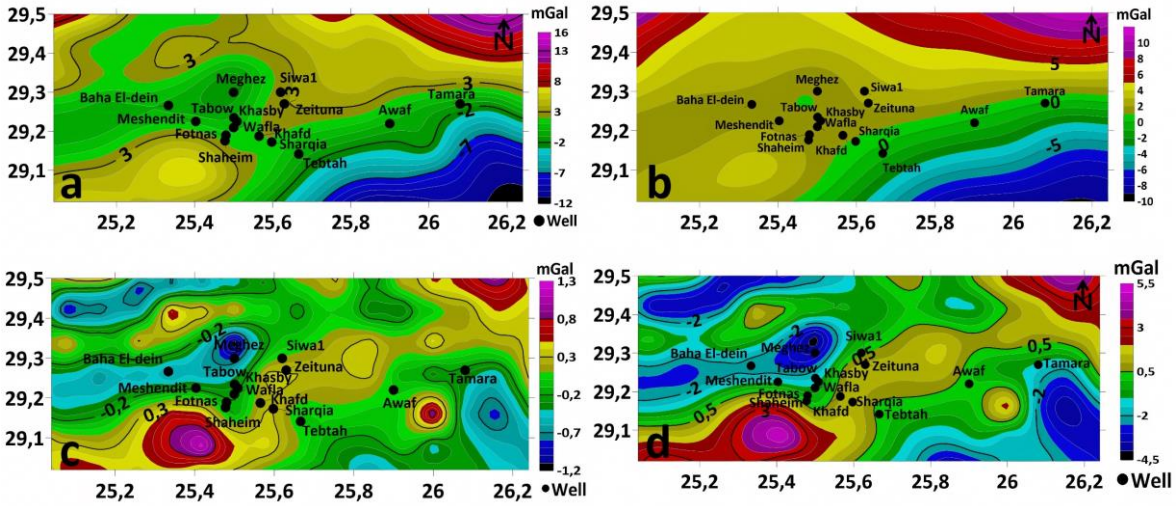

Figure 25. Gravity Upward continued to height of 1000m to image sources buried at and below 500m depth (a) and to height of 7000m to image sources buried at and below 3500m (b), Residual anomaly map after the anomaly sources deeper than 0.5km (upward continued 1km) (c), and 3.5km (upward continued 7km) (d) are removed which is characterized by negative and positive gravity values.

5.1.8.1.2. Lineament extraction using edge filtering technique

Different edge-detection filters and techniques emphasize various aspects of the gravity data due to their sensitivity to distinct spatial frequencies, depths, and structural features. Consequently, each method may highlight slightly different sets of lineaments some overlapping and others unique reflecting the complexity of the subsurface geology. To reconcile these differences, an integrative approach was adopted rather than relying on a single filter. The results from multiple techniques including FVD, SVD, AS, TA, TAHG, and THD were applied on the residual maps obtained after subtracting the upward continuation at 1000 m and 7000 m (**Fig 26**), to identify consistent lineaments that appear across several methods. These recurring features are considered the most reliable structural indicators. Lineaments appearing in only one method may represent subtle structures or noise/artifacts, thus warranting cautious interpretation.

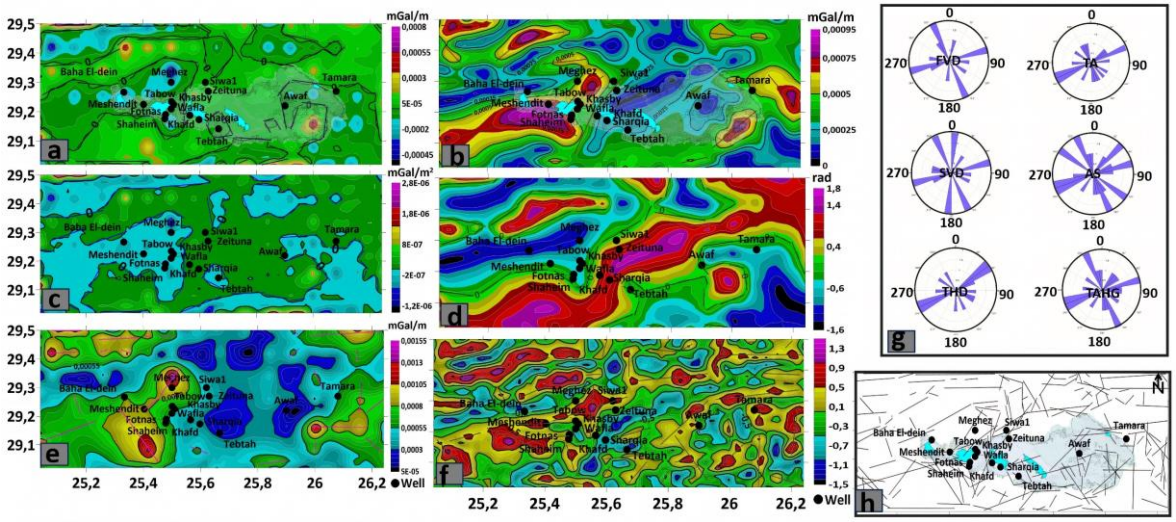

Figure 26. Structural pattern maps and extracted lineaments from following filters, **(a)** FVD**, (b)** THD, (c) SVD, (d) TA, (e) AS and (f) TAHG, applied on the residual anomaly (upward continued 1km), (g) Rose diagrams illustrate lineament orientations filtered by the gravity datasets revealing predominant trends that align closely with the orientations of major structures in the study area, and (h) Combined Lineament map from different edge filtering techniques applied on the residual (upward 1 km).

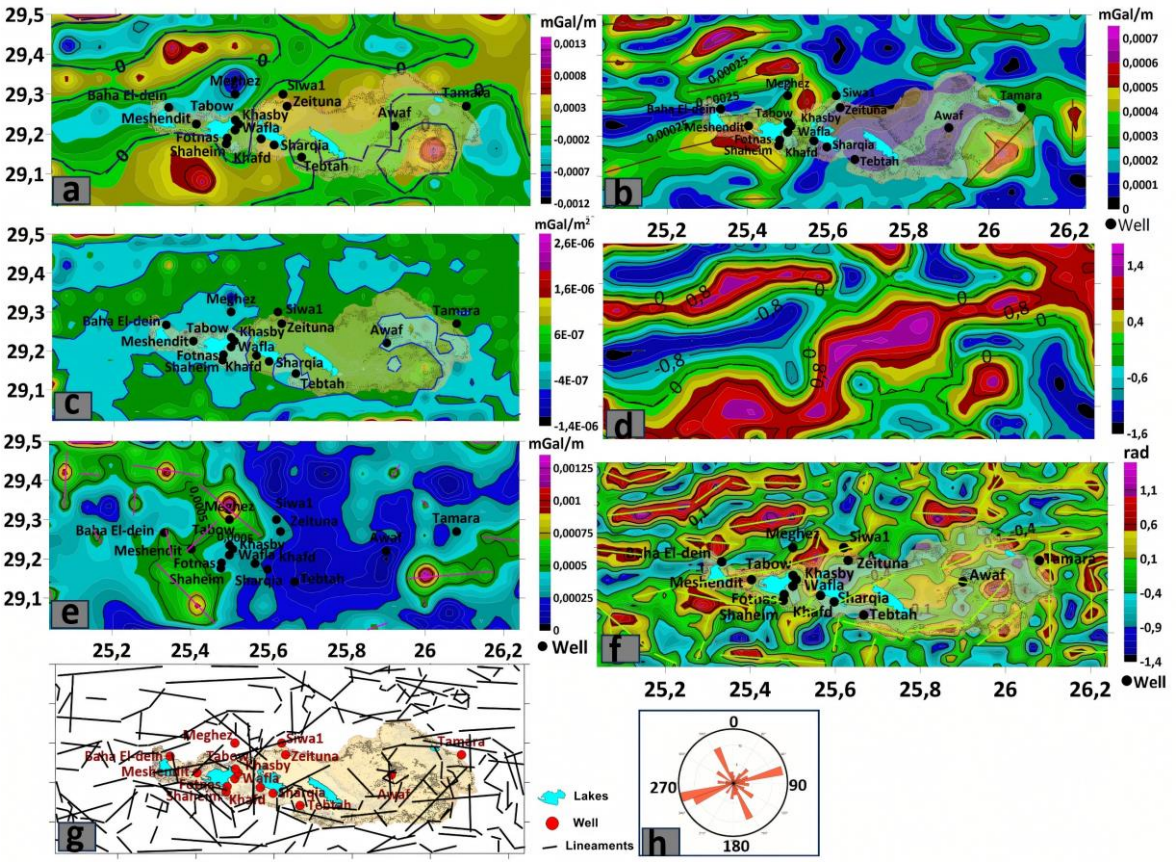

Figure 27. Structural pattern maps and extracted lineaments from following filters, (a) FVD, (b) THD, (c) SVD, (d) TA, (e) AS and (f) TAHG, applied on the residual anomaly (upward continued 7 km), (g) Combined Lineament map from different edge filtering techniques applied on the residual (upward 7 km), and (h) rose diagram showing predominantly NE-SW, NW-SE

This multi-filter integration leverages the complementary strengths of each technique. For example, upward continuation and vertical derivatives are effective at isolating signals from different depths, while phase-based filters like TA and TAHG highlight edges with varying directional sensitivities. Amplitude-based filters such as the AS and THD improve edge clarity by balancing contributions from multiple sources. By combining these diverse results, a composite structural map was produced that captures the spatial complexity of faults (**Fig 27**), fractures (**Fig 26**), and other geological features across different depth ranges and scales. This integrative strategy enhances confidence in the identified lineaments, reduces ambiguity inherent in individual filter outputs, and ultimately provides a more comprehensive and geologically sound interpretation of the subsurface structures.

5.1.8.2.3D Gravity Inversion modelling

This study employed 3D gravity inversion modeling (**Fig 28, 29**) to interpret residual gravity anomalies at depths of 1 km and 7 km (**Fig 28 a-h**), aiming to map subsurface density variations and structural features. The inversion process, guided by an iterative algorithm, successfully reconstructed the geometry of horizontal density interfaces, providing detailed insights into both shallow and deep subsurface structures. To reduce the inherent ambiguity in potential field data interpretation, the model was constrained using prior knowledge of the Siwa oasis area, where previous studies estimated the maximum basin depth around 3.5 km [36,38,82,122].

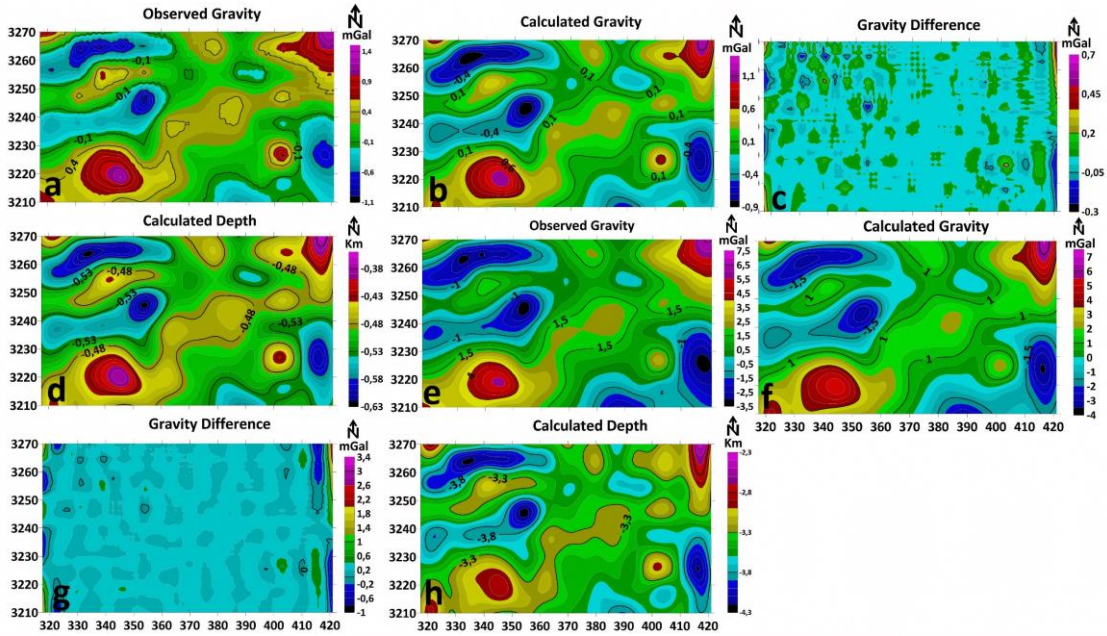

Fig 28. Inversion Results Gravity Model for 0.5 km including (a) Observed gravity anomalies, (b) Computed gravity anomalies from the inverted interface, (c) Error and gravity difference, and (d) Estimated depths from inversion. inversion results gravity model for 3.5 km including (e) Observed gravity anomalies, (f) Computed gravity anomalies from the inverted interface, (f) Error and gravity difference, and (g) Estimated depths from inversion, (h)

The density assigned were the following: the Limestone and dolomite (TCA) density 2.65 g/cm³, Shale density 2.75 g/cm³, Sandstone density 2.9 g/cm³, while the basement rock density

was set at 3.1 g/cm³ based previous studies on the area [82]**.** A trial-and-error approach was applied to achieve the best fit between the observed and calculated gravity data. For the 1 km residual gravity data, the inversion revealed shallow causative bodies at depths of less than 0.5 km, highlighting near-surface features such as fault and fractures zones and lithological boundaries. The results showed a strong correlation between the calculated gravity anomalies and the observed data (**Fig 28 a, b**), with error ranging from −0.3 to 0.7 mGal (**Fig 28 c**), and the RMS error reduced to 9.9707×10^{-5} km after 25 iterations (**Fig 29 c**). For the 7 km residual gravity data, the inversion identified deeper density variations extending to approximately 3.5 km, aligning with regional tectonic controls and providing critical insights into fault extensions at greater depths. The results showed a strong correlation between the calculated gravity anomalies and the observed data (**Fig 28 d, e**), with error ranging from −1 to 3.4 mGal (**Fig 28 f**). The RMS error decreased from 0.014 km to 9.09×10^{-5} km after 55 iterations (**Fig 17 d**), demonstrating the robustness of the inversion process. The calculated basement depths and fracture/faults delineation from the 3D gravity inversion (**Fig 28a, b**) showed strong agreement with well logs clusters correlation (**Fig 19 and Fig 3a**), particularly in delineating the Precambrian basement rock and fault plane, which represents the total thickness of sedimentary rocks.

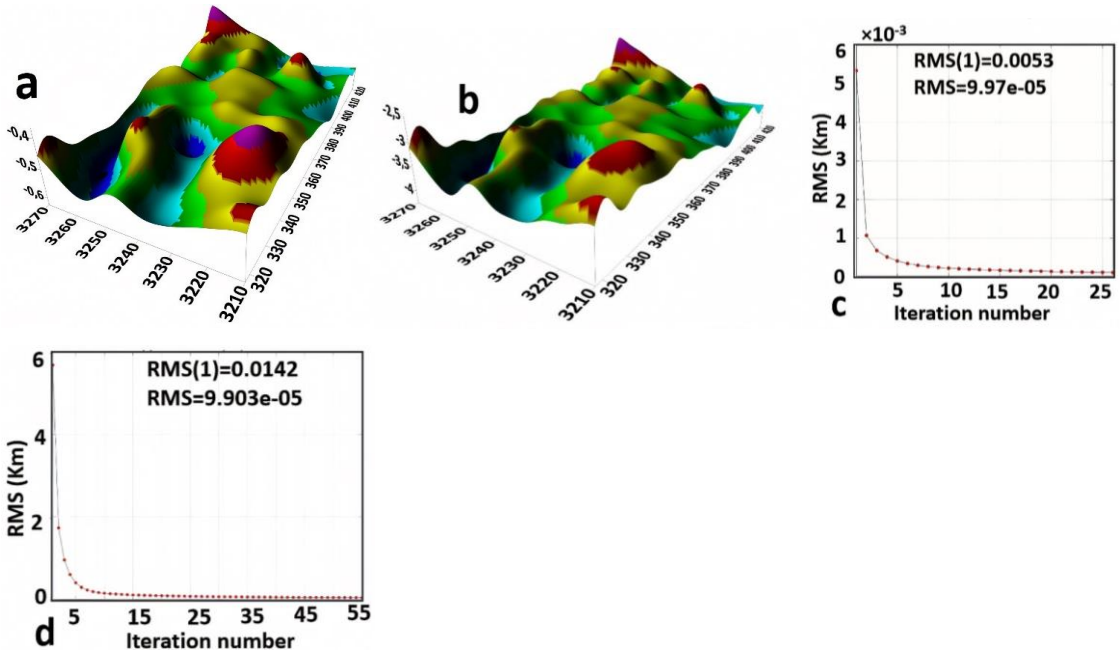

Figure 29. (a, b) 3D model of estimated depth, (c, d) RMS for 0.5 and 3.5 km, respectively in the study area.

Depths to the basement ranged from 2.5 km to over 4 km, with a clear SW-NE trend separating two major basins in the southeast and northwest regions.

The integration of gravity inversion results with geological well data validated the accuracy of the model, confirming its reliability for mapping subsurface structures. The findings proved the possibility for connection between NSSA and TCA through the fault planes as well as the location of the shallow fracture system in TCA that facilitate salt lakes leakage downward.

5.1.8.3.Magnetic and gravity Lineament integration

The lineaments extracted from the gravity analysis were validated with lineaments extracted from magnetic data (RTP) analysis with edge detection applied on residual 0.5km and 3.5km. The FVD, SVD, TA, and TAHG were applied (**Fig 1s and Fig 2s. Appendix 1**). The results showed agreement between gravity and magnetic data analysis and some differences exist due to the limitation of each method. Gravity Data responds to variations in rock density. A fault is detected if it juxtaposes rocks of different densities (e.g., dense basement rock against less dense sedimentary rock). Gravity is excellent at mapping large-scale structures like basins, basement uplifts, and major fault blocks.

Magnetic Data responds to variations in the magnetic susceptibility of rocks, which is primarily determined by the concentration of magnetic minerals. It is highly effective at mapping igneous and metamorphic basement rocks, which are typically rich in magnetic minerals, and the faults within them. Sedimentary rocks usually have a very low magnetic signature. To overcome this limitation, the two methods were integrated in **Fig 3s (Appendix 1)**. Integrating gravity and magnetic data is crucial for a reliable geological interpretation because it reduces the inherent ambiguity of each method, allowing for a more complete and robust characterization of subsurface structures by simultaneously constraining both the density and magnetic properties of the underlying rocks. The integrated analysis of gravity and magnetic data reveals a complex structural framework in Siwa Oasis, characterized by dominant NE-SW, NW-SE, and E-W lineament trends (**Fig 3s. Appendix 1**). These trends align with surface geological features and reflect significant tectonic activity, consistent with previous studies [82,122]. The integration of gravity and magnetic anomaly filters with topographic derivatives provides a robust framework for precise lineament delineation (**Fig 3s. (Appendix 1**).

5.2.Soil salinization origin and hydrochemical evaluation

This thesis provides a comprehensive diagnosis of the escalating soil salinization in Siwa Oasis by pioneering an integrated approach that combines multi-temporal remote sensing, machine learning, and detailed hydrogeochemical analysis. This thesis moves beyond simply identifying salinization to quantitatively linking it to specific land-use changes and elucidating the complex geochemical processes that govern water quality degradation.

5.2.1. Monitoring salt lakes and soil salinization

By examining the spectral properties of visible features in the study area, the optimal band combinations for differentiation were determined to be 7-4-2 in RGB for Landsat TM and 7-5-2 in RGB for Landsat 8. These color blends offer realistic depictions that are straightforward to analyze. Band 7 (2.08–2.35 µm) clearly distinguishes water (high absorption) from land (high reflectance) and aids in identifying four primary land cover categories: shallow water, lake water, Moghra Formation, and sand dunes. Band 4 (0.76–0.90 µm) is essential for distinguishing vegetation due to its elevated NIR reflectance (green hue). It also emphasizes water (strong NIR absorption, varying

with depth) and differentiates barren lands and urban regions with darker shades. Band 2 (0.52–0.60 µm) enhances the combination by separating water based on turbidity levels and highlighting barren lands and urban areas with lighter tones. The SVM classification outcomes for these features (six categories) are shown in **Fig 30** and statistically analyzed in **Table 3s (Appendix 2)** using confusion matrices and kappa coefficients (k), which are commonly used metrics for evaluating classifier effectiveness and the precision of thematic maps. Temporal and spatial changes in land cover categories were tracked across the research area, with a focus on the four main lakes (**Table 2** and **Fig 30**). The total area of hypersaline lakes increased significantly over the decades, measuring 22.6 km² in 1990, 42.6 km² in 2000, 53.1 km² in 2010, and 60.6 km² in 2020. Among the lakes, Siwa Lake is the largest at 29 km², while Aghormi Lake is the smallest at 6.6 km².

Table 2. Surface area of different land cover in Siwa Oasis

Land cover	1990	2000	2010	2020
	area	area	area	area
Wet sabkha	80.289	35.6697	25.2837	31.1913
Salt Lakes	22.6323	42.5781	53.1396	60.678
Cultivated land	23.9607	34.5114	82.5201	89.0658
Moghra fm	530.2197	520.1874	517.6179	502.974
Dry sabkha	145.6758	174.0438	157.7565	143.7579
Sand dunes	546.7005	542.4876	513.1602	521.811

The surface area expansion is most notable for El Maraqi, Siwa, and Aghormi lakes. In contrast, Zeitun Lake has no significant increase, likely due to an evaporation rate nearly equal to its inflow rate or potential seepage into the shallow aquifer. The findings revealed a rapid increase in the surface area of salt lakes from 1990 to 2020, except for Zeitun Lake, which experienced a decline between 2010 and 2020. The significant expansion of Siwa, Aghormi, and El Maraqi Lakes highlights the impact of excess discharge from the TCA and NSSA due to the reclamation of new agricultural lands. The reduction in the surface area of Zeitun Lake between 2010 and 2020 was primarily caused by enhanced irrigation and drainage systems, as well as the shutdown of inefficient wells, which decreased the water flow into the lake [67]. In contrast, the growth of other saltwater lakes is strongly associated with the expansion of farmland, which necessitates more pumping wells and agricultural drainage flowing into these lakes. The cultivated land area in Siwa Oasis experienced a substantial increase, expanding from 23.9 km² in 1990 to 89 km² in 2020. This growth was primarily driven by the development of new agricultural zones, particularly in the central region of the oasis. Concurrently, the extent of shallow water bodies (wet sabkha) adjacent to the four lakes decreased significantly, declining from 80.2 km² in 1990 to 25.3 km² in 2010. This reduction was largely attributed to the transformation of wet sabkha into dry sabkha, a process driven by evaporation and changing hydrological conditions.

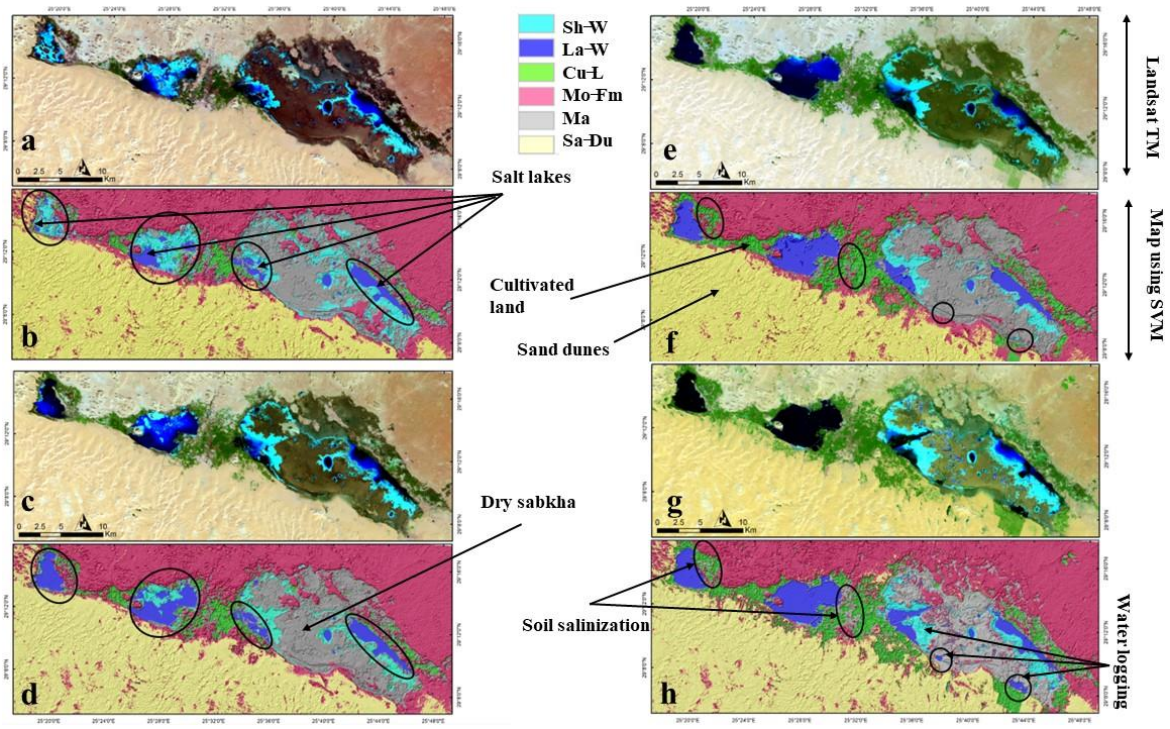

Figure 30. FCC 7-4-2 in RGB respectively for Landsat TM a) 1990, c) 2000, e) 2010, g) OLI 2020 and their corresponding resultant thematic map using SVM (b, d, f, and h respectively).

From 2010 to 2020, the region experienced notable environmental changes, particularly in its water bodies, dry sabkha areas, and soil conditions. Shallow water areas increased slightly from 25.2 km² to 31.1 km², largely due to new agricultural drainage systems implemented between Aghormi and Zeitun lakes, which redirected water into these areas. Meanwhile, dry sabkha areas, which had expanded significantly from 145.6 km² in 1990 to 174 km² in 2000 as shallow water evaporated and left behind saline deposits, began to gradually decrease. By 2020, dry sabkha areas had reduced to 143.7 km², likely due to the expansion of the lakes surface area. Sand dunes also shrank over time, primarily because of land reclamation for agriculture in the southern part of the Oasis. However, from 2010 to 2020, some cultivated areas transitioned to dry sabkha as waterlogged soil evaporated, leaving behind salinized soil, particularly in the central study area. Field observations confirmed widespread waterlogging and soil salinization, with a notable acceleration in the rate of salinization during this period. Vegetation depletion was most pronounced near saline lake waters and wet sabkha areas, as high salinity levels negatively impacted plant production. These trends highlight the complex interplay between agricultural expansion, water management, water logging, and soil degradation in Siwa Oasis (Fig 31). Addressing these challenges will require sustainable water and land management practices, soil rehabilitation, and ongoing monitoring to balance agricultural development. The growth of Siwa and El Maraqi lakes stems directly from the overextraction of groundwater for irrigation, which potentially can cause decline in water tables in this area (Fig 3b). Over time, the rise in dry, salt-encrusted plains or deposits, soil salinity, and water logging highlights

the consequences of using poor quality of irrigation water from TCA which need softening and desalination process before irrigation.

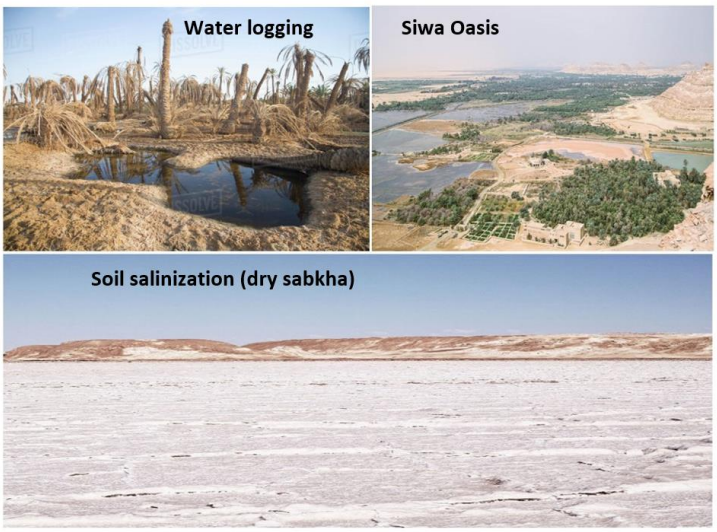

Figure 31. Field observation of the water logging and soil salinization (dry sabkha)

5.2.2. Hydrochemical evaluation of the aquifer systems

The chemical and physical properties, along with heavy metal concentrations, are outlined in **Table 4s (Appendix 2)**. The findings indicate that the TCA is categorized as brackish water, with an average TDS value of 4603 mg/L. On the other hand, the NSSA is classified as freshwater, with TDS levels varying between 160 and 928 mg/L. Springs display TDS concentrations ranging from 1463 to 38,295 mg/L, placing them in the brackish to saline classifications. Surface water demonstrates high salinity, with average TDS measurements of 8585 mg/L for drainage channels and 106,136 mg/L for salt lakes. The growth of hypersaline lakes could significantly decrease soil fertility due to salinization, particularly in farmlands adjacent to these lakes. In the NSSA, all primary ions remain within permissible irrigation thresholds (FAO standard) [123] except for K^+, which surpasses 2 mg/L in every sample. In the TCA, elevated levels of K^+, Cl^-, Mg^{2+}, Na^+, EC, and TDS exceed acceptable irrigation standards ($K^+ > 2$, $Cl^- > 1100$, $Mg^{2+} > 60$, $Na^+ > 900$, EC > 3000, and TDS > 2000), while other parameters stay within recommended limits. Since the TCA is the main aquifer utilized for irrigation, its inferior water quality can contribute to soil salinization and sodicity, particularly in the central and northern sections of the study area (**Fig 4s. Appendix 1**).

Samples collected from springs, drainage systems, and lakes reveal that all primary ions surpass permissible irrigation thresholds except for HCO_3^-, CO_3^{2-}, and NO_3^-. EC measurements indicate that 88.5% of TCA samples, 87.5% of spring samples, and all surface water samples exceed the FAO standard irrigation limit of 3000 µS/cm [123], while NSSA samples remain within acceptable ranges. The high TDS and EC levels are concentrated in the central and northern regions of the study area due to intensive farming and activities related to salt lakes (**Fig. 4s. Appendix 1**), making these zones the most susceptible to soil salinization. The water samples exhibit slightly alkaline condition with pH values ranging from 6.4 to 8.8. The relative dominance of ions in surface water, springs, and TCA

follows this sequence: Cl > Na > Mg > SO_4 > Ca > HCO_3 > K > CO_3 > NO_3. In the NSSA, the order is: HCO_3 > Cl > Na > SO_4 > Ca > K > Mg > NO_3 > CO_3. The average NO_3^- concentrations are 5.2 mg/L (NSSA), 6.4 mg/L (TCA), 7.6 mg/L (springs), 3.7 mg/L (drains), and 3.2 mg/L (lakes). Natural NO_3 levels in groundwater can reach up to 10 mg/L, but human activities such as agriculture, septic systems, and animal waste can elevate these levels [124].

Soil biochemical processes also play a role in NO_3 availability in groundwater [125]. The average concentrations of Fe, Mn, Sr, B, and Ba in most water samples are within acceptable irrigation limits. However, Fe and Mn levels exceed the WHO drinking water standards [111] (Fe > 0.3 mg/L, Mn > 0.1 mg/L), necessitating further investigation into potential health risks. Water quality issues are often associated with human activities (industrial and agricultural) and can lead to various health risks. The elevated Fe and Mn concentrations in the TCA may stem from water-rock interactions and hydraulic connections with the underlying Fe-rich NSSA.

Miocene carbonate rocks contain significant amounts of glauconite and detrital Fe oxides, and the Moghra Formation includes 1.6–36.1% Fe_2O_3 and 0–0.6% MnO, suggesting a natural geological source for these elements [126] while the remaining metals could increase in water from anthropogenic sources. **Fig 4s, 5s (Appendix 1)** depict the spatial distribution of measured parameters across various water sources in the study area. These maps highlight clear differences in ion concentrations between the TCA and the NSSA. In the TCA, the levels of dissolved ions rise progressively from the southern to the northern regions, reaching their highest levels in the central portion of the oasis. Likewise, the NSSA demonstrates increased ion concentrations moving from the western to the eastern zones, especially in the central area located between Siwa and Aghormi lakes.

5.2.2.1. Mechanisms controlling water chemistry

The Piper diagram [87] was utilized to classify the water types of the water resources (**Fig 32a**). The samples were grouped into four categories (**Fig 32a**). The Ca-Mg-SO_4 facies accounting for 26.8% of the samples, including 35 from the TCA, 3 from drains, 2 from springs, and 1 from Zeitun Lake. The Na-Cl facies comprising 44 samples from the TCA, 5 from the NSSA, 4 from lakes, 3 from springs, and 3 from drains. The Mixed Ca-Mg-Cl-SO_4 and mixed Na-Ca-HCO_3 facies representing the remaining samples from the NSSA and TCA. The variation in facies within the NSSA is likely due to water-rock interactions during upward and horizontal movement through fault planes, supported by differences in water salinity and temperature at varying depths. Most samples revealed that the salinity index (SO_4^{2-} + Cl^-) exceeds alkalinity (HCO_3^- + CO_3^{2-}), and alkalis (Na^+ + K^+) surpass alkaline earth elements (Ca^{2+} + Mg^{2+}) in 62.7% of the samples, aligning with the general characteristics of the TCA and NSSA in the study area. The low HCO_3^- content in groundwater suggests limited annual recharge, indicating that groundwater is a non-renewable resource, which could be further confirmed using stable isotope analysis. The geochemical evolution shows that groundwater samples transitioned from Ca-Mg-HCO_3 and Na-HCO_3 types in the initial stage to Ca-Mg-Cl/SO_4 and Na-Cl types in the final stage, reflecting changes in water characteristics within the

aquifer systems. The Gibbs scatter plot [89] (Fig 32b) shows that water samples from lakes, drains, springs, and the TCA fall within the evaporation/crystallization dominance zone. In contrast, NSSA samples and one TCA sample, indicate rock weathering dominance. This anomaly may result from direct dilution from the NSSA due to the destruction of some wells penetrating the NSSA in the study area. The findings suggest that water-rock interaction and evaporation are the primary factors controlling the chemical composition of groundwater in the NSSA and TCA, respectively. Springs, drains, and lakes exhibit a similar trend of increasing TDS as observed in the TCA, driven by the evaporation/crystallization process. The relationship between TDS and Na^{+}/ (Na^{+} + Ca^{2+}) indicates that evaporation significantly influences salinity increase in the TCA and surface water (lakes and drains), while rock weathering and ion exchange are the main processes governing the chemistry of the NSSA. The Durov diagram (Fig 32c) highlights that ion exchange, mixing/dissolution, and reverse ion exchange control the water chemistry. All TCA, spring, lake, and drain samples fall within the ion exchange zone, while the remaining NSSA samples align with the mixing/dissolution zone, consistent with earlier statistical interpretations.

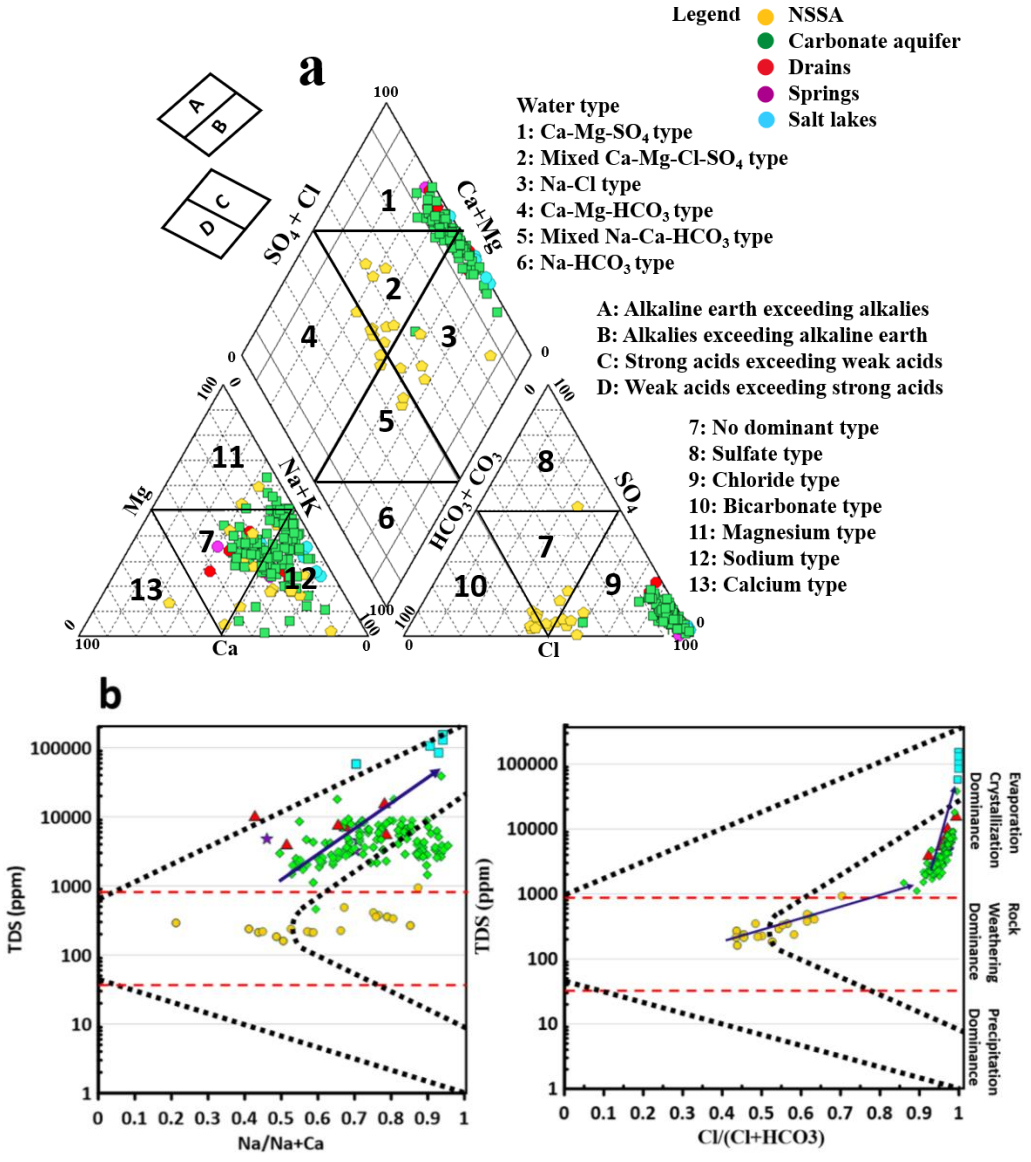

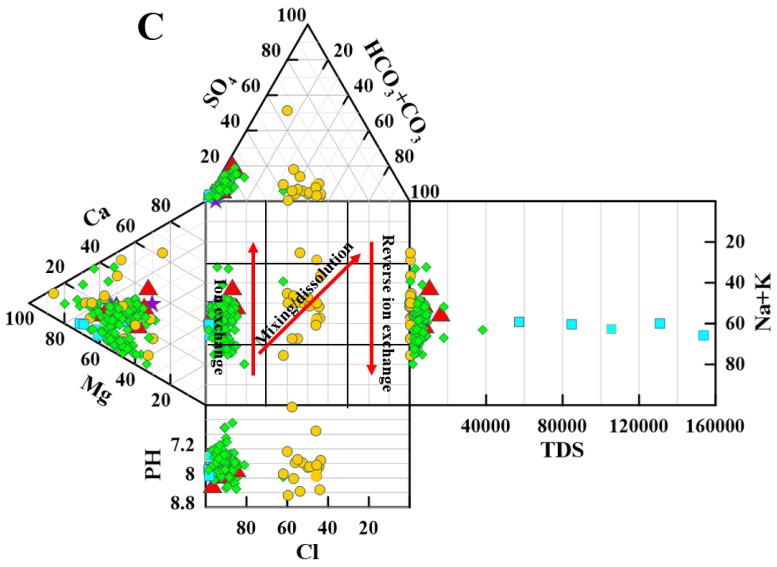

Figure 32. Graphical representation of Piper (a), Gibbs (b), and Durov (c) diagrams

5.2.2.2. Geochemical modeling

In this research, the saturation levels of minerals and salts in water were computed to identify minerals that might precipitate in the soil, close pore spaces, decrease permeability/infiltration rates, lead to waterlogging, and trace the origins of chemical components. These computations were conducted using a PHREEQC model, with input parameters including physicochemical and heavy metal data. Mineral saturation indices (SI) were determined for calcite, aragonite, Ca-montmorillonite, gypsum, chlorite, anhydrite, dolomite, albite, hematite, kaolinite, illite, and chalcedony, and displayed in a box plot (Fig 33). The model also estimated the partial pressure of CO_2, which was under-saturated (negative values), indicating diminished aquifer recharge. Water samples from the NSSA contained a mixture of salts, such as NaCl, Na_2SO_4, Mg $(HCO_3)_2$, $NaHCO_3$, and Ca $(HCO_3)_2$, resulting from leaching, dissolution of terrestrial salts, and cation exchange processes. These cation exchange processes increased Na^+ concentrations while reducing Ca^{2+} and Mg^{2+} levels, significantly elevating water salinity. The reduction in Ca^{2+} levels decreased the saturation states of anhydrite, calcite, aragonite, and gypsum minerals. All water samples were under-saturated with respect to anhydrite, halite, and gypsum, suggesting that the water can dissolve more of these minerals, further elevating salinity. In contrast, hematite, kaolinite, and chlorite minerals exhibited positive SI (supersaturation) in all water samples. The majority of samples are supersaturated regarding calcite, dolomite, Ca-montmorillonite, illite, chalcedony, and albite, with minimum values −0.9, −0.2, −1.45, −0.1, −0.3, and −2.1 respectively, and maximum value 1.5, 4.4, 8.9, 9, 1.7, and 4.6, respectively (Fig 33). The supersaturation of montmorillonite in 87% of the samples likely results from the decomposition of feldspar minerals, which release ions that react with other minerals to form montmorillonite. The presence of illite and kaolinite in the aquifer systems could stem from the alteration of other minerals, such as feldspars. Hematite may form from the oxidation of iron-bearing minerals. The SI index is a valuable tool for predicting the geological composition of the aquifer system, the sources of primary and trace ions in surface and groundwater,

and the mineralization processes. For example: Calcite, dolomite, aragonite, anhydrite, gypsum, anorthite, and Ca-montmorillonite could be the primary sources of Ca^{2+}, Dolomite and chlorite may contribute to Mg^{2+} concentrations, Halite and albite could increase Na^{+} levels, Illite may be sources of K^{+}, and Hematite and chlorite could provide Fe.

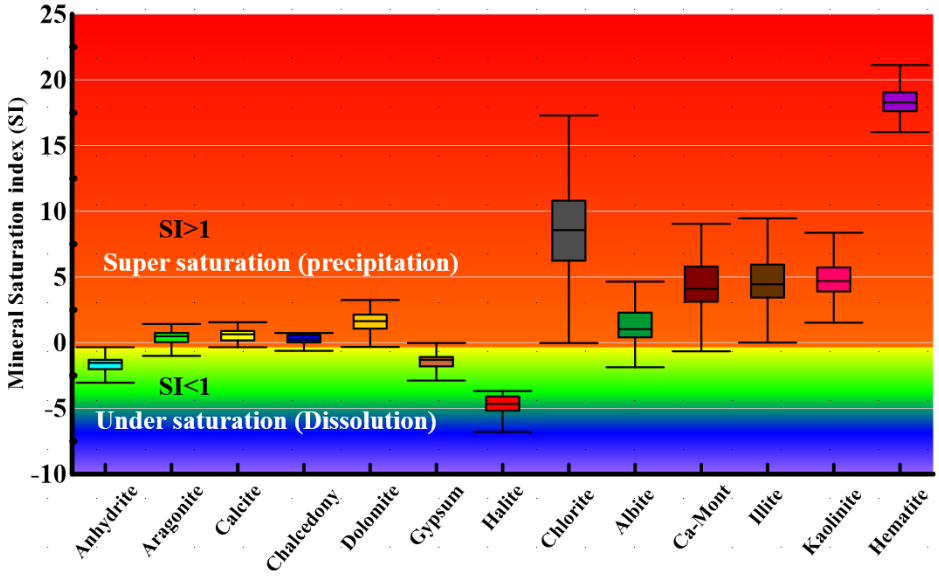

Figure 33. Minerals saturation index extracted from PHREEQC model.

It is important to acknowledge a key limitation of geochemical modeling. While the PHREEQC program may calculate supersaturation for certain minerals, this does not always mean that these minerals will precipitate in the real condition. The kinetics of mineral precipitation can be slow, and other environmental factors can inhibit crystal growth. Therefore, the calculated supersaturation should be interpreted as a potential for precipitation rather than a direct observation of it. For example, while the model may indicate supersaturation for minerals like hematite may not readily precipitate under the conditions found in the Siwa Oasis. However, these minerals can precipitate on the ground surface due to high air and soil temperature with high evaporation rate. The supersaturation of irrigation water with these minerals can reduce soil permeability, fertility, infiltration rates, and crop yields, while increasing waterlogging. However, minerals like chlorite and hematite are often associated with hydrothermal systems and may indicate the presence of geothermal water at greater depths. Further investigation is needed, as Siwa Oasis is situated in a tectonically active region.

5.2.2.3. Ion source detection

The analysis of major ion relationships and ratios was used to identify the key processes influencing groundwater chemistry (Fig 34). The linear relationship between Na^{+} and Cl^{-} (Fig 34a) revealed a balanced distribution of these ions in samples from TCA, drains, springs, and the lake, with a strong correlation coefficient of 0.99 (Fig 35). This close association points to halite dissolution as a major contributor to sodium and chloride ions, confirming a Na-Cl water type. However, some samples deviated to the right of the 1:1 line, implying additional sources of Cl^{-}. These could include minerals

such as sylvite (KCl), bischofite ($MgCl_2 \cdot 6H_2O$), and tarapacaite [(K, Na, Sr)2(SO4, Cl)2], as well as anthropogenic activities leaching from topsoil due to high correlation between Cl^- and Mg^{2+} .

Most samples from the NSSA region closely followed the 1:1 line, suggesting that halite dissolution is the main source of Na^+ and Cl^- in these waters. This conclusion is reinforced by the strong correlation (0.74) between Cl^- and Na^+, alongside the notably weaker relationships observed with other cations. Some NSSA samples deviated to the right of the 1:1 line, which can be explained by the removal of Na^+ through reverse ion exchange or the presence of additional Cl^- sources, such as sylvite mineral. This interpretation is supported by the moderate correlation (0.43) between Cl^- and K^+ (**Fig 35**). In the TCA, the relationship between Na^++K^+ and Ca^{2+}+Mg^{2+} (**Fig 34b**) showed that all water samples fell to the right of the 1:1 line, pointing to processes like silicate weathering, ion exchange, and carbonate precipitation. Silicate weathering increases the Ca^{2+}+Mg^{2+}/ HCO_3^-+SO_4^{2-} ratio above 1 (**Fig 34c**), while carbonate precipitation reduces the concentrations of HCO_3^- and SO_4^{2-} in the water. The higher concentrations of Na^+ and K^+ compared to Ca^{2+} and Mg^{2+} in most samples suggest an ion exchange process, where Ca^{2+} and Mg^{2+} are replaced by Na^+ and K^+ ions [127]. Plotting the sum of Ca^{2+} and Mg^{2+} against HCO_3^- and SO_4^{2-} on a linear graph helped identify the sources of Ca^{2+} and Mg^{2+} in the water samples [128]. Samples from TCA, drains, springs, and the lake clustered above the 1:1 line, indicating the influence of carbonate precipitation and silicate weathering.

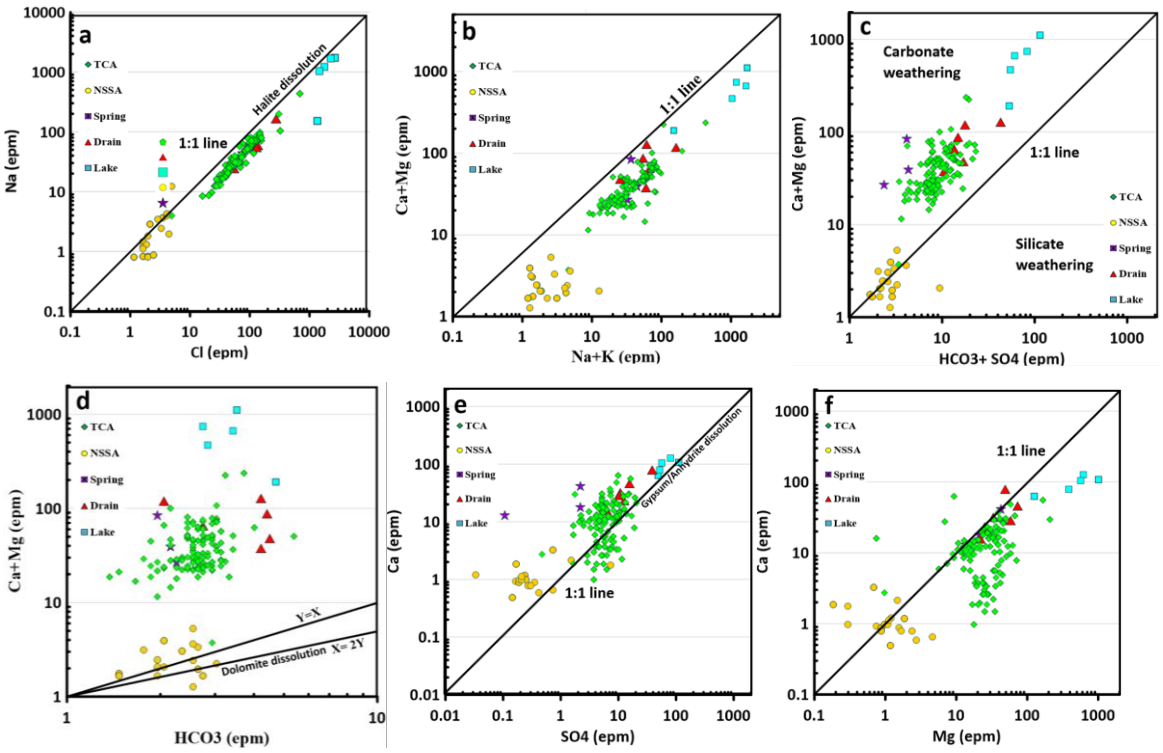

Figure 34. The ionic ratio between the major ions in the different water resources of Siwa Oasis.

In the NSSA, most samples crossed the 1:1 line primarily due to the dissolution of gypsum, calcite, and dolomite. The ratio of Ca^{2+}+Mg^{2+} to HCO_3^- was used to identify the sources of these ions in the groundwater (**Fig 34d**). A ratio close to 0.5 suggests that Ca^{2+} and Mg^{2+} are derived exclusively from the weathering of carbonate minerals. In contrast, a ratio below 0.5 may indicate processes such as

ion exchange or bicarbonate enrichment, leading to a reduction in calcium and magnesium levels. Samples from TCA, drains, springs, and the lake exhibited a higher $Ca^{2+}+Mg^{2+}/HCO_3^-$ ratio, while most NSSA samples had ratios near 0.5. This implies that the elevated Ca^{2+} and Mg^{2+} concentrations in TCA, springs, and surface water are influenced by processes other than carbonate dissolution, such as silicate weathering [127]. For NSSA, the $(Ca^{2+} + Mg^{2+})/HCO_3^-$ ratio indicated that calcium, magnesium, and bicarbonate ions primarily originate from the dissolution of calcite, dolomite, and gypsum, as well as silicate weathering. However, some NSSA samples fell below the 1:1 line, reflecting higher proportions of HCO_3^- compared to Ca^{2+} and Mg^{2+}. Moderate correlations (0.49 and 0.37) between Fe, Mn, and HCO_3^- (**Fig 35**) suggested that minerals like siderite and rhodochrosite could also contribute to the bicarbonate content in NSSA groundwater.

a

	TDS	T°c	pH	EC	Na^+	K^+	Mg^{2+}	Ca^{2+}	Mn	Fe	Cl^-	SO_4^{2-}	HCO_3^-	NO_3
TDS	1	-0.08	0.02	0.93	0.98	0.13	0.93	0.53	0.38	0.24	1.00	0.50	0.26	0.01
T°c		1	-0.01	-0.08	-0.03	0.03	-0.05	-0.35	0.17	0.12	-0.07	-0.17	-0.04	0.12
pH			1	0.03	0.02	-0.17	0.03	0.01	-1E-04	-0.03	0.02	-0.02	-0.04	-0.12
EC				1	0.93	0.04	0.86	0.42	4E-01	0.27	0.93	0.38	0.20	0.01
Na^+					1	0.10	0.89	0.43	4E-01	0.25	0.99	0.42	0.21	0.01
K^+						1	0.04	0.30	-1E-01	-0.15	0.09	0.38	0.17	0.06
Mg^{2+}							1	0.40	4E-01	0.25	0.94	0.43	0.28	0.11
Ca^{2+}								1	-7E-02	-0.01	0.49	0.61	0.20	-0.19
Mn									1	0.79	0.39	0.12	0.06	0.16
Fe										1	0.25	0.06	0.03	0.16
Cl^-											1	0.44	0.24	0.01
SO_4^{2-}												1	0.37	-0.01
HCO_3^-													1	0.19
NO_3														1

b

	TDS	T°c	pH	EC	Na^+	K^+	Mg^{2+}	Ca^{2+}	Mn	Fe	Cl^-	SO_4^{2-}	HCO_3^-	NO_3
TDS	1	-0.08	0.01	0.32	0.96	0.25	-0.01	0.31	0.30	0.15	0.85	0.91	0.28	-0.14
T°c		1	-0.14	-0.57	0.01	-0.19	-0.55	0.13	-0.45	-0.53	-0.25	0.14	-0.59	0.17
pH			1	0.32	0.01	-0.17	-0.16	0.34	0.16	0.08	0.11	-0.14	0.32	-0.14
EC				1	0.25	0.42	0.37	0.01	0.55	0.46	0.64	-0.04	0.75	-0.14
Na^+					1	0.15	-0.19	0.21	0.26	0.17	0.74	0.90	0.24	-0.10
K^+						1	0.36	-0.11	0.25	0.28	0.43	0.10	0.20	0.00
Mg^{2+}							1	-0.39	-0.06	-0.11	0.33	-0.18	0.23	0.04
Ca^{2+}								1	0.35	0.13	0.20	0.31	-0.05	-0.13
Mn									1	0.76	0.34	0.11	0.37	-0.10
Fe										1	0.17	-0.03	0.49	-0.17
Cl^-											1	0.58	0.52	-0.10
SO_4^{2-}												1	-0.06	-0.12
HCO_3^-													1	-0.19
NO_3														1

Figure 35. Spearman correlation matrix of the measured parameters.

In theory, the ratio of Ca^{2+} to SO_4^{2-} should be 1 if gypsum dissolution is the dominant process, as observed in some samples from the study area. However, many samples deviated from the 1:1 line, showing excess Ca^{2+} (**Fig 34e**). This suggests a stronger influence of carbonate weathering, particularly in samples from NSSA, springs, drains, and some TCA locations. Samples falling below the 1:1 line indicate additional sources of SO_4^{2-} beyond gypsum and anhydrite dissolution. The relationship between Ca^{2+} and Mg^{2+} (**Fig 34f**) categorized the samples into two main groups. The first group, comprising 13% of the samples, aligned closely with the 1:1 line, pointing to dolomite dissolution as the primary source of Ca^{2+} and Mg^{2+}. The second group, representing 78% of the samples, deviated to the lower right of the 1:1 line, suggesting an alternative source of Mg^{2+}, such as

silicate minerals. This interpretation is supported by the saturation index. The remaining 8.4% of samples, positioned above the 1:1 line, indicate that calcite dissolution and silicate minerals contribute additional Ca^{2+} to the groundwater. The weak correlations between Ca^{2+} and Mg^{2+} in TCA (0.4) and NSSA (-0.3) (**Fig 35**) suggest that groundwater in the study area is unlikely to dissolve dolomite minerals. This hypothesis is further validated by the SI for dolomite, which is greater than 0 (**Fig 33**). Similarly, the weak correlations between Ca^{2+} and HCO_3^- in TCA (-0.05) and NSSA (0.2) indicate that the water is supersaturated with respect to calcite, making it unable to dissolve this mineral. Instead, silicate weathering appears to be a key process driving the high concentrations of Ca^{2+} and Mg^{2+} in the groundwater.

5.3.Mixing model to detect the recharge and salinity source

This thesis provides a definitive identification of the recharge sources and salinity origins in the Siwa Oasis aquifer system by employing combination of stable isotope analysis (δ^2H, $\delta^{18}O$), advanced statistical techniques (PCA, K-means), and inverse NETPATH mixing models. This thesis moves beyond qualitative descriptions to deliver a quantitative assessment of the complex mixing processes that govern the oasis's water quality.

5.3.1. Recharge origin based on Stable Isotope

In this study, δ^2H and $\delta^{18}O$ were measured in groundwater and surface water (**Table 8s. Appendix**) to identify the recharge sources of various water resources and to understand the processes influencing water chemistry. The isotopic composition of the NSSA ranged from -10.71 to -8.57‰ for $\delta^{18}O$ and from -80.41 to -66.33‰ for δ^2H. For the TCA, $\delta^{18}O$ values varied between -10.62 and -8.45‰, while δ^2H values ranged from -80.34 to -65.63‰. Springs exhibited $\delta^{18}O$ values from -10.52 to -7.40‰ and δ^2H values from -79.73 to -63.54‰. Drains showed $\delta^{18}O$ values between -9.52 and -7.62‰ and δ^2H values between -75.62 and -68.96‰. The salt lakes showed $\delta^{18}O$ ranging from -7.09 to -0.85‰ and δ^2H ranging from -61.71 to -29.72‰. These isotopic signatures provide insights into the distinct recharge mechanisms and evaporation processes affecting the different water bodies in the study area.

The isotopic composition of surface water was found to be more enriched compared to groundwater (**Table 5s. Appendix 2**), primarily due to higher evaporation rates. Distribution maps of $\delta^{18}O$ in the NSSA and TCA (**Fig 36a)** revealed a trend of isotopic enrichment from west to east, which is opposite to the direction of groundwater flow in the study area. The relationship between δ^2H and $\delta^{18}O$ serves as a valuable tracer for identifying groundwater recharge sources and assessing the effects of prior evaporation [129]. During evaporation, lighter isotopes are preferentially lost, leaving the remaining water enriched in heavier isotopes [130]. The stable isotope data are plotted in **Fig 36b**, alongside the Global Meteoric Water Line (GMWL) and the Paleo Meteoric Water Line (PMWL). The GMWL is defined by the equation $\delta^2H = 8 \times \delta^{18}O + 10$ [131], while the PMWL is represented by $\delta^2H = 8 \times \delta^{18}O + 5‰$ [132]. The slope of the trend line for the different water resources in the study area is lower than that of the GMWL, indicating that groundwater samples have experienced some degree

of evaporation before rainwater infiltrates and recharges the aquifers [133]. This suggests that evaporation plays a significant role in modifying the isotopic composition of water in the region. Most $\delta^{18}O$ and $\delta^{2}H$ values for groundwater and surface water fall within the lower right quadrant of the GMWL, indicating that atmospheric precipitation is their primary source. However, the enrichment of heavy isotopes in these samples is a result of intense evaporation and water-rock interactions. The depletion in $\delta^{2}H$ and $\delta^{18}O$ suggests that the NSSA and TCA contain non-rechargeable paleowater (paleo-meteoric water). The NSSA is the only source capable of recharging the TCA through upward groundwater flow. However, the salinity of the TCA has increased significantly from 1998 to 2022 (**Fig 36c**), suggesting that there are other factors besides evaporation including mixing with salt water from salt lakes or old trapped sea water in fracture system and water rock interaction. The TCA is predominantly composed of shallow marine deposits (limestone and dolomite), raising the possibility of residual ancient seawater influencing the system after the regression of the Mediterranean Sea from the study area. Seawater is typically characterized by elevated concentrations of Cl^{-}, Na^{+}, Mg^{2+}, and Ca^{2+}, with the order of abundance being $Cl^{-} > Na^{+} > SO_4^{2-} > Mg^{2+} > Ca^{2+}$. These characteristics align with those observed in the TCA. Additionally, a strong correlation between Cl^{-} and Na^{+}, Mg^{2+}, and EC, along with higher concentrations of Mg^{2+} compared to Ca^{2+} across all water samples, supports the hypothesis of mixing with ancient marine water. To explore this mixing process, binary relationships such as EC and $\delta^{18}O$ were analyzed. **Figure 36d** shows that the water samples can be divided into two groups. In the first group, representing the TCA, an increase in EC is accompanied by an enrichment of $\delta^{18}O$.The observed patterns suggest a combination of evaporation and mixing between waters of varying depths and salinities, influenced by both horizontal and vertical groundwater flow within the fracture system, as well as mineralization processes. In the second group of TCA samples, while EC values increase, $\delta^{18}O$ remains relatively constant, typically below -10‰. This consistency points to water-rock interactions. This finding is consistent with a previous study in Siwa Oasis [134], which also identified the presence of trapped ancient seawater in the TCA. The regression line between $\delta^{18}O$ and $\delta^{2}H$, defined by the equation $\delta^{2}H = 7.8\ \delta^{18}O - 0.12‰$, further strengthens the evidence of these interactions [134].

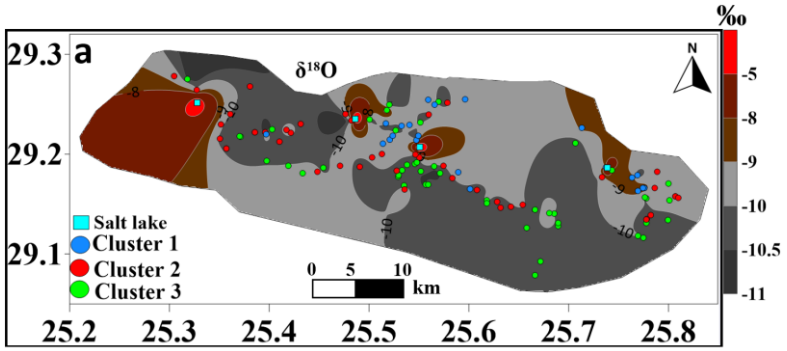

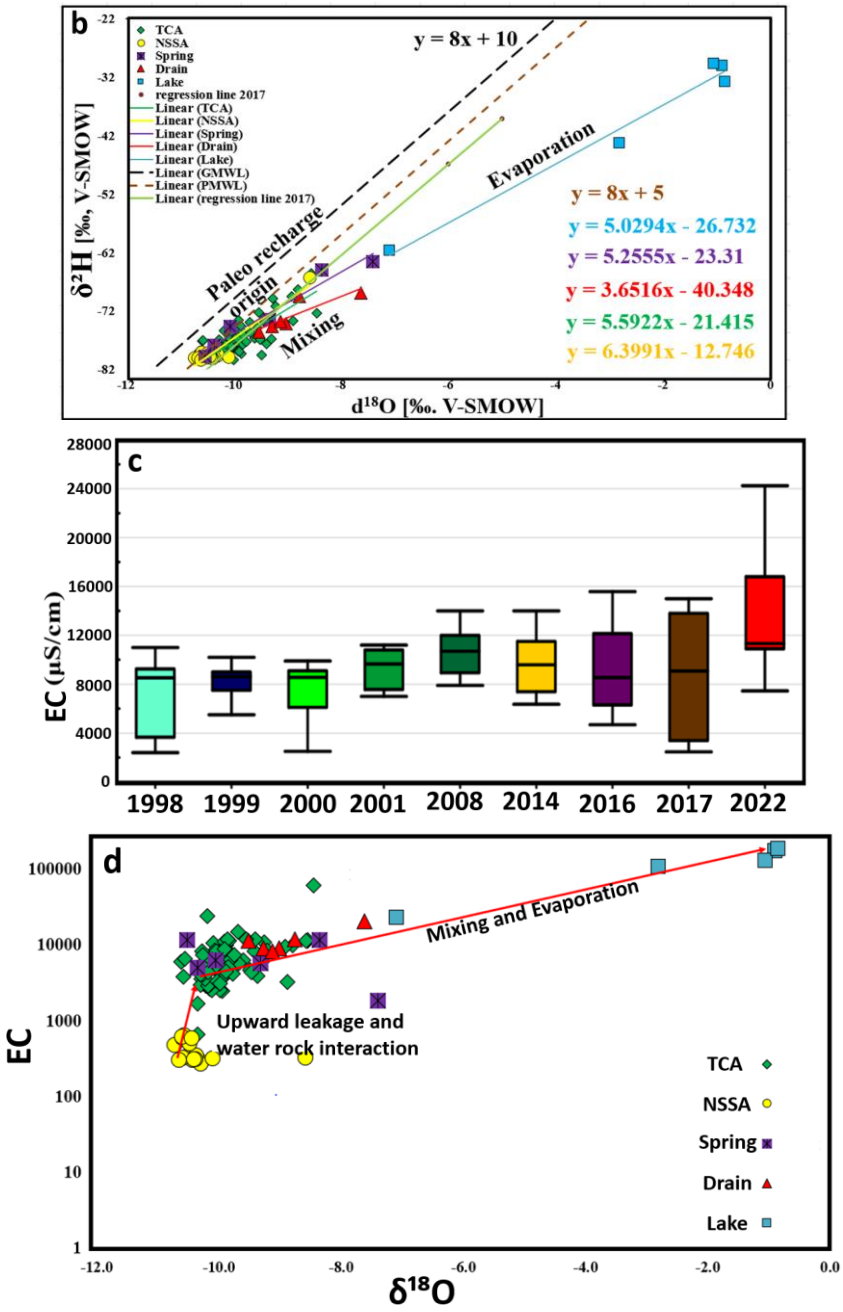

Figure 36. Distribution map of $\delta^{18}O$ (a), Plotting graph of $\delta^{2}H$ and $\delta^{18}O$ (b), EC of the TCA from 1998 to 2022(c), and plot of EC vs $\delta^{18}O$ (d)

5.3.2. Principal component analysis

To pinpoint the primary mechanisms influencing water chemistry and the shared origins of dissolved ions, Principal Component Analysis (PCA) was employed. PCA is a reliable method for identifying critical parameters that can later be used in K-means clustering based on cumulative explained variance. This method ensures that the most influential factors driving water chemistry are identified, providing a solid basis for further analysis, such as K-means clustering, to categorize water samples based on their chemical properties. Based on PCA results, four principal components with eigenvalues exceeding one were identified, collectively accounting for 75% of the total variance

(Table 3). Each component (PC) is connected to specific sets of water quality parameters, with high correlation coefficients indicating strong and meaningful relationships.

PC1, which explains 40.5% of the total variance, is strongly linked to TDS, Mg^{2+}, Cl^{-}, Ca^{2+}, K^{+}, and SO_4^{2-}. This suggests that PC1 represents the overall mineralization and salinity of the groundwater. The high correlations with TDS, Mg^{2+}, Cl^{-}, Ca^{2+}, and SO_4^{2-} point to dominant processes such as mineral dissolution and ion exchange. PC2 accounts for 15% of the total variance and is primarily associated with $\delta^{18}O$ and $\delta^{2}H$. The strong relationship with these stable isotopes indicates the influence of recharge sources and evaporation effects on water quality.

Table 3. The extracted PCs from PCA based on chemical parameter and isotopes

Parameters	PC1	PC2	PC3	PC4
$\delta^{2}H$	0.41	0.88	-0.08	0.14
SiO_2	-0.08	-0.02	-0.21	-0.40
NH_3	0.12	0.25	-0.09	0.68
NO_3	0.04	0.01	0.09	0.81
HCO_3	0.40	0.03	-0.03	0.13
$\delta^{18}O$	0.32	0.84	-0.07	0.16
SO_4	0.73	0.15	0.04	-0.01
Cl	0.94	0.21	0.03	0.11
Fe	-0.04	-0.06	0.81	0.06
Mn	0.02	-0.5	0.89	0.12
Ca	0.74	0.28	-0.07	-0.24
Mg	0.83	0.11	0.06	0.23
K	0.67	0.30	-0.07	0.12
TDS	0.97	0.22	0.02	0.09
Eigenvalues	5.73	2.11	1.68	1.07
% of Variance	40.5	15	11.9	7.64
Cumulative %	40.5	55.5	67.4	75.07

PC3 explains 11.9% of the total variance and is strongly correlated with Fe and Mn concentrations and reflects the presence of trace metals influenced by specific hydrogeochemical conditions. Elevated levels of Fe and Mn may indicate redox processes or the impact of particular geological formations (common sources) on water quality. This component provides valuable insights into localized processes affecting trace metal concentrations in the groundwater. In the TCA, the increased levels of Fe and Mn are likely the result of interactions between water and surrounding rock formations enriched in Fe and Mn. Additionally, glauconite and iron-rich particles found in Miocene carbonate rocks in the northern Western Desert have been documented [126]. For instance, the Moghra Formation contains iron oxide (Fe_2O_3) in amounts ranging from 1.6% to 36.1% and manganese oxide (MnO) levels between 0% and 0.6% [135], further supporting the idea that these elements originate naturally from the geological composition. PC4 represents 7.64% of the total variance and is defined by strong relationships with NO_3 and NH_3. The connection of NO_3 and NH_3 to PC4 highlights the impact of human activities on groundwater quality, such as farming practices, household wastewater, or fertilizer application. Elevated levels of NO_3 and NH_3 in PC4 may indicate contamination sources or nitrate seepage from agricultural operations. In conclusion, the PCA results provide significant insights into the primary factors influencing groundwater chemistry in Siwa

Oasis. The identified principal components highlight key aspects such as mineralization, salinity, evaporation impacts, trace metal presence, human-related influences, and carbonate-related processes that shape groundwater quality.

5.3.3. K-Mean Cluster Analysis

The K-means cluster analysis (**Fig 37 a, b**) aimed to explore the hydrogeological behaviors and water quality differences in the Siwa Oasis area through grouping the samples with similar chemistry in specific clusters. The clusters could be significant to select appropriate endmembers to build NETPATH mixing model to determine the recharge contribution % from NSSA and leakage of salt lake's water to shallow TCA. The analysis concentrated on groundwater samples from the NSSA, TCA, springs, and drains to better understand their salt content and isotopic makeup. Input parameters for K-means were derived from PCA outcomes (**Table 2**), which condensed the original 24 physicochemical parameters to 14 key parameters. The elbow curve (**Fig 9**) suggested that the sampling points could be divided into three groups (Clusters) based on the within-cluster sum of squares (WCSS). Beyond three clusters, the reduction in WCSS showed diminishing returns, indicating no significant improvement in clustering quality. The silhouette curve (**Fig 9**) was used to assess the clustering effectiveness by measuring how well-defined and separated the clusters were. The silhouette score for the three clusters was 0.54 (**Fig 9**), showing that the objects within each cluster were reasonably well-matched and distinguishable from those in other clusters. The p-values obtained from statistical tests, such as ANOVA and Kruskal-Wallis, were used to determine whether there were significant differences in the means or distributions of variables across the identified clusters. The results were evaluated using ANOVA and Kruskal-Wallis tests (**Table 6s. Appendix 2**), which reveal significant differences in the mean or spread of water quality variables within the clusters. Specifically, variables like TDS, K, Mg, Ca, Cl, SO_4, HCO_3, NO_3, NH_3, δ^2H, and $\delta^{18}O$ consistently show variations across clusters. These findings suggest that the K-means algorithm effectively identified distinct patterns in water quality characteristics. However, while the ANOVA test did not detect significant differences in the mean values for variables like Fe and Mn, the Kruskal-Walli's test highlighted differences in their distributions. This discrepancy highlights the importance of considering non-normality in the data.

The cluster analysis identified three distinct clusters, each representing unique hydrochemical characteristics of the groundwater sources. The first and second clusters consisted of samples from the TCA, with average EC values of 7,000 µS/cm and 10,000 µS/cm, respectively. The higher EC levels in these clusters indicate increased mineralization and dissolved salt content in the groundwater. These elevated EC concentrations can be attributed to two primary factors:

- **Evaporation**: The region's dry climate and high temperatures can lead to significant evaporation of shallow groundwater, concentrating dissolved salts and minerals. As a result, the TDS levels in the TCA might increase with increasing $\delta^{18}O$ composition (**Fig 37b**).

- **Mixing with old sea water or recent salt lakes**: The TCA may contain trapped ancient marine water from past sea before regression. The over extraction of water for irrigation could increase the possibility of leakage salt water from the lakes through the fracture system and increase the groundwater salinity. This assumption could be confirmed with mixing model and numerical flow model. Mixing this old saline water and/or recent salt lakes with meteoric water along the groundwater flow path could contribute to high variation in TDS values and increase $\delta^{18}O$ composition in the first and second clusters (Fig 37b).

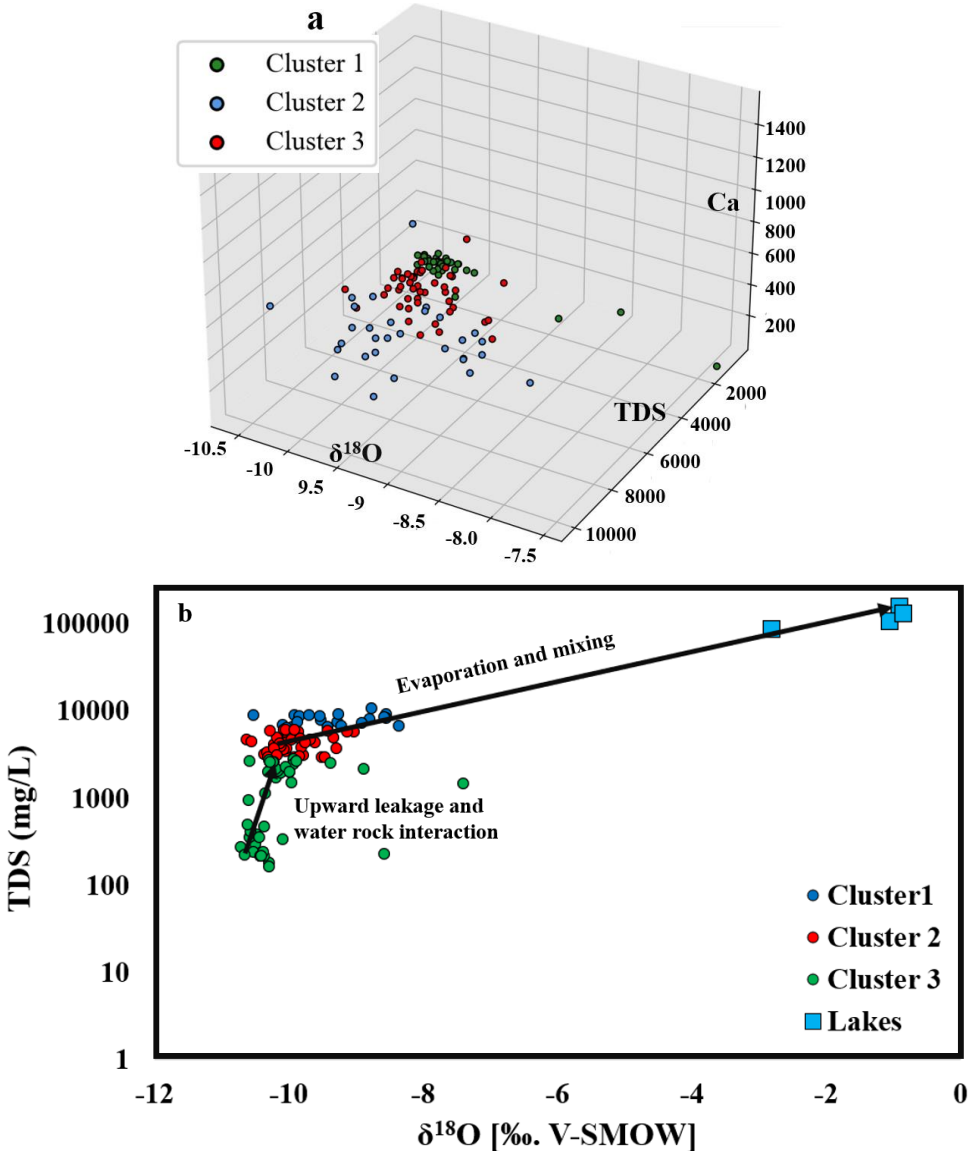

Figure 37. 3D scatter plot (a) and 2D scatter plot between TDS and $\delta^{18}O$ (b) of the 3 clusters extracted from K-means cluster analysis

The third cluster included samples from both the NSSA and the TCA, with depleted $\delta^{18}O$ and lower salinity (average EC of 2,500 µS/cm) suggests areas where direct recharge from the NSSA to the TCA occurs and made dilution of the groundwater salinity. Cluster 3 indicating favorable locations for drilling new irrigation wells (southern part of the study area) due to the influence of mixing,

evaporation, and interactions with shale and clay minerals is significantly lower compared to clusters 1 and 2. The processes influencing water chemistry in cluster 3 can be summarized as follows:

Water-Rock Interaction: As groundwater flows through the TCA, it interacts with limestone and dolomite formations, which are interbedded with shale and clay layers. These interactions result in the dissolution of minerals, releasing ions such as calcium, magnesium, sodium, and sulfate into the water. This process contributes to the observed increase in TDS without significantly altering the $\delta^{18}O$ isotopic composition.

long Residence Time: Longer residence times allow for more extensive interactions between water and surrounding rock formations, leading to greater mineral dissolution and higher salinity levels in the TCA compared to NSSA. Importantly, this process does not affect the $\delta^{18}O$ isotopic composition. This scenario is particularly relevant in the study area, where the aquifer systems are non-rechargeable.

The clustering method provides insights into the origin of drains and springs, suggesting a strong connection to the TCA. Samples from springs, which fall within the first and second clusters, indicate that these springs are likely fed by the TCA. Similarly, drain samples also grouped within the first and second clusters, implying that the drains primarily receive water from the TCA more than NSSA where the irrigation water from TCA consume large quantity of water than NSSA that mainly used for drinking. The elevated EC levels in these samples may result from groundwater interacting with minerals in the aquifer, as well as contributions from human activities or agricultural runoff. Overall, the results demonstrate the effectiveness of K-means clustering in identifying meaningful patterns within the dataset. These findings offer valuable insights into the variability of water quality parameters and help in selecting appropriate end-member and mixing samples for use in the mixing model later.

5.3.4. Evaporation effect using d-excess

The point where the LMWL intersects the y-axis is known as the deuterium excess (d-excess = $\delta^{2}H - 8\ \delta^{18}O$), calculated using the equation established by Dansgaard [136]. Globally, d-excess values in precipitation average around 10‰. However, regional variations can occur due to differences in evaporation processes and moisture sources. For instance, precipitation in North America, tropical island regions, and Japan exhibits distinct isotopic compositions, deviating from the global average. These variations are captured by the following LMWL equations: in North America, the relationship is expressed as $\delta^{2}H = 7.95\ \delta^{18}O + 6.03$ [137]; in tropical island regions, it follows $\delta^{2}H = 6.17\ \delta^{18}O + 3.97$ [137]; and in Japan, the equation is $\delta^{2}H = 8\ \delta^{18}O + 17.5$[138]. These regional differences highlight the significant influence of local climatic conditions on isotopic signatures, particularly the role of evaporation in shaping d-excess values. In general, faster evaporation or the evaporation of precipitation leads to a decrease in d-excess [139]. Negative d-excess values often indicate older recharge events and higher levels of evaporation, which are typically associated with heavier $\delta^{18}O$ values. Fig 38 illustrates the relationship between $\delta^{18}O$ and d-excess for both surface and subsurface

waters, providing insights into the hydrological processes influencing water resources in the study area. The d-excess values exhibited significant variation across different water resources in the study area. For the NSSA, the d-excess values ranged from 0.76‰ to 5.7‰, while in the TCA, they varied between -3.78‰ and 7.47‰. Springs displayed a broader range, with d-excess values spanning from -4.35‰ to 5.86‰.

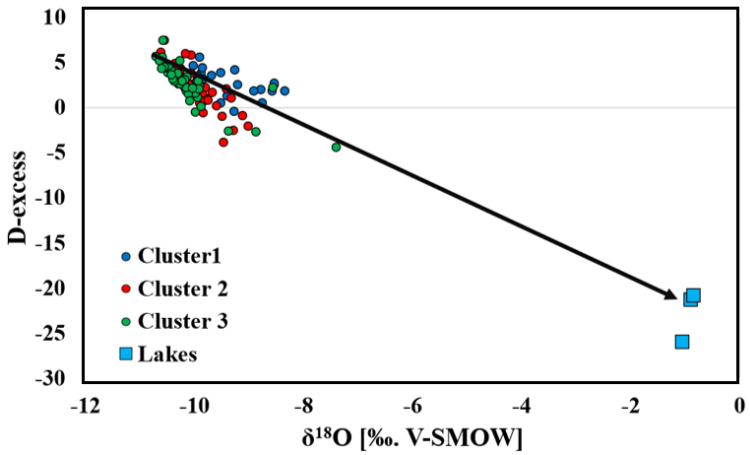

Figure 38. scatter plot of $\delta^{18}O$ vs D-excess showing the effect of evaporation on isotopic signature

In contrast, drains showed a narrower range, with values between -2.01‰ and 0.53‰. The most depletion in d-excess was observed in the salt lakes, where values ranged from -26.01‰ to -20.8‰, reflecting the strong influence of evaporation and saline conditions. These variations highlight the distinct isotopic signatures and hydrological processes associated with each water source. The inverse relationship between the d-excess and $\delta^{18}O$ (**Fig 38**) suggests that evaporation rates differ significantly between sites and groundwater zones. Samples from salt lakes, drains, and springs exhibit higher $\delta^{18}O$ values (**Fig 38**) and lower d-excess values indicating the influence of evaporation. In contrast, groundwater samples generally show lower d-excess and $\delta^{18}O$ values, pointing to paleo-recharge conditions. Here, evaporation and water-rock interactions are the primary factors controlling stable isotope composition. Notably, TCA and spring waters have lower d-excess values compared to NSSA waters. This difference may be attributed to evaporation and the mixing of TCA and spring waters with ancient trapped seawater or leakage downward from salt lakes.

The deterioration of water quality in the TCA due to the influence or leakage downward of salt lakes cannot be neglected. As the TCA serves as the primary aquifer for irrigation and is a non-rechargeable water resource, declining water pressure could allow saltwater to seep downward, increasing groundwater salinity. The previous investigation in thesis 2, the past three decades (1990–2020), the surface area of the salt lakes has expanded rapidly. This expansion, combined with reduced water pressure in the aquifer, likely accelerates the infiltration of saline water from the lakes into the TCA, particularly in highly permeable, fractured zones. This hypothesis is supported by the observed increase in TDS levels from the Salt Lake belt northward along the groundwater flow path in the

TCA (Fig 39b, c). Such a trend underscores the potential impact of downward leakage of saltwater from surface lakes on the aquifer's salinity and overall water quality.

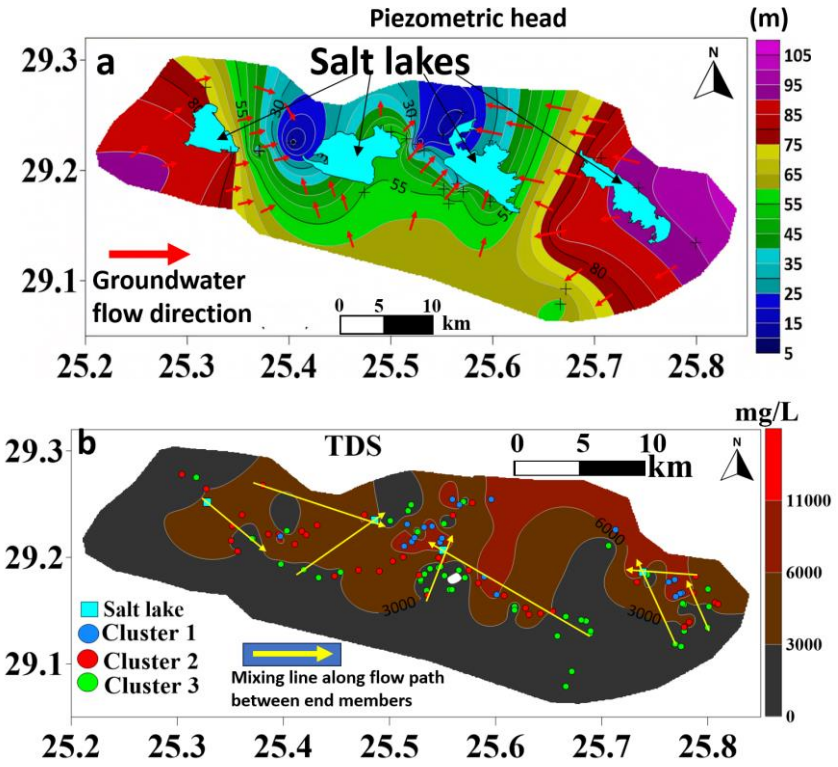

Figure 39. Groundwater flow direction (a), and TDS with the mixing line between the endmembers (b)

5.3.5. Groundwater salinity origin

Stable isotope ($\delta^{18}O$) is a valuable tool for understanding groundwater salinization processes [140]. Fig 37b illustrate the relationship between TDS and $\delta^{18}O$, as well as the distribution of oxygen isotopes across the three clusters extracted from K-means cluster analysis. Cluster 1 shows an increase in TDS with relatively constant $\delta^{18}O$ values, suggesting upward leakage and water-rock interactions along the vertical flow path from the NSSA to the TCA. Cluster 2 and 3 exhibit higher TDS levels alongside enriched $\delta^{18}O$ values, indicating the influence of evaporation and mixing with different water sources. Samples from the NSSA with low TDS (freshwater) and enriched $\delta^{18}O$ suggest evaporation during recharge period. By integrating stable isotope data with physicochemical parameters and K-means cluster analysis, NETPATH mixing model can be performed with optimum two end members and mixed samples along the flow path to determine the contribution of salt lakes to increase the salinity of TCA and contribution of NSSA to make dilution of TCA. Using a mixing model is often necessary in hydrogeochemistry to understand and measure the contributions of different water sources or endmembers to a mixed water sample [94,141].

The end members were identified based on K-means clusters, relationships between $\delta^{18}O$ and $\delta^{2}H$, TDS and $\delta^{18}O$, and the direction of groundwater flow. In the first scenario, the end members included salt lakes and samples from cluster 1, with mixing samples from clusters 2 and 3 (TCA). In the second scenario, the two end members were from the NSSA and cluster 3, with mixing samples from clusters 1 and 2 (TCA). The major ions, heavy metals, mineral saturation index (SI), reaction type

(precipitation/dissolution), cation exchange, and evaporation factor were used in the NETPATH model to account for geochemical reactions and mixing with different waters.

Therefore, the NETPATH model was used to simulate mass-balance transport through water-rock interaction processes and mixing. The input parameters, mineral phases and samples selected were mentioned previously in methodology section and visualized in **Table 4 and Fig 39a, b.** Based on the saturation indices of the two endmembers (initial water) water, precipitation and/or dissolution processes were identified. **Table 4** outlines the seven models developed showing the model number, location of mixing, model type, initial water (endmembers) with sample number, final water (mixed sample from TCA), calculated and computed mixing % of each endmember extracted from NETPATH model and validation from stable isotope signature (^{18}O), and the output value of each mineral phase and evaporation factor. The first scenario for salt water leakage from the lakes: the first endmembers were selected from TCA (sample 9, 10, 144, 117 and 7) with low $\delta^{18}O$, $\delta^{2}H$ (**Fig 40a**), and TDS values and the second endmember from the salt lakes (sample 27 and 92) with high $\delta^{18}O$, $\delta^{2}H$, and TDS values. The final water (mixed samples) was selected from the TCA with intermediate $\delta^{18}O$, $\delta^{2}H$, and TDS values (samples 20, 21, 93, and 87). The second scenario of upward flow of fresh water from the NSSA to TCA (**Fig 40b**), the first end members were selected from TCA (sample 21 and 87) with high $\delta^{18}O$, $\delta^{2}H$, and TDS values and second endmember from NSSA (sample 4 and 56) with low $\delta^{18}O$, $\delta^{2}H$, and TDS and final water from TCA (sample 15 and 68) with intermediate $\delta^{18}O$, $\delta^{2}H$, and TDS.

Table 4. The seven models, including the two initial water, the final water from the cluster as well as the mixing percentage

Model number	Site	Model type	Initial 1	Initial 2	Final	Mixing % calculated		Mixing % computed	
						Initial 1	Initial 2	Initial 1	Initial 2
1	Zeitun	Reaction and mixing	9 (TCA, cluster 3)	27	20	0.84	0.16	0.97	0.02
2	Zeitun		10 (TCA, cluster 3)	27	21	0.82	0.18	0.99	0.009
3	Zeitun		7 (TCA, cluster2)	27	21	0.82	0.18	0.96	0.04
4	Siwa		144 (TCA, cluster3)	92	93	0.98	0.02	0.99	0.006
5	Siwa		117 (TCA, cluster2)	92	87	0.96	0.04	0.98	0.02
6	Zeitun		21 (TCA, cluster1)	4	15	0.26	0.74	0.13	0.87
7	Siwa		87 (TCA, cluster1)	56	68	0.14	0.86	0.37	0.63

Model number	Phase precipitated or dissolved									
	Calcite	Dolomite	Halite	Gypsum	Ca-Montmorillonite	Na-Montmorillonite	Chalcedony	Illite	Exchange	Ev
1	-1.2	0.8	41.7	-1.6	-	-1.2	-	1.2	1.2	1.04
2	-3.15	1.5	30.3	-	-0.72	-	0.03	0.73	-7.3	1.6
3	-	1.2	58.4	0.9	-	-4.38	1.87	4.4	-19.4	1.5
4	-	-0.48	38.4	-0.69	-	-0.6	0.01	0.6	-5.7	1.6
5	-15.3	7.2	0	-2.01	-	0.41	-0.15	-0.4	-10.8	1.4
6	3.29	-2.29	0	0.98	-	0.25	-0.17	-0.27	1.27	2.07
7	-	1.3	20.9	5.34	-	-1.42	2.21	1.44	-4.36	2.3

The model was calibrated by determining the mixing percentages based on $\delta^{18}O$ values and comparing these results with the mixing percentages calculated from physicochemical parameters using the NETPATH model. The calibration showed strong agreement between the two methods,

with a high correlation coefficient (R^2 = 88%), as illustrated in Fig 40c, confirming the model's reliability in simulating the mixing processes.

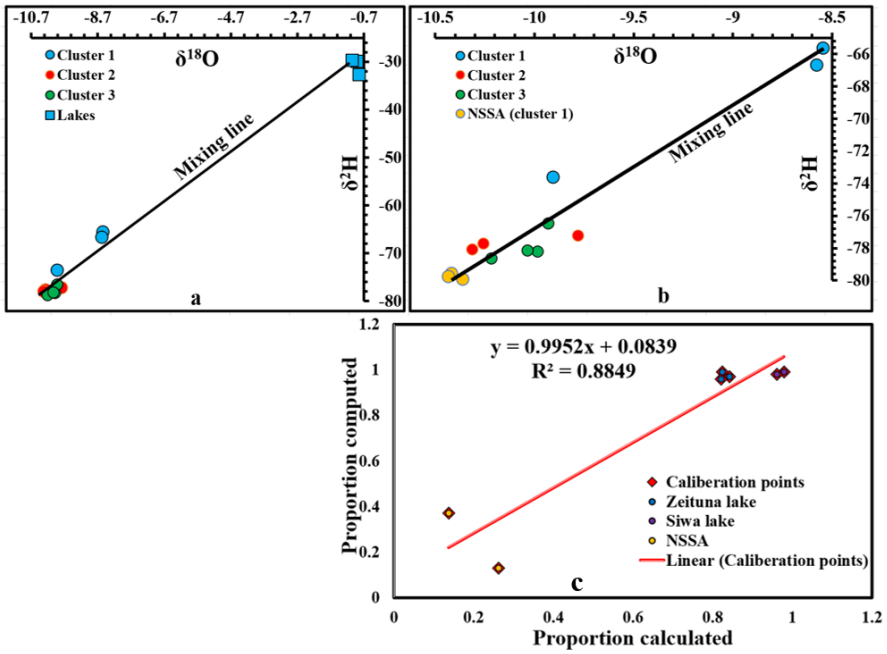

Figure 40. linear graph between δ^2H and $\delta^{18}O$ including lakes and TCA (cluster 3,2) as two end members (a), linear graph between δ^2H and $\delta^{18}O$ including NSSA and TCA (cluster 1) as two end members (b), and calibration curve between the calculated mixing percentage from $\delta^{18}O$ and the computed from the geochemical reaction (C)

The mixing model in the eastern part of the study area revealed that the estimated mixing percentage from Zeitun Lake ranged from 0.9% to 4%, while the TCA accounted for 99% (cluster 3) to 96% (cluster 2). In the central part of Siwa, the calculated mixing percentage from Siwa Lake ranged from 0.6% to 2%, and the TCA ranged from 99% (cluster 3) to 96% (cluster 2). In the eastern part of the study area, the mixing model indicated that the computed mixing percentage from Zeitun Lake ranged from 16% to 18%, while the TCA accounted for 84% (cluster 3) to 82% (cluster 2). In the central part of Siwa Oasis, the estimated mixing percentage from Siwa Lake ranged from 2% to 4%, and the TCA ranged from 98% (cluster 3) to 96% (cluster 2). The mixing model between the NSSA and TCA (cluster 1) showed that the calculated mixing percentage from the NSSA ranged from 87% to 63%, while the computed percentage ranged from 74% to 86% in the eastern and central parts of the study area, respectively.

The obtained mineral saturation indices (SI) values aligned with the mineral phase changes calculated by NETPATH, as shown in Table 7s (Appendix 2). The model results indicated the dissolution of gypsum and halite and the precipitation of calcite, dolomite, and clay minerals, accompanied by cation exchange, where calcium in groundwater replaces sodium in clay minerals within the aquifer matrix. The estimated evaporation factors (Ev) were 1.04, 1.6, and 1.5 at sites 9, 10, and 7, respectively, while Ev values ranged between 2.07 at site 21 and 2.3 at site 87. Although the contribution of Salt Lake to the TCA does not exceed 4%, the TDS of Zeitun Lake and Siwa Lake

are 153,589 mg/L and 130,992 mg/L, respectively, which can significantly increase the salinity of the TCA groundwater. This assumption can be verified by calculating the TDS obtained from mixing the lake sample with cluster 3 samples (TCA) and the mixing percentage of the lake derived from NETPATH (2% to 4%) using the following equation:

$$\text{TDS final} = \sum_{i=1}^{n}(\text{Pi} \times \text{TDSi})$$

Where: n is the number of solutions being mixed. i represents each solution. Pi is the percentage of the ith solution in the mixture. TDS_i is the TDS value of the ith. Using the TDS of the initial water of TCA (2837 mg/L), the initial water of Zeitun Lake (153,589 mg/L) showed that the final water from TCA ranged from 5823 mg/L to 8867 mg/L, which represents the TDS range of cluster 1. The computed and calculated mixing percentage of the NSSA, cluster analysis, and stable isotopes revealed that the source of the groundwater in the tertiary carbonate aquifer originated mainly from freshwater of the NSSA through upward leakage along the fault planes and the salinity increased through several factors including evaporation, water-rock interaction, ion exchange with clay minerals and mixing with old seawater, and downward leakage from hypersaline lakes. The excessive abstraction of water from the non-rechargeable aquifers, irrigation by flooding, and lack of an appropriate drainage system will deteriorate all the water resources in Siwa Oasis and increase soil salinization and water logging problems. Decreasing the freshwater pressure in NSSA due to excessive pumping for drinking and irrigation purposes will change the vertical groundwater flow from upward to downward, which means the freshwater will deteriorate from the brackish water of TCA. The mixing model was supported by conceptual model that was performed based on lithological log correlation and lineaments extracted from remote sensing and aeromagnetic data analysis in the catchment area (Fig 41).

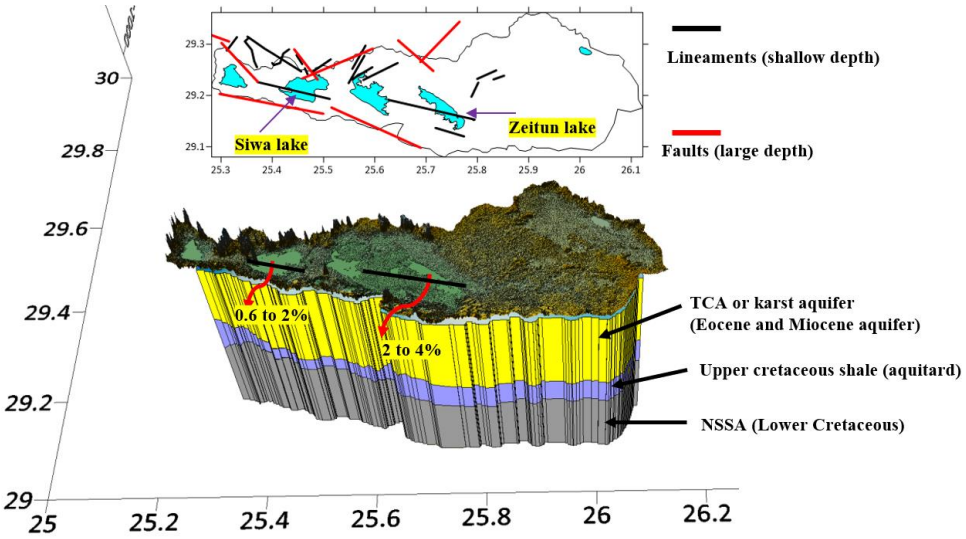

Figure 41. Conceptual model based on geological boundary illustrate the contribution percentage from hyper saline lake to the karst aquifer (TCA) supported with shallow depth lineaments in karst aquifer and deep faults in NSSA

The results showed that the lineaments could cross only two lakes (Zeitun and Siwa lakes) which indicate the possibility of connection between these two lakes and the shallow aquifer. The mixing model proved that these two lakes only were the reason for increasing the salinity in the TCA. The other lakes did not show any contribution to the salinity of the TCA which could be because the Aghormi lake and El-Maraki Lake are located in a normal depression above impermeable layer and no significant fracture system could reach these locations. However, increasing the surface area of this lake could cross the fracture system and contribute in the groundwater salinity.

5.4.Residence time and recharge location of the TCA from NSSA

This thesis provides a quantitative and spatially explicit understanding of the recharge dynamics and groundwater residence times in the Siwa Oasis aquifer system. The application of multi-isotopic tracers (δ^2H, $\delta^{18}O$, ^{13}C, ^{14}C, $^{87}Sr/^{86}Sr$) and radiocarbon dating (**Table 8s and 9s. Appendix 2**), combined with geochemical analyses and inverse mixing models such as NETPATH and Faure models, provides a powerful toolkit for investigating groundwater recharge sources, salinity origins, and residence times in aquifer systems. Strontium isotopes ($^{87}Sr/^{86}Sr$), which are not subject to natural fractionation, are particularly effective for identifying recharge sources, quantifying mixing ratios, and assessing water–rock interactions. Additionally, the use of radiocarbon (^{14}C) dating allows for the estimation and correction of groundwater residence times, providing a clearer understanding of the age distribution within different aquifer systems, which is crucial for sustainable groundwater resource management. Furthermore, this integrated approach helps delineate the most promising locations for future drilling wells, ensuring optimal exploitation of groundwater resources while minimizing environmental impact.

5.4.1. Spatial variation of isotopic signature

The spatial analysis of TDS, Sr, $^{87/86}Sr$ and $\delta^{18}O$ concentrations in the NSSA and the TCA highlights distinct hydrochemical trends influenced by geographic location and aquifer dynamics along the flow path supported with flow direction in NSSA and TCA (**Fig 42**). The TDS in the NSSA shows a clear south-to-north gradient, increasing from 160 mg/L in the southeastern (sample 39) to 550 mg/L in the northern regions. This gradual increase reflects the influence of longer groundwater residence time and potential mixing with older or more mineralized water in the northern parts of the aquifer. The Sr concentrations in the NSSA remain relatively uniform across the study area, ranging from 0.04 mg/L in the northeastern region to 0.28 mg/L in the northwest near El Maraki Lake. This consistency indicates limited water-rock interaction with Sr source or minimal contributions from external sources, such as evaporites or carbonate dissolution, within the NSSA.

The TDS in the TCA exhibits a more variation, with the lowest value of 1120 mg/L recorded in the southeast (sample 40) while the highest TDS values exceed 8000 mg/L, concentrated in the northeast near Zeitoun Lake (samples 17, 20, and 21) and in the northern region between Siwa Lake and Aghormi Lake (samples 93, 77, 86, 82, and 127). This variation suggests that the TCA is more vulnerable to salinization in the northern part, likely due to interaction with surface lakes and

potential evaporitic deposits. The Sr concentration in the TCA mirrors the TDS trend, with a minimum value of 1.074 mg/L in the southeast (sample 40) and a maximum of 10.1 mg/L in the northeast near Zeitoun Lake (sample 20). Northern regions between Siwa Lake and Aghormi Lake also show elevated Sr values up to 8.2 mg/L (sample 82). This correlation between Sr and TDS suggests that Sr enrichment is closely tied to salinization processes, including lake water leakage, carbonate dissolution, and potential ion exchange. Comparison Between NSSA and TCA reveals contrasting behaviors in hydrochemistry:

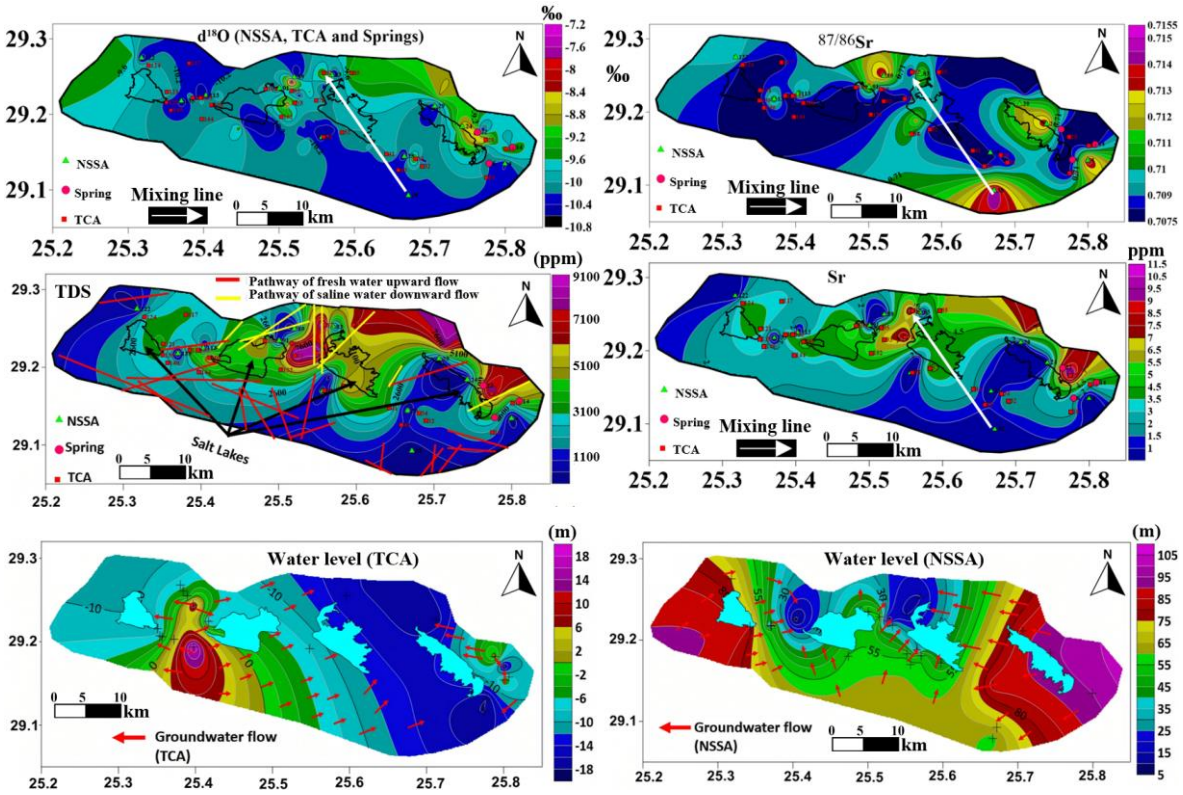

Figure 42. The distribution maps of the 18O, 87/86Sr, TDS, Sr, and groundwater flow direction in NSSA and TCA

The NSSA exhibits stable Sr concentrations, which may reflect its lower vulnerability to external influences and lithology dominated by sandstone. The TCA, however, demonstrates significant variability in Sr and TDS, indicative of active interactions with surface lakes, localized groundwater recharge, and evaporite and carbonate dissolution. The increasing TDS and Sr concentrations in the northern and northeastern TCA near Zeitoun Lake and between Siwa and Aghormi Lakes suggest potential contributions from lake water. This is supported by the artesian conditions in some TCA wells to be non-artesian, which facilitate downward migration of salt lake's water, especially in areas influenced by over-extraction or seasonal water-level fluctuations in the north east and north part of study area. Siwa Lake and Zeitun lake are located above fracture system that could facilitate the leakage downward from these lakes. The uniform Sr distribution in the NSSA emphasizes its isolation from the surface processes affecting the TCA, possibly due to the over pressure condition of water in the NSSA where the water level reach 100 m above ground surface.

Spatial Distribution of $^{87/86}Sr$ and $\delta^{18}O$ across the NSSA and the TCA reflects their distinct hydrochemical processes, recharge sources, and aquifer dynamics. $^{87/86}Sr$ ratios in the NSSA range from 0.709 (sample 35 in central Siwa Oasis) to 0.715 in the southeast (samples 38 and 4). The highest values are observed in the southeastern and northern regions (sample 89), with a general trend of decreasing ratios from east to west. The elevated $^{87/86}Sr$ values in the southeast and north suggest prolonged water-rock interactions with radiogenic silicate minerals or mixing with older groundwater influenced by crustal material where the NSSA overlain the basements rocks. The westward decline in $^{87/86}Sr$ ratios reflects potential dilution by younger, less radiogenic recharge or reduced contact with silicate-rich formations. The $\delta^{18}O$ values in the NSSA range from -10.713‰ in the southeast (sample 35) to -8.571‰ in the northeast (sample 24). The enrichment of $\delta^{18}O$ towards the northeast is indicative of evaporation effects during recharge period. The depleted values in the southeast suggest recharge under cooler or wetter paleoclimatic conditions, consistent with the deep, confined nature of the NSSA. The $^{87/86}Sr$ ratios in the TCA show minimal variation, ranging from 0.708 (sample 82) in the north, between Siwa and Aghormi Lakes to 0.709 (sample 34) in the southeast. The uniformity of $^{87/86}Sr$ ratios in the TCA indicates a consistent lithological influence dominated by carbonate rocks. Higher values in the southeast suggest significant contribution input from deep sources or localized interactions with silicate-rich waters, while lower values in the northern part are indicative of a stable, carbonate-dominated system. The $\delta^{18}O$ values in the TCA are more enriched compared to the NSSA, with a minimum of -10.624‰ in the western part near El Maraki Lake (sample 133) and a maximum of -8.55‰ in the northeast near Zeitoun Lake (sample 20). Northern areas between Siwa and Aghormi Lakes also show enriched values (sample 82) with $\delta^{18}O$=−9.26‰). The enrichment trend reflects the influence of evaporation and lake water leakage, and localized recharge processes. The depleted values in the west suggest less evaporative influence, or minimal interaction with surface water and high contribution from deep NSSA.

5.4.2. Mixing approach and recharge source of TCA

The proposed approach aims to delineate the sources and mixing dynamics of groundwater between the NSSA and the TCA using isotopic and geochemical signatures, specifically $^{87/86}Sr$, Sr concentration, salinity, and stable isotopes ($\delta^{18}O$ and $\delta^{2}H$). The hypothesis is that distinct isotopic and geochemical signatures of NSSA and TCA waters, shaped by lithology, water-rock interactions, and residence time can be used to identify mixing proportions and infer hydrological connectivity. By employing mixing models such as the Faure model and validating these results with NETPATH geochemical modeling, it is feasible to quantify the contributions from the deep NSSA to the TCA. Furthermore, the analysis of saturation indices and dissolution/precipitation phases provides additional insights into the chemical evolution of groundwater during mixing. This approach is robust due to its reliance on well-established geochemical principles and the integration of multiple data sources, allowing for a comprehensive evaluation of mixing processes and their impact on aquifer chemistry[86,94,104]. The graph plotting $^{87/86}Sr$ against salinity (**Fig 43**) reveals distinct trends for

the NSSA, TCA, and springs, offering critical insights into the groundwater system dynamics and interactions. The NSSA samples exhibit a sharp vertical trend with nearly uniform salinity (< 500 mg/L, indicative of freshwater) and increasing $^{87/86}Sr$ values. This pattern reflects the isotopic stability of the NSSA water in a chemically homogenous environment with limited interaction with evaporite minerals or surface water-derived salts.

The vertical trend emphasizes that changes in $^{87/86}Sr$ are primarily due to isotopic variations in the aquifer's geological materials, rather than significant geochemical processes affecting salinity. TCA samples show a sharp horizontal trend with a rapid increase in salinity (1120 to 9000 mg/L) and low, uniform $^{87/86}Sr$ values. This horizontal trend suggests that the rapid salinity increase is predominantly driven by processes such as evaporation and dissolution of salts, and mixing with salt water with minimal contributions from isotopically distinct sources. Springs align along the same trend as TCA samples, confirming their origin as mixed water dominated by the TCA with limited input from the NSSA. This graph emphasizes the contrasting geochemical environments of the NSSA and TCA, while confirming the dominant role of the TCA in influencing spring water chemistry. The observed trends also suggest that while vertical hydraulic connectivity exists, it is likely localized and influenced by structural controls.

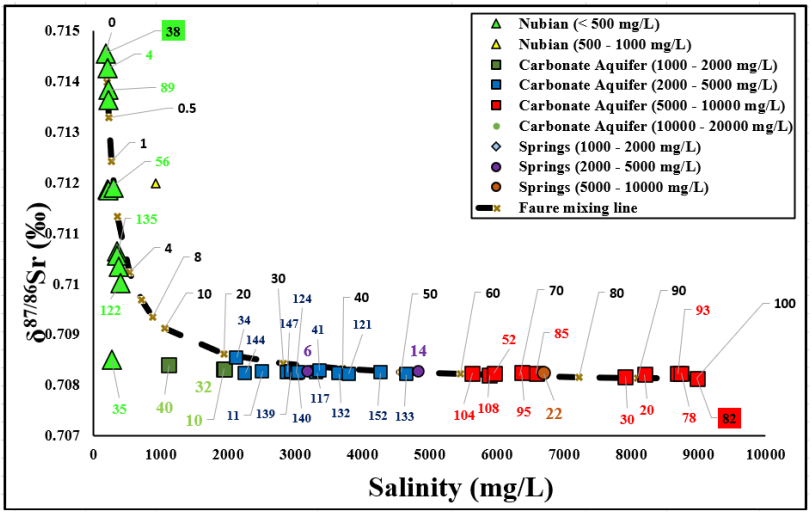

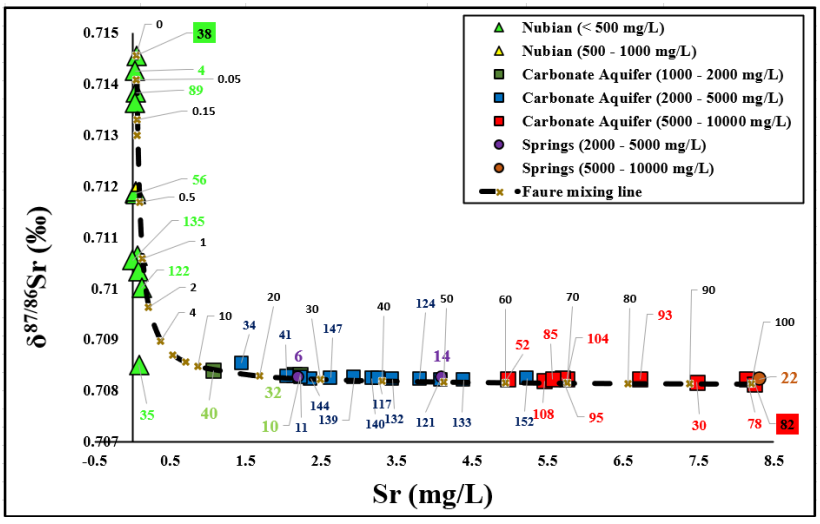

Figure 43. The relationship between salinity vs $^{87/86}Sr$ and Sr vs $^{87/86}Sr$ supported with mixing line based on Faure model

5.4.2.1. Mixing Line based on Faure model

The mixing line observed in the $^{87/86}Sr$ vs salinity graph (Fig 43) highlights the significant contribution of NSSA to TCA recharge, particularly along fault planes where the upper Cretaceous shale is impermeable layer separate the TCA from NSSA. Faults act as conduits, allowing upward flow of NSSA water through the shale barrier into the overlying TCA. This localized recharge is evident in areas where low-salinity TCA samples align closely with the NSSA end-member on the mixing line. This recharge mechanism explains the spatial variability in salinity and isotopic signatures within the TCA, particularly the presence of fresher water in fault-proximal areas. The sharp horizontal trend in salinity for TCA samples with minimal variation in $^{87/86}Sr$ at higher salinity levels reflects limited mixing with NSSA in regions distant from fault zones or where the shale layer remains intact. The higher $^{87/86}Sr$ values in low-salinity TCA samples near fault zones support significant NSSA contribution, as these isotopic signatures are characteristic of the deeper NSSA water. Conversely, TCA samples in regions without active faulting or with intact shale layers show higher salinity and lower $^{87/86}Sr$, indicating minimal interaction with the NSSA.

The $^{87/86}Sr$ vs Sr relationship (Fig 43) highlights the geochemical and structural dynamics influencing the NSSA and TCA interaction, similar to the trends observed in the salinity relationship. The graph shows a sharp vertical trend for NSSA samples, with significant variation in $^{87/86}Sr$ (0.709 to 0.715) while maintaining almost uniform and relatively low Sr concentrations (<0.3 mg/L). This pattern reflects the isotopic variability within the NSSA, potentially influenced by lithological heterogeneity and varying degrees of water-rock interaction within the sandstone aquifer. The TCA samples exhibit a sharp horizontal trend with rapidly increasing Sr concentrations (1 to 10 mg/L) but almost uniform and lower $^{87/86}Sr$ values (0.708 to 0.709). This behavior suggests a strong influence of geochemical processes within the TCA, such as dissolution of evaporite minerals, mixing with saline water, or limited interaction with the NSSA isotopic signature in high-Sr zones.

The springs align closely with the TCA samples on the graph, indicating their source is primarily influenced by the TCA. The mixing line performed based on Faure model connects the vertical trend of the NSSA to the horizontal trend of the TCA, reflecting varying contributions of NSSA recharge to the TCA. Low-Sr TCA samples align closer to the NSSA end-member, indicating significant recharge from the deeper aquifer, while high Sr in TCA samples reflect minimal NSSA contribution. The mixing line analysis using the Faure model provides critical insights into the interaction between the NSSA and TCA, delineating the recharge dynamics and spatial variability in contributions from the NSSA. Two distinct end members were identified. One represents the TCA with the lowest $^{87/86}Sr$ ratios, highest salinity, and maximum Sr concentrations, and the other representing the NSSA with the highest $^{87/86}Sr$ ratios, lowest salinity, and minimum Sr concentrations. The mixing model revealed that the group of TCA samples with salinities ranging from 1000 to 2000 mg/L receives substantial

recharge from the NSSA, with contributions of 80–90%. These samples are primarily located along fault planes and fracture systems in the southeastern and southwestern parts of the study area, emphasizing the critical role of structural features in facilitating vertical recharge. In contrast, samples with salinities between 2000 and 5000 mg/L exhibit intermediate NSSA contributions (50–80%) and are found in transitional zones near the faults but extending farther from direct recharge points. This group reflects a mixing process between NSSA recharge and more saline TCA water. The third group, characterized by salinities ranging from 5000 to 9,000 mg/L, has minimal NSSA contributions (0–40%). These samples are predominantly located in the northern regions between Siwa Lake and Aghormi Lake and in the northeastern areas near Zeitun Lake. The high salinity in these areas is attributed to evaporative concentration processes and downward leakage of brine from salt lakes, exacerbated by over-extraction of TCA groundwater for irrigation purposes. This over-extraction likely reduces aquifer pressure, transitioning some regions from artesian to non-artesian conditions and promoting the influx of saline water from the overlying lakes (Siwa lake and Zeitun lake). Notably, the $^{87/86}$Sr ratios remain consistent despite the increase in salinity, indicating that the isotopic signature of the saline lake water aligns with that of the TCA. These findings highlight the critical role of fault planes and fractures as conduits for NSSA recharge and emphasize the impact of anthropogenic activities, such as groundwater over-extraction, on the salinity and water quality in the TCA. Managing extraction rates and protecting structural recharge zones are essential to preserving the aquifer system's balance and mitigating salinization risks.

The relationships between δ^{18}O and $^{87/86}$Sr and between δ^{18}O and Sr concentrations (**Fig 44**) further support the proposed interpretations of the hydrological and geochemical processes governing the NSSA and TCA systems. The graph of δ^{18}O versus $^{87/86}$Sr reveals distinct patterns: samples from salt lakes, the TCA, springs, and agricultural drains align vertically with uniform low $^{87/86}$Sr values and varying δ^{18}O.

This suggests a shared isotopic signature influenced by evaporative processes and minimal variations in Sr isotopes across these systems. The δ^{18}O values range from -7.089 to -0.845 for salt lakes, -10.624 to -8.545 for the TCA, -10.356 to -8.350 for springs, and -9.273 to -7.621 for agricultural drains, reflecting varying degrees of evaporation and mixing. In contrast, the NSSA samples exhibit a horizontal trend in the δ^{18}O versus $^{87/86}$Sr graph, indicating sharp changes in $^{87/86}$Sr with consistently low δ^{18}O values (-10.713 to -10.295). This trend underscores the distinct geochemical nature of the NSSA, characterized by minimal evaporation and a more radiogenic Sr isotope signature. The exception is sample 24 from the northeastern Siwa Oasis, which shows a higher δ^{18}O value (-8.57), suggesting localized mixing, possibly influenced by hydraulic connections with the TCA or proximity to surface features. Similarly, the relationship between δ^{18}O and Sr concentration reveals a progression of Sr enrichment from the NSSA, through low-salinity TCA, intermediate-salinity TCA, high-salinity TCA, and finally to the salt lakes. The NSSA samples consistently exhibit low Sr concentrations, reinforcing their role as a fresh water source with limited interaction with evaporative

processes. In the TCA, Sr concentrations increase with salinity and $\delta^{18}O$, reflecting progressive mixing with more saline end-members, such as brine from salt lakes or concentrated groundwater. The highest Sr concentrations are found in salt lakes, confirming their role as terminal sinks for solutes and their potential to contribute salinity and Sr to the TCA during periods of over extraction for irrigation. These graphs corroborate the mixing line interpretations and emphasize the hydrological connection between the NSSA, TCA, and surface water systems. They highlight the importance of evaporative concentration, structural conduits (faults and fractures), and anthropogenic impacts (over-extraction) in shaping the isotopic and geochemical characteristics of the aquifers and associated water bodies. The consistency in $\delta^{18}O$ and $^{87/86}Sr$ signatures for TCA, springs, and drains further indicates the significant influence of NSSA recharge and lake-derived salinity on the TCA system.

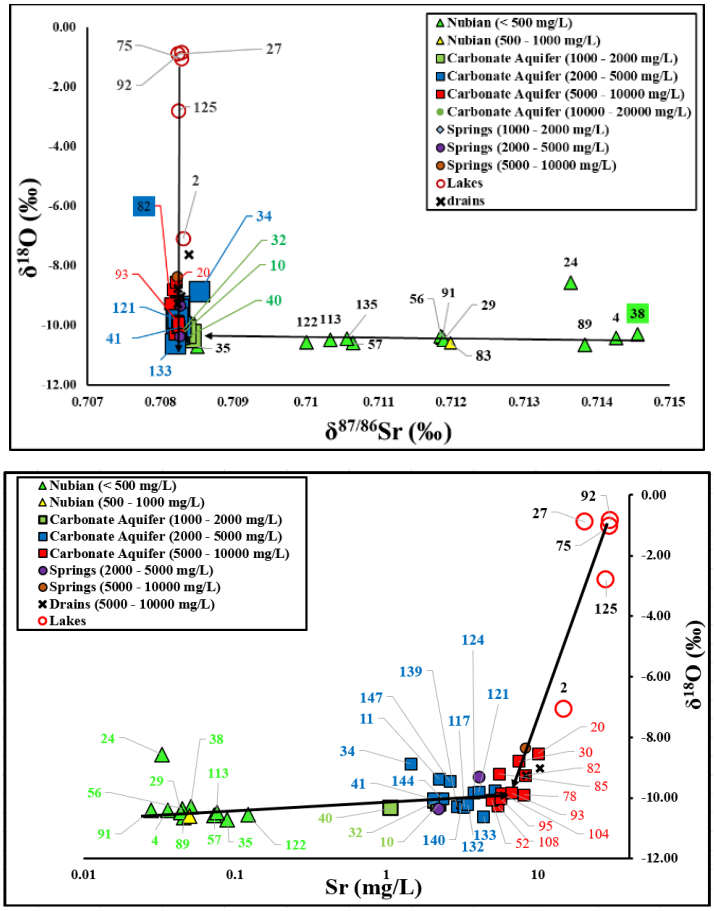

Figure 44. The relationship between $\delta^{18}O$ vs $^{87/86}Sr$ and Sr vs $\delta^{18}O$

The relationship between depth and $^{87/86}Sr$ (Fig 45) reveals key insights into the vertical dynamics within the aquifer systems. Sample 82, which serves as the end-member for the TCA, exhibits the greatest depth, aligning with its role as a baseline for the TCA's geochemical signature. The upward flow from deeper levels demonstrates a clear salinity gradient from low to high, emphasizing the influence of fault systems and fractures in controlling water movement and the mixing of waters with distinct chemical signatures. These structural features facilitate the upward migration of fresher NSSA water, contributing to the dilution of the TCA. Conversely, regions without significant

recharge from the NSSA or with downward leakage from overlying saline sources exhibit higher salinity in the TCA, indicating salinization due to evaporation, dissolution, and mixing processes.

The δ^2H versus $\delta^{18}O$ plot (**Fig 45**) offers insights into the recharge history and evaporation processes affecting the water samples. All samples plot below the Global Meteoric Water Line (GMWL), reflecting the influence of evaporation and water-rock interactions in the time of recharge. The Paleo Meteoric Water Line (PMWL) indicates that NSSA samples are more depleted in $\delta^{18}O$ and δ^2H, consistent with recharge under cooler paleo-climatic conditions.

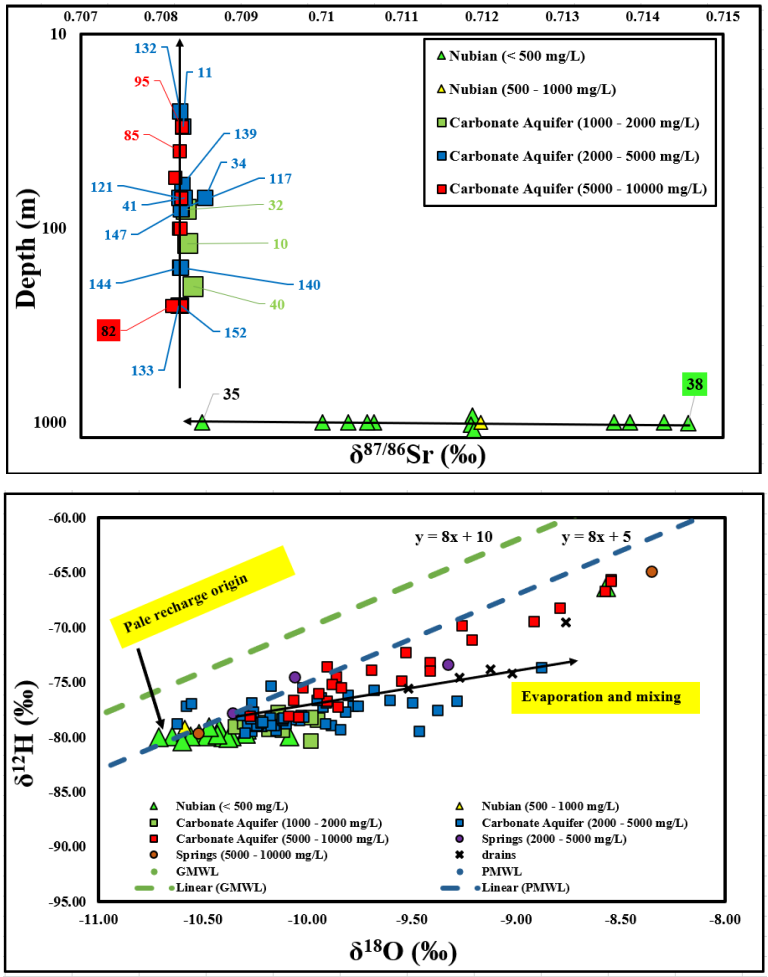

Figure 45. The relationship between depth vs $^{87/86}Sr$ and δ^2H vs $\delta^{18}O$

The presence of TCA samples on the PMWL suggests mixing with NSSA waters or recharge under similar paleo conditions. Samples from the TCA, springs, and drains that plot to the right of the PMWL exhibit $\delta^{18}O$ enrichment, indicating the impact of modern evaporative processes and mixing with other source, likely from salt lakes and agricultural drains. This enrichment supports the hypothesis of downward leakage from evaporated surface waters into the TCA during periods of over-extraction, as well as interaction with recharge from NSSA.

5.4.2.2. NETPATH inverse mixing model

The use of the NETPATH mixing model provides a robust validation of the contributions from the NSSA to the TCA, offering a comprehensive approach that incorporates the geochemical evolution

of water. By utilizing a suite of physicochemical parameters (pH, TDS, EC, temperature, major ions such as Ca, Mg, K, Na, Cl, SO_4, HCO_3) and incorporating saturation index values, this model goes beyond the simpler isotopic mixing line approach. It allows for the quantification of mass transfer and geochemical processes such as dissolution, precipitation, and ion exchange. The model employed two well-defined end members: the NSSA (Sample 38), characterized by low salinity, high $^{87/86}Sr$, and low Sr concentration, and the TCA (Sample 82), which exhibited high salinity, low $^{87/86}Sr$, and high Sr concentration. Samples representing mixed water were selected to quantify the contribution percentages and track geochemical evolution through mass transfer processes.

The saturation indices (**Table 7s. Appendix 2**) revealed under-saturation of halite, gypsum, and anhydrite, across all samples, while minerals such as dolomite, illite, chlorite, montmorillonite, and hematite were predominantly supersaturated. Spatial variability was observed for calcite, albite, and aragonite, which fluctuated between under-saturation and supersaturation. For the mixing model, constraints were established using carbon, sulfur, magnesium, sodium, chloride, silica, aluminum, and calcium. Selected phases reflective of the aquifer's geological composition included calcite, halite, gypsum, dolomite, montmorillonite, illite, and cation exchange processes (Ca/Na). The model results are summarized in **Table 5**, showing 14 inverse mixing models with mixing percentages calculated for each scenario as well as comparison with the results of the previous mixing line (Faure model). The NSSA contribution to the TCA ranged from ~90% in low-salinity areas (Model 1) to ~52% in high-salinity zones (Model 14). The spatial distribution of recharge highlighted significant NSSA contributions along fault planes and fracture systems, particularly in the southeastern and southwestern study areas. Reduced NSSA contributions corresponded to regions near salt lakes, such as Siwa and Zeitun, where the upper cretaceous shale prevents upward flow on the absence of faults. over-extraction and evaporative concentration led to increased salinity without altering $^{87/86}Sr$ values in TCA in these locations of low contributions from NSSA.

Phase dissolution and precipitation patterns corroborated these findings. NSSA-dominated regions showed calcite and dolomite precipitation, consistent with the mixing of supersaturated NSSA water. In contrast, high-salinity areas exhibited gypsum and halite dissolution, reflecting evaporative concentration and salt dissolution from lake leakage. Ion exchange processes, such as sodium enrichment and calcium depletion, were prominent in transitional zones. The robust integration of isotopic and geochemical data within the NETPATH framework provided a detailed understanding of aquifer mixing, structural influences, and geochemical transformations, validating the earlier interpretations derived from isotopic mixing lines. The results demonstrated a strong agreement between the inverse mixing model from NETPATH and the direct mixing model based on the Faure approach, with only minor variations in the calculated contribution percentages (**Table 5 and Fig 46**). These differences can be attributed to the additional parameters and constraints considered in the NETPATH model, such as pH, temperature, major ions, and the saturation indices of specific

minerals, which allow for a more detailed accounting of geochemical evolution and mass transfer processes.

Table 5. The 14 models, including the two initial water, the final water as well as the recharge percentage from NSSA to TCA

Model number	Model type	Initial 1 (NSSA)	Initial 2 (TCA)	Final water (TCA)	Mixing Percentage (NETPATH)		Mixing Percentage (Faure)	
					Initial 1	Initial 2	Initial 1	Initial 2
1	mixing	38	82	40	89.962	10.038	89.0	11.0
2				10	81.585	18.415	80.0	20.0
3				34	79.349	20.651	79.5	20.5
4				144	77.115	22.885	77.0	23.0
5				11	74.316	25.684	74.0	26.0
6				147	70.399	29.601	69.5	30.5
7				139	73.198	26.802	69.5	30.5
8				140	67.603	32.397	68.5	31.5
9				117	66.477	33.523	65.0	35.0
10				41	63.2	36.8	64.5	35.5
11				132	62.32	37.68	60.5	39.5
12				121	56.952	43.048	59.5	40.5
13				152	59	41	54.5	45.5
14				133	51.895	48.105	49.5	50.5

Model number	Phase precipitated or dissolved							
	Calcite	Dolomite	Halite	Gypsum	Ca-Montmorillonite	Na-Montmorillonite	Illite	Exchange
1	-1.22	0.80	-	-0.07	297.1	-296.2	-0.91	74.73
2	-1.41	0.82	-	-18	937.1	-939.4	2.38	152.3
3	-5.40	2.42	-	0.07	1063.6	-1062.6	-0.99	174.18
4	-5.78	3.26	-	-0.44	72.6	-78.28	5.73	9.56
5	-1.13	0.70	-	-0.21	697.8	-700.6	2.78	111.33
6	-8.63	4.66	-	-0.38	691.8	-696.7	4.98	112.5
7	-11.85	6.14	-	-0.42	1659.8	-1665.3	5.56	272.3
8	-7.89	4.13	-	-0.50	236.9	-243.3	6.54	36.96
9	-12.14	6.50	-	-0.34	1264	-1268	4.46	207.4
10	1.13	-0.31	-	0.2	701.7	704.2	-2.6	-117.2
11	-1.7	1.16	-	-0.14	-	-1.87	1.89	-3.92
12	-15.32	8.25	-	-0.30	-793.6	789.6	3.98	-136
13	11.16	-5.69	-	-0.33	0	-4.36	4.42	6.31
14	-5.54	2.92	-	-0.28	823.1	-826.7	3.72	133.4

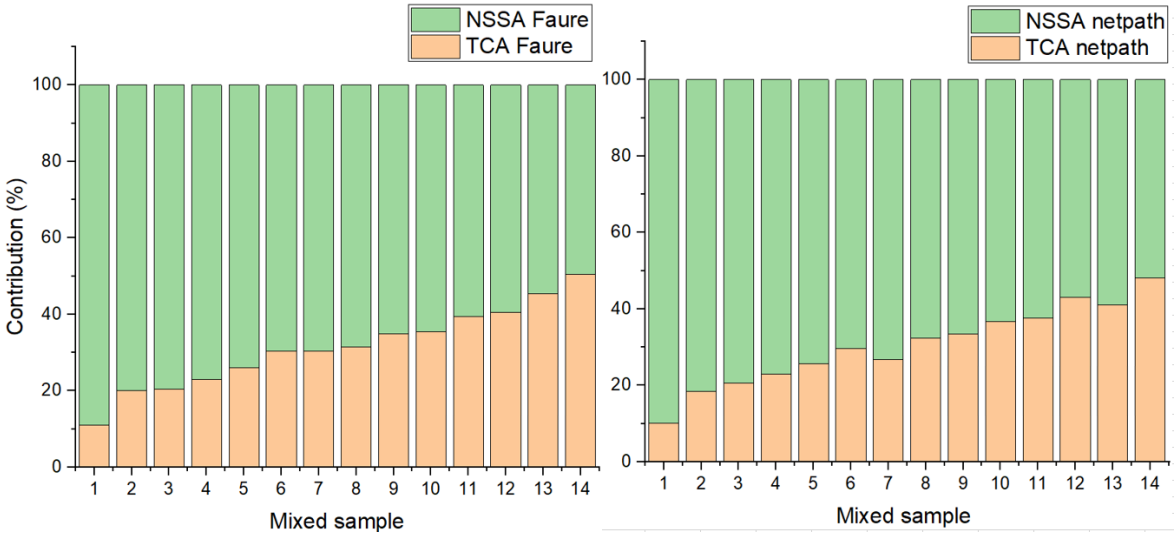

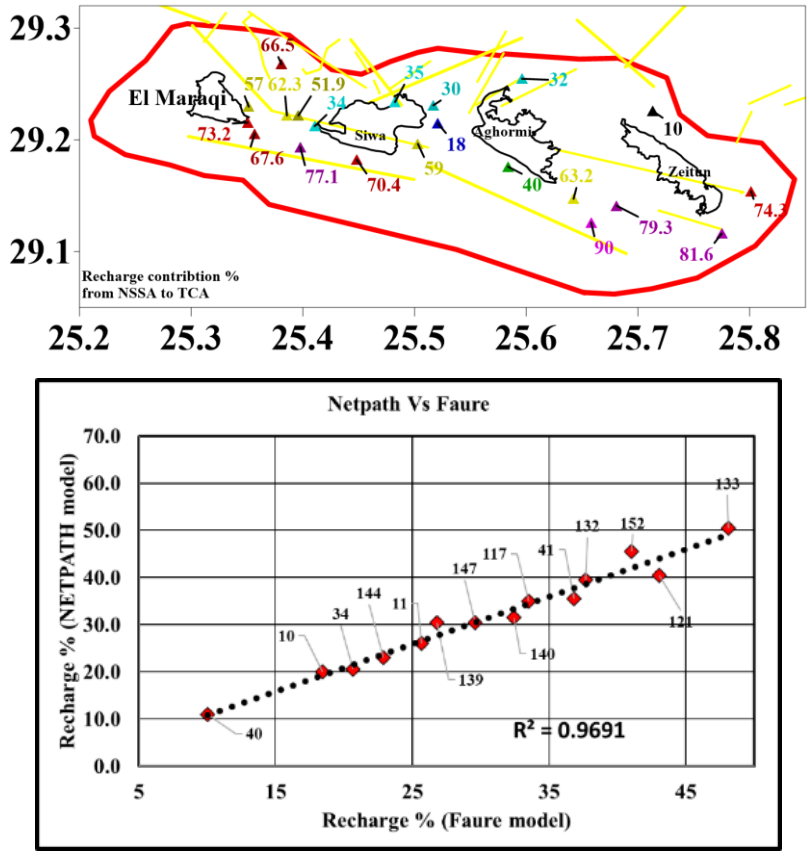

Figure 46. The spatial comparison between NETPATH model and Faure model in estimation of contribution % from NSSA to TCA along the fault plane and calibration curve between NETPATH model and Faure model.

In contrast, the Faure model primarily relies on isotopic ratios and salinity (only two parameters), simplifying the complexity of interactions within the aquifer system. Fig 46 demonstrates the contribution percentage from the NSSA to TCA in different locations in the study area showing the highest contribution close the lineaments in the south and the lowest contribution in the north. Despite these differences, the calibration curve (Fig 46) comparing the two models displayed a high correlation coefficient (R^2=0.96), confirming the reliability of both approaches. This close alignment underscores the robustness of the combined geochemical and isotopic methodologies in interpreting groundwater mixing and recharge processes.

5.4.3. Groundwater age correction

The age correction for the NSSA and TCA was performed using the NETPATH model, incorporating initial water from the soil before infiltration and final water from the aquifers. Input parameters included pH, temperature, electrical conductivity (EC), total dissolved solids (TDS), major ions, and $\delta^{13}C$ and $\delta^{14}C$ isotopic data. The model constraints comprised carbon, sulfur, sodium, chloride, calcium, magnesium, silica, and potassium, while the selected geochemical phases included calcite, dolomite, halite, gypsum, illite, chlorite, montmorillonite, SiO_2, Na_2SO_4, Ca/Na exchange, and CO_2 gas. The age correction algorithm employed the Fontes and Garnier approach [98], with the initial $\delta^{14}C$ activity assumed to be 96.40% modern carbon (pMC) using Rayleigh calculation and carbon fractionation corrections based on Mook's model[103]. After running the model, calibration was

performed by adjusting isotopic exchange amounts in calcite, and CO_2 gas, which did not exceed 1.5, to match computed $\delta^{13}C$ with observed $\delta^{13}C$ values. This calibration step also accounted for evaporation factors to refine the corrected age. The corrected ages were calculated for samples from the NSSA, TCA, springs, and lakes, providing insights into the groundwater flow paths and recharge sources. The results, including computed and observed ^{13}C values and the corrected ages, are summarized in **Table 8s (Appendix 2)**. The results of the NETPATH model (**Table 9s. Appendix 2**), after adjustment for isotopic changes related to the calcite phase, demonstrated a high degree of accuracy in age correction, as evidenced by the close agreement between computed and observed ^{13}C values. The observed ^{13}C values ranged from −12.13 to −6.25 in TCA samples, −10.26 to −7.25 in spring samples, −11.44 to −11.43- in NSSA samples, and −8.8 to −7.7 in lake samples. Similarly, the observed ^{14}C values ranged from 15.45 to 57.91 in TCA samples, 18.19 to 20.54 in spring samples, 16.12 to 42.55 in NSSA samples, and 73.66 to 77.88 in lake samples. The corrected ages obtained from the model revealed significant spatial variation across the aquifer systems (**Fig 47**). In the TCA, the corrected ages ranged from 640 to 13,551 years. The lowest ages were observed in the northern part of Siwa Oasis, particularly between Siwa Lake and Aghormi Lake, and near El Maraki Lake in the northwest. The highest ages were recorded in the eastern part of Siwa Oasis. Non-artesian wells in the TCA indicated groundwater flow from the southwest to the northeast, with lower levels near Siwa Lake.

The corrected age trend in both the NSSA and TCA indicated a general decrease in age from the southeastern part of Siwa Oasis toward the north, particularly near Siwa Lake, where the youngest ages were observed. The springs exhibited corrected ages ranging from 6,642 to 12,138 years, while the lakes showed recent ages. TCA samples located near lineaments (faults and fractures) in the southern part of the study area were characterized by older ages compared to samples from the northern areas near Siwa Lake. This trend suggests that structural features and recharge pathways from the deep layers of NSSA play a significant role in determining groundwater age and flow dynamics. The corrected groundwater ages provide valuable insights into the dynamics of recharge, flow, and mixing processes in the Siwa Oasis aquifer systems. The spatial variability in ages highlights the significant influence of structural features, recharge pathways, and geological controls on groundwater movement and evolution. In the TCA, the corrected ages ranging from 640 to 13,551 years indicate a combination of recent recharge near Siwa Lake and older waters in the eastern parts of the Oasis. The younger ages near Siwa Lake and Aghormi Lake in the northern and northwestern regions align with the proximity of these areas to recharge zones and active mixing with more recent water, potentially influenced by surface water interaction and anthropogenic activities. The presence of older ages in the eastern TCA and along faults in the southern areas suggests significant recharge from deeper layers of NSSA and limited recharge from surface lakes or anthropogenic activities.

The NSSA displayed a similar age variation, with corrected ages ranging from 4,296 to 14,184 years. The older ages in the southern regions and near structural features, such as faults, indicate upward

flow from deeper layer of the NSSA, and slower-flowing groundwater system with limited direct recharge. In contrast, the younger ages toward the north reflect circulation and mixing with TCA waters through fractures and fault systems due to over extraction, as suggested by the piezometric head gradients. The springs, with corrected ages between 6,642 and 12,138 years, reflect their role as discharge points for groundwater that has undergone mixing and isotopic exchange during its flow. These ages suggest that spring water is predominantly older than surface waters but influenced by intermediate aquifer flow paths. The lakes, showing recent ages, confirm their role as collection basins for both groundwater discharge and surface water input. The recent ages in the lakes further emphasize the active interaction between surface processes and shallow aquifer zones (TCA) that change its age signature and create variation in the residence time.

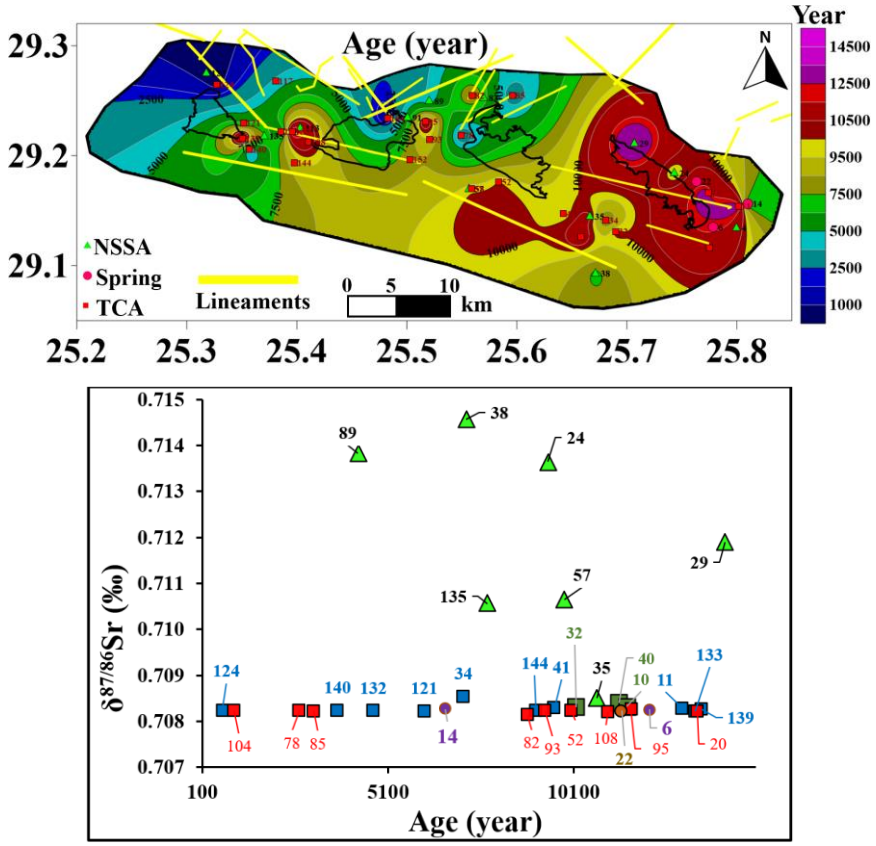

Figure 47. The distribution map of the corrected age in Siwa Oasis and the relationship between age and depth of water samples

The overall trends in age, particularly the decrease in age from southeast to north and near Siwa Lake, underscore the importance of structural features and fault-controlled recharge pathways in facilitating upward flow and mixing between the TCA and NSSA and mixing between salt lakes and TCA. This supports earlier findings from mixing models and isotopic relationships, where fractures and lineaments were identified as critical pathways for water movement and salinity variation. these areas exhibited older corrected ages, underscoring the impact of deep aquifer contributions on residence times and geochemical evolution. Conversely, TCA samples with low contributions from the NSSA,

such as those samples closer to Siwa Lake, showed younger ages due to more dynamic recharge and mixing processes with surface water.

Older groundwater (>10,000 years) was concentrated near faults and fractures, suggesting preservation of paleowater from the early to mid-Holocene. The presence of groundwater recharged during the African Humid Period aligns with evidence of a wetter climate in North Africa during the early to mid-Holocene. The transition to drier conditions after ~5,000 years ago likely reduced recharge rates, leading to the preservation of older groundwater in deeper aquifers. Faults and fractures act as critical recharge pathways, facilitating deep infiltration and long-term storage, but over-extraction and surface water interaction have led to mixing of younger and older groundwater, altering TCA chemistry and dynamics.

The relationship between $^{87}Sr/^{86}Sr$ ratios and groundwater age (**Fig 47**) offers important insights into the geochemical evolution and mixing processes within the aquifer system. In the NSSA, the significant variation in $^{87}Sr/^{86}Sr$ ratios and groundwater age reflects the aquifer's complex geological setting. The NSSA sits above basement rocks rich in radiogenic minerals like feldspar and mica, which release ^{87}Sr over long geological timescales through weathering. Additionally, the presence of Upper Cretaceous shale, known for its high radiogenic strontium content, contributes further to the radiogenic input. The variability in $^{87/86}Sr$ ratios highlights the diverse mineral composition of these rock types and the impact of localized groundwater flow, particularly along fault zones that enhance mineral dissolution. In contrast, the TCA (Tertiary Carbonate Aquifer) shows much less variation in $^{87}Sr/^{86}Sr$ ratios, indicating a more consistent strontium source dominated by carbonate dissolution. Carbonate rocks, such as limestone and dolomite, typically have lower $^{87}Sr/^{86}Sr$ ratios compared to radiogenic sources like basement rocks or shale. This is because the strontium in carbonate minerals originates from marine environments, which generally have uniform and low $^{87}Sr/^{86}Sr$ ratios. As groundwater interacts with these carbonate minerals, it dissolves their strontium content, diluting the overall $^{87}Sr/^{86}Sr$ ratio. This effect is particularly common in carbonate-dominated aquifers like the TCA. The observed decrease in groundwater age in the northern parts of Siwa Oasis within the TCA is likely due to mixing with younger water sources, such as recharge from salt lakes or irrigation return flows. Over-extraction of groundwater facilitates this process, introducing younger water with lower $^{87}Sr/^{86}Sr$ ratios and altering the original groundwater chemistry. On the other hand, older groundwater ages in the southern parts particularly near fault lines, suggest a greater influence of water from the NSSA. This indicates that geological structures, such as faults and fractures, play a key role in enabling the upward movement of radiogenic water from the NSSA into the TCA. The higher $^{87}Sr/^{86}Sr$ ratios in the NSSA, resulting from interactions with basement rocks and Upper Cretaceous shale, support this interpretation. Overall, the interplay between radiogenic sources, geological structures, and human activities underscores the complex hydrogeochemical evolution of the aquifer system. These findings reveal how both natural processes and human interventions shape the characteristics of groundwater in the region.

5.5. Groundwater numerical flow model

The current study aims to examine if the deep groundwater from the NSSA recharges the shallow fractured TCA through faults and fractures system and validate the isotope results. This is a critical finding, especially in arid regions like Siwa Oasis, where groundwater is the primary source of water for agriculture, drinking, and ecosystems. The NSSA is over pressured and all wells penetrating this aquifer are artesian and flowing wells while the wells penetrating TCA are flowing in some locations and non-flowing in other locations due to variation in the ground surface elevation and over extraction of groundwater from TCA. The stable isotopes and radiocarbon confirmed that the aquifer system in Siwa Oasis contain pale-meteoric water and there is no significant recent recharge due to the arid and hot climate and the main source recharge the TCA is the NSSA. The groundwater flow model in FEFLOW environment was performed to predict the future water level changes and drawdown in the NSSA and TCA till 2100 as well as the discharge of springs. This forecasting of the water level can determine the sustainability of the non-rechargeable aquifer and delineate the most sensitive location for drawdown. This study presents the first fully integrated, three-dimensional numerical model of the Siwa Oasis that couples the NSSA with the TCA while explicitly incorporating major fault systems as discrete flow conduits. By integrating detailed hydrostratigraphy, pumping data, and, for the first time, validating the model against multi-isotope and radiocarbon data, this work provides an unprecedentedly clear and quantitative confirmation of the hydraulic connectivity and recharge mechanisms between the two aquifer systems. this is the first model to use reverse particle tracking to visually and quantitatively trace the recharge pathways from the NSSA to the TCA, directly validating the conceptual model derived from geochemical data.

5.5.1. Model performance and calibration

Following the initial successful run of the unstressed steady-state model, calibration was performed by systematically adjusting input parameters such as hydraulic conductivity until the calculated and observed heads for monitoring wells penetrating NSSA and TCA had strong agreement (**Fig 48**). In springs, the discharge rate was used for calibration. In the steady state condition, the calibration curve showed strong agreement and high correlation between observed and computed head with R^2=99% for NSSA and 93% for TCA. The calibrated steady-state hydrodynamic model was transformed into a transient one to ensure that the changes in the recharge areas can be well-tracked within the variable depression fields caused by water extractions. The investigated time period was 140 years (1960-2100). In the transient state, 63 wells from TCA, 145 springs, and 20 wells from NSSA were used to extract 288,000 m^3/d and the water level measured from 19 wells of TCA and 10 wells from NSSA were used for calibration. **Fig 49** illustrates the simulated head distribution in the NSSA under the calibrated transient state conditions and calibration curve in NSSA and TCA. The calibration curve in transient state conditions in the NSSA and TCA showed strong agreement between the measured and simulated head with R^2 value of 0.98 and 0.83 respectively. The model demonstrates excellent

accuracy and reliability in predicting water levels of the NSSA, with an RMSE of 0.66 m, MAE of 0.56 m, and a correlation coefficient exceed 95%.

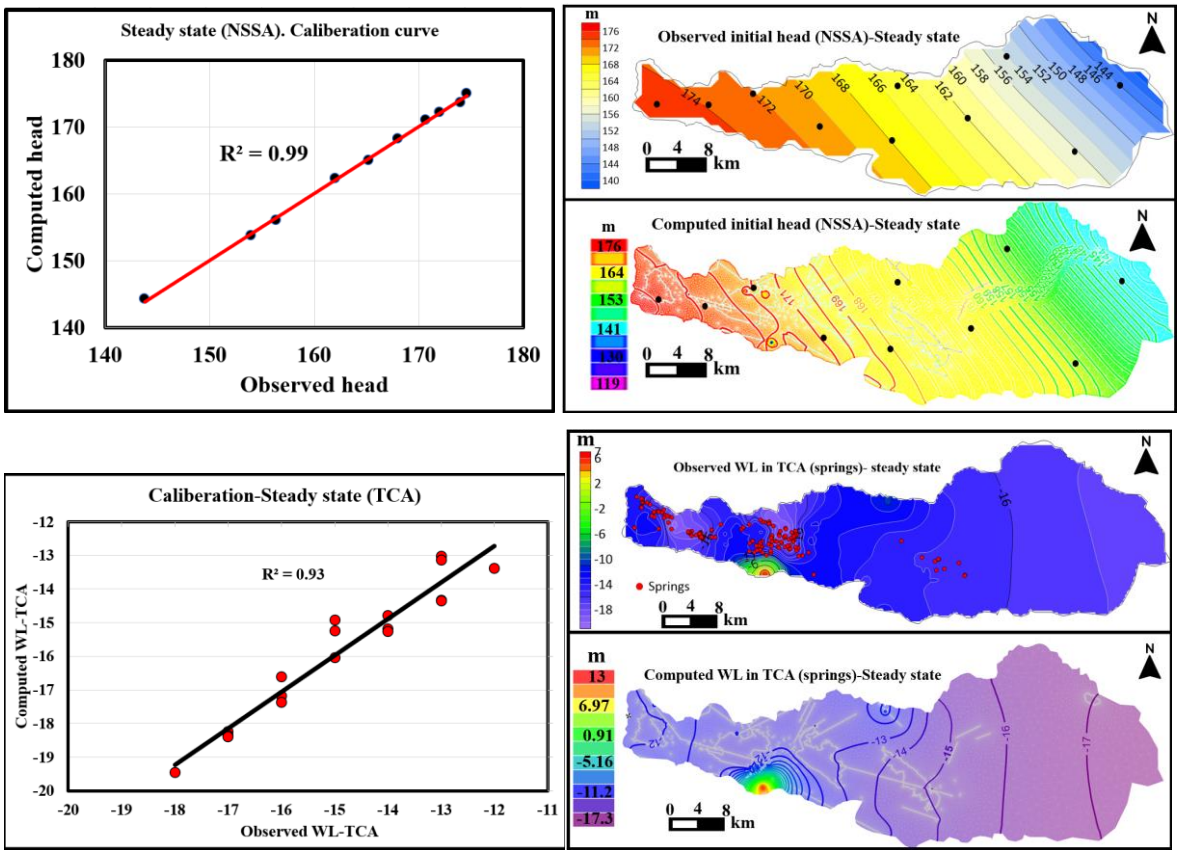

Figure 48. The calibration curve and maps showing the observed and computed initial head in NSSA and springs water level (TCA) in steady state condition.

In case of TCA, the model demonstrates acceptable accuracy and reliability in predicting water levels, with an RMSE of 0.62 m and MAE of 0.39 m. The small errors (ranging from -0.9 m to 0.8 m in TCA and from -1.37 m to 0.17 m in NSSA) and consistent performance across all observations suggest the model is reliable for predicting water levels. The head distribution of the calibrated transient model generally followed the steady-state trends, with minor variations.

The high R^2 value for the NSSA in the steady state indicates that the model accurately captures the regional piezometric surface, suggesting that the assigned boundary conditions and the large-scale hydraulic conductivity distribution are representative of the natural system. The slightly lower, yet still strong, R^2 of 0.93 for the TCA reflects the greater heterogeneity and complexity of the fractured carbonate system, where local variations in fracture density can cause minor deviations from the simulated head. The low RMSE for the NSSA demonstrates the model's high predictive power for regional head values. The small errors suggest that while the model is robust, minor discrepancies may exist in areas far from calibration points, potentially due to unmapped smaller-scale faults or variations in aquitard thickness. It is important to acknowledge the uncertainties associated with the calibration process. The initial head data for 1960 were digitized from historical maps, which may

have inherent inaccuracies. Furthermore, the distribution of calibration wells is not uniform across the entire oasis, leading to higher model certainty in areas with dense data coverage (central Siwa) and lower certainty in data-scarce regions (the far western and eastern part). For future stress predictions, the model was divided into 140 one-year time steps. Four stress periods (1960, 1970, 2025, and 2100) from the 140 were selected to represent the time of extraction in 1960, the past condition in 1975-1980, the current situation in 2025 and 2100 for future prediction (**Fig 50**).

The groundwater flow before extraction in 1960 showed that the initial head in the NSSA flow from south west to north east follow the regional flow of the NSSA in all Egypt (**Fig 50**). The calibrated head in the transient model proved that the central and western part of Siwa Oasis was significantly affected with decline in the water level due to over extraction of groundwater which can be because of intensive agricultural land in this area compared with eastern region. The eastern region of Siwa Oasis was not significantly affected with drawdown in water level where less wells penetrating the NSSA due to unsuitability of soil for agriculture in this area where the soil salinization and water logging are intensive. The over extraction of water for irrigation, drinking, and industrial purposes could create different local groundwater flow dominated from east to west direction with neglected rainfall. The local groundwater flow was shifted toward the centers of Maraqi and Siwa Lakes in the central area of the oasis, indicating zones of high vertical hydraulic conductivity due to intersecting fault systems. The hydraulic conductivity ranges from 1.2 to 6.6 m/d. The lowest values are found in the near Zeitun lake, and the highest values are observed in the central part of the oasis near Siwa and Aghormi lakes. This convergence, combined with high groundwater discharge through springs and uncontrolled dug wells, has led to the expansion of salt lakes (**Fig 30**) and the Siwa lake increased rapidly from 1990 to 2020.

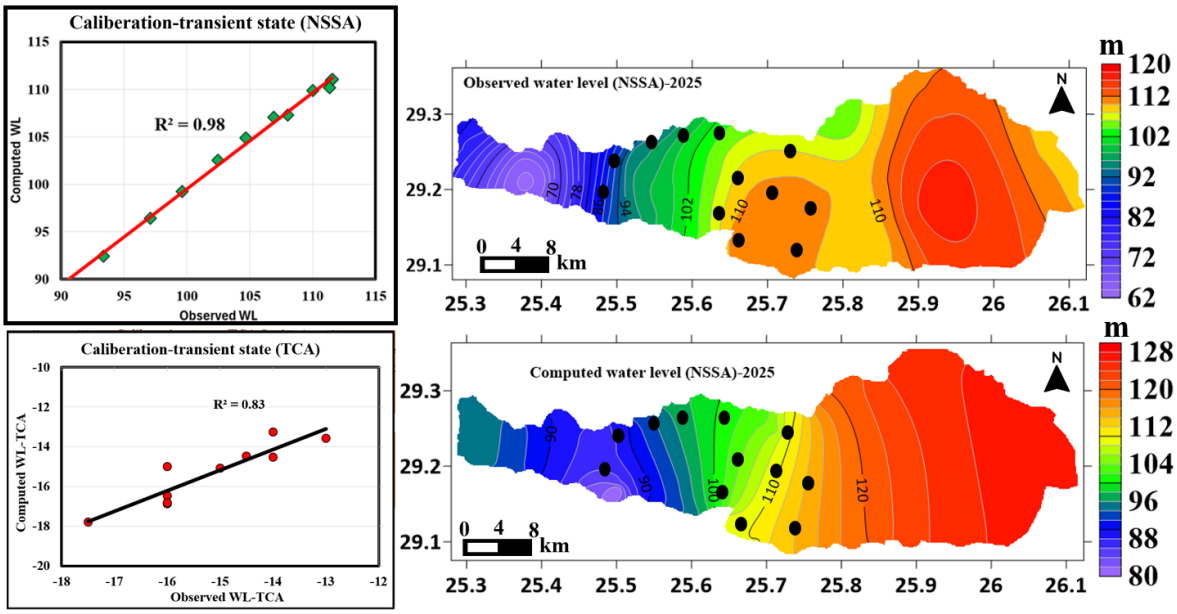

Figure 49. The transient state calibration curve for NSSA and TCA and boreholes distribution map used for calibration of NSSA.

5.5.2. Groundwater level Predictions model

Groundwater development strategies were evaluated over a 140-year period to assess the impact of fixed abstraction rates on drawdown. The baseline scenario assumed a fixed abstraction rate of 288,000 m³/day, representing the current abstraction rates primarily from wells and springs. This scenario was designed to reflect the minimum and reliable risk that could exist in the future, considering the government's practice of periodically closing wells with high salinity and drilling new, safer wells. The current average pressure head (2025) in artesian flowing deep wells ranges from 70 m (a.s.l.) in discharge areas (between El-Maraqi Lake and Siwa Lake) to 125 m (a.s.l.) in the eastern region between Tamera Lake and Zeitun lake (recharge area). The transient model revealed that from 1960 to 2025 there was a rapid drawdown in the piezometric head from 175m to 75m above sea level in the western part and slow drawdown from 142m to 128m in eastern part. The drawdown of the piezometric head with about 100 m in non-rechargeable aquifer showed that there is high risk in western and central Siwa oasis threaten the sustainability of limited water resources due to over extraction. The future water level in 2100 based on the prediction model will be approximately between 30 to 70 m with significant drawdown in central and western area. **Fig 6s. (Appendix 1)** shows the drawdown in the hydraulic head of the NSSA from 1961 to 2100. Reclamation of new agricultural land with the current method of irrigation by flooding can increase the rate of the drawdown. These findings demonstrate the risk of the drawdown in the pressure head of the NSSA that is main source recharge and dilute the water salinity of the TCA. The worst scenario that threatens the life in Siwa Oasis is the critical time when the NSSA stop recharge the TCA and changing the flow dynamics of the aquifer system where the saline water of the TCA will flow downward to the NSSA and deteriorate the only available fresh water resources in the Oasis. Based on the current model, this case can happen within 150 to 200 years.

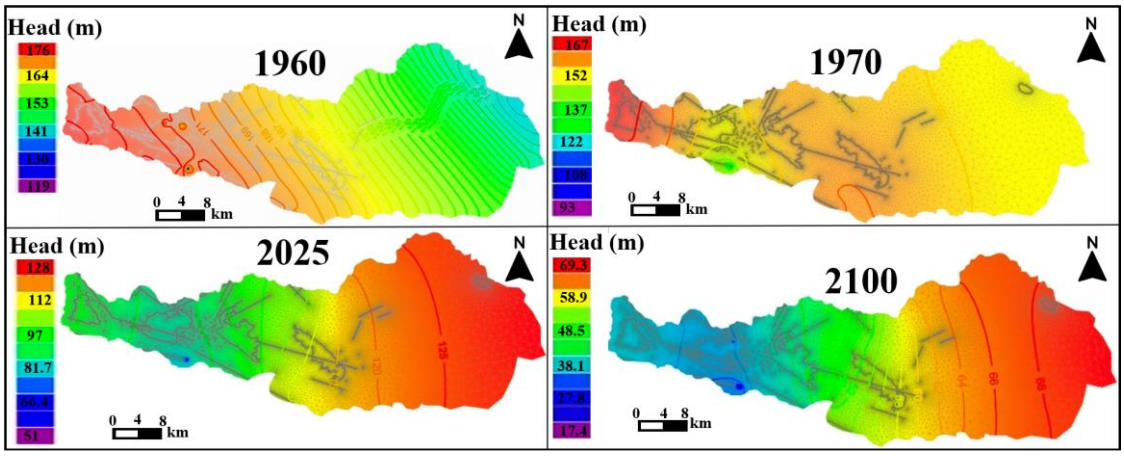

Figure 50. The changes in the water level in the NSSA from 1960 (initial head) to the current state (2025) and predicted water level in 2100.

The predicted drawdown in the western part of the oasis is not just a numerical output; it represents a critical threat to the livelihoods of the local population. This level of depletion will render many

shallow wells inoperable, increase pumping costs significantly for deeper wells, and threaten the existence of historic springs that are central to Siwa's cultural heritage and tourism. Previous studies have acknowledged the over-extraction, but this model, for the first time, quantifies the spatial heterogeneity of the impact, clearly delineating the western and central areas as 'hotspots' of unsustainable abstraction. This finding has direct implications for policy, suggesting that management strategies should not be uniform but rather targeted to these high-risk zones. The most alarming finding of this study is the potential for a complete reversal of the hydraulic gradient between the TCA and NSSA within 150-200 years. Such an event would be catastrophic, as it would allow the highly saline water of the TCA to permanently contaminate the pristine fossil water of the NSSA, effectively destroying the only source of fresh water in the Oasis. This finding elevates the issue from a problem of water scarcity to a potential ecological and humanitarian crisis. The model indicated that without sustainable management of non-rechargeable aquifer system, the salinization of the TCA will increase rapidly through water rock interaction and leakage downward from hypersaline lakes and consequently increase soil salinization and decrease plant production. Monitoring the discharge rate of the springs showed rapid decrease with time from 3900 m^3/d in 1960 to 3000 m^3/d in 2025 and it is expected to decrease to 2400 m^3/d in 2100 (**Fig 51**). Decreasing the discharge rate of the springs will affect the available natural water resources that are mainly used for agriculture and heath tourism.

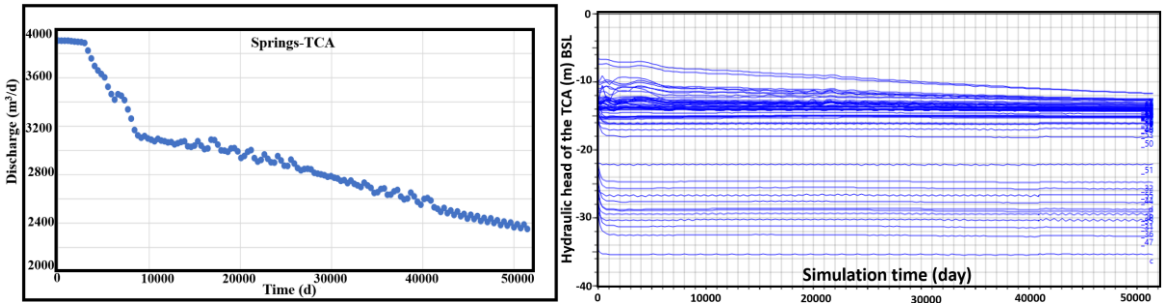

Figure 51. The changes in the discharge rate and hydraulic head of the springs (TCA) from 1960 to 2100 based on the transient model

5.5.3. Recharge source using reverse particle tracking

Reverse (backward) particle tracking was performed to validate previous findings from mixing models which confirmed the main source recharge the TCA is the NSSA through faults and fractures and to identify the recharge area. The reverse particle tracking was represented by pathlines, which extend from the pumping wells and springs with particles moving toward the main potential zone (recharge area) during extraction. For each spring and wells from the TCA, 24 particles were released to be monitored with pathlines withing specific time interval.

Tracking the pathlines from 1960 to 2025 showed that particles traced back to the high-potential recharge area in the eastern part of the Siwa Oasis from the wells penetrating the TCA. The tracking particles from springs and wells penetrating TCA revealed that the pathlines moved toward the NSAS

along fault planes, confirming that the original source of groundwater in the TCA is the NSAS (Fig 52). The main proportion of the recharge of the wells are comes from the NSSS, but a small amount comes from the surface water (salt lakes) along the lineaments (fractures/faults). Extending the pathlines to Siwa lake and Zeitun lake confirm the findings from the mixing model that the leakage of salt water from the lakes is a significant factor for groundwater salinization in the TCA.

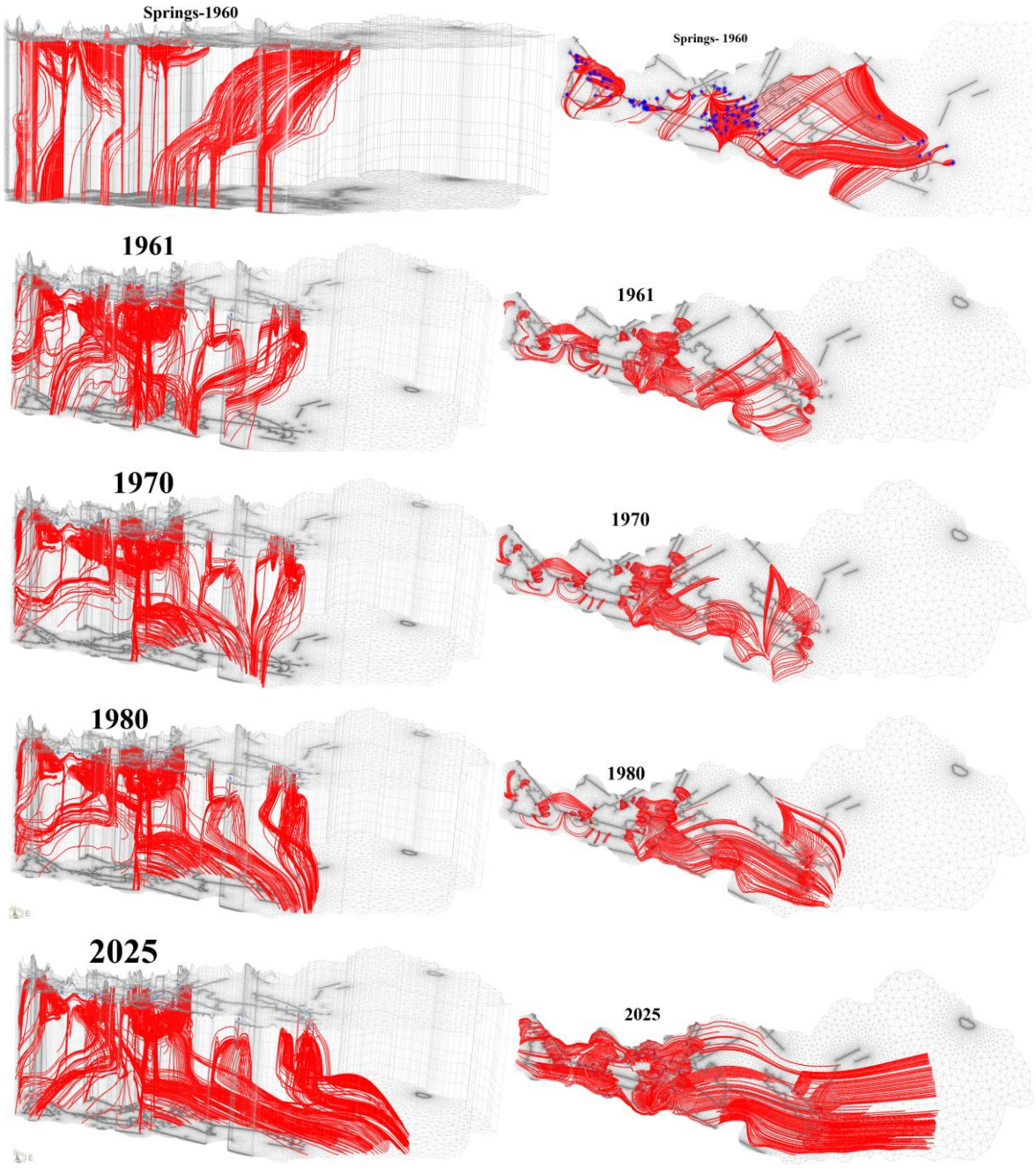

Figure 52. Reverse particle tracking from wells in 2D and 3D showing the recharge area in east of Siwa Oasis and recharge of TCA from NSSA through faults and fracture system based on the pathlines.

The travel times for particles depends on the distance and the seepage velocity of the flow paths. The velocity is higher in zones where large water level fluctuations occur over small areas, i.e. in depression cones around extraction wells. As time progresses in each time step, the depression in the

aquifers becomes larger and the primary flow directions change significantly. As a consequence, the recharge areas of the wells also change. To illustrate the above, the total recharge area of the wells and springs was determined and through monitoring of the pathlines extension from 1961 to 2025 (Fig 52). It can be clearly seen, that the recharge area of the wells becomes increasingly larger and the pathlines turn East direction towards the higher potential fields. The particles also following highly conductive fault zones. These pathlines suggest that recharge from the NSSA to the TCA is a continuous process, influenced by the structural geometry of the aquifer system. The zones of contribution for the TCA are primarily located in the southeastern and southwestern parts of the Siwa Oasis, which aligns with the findings of isotopic analyses and low salinity of TCA in these locations. These zones correspond to the locations of major faults and fractures, further supporting their role in facilitating recharge and mixing of different water resources.

Overall, the study provides a clear understanding of the recharge mechanisms and flow pathways in the Siwa Oasis aquifer system, emphasizing the importance of sustainable groundwater management to mitigate the risks of drawdown and salinization.

5.5.4. Model limitations and future work

Data Uncertainty: The model's accuracy is inherently limited by the quality and distribution of the input data. Hydraulic conductivity, for instance, was interpolated between a limited number of pumping test and well logs locations, and the actual heterogeneity of the aquifer is likely more complex than represented in the model.

Simplification of Faults: Faults were modeled as vertical conduits with uniform hydraulic properties. In reality, fault zones are highly complex, with varying degrees of permeability and potential for acting as barriers in some segments and conduits in others. This simplification is a necessary abstraction but represents a source of uncertainty.

Climate Change: The future prediction scenarios assume a constant abstraction rate and do not account for potential changes in climate, such as increases in temperature and evaporation, which could further exacerbate the water deficit.

Future modeling efforts should focus on collecting more field data to better characterize the spatial variability of hydraulic parameters, particularly within the fault zones. A solute transport model could be coupled with the flow model to more accurately simulate the movement of salt and predict future salinity changes in both aquifers. Future scenarios should incorporate climate change projections to provide a more comprehensive assessment of the long-term sustainability of the oasis's water resources.

5.6.Water quality and health risk assessment

This research aimed to achieve several key objectives. First, it applied an Integrated Weighted Water Quality Index (IWQI) to evaluate the suitability of various water resources in the Siwa area for drinking purposes instead of traditional methods. This involved analyzing water quality based on critical physicochemical parameters and heavy metals. Second, the study conducted a health risk

assessment supported with monte Carlo simulation to identify potential hazards associated with exposure to nitrates and heavy metals in the water, providing insights into the risks to human health. Third, the research developed a predictive model using Feedforward Backpropagation Neural Networks (FFBP-NN) to estimate the IWQI, aiming to improve the accuracy and efficiency of water quality evaluation using few parameters for cost and time effective monitoring system.

5.6.1. Water quality assessment based on IWQI

The water quality index and health risk assessments were carried out by analyzing key physicochemical parameters and heavy metals, as outlined in **Table 10s (Appendix 2)**. The water quality index (IWQI) for drinking purposes categorizes water into four main types: extremely poor, poor, medium (or intermediate good), and excellent quality. These categories are based on specific IWQI value ranges: >200 for extremely poor, 150–200 for poor, 100–150 for medium, 50–100 for good, and 0–50 for excellent quality. As illustrated in **Fig 53a**, the analysis revealed that 49.16% of the water samples fell into the extremely poor category (IWQI >200). This included all surface water samples, five spring samples (S104, S105, S106, S107, and S108), three samples from the NSSA (S16, S18, and S19), and 32 samples from the TCA. Additionally, 20.83% of the samples, represented by 25 TCA samples, were classified as poor quality, with IWQI values ranging from 150 to 200. Approximately 25% of the samples fell within the medium quality range (IWQI 100–150), including 11 NSSA samples, 1 spring sample, and 18 TCA samples. The remaining 6% of samples, primarily from the NSSA and one TCA sample, were classified as good to excellent quality.

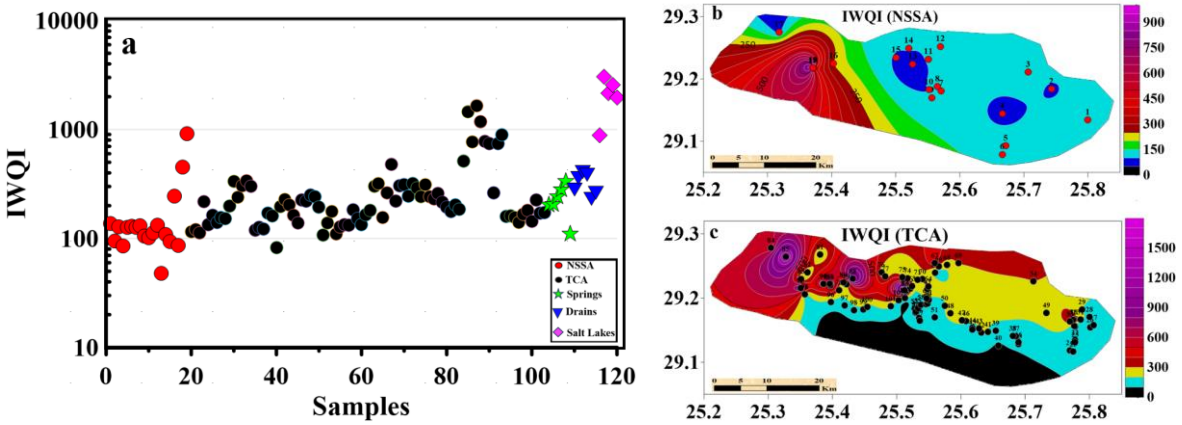

Figure 53. Ploting of samples with the values of IWQI (a) and distribution map of IWQI in NSSA (b) and TCA (c)

The findings highlight that the deep NSSA generally contains fresh water suitable for drinking, except in some samples of western areas between El-Maraqi Lake and Siwa Lake. The drinking water quality of the NSSA improves from west to east (**Fig 53b**). In contrast, the groundwater from the TCA is only suitable for drinking in the southeastern part of Siwa Oasis (**Fig 53c**), while the central and western parts are more degraded and unfit for human consumption. The study area is predominantly relied on agricultural activities with extensive crop cultivation, fertilizer use, and significant animal husbandry activities. **Table 10s (Appendix 2)** shows the main parameters used for calculation of

IWQI the integrated wight for each parameter. The deterioration of TCA water quality is primarily attributed to increasing salinity caused by water-rock interactions, over-extraction of groundwater for irrigation, and the return of agricultural drainage through fracture systems. Previous studies have also noted a minor contribution to TCA salinity from downward leakage from salt lakes. In contrast, the NSSA is protected by a thick layer of Upper Cretaceous shale, which creates confined conditions and prevents contamination or salinity increases.

5.6.2. Prediction model using FFBP-NN

A prediction model utilizing Feedforward Backpropagation Neural Networks (FFBP-NN) was developed to forecast the Integrated Weighted Water Quality Index (IWQI) based on a limited set of parameters. This innovative approach aims to optimize the monitoring process by reducing the reliance on numerous expensive and time-consuming measurements. By leveraging the predictive power of FFBP-NN, the model can accurately estimate water quality using fewer inputs, making it a cost-effective and efficient tool for future water quality monitoring. This advancement not only simplifies the data collection process but also enhances the feasibility of large-scale and continuous water quality assessments, ensuring timely and informed decision-making for water resource management. To determine the most accurate model, multiple iterations were run with 1,000 epochs, and the model's performance was evaluated based on maximizing the coefficient of determination (R^2) while minimizing errors such as mean square error (MSE), mean absolute error (MAE), relative square error (RSE), and root mean square error (RMSE). The optimal input parameters for predicting the IWQI were identified as electrical conductivity (EC), total dissolved solids (TDS), pH, total hardness (TH), sodium (Na^+), potassium (K^+), chloride (Cl^-), bicarbonate (HCO_3^-), iron (Fe), manganese (Mn), nitrate (NO_3^-), and sulfate (SO_4^{2-}).

The best-performing FFBP-NN structure for predicting the IWQI based on physicochemical parameters consisted of one hidden layer with five neurons and employed the Levenberg-Marquardt optimization algorithm. The model achieved its optimal prediction at epoch 86 out of the 1,000 iterations, demonstrating a consistent decrease in MSE and an increase in R^2 across the training, validation, and testing phases. This indicates that the model effectively learned the relationships between the input parameters and the IWQI, providing reliable predictions for water quality assessment. **Table 6** summarizes the performance metrics of the FFBP-NN model during network training, validation, and testing, including mean square error (MSE), mean absolute error (MAE), relative square error (RSE), root mean square error (RMSE), and regression R-values. The regression values (R) for the training, validation, and testing datasets were 0.999, 0.998, and 0.963, respectively. In all cases, R exceeded 0.95, indicating an excellent fit for the network. The overall regression coefficient of 0.99 further confirmed a strong alignment between the measured data points and the predicted values, closely matching the ideal Y = T prediction line. This high correlation demonstrates that the FFBP-NN model effectively captured the relationships between the input variables and the IWQI, providing reliable predictions across all datasets. To optimize the model, different

configurations were tested by systematically removing one feature at a time from the input data. The best-performing model utilized 12 out of the original 14 features, excluding calcium (Ca^{2+}) and magnesium (Mg^{2+}). This optimized model achieved the following performance metrics: for training, MSE = 0.57, MAE = 0.59, RSE = 1.0E-05, and RMSE = 0.75; for validation, MSE = 0.45, MAE = 0.47, RSE = 2.9E-05, and RMSE = 7.9E-05; and for testing, MSE = 0.66, MAE = 0.63, RSE = 2.5E-05, and RMSE = 0.81. The slight variations in MSE, MAE, RSE, and RMSE across the training, validation, and testing phases indicate the model's accuracy and robustness with no signs of overfitting. This confirms that the model successfully predicted the IWQI for unseen data.

Table 6. The main target (IWQI) used by FFBP-NN, beast attributes utilized as input, number of hidden layers and neurons, and the performance of models in the training, validation, and testing based on MSE, MAE, RSE, RMSE, and R^2

Target		IWQI
inputs		EC, TDS, pH, TH, Na^+, K^+, Cl^-, HCO3-, Fe, Mn, NO3-and SO_4^{2-}
Hidden layer, neurons		(1,5)
Training	R^2	0.999
	MAE	0.596
	MSE	0.573
	RSE	1.0E-05
	RMSE	0.757
Cross-validation	R^2	0.998
	MAE	0.469
	MSE	0.447
	RSE	7.9E-05
	RMSE	0.669
Testing	R^2	0.963
	MAE	0.628
	MSE	0.668
	RSE	2.49E-05
	RMSE	0.817

As shown in Fig 54, there was a strong correlation between the true IWQI (calculated data) and the predicted IWQI generated by the FFBP-NN model, with an R^2 value of 0.963.

The model was applied to predict the IWQI across the aquifer system of Siwa Oasis, encompassing both shallow and deep aquifers. The NSSA and the TCA were analyzed together, as the NSSA recharges the TCA, and both aquifers share similar chemical characteristics. However, the salinity of the shallow aquifer (TCA) is higher due to water-rock interactions and mixing with salt water in certain areas. This application highlights the model's ability to provide accurate predictions for complex aquifer systems, offering valuable insights for water quality management in the region. This research demonstrated that Feedforward Backpropagation Neural Network (FFBP-NN) models are highly effective tools for predicting water quality indices with remarkable accuracy.

The developed prediction model offers significant practical value for decision-makers involved in water management, as it reduces the time and cost associated with traditional water quality analysis. This was particularly evident in the case of the IWQI prediction, where the model successfully predicted IWQI values without requiring measurements of Ca^{2+} and Mg^{2+}.

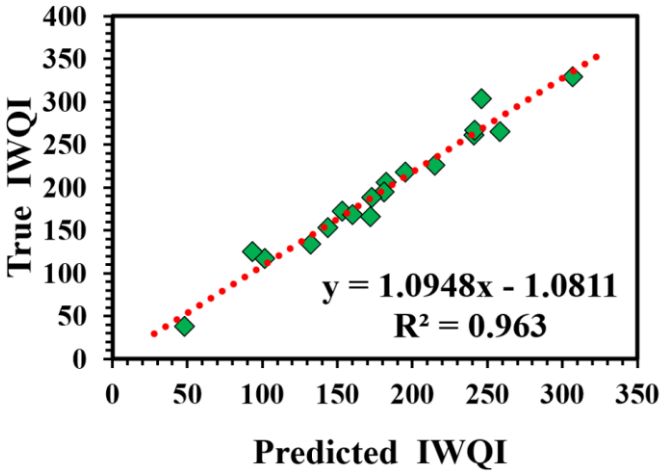

Figure 54. The relationships between the true values and predicted values of the water quality

5.6.3. Health risk assessment

The study assessed both non-carcinogenic and carcinogenic health risks of the potential toxic elements (Table 7) by calculating hazard indices (HI) based on hazard quotients (HQ) for two exposure pathways: ingestion and dermal absorption. The findings reveal the combined potential health risks for humans, including children and adults, due to exposure to various heavy metals. This analysis provides important insights into the cumulative health impacts of these contaminants, underscoring the need for targeted measures to reduce exposure and safeguard public health.

Table 7. Statistical properties of the investigated toxic elements in water samples.

Parameters	Min	Max	Mean	SD
Cd	0.002	0.19	0.04	0.03
Cr	0.0015	12.3	0.6	1.63
Cu	0.002	15.6	1.14	3.004
Fe	0.003	36.2	2.16	5.35
Mn	0.0002	3.37	0.28	0.68
Ni	0.0001	0.72	0.1	0.12
Pb	0.002	2.23	0.33	0.34
Zn	0.0002	0.1	0.03	0.024

a) Non-carcinogenic health risk

The study evaluated the non-carcinogenic risks posed by toxic elements (Cd, Cr, Cu, Fe, Mn, Ni, Pb, and Zn) for two age groups (child & adult). For adults, the hazard quotient (HQ) for ingestion ranged as follows: Cd (1.12 to 11.58), Cr (0.015 to 123.8), Cu (0.0013 to 11.7), Fe (0.0001 to 1.5), Mn (0.0002 to 4.2), Ni (0.00015 to 1.08), Pb (0.03 to 28.04), and Zn (2.01E-5 to 0.01) (Fig 55a). For children, the HQ for ingestion (oral contact) showed higher values: Cd (0.46 to 44.2), Cr (0.06 to 472.9), Cu (0.005 to 44.9), Fe (0.0005 to 5.9), Mn (0.001 to 16.17), Ni (0.0006 to 4.1), Pb (0.1 to 107.06), and Zn (0.0001 to 0.04) (Fig 55b). The results indicate that the health risks associated with ingesting these heavy metals are generally greater for children compared to adults. This highlights the heightened vulnerability of children to toxic elements and underscores the necessity for targeted

measures to diminish contact and protect individuals from negative health issues, particularly for younger populations.

It is important to note that the risk indicator (HQ) values for ingestion (oral exposure) were within the permissible limit (below 1) for copper (Cu), iron (Fe), manganese (Mn), nickel (Ni), and zinc (Zn) in both children and adults. However, for three toxic metals (Cd, Cr, and Pb), the HQ oral index values exceeded 1 in a significant proportion of the water samples. Specifically, for adults, the HQ oral values were greater than 1 in 76.7% of samples for Cd, 45.8% for Cr, and 79.7% for Pb. For children, the HQ oral values exceeded 1 in an even higher percentage of samples: 95.5% for Cd, 86.9% for Cr, and 94% for Pb. These findings are detailed to the site and period studied, and actual risks may fluctuate with exposure period, frequency, individual vulnerability, and environmental situations. In contrast, the HQ index values for dermal exposure in older age group were relatively lower, ranging as follows: Cd (0.01 : 1.1), Cr (0.005 : 47), Cu (2.15E-5 : 0.2), Fe (2.96E-6 : 0.03), Mn (2.98E-5 : 0.5), Ni (3.58E-6 : 0.02), Pb (7.15E-5 : 0.1), and Zn (2.86E-7 : 0.0002) (**Fig 55c**). These results suggest that while dermal exposure poses a lower risk compared to ingestion, the elevated HQ oral values for the three metals (Cd, Cr, & Pb) highlight significant health concerns, particularly for children, who are more vulnerable to the toxic effects of these heavy metals.

For children, the hazard quotient (HQ) values for dermal exposure ranged as follows: Cd (0.03 : 3.23), Cr (0.02 : 3.1), Cu (6.3E-5 : 0.5), Fe (8.74E-6 : 0.1), Mn (8.79E-5 : 1.5), Ni (1.05E-5 : 0.1), Pb (0.0002 : 0.2), and Zn (8.44E-7 to 0.0004) (**Fig 55d**). For adults, the HQ dermal index values remained under the allowable boundary limits (below 1) for all metals. However, for younger age group (child), the HQ dermal index values exceeded 1 in 24% of samples with respect to Cd and 50.3% to Cr, while the remained metals showed no risk or threats.

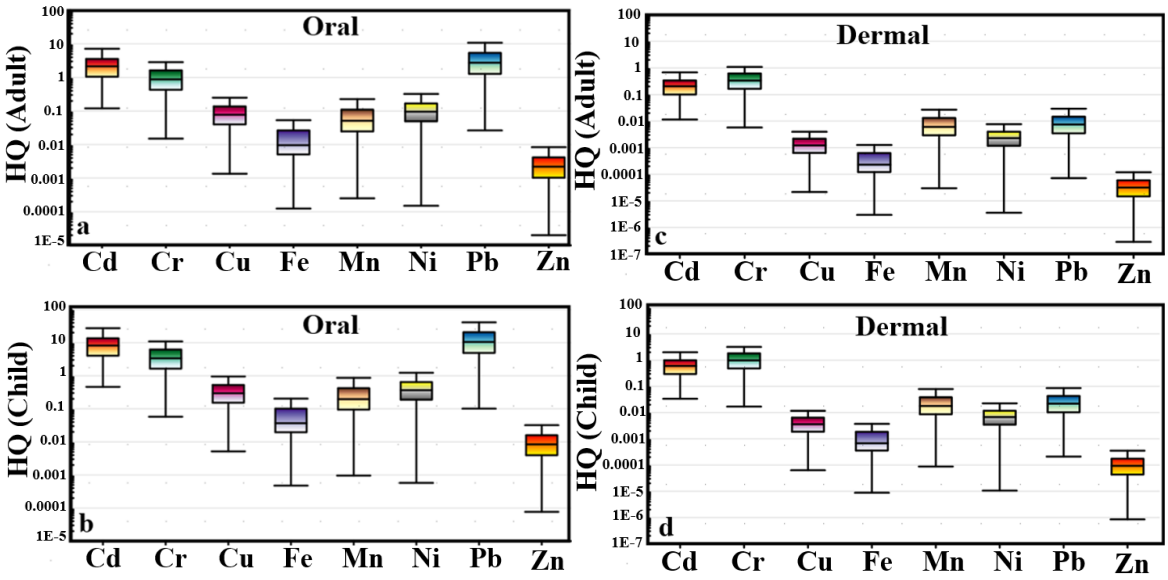

Figure 55. The interval values of HQ in different age group with different exposure routes represented by Box plot graph.

These findings indicate that the health risks associated with dermal exposure to metals are mostly high for younger group (child) compared to older individuals (adult). Specifically, Cd and Cr pose significant risks to children through dermal contact, while adults face no such risks. In contrast, for oral exposure, Cd, Cr, and Pb were identified as the primary contributors to human health risks for both adults and children. In summary, the study highlights that lead, Cromium, and Cadmium are the most concerning metals for oral exposure, affecting both adults and children. For dermal exposure, child (Young) are particularly vulnerable to Cromium, and Cadmium exposure, while adults remain unaffected. This highlights the heightened vulnerability of children to toxic elements and underscores the necessity for targeted measures to diminish contact and protect individuals from negative health issues, particularly for younger populations.

The hazard index (HI) serves as a crucial tool for evaluating the total risks gained by toxic metals in water. It takes into account all potential exposure pathways, counting oral contact (ingestion exposure) and skin contact (dermal expossure), by summing up HQs for each toxic metal. This holistic approach offers a more comprehensive understanding of the cumulative risks associated with metal toxicity in the investigated area. The HI index value is a key metric for evaluating the safety and potential impacts of these contmination in drinking and irrigation water in Siwa region.

For oral exposure, the HI index values fluctuated between low value (1.6) to maximum value (142) for older individuals and from 6 to 542 for young group or children (**Table 12s. Appendix 2**).

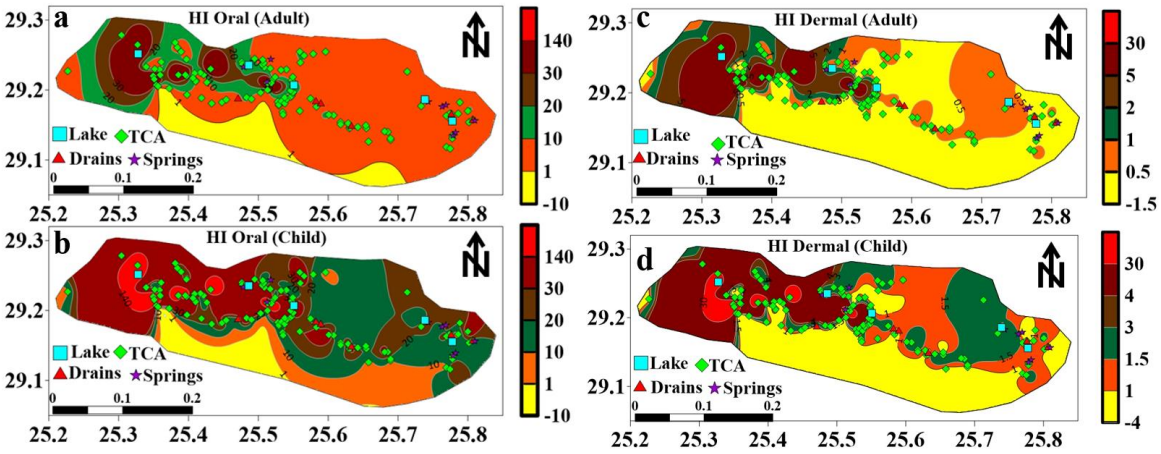

Figure 56. Distripution maps of Hazard index ina adult and child through oral and dermal contact

For dermal exposure, the HI score fluctuated between low value (0.07) to maximum value (48) for adults and between minum score (0.2) to maximum score (141) for children (**Table 12s. Appendix 2**). These results highlight that children face significantly higher health risks compared to adults, particularly through oral exposure. The elevated HI values emphasize the necessity for urgent measures to mitigate toxic metal contamination and avoid negative health impact, especially for vulnerable populations like children. This assessment provides valuable insights for policymakers and stakeholders to prioritize actions aimed at ensuring the safety of water resources in Siwa Oasis.

Incase of oral exposure to toxic metals in all age groups, it was demonstrated that the hazard index was gerneraly high almost in all samples collected (HI > 1), and reflect the high risk or vulnerability to these metals in Siwa Oasis (High non-carcinogenic threats). In contrast, 80.6% of samples confirmed the low-risk regarding adults skin/dermal exposure to toxic metals with HI less than the acceptable boundry (HI<1), while 19.4% posed a high risk. Incase of children, only 22.5% of sampling locations were classified as low-risk, with 77.5% falling into the high-risk category (**Table 12s. Appendix 2**). These results clearly indicate that children are significantly more vulnerable to the health risks associated with both oral and dermal exposure to heavy metals compared to adults. Given these findings, it is crucial to continuously monitor the levels of heavy metals in the TCA of Siwa Oasis and assess their potential health impacts. Groundwater in the study area is non-rechargeable and serves as the primary water source for multiple uses, making its protection and management even more critical.

The distribution maps of the Hazard Index (HI) for non-carcinogenic impacts across two different age groups reveal a significant increase in toxicity and vulnerability to toxic metal exposure in the western and central areas of the Siwa Depression (**Fig 56**). These regions exhibit elevated health risks, particularly for children, who are more susceptible due to their heightened sensitivity to toxic elements. The findings highlight the urgent need for targeted interventions to diminish exposure and mitigate associated risks. This study emphasizes the importance of proactive measures to protect water quality and safeguard public health, particularly in vulnerable communities within the region.

b) Carcinogenic risk

Carcinogenic risk (CR) assessment evaluates the likelihood of developing cancer through long-term contact to pollutants such as carcinogenic toxic metals. In this study, the traditional method of CR calculation was performed to establish baseline values, which were later compared with predicted CR values obtained from Monte Carlo simulations. For adults, the CR values for oral exposure ranged as follows: cadmium (Cd) (0.0003 to 0.03), chromium (Cr) (2.26E-05 to 0.18), and lead (Pb) (3.16E-05 to 0.03) (**Fig 57a**). For children, the CR values for oral exposure were higher, ranging from 0.001 to 0.1 for Cd, 8.63E-05 to 0.7 for Cr, and 0.0001 to 0.1 for Pb (**Fig 57b**). These results indicate that children face a greater carcinogenic risk compared to adults when exposed to these heavy metals through ingestion. The study revealed significant carcinogenic risks (CR) associated with oral and dermal exposure to heavy metals in the water resources of Siwa Oasis particularly TCA.

For oral exposure, the high risk was observed in a substantial proportion of water samples specifically, for adults, high CR values ($CR > 1\times10^{-4}$) were found in 77.6% of samples for cadmium (Cd), 96.3% for chromium (Cr), and 98.5% for lead (Pb). For children, the risk was even more pronounced, with high CR values detected in 98.5% for Cr, and in all locations for Pb and Cd (**Table 12s. Appendix 2**). For dermal exposure, the CR values for adults ranged as follows: Cd (0.002 to 0.2), Cr (0.0002 to 1.7), and Pb (1.5E-05 to 0.01) (**Fig 57c**). For children, the CR dermal values were higher, ranging from 0.005 to 0.5 for Cd, 0.0006 to 5.2 for Cr, and 4.43E-05 to 0.04 for Pb (**Fig 57d**,

Table 12s. Appendix 2). The high risk from dermal exposure was found in all sites with respect to two metals (Cd and Cr), and 94.7% for lead (Pb) in adults. These findings underscore the severe carcinogenic risks gained by toxic metals in the water resources, affecting both adults and children. The results highlight the urgent need for comprehensive treatment of all water sources in the region to mitigate these risks and protect public health. The high carcinogenic risk levels, particularly for children, emphasize the importance of implementing effective treatment and actions to decrease contact with these toxic and carcinogenic metals to ensure the safety of water for all users.

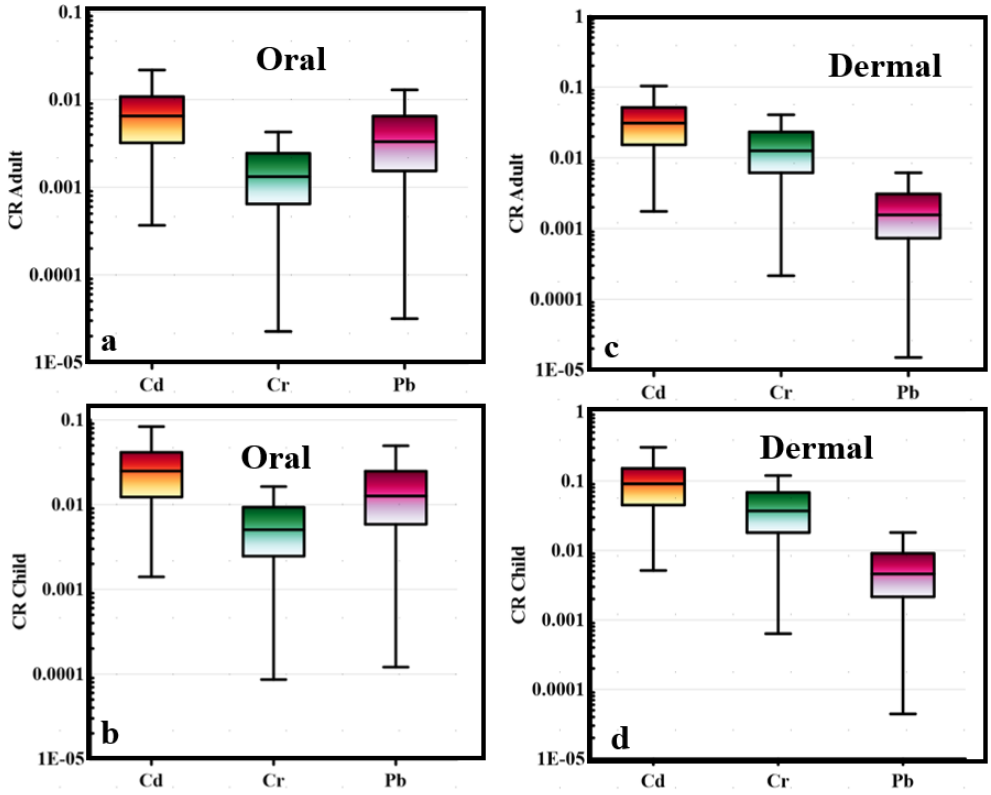

Figure 57. Box plot of the carcinogenic risk (CR) in adult and child through oral (a and b) and dermal (c and d) contact.

5.6.4. Monte Carlo Simulation (MCS)

The Monte Carlo simulation was employed to predict the hazard quotient (HQ) values in two different age groups with respect to different type of contact with toxic metals (Cd, Cr, Cu, Fe, Mn, Ni), Pb, and Zn, as well as the carcinogenic risk (CR) index values for three metals (Cd, Cr, and Pb). This advanced modeling approach provides a probabilistic assessment of the potential health risks, accounting for variability and and decrease uncertainty in exposure parameters. By simulating a wide range of possible outcomes, the Monte Carlo method offers a more comprehensive and realistic estimation of different risks linked to toxic metals in water. This information is critical for developing effective risk management strategies and ensuring the safety of water for all users.

a) Non-carcinogenic health risk

The findings from MCS offer insights into the health hazards gained from exposure to toxic metals through different types of expossure or contact. It is reassuring to note that according to the estimated

dermal hazard quotient (HQ dermal), there are no indications of any metal exceeding limits (**Fig 58a, b**). This suggests that there is no health risk of metals due to skin contact with water resources for adults and children. However, when oral exposure routes are considered, the situation changes. While some toxic metals like Cu, Fe, Mn, Ni, and Zn have predicted HQ values within limits (low risk) for adults, Cd, Cr, and Pb showed estimated HQ values higher than 1 (high risk). This implies a health risk for adults consuming water contaminated with Cd, Cr, and Pb through ingestion. Similar patterns are also observed for children (**Fig 58c, d**).

The Monte Carlo simulation results reveal that while some metals, such as Fe, Ni, and Zn do not pose significant risks for young individuals (child) from oral contact, five metals (Cd, Cr, Cu, Mn, and Pb) showed HQ predicted values greater than 1. This indicates potential risks and health threats for children consuming water enriched in these toxic metals. It is essential to note that these risk or threats estimation are based on certain assumptions to the data sources. Therefore, continuous monitoring of toxic metals levels and regular updates to their risk are essential to ensure the safety of water resources and protect the health of the population in Siwa Oasis.

By comparing the calculated HQ values (**Fig 55**) with HQ predicted values from the MCS (**Fig 58**) for both oral and dermal exposure, it is evident that the three metals (lead, cromium, and cadmium) are the primary contributors to high non-carcinogenic risks for both age groups in the region. The MCS proved to be an effective tool for accurately predicting HQ values, providing a reliable basis for assessing and managing the risks gained from toxic metals in water.

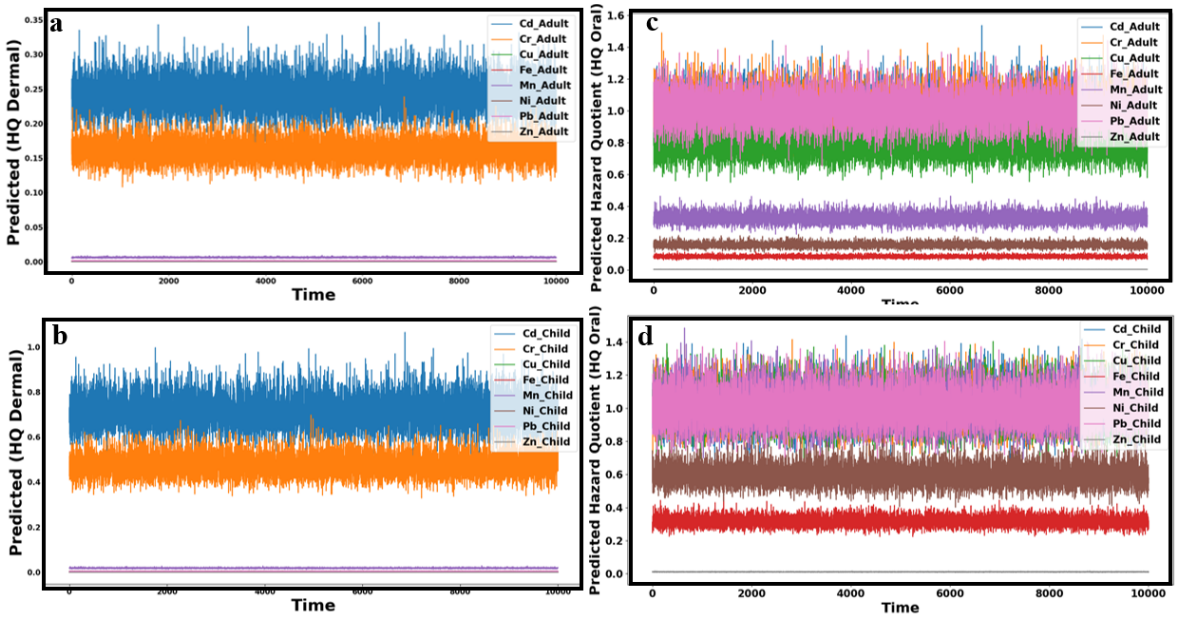

Figure 58. The predicted HQ dermal in old age group (adult) (a), $HQ_{predicted}$ dermal in young age group (child) (b), $HQ_{predicted}$ oral for adult (c), and $HQ_{predicted}$ oral for child.

b) Carcinogenic risk prediction through oral contact

The cancer risk estimates for adults were notably lower across their percentiles. For adults, the minimum risk estimates (5th percentile CR ingestion values) were 0.0047, 0.005, and 0.003 for Cd,

Cr, and Pb, respectively (Fig 59a, b, c). Additionally, at the 95th percentile, the CR values were 0.011, 0.0118, and 0.0072 for Cd, Cr, and Pb, respectively (Figures 7d, e, f), reflecting reduced risks relative to children. Nonetheless, the projected CR from ingestion exposure indicated that the majority of water samples from Siwa Oasis pose a high risk for both children and adults, with CR values exceeding 1×10^{-4}. The evaluation of cancer risk likelihoods (CR) from ingestion exposure in both age categories highlight significant trends. For all variables, the CR ingestion levels are invariably greater in younger individuals compared to older ones. In children, the 5th percentile CR ingestion figures (the minimum estimates of cancer risk) were 0.017, 0.019, and 0.012 for cadmium (Cd), chromium (Cr), and lead (Pb), respectively (Fig 59d, e, f). Conversely, at the 95th percentile (the maximum estimates of risk), the CR ingestion values were recorded as 0.044, 0.045, and 0.0275 for Cd, Cr, and Pb, respectively, indicating elevated risks for children.

By contrasting the computed CR (Fig 57) with the projected CR (Fig 59) from ingestion exposure to heavy metals, it was evident that Cd, Cr, and Pb could significantly increase cancer risks for both age groups in all TCA samples and surface water. The Monte Carlo simulation proved to be a reliable approach for accurately predicting CR ingestion.

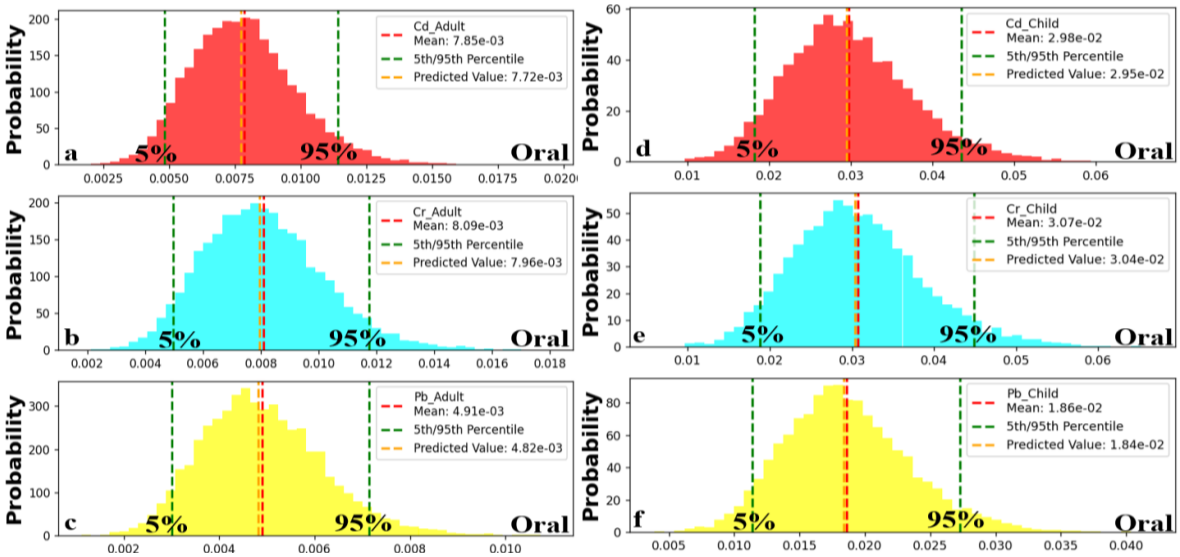

Figure 59. Predicted carcinogenic risk (CR) in adult (a, b and c) and child (d, e and f) through oral contact for Cd, Cr, and Pb respectively

c) Carcinogenic risk prediction through dermal contact

The cancer risk due to dermal exposure in both younger and older individuals indicates that children consistently have greater CR levels than adults for all elements (Cd, Cr, and Pb). Adults exhibited lower CR levels for cancer development through dermal contact. The 5th percentile CR skin values for adults were 0.022 for Cd, 0.047 for Cr, and 0.0013 for Pb (Fig 60 a, b, c). At the 95th percentile, these figures increased to 0.055 for Cd, 0.112 for Cr, and 0.0034 for Pb (Fig 60 d, e, f), representing the upper limits of cancer risk estimates for adult skin exposure. Conversely, for children, the minimum estimates of cancer risk (5th percentile CR skin values) were 0.071 for Cd, 0.13 for Cr, and 0.0041 for Pb (Fig 60 d, e, f). At the maximum estimates (95th percentile), these values reached

0.162 for Cd, 0.33 for Cr, and 0.0102 for Pb (Fig 60 a, b, c), reflecting the highest potential hazards from skin exposure in children. The findings reveal that both children and adults are at considerable risk of developing cancer due to exposure to Cd, Cr, and Pb found in the water supplies of Siwa Oasis. The predicted cancer risk levels, calculated using Monte Carlo simulations, exceed the acceptable limit (CR > 1.0E-04) in most water samples. This implies that long-term exposure to these metals could result in cancer development in the future for both age groups. These results highlight the critical need to address metal pollution in water sources to reduce cancer-related health risks. Regular monitoring, updated risk assessments, and targeted mitigation strategies are essential to ensure the safety of water resources and safeguard public health in Siwa Oasis.

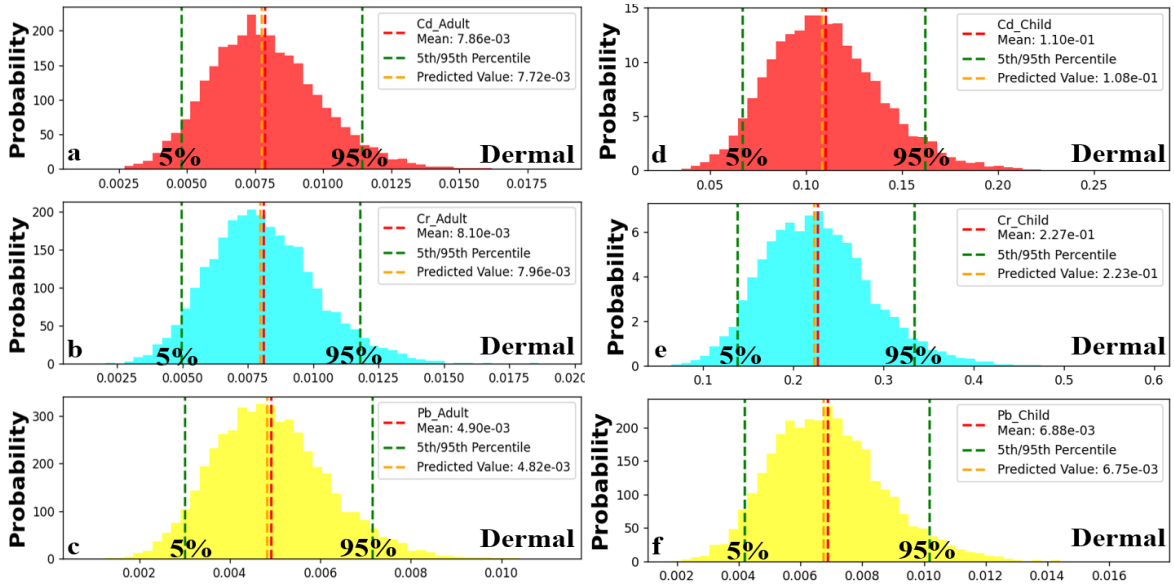

Figure 60. Predicted carcinogenic risk (CR) in adult (a, b and c) and child (d, e and f) through dermal contact for Cd, Cr, and Pb respectively

5.7.Effective desalination using innovative natural material

The current study test effective and low-cost water treatment plane through the previous recommendations where the fresh water of NSSA were mixed with brackish water from TCA as a first step and followed by treatment process using natural material for desalination. This method, supported by the addition of low-cost inorganic materials, aims to prevent soil and groundwater salinization, ensuring sustainable development in a region where the aquifers do not receive recharge from rainfall due to the prevailing arid and hot climate. The treatment of mixed NSSA and TCA water using a dual approach of dilution and geopolymer-based desalination demonstrates considerable potential to address the salinity issues in Siwa Oasis. This process was further optimized using a zeolite/geopolymer (Z/GP) membrane, an innovative ecofriendly material created from abundant natural resources, including kaolinite and diatomite. This integrated strategy not only mitigates salinization but also provides a practical framework for managing water resources sustainably in arid regions like Siwa Oasis, where water and soil quality are critical for long-term development.

5.7.1. Characterization of the Membrane

a) XRD Analysis

XRD analysis was conducted to evaluate the crystalline and amorphous phases of the Z/GP membrane and its precursors. The starting material, kaolinite, exhibited well-defined crystalline peaks at 12.3° (001), 20.8° (110), 24.9° (002), and 26.6° (111) (XRD No. 04-012-5104), confirming its highly crystalline structure (**Fig 61A**). Upon thermal conversion to metakaolinite, the characteristic kaolinite peaks disappeared, indicating a significant loss of crystallinity and the formation of a predominantly amorphous phase (**Fig 61B**). Similarly, the diatomite/kaolinite (D/K) geopolymer displayed a pattern dominated by amorphous phases (**Fig 61C**). In contrast, the zeolitized geopolymer membrane revealed the formation of multiple synthetic zeolite phases, including zeolite-A, zeolite-X, sodalite, and zeolite-P (**Fig 61D**). These results demonstrate the successful transformation of the geopolymer matrix into a zeolitized structure, highlighting its enhanced potential for applications such as desalination membranes.

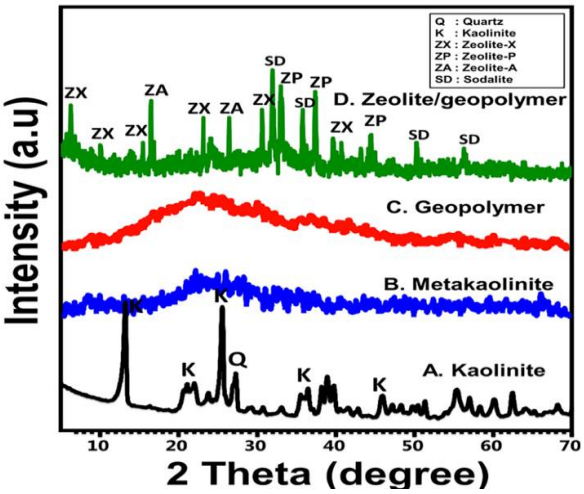

Figure 61. XRD patterns of raw kaolinite (A), metakolinite (B), synthetic D/K geopolymer (C), and the synthetic Z/GP membrane (D).

b) SEM and HRTEM Analyses

The D/K geopolymer exhibited a dense, ceramic-like morphology with agglomerated structures visible under SEM (**Fig 62A**). The material's surface featured oriented pores likely associated with diatomite's silica skeleton (**Fig 62B**). After zeolitization, SEM images revealed a crystalline morphology indicative of zeolite crystal growth, resulting in a highly porous structure with interstitial nanopores (**Fig 62C and 62D**).

The intersection of zeolite crystals with the polymeric matrix contributed to a uniform and porous network ideal for membrane applications. HRTEM images further confirmed these observations. The D/K geopolymer appeared as agglomerated particles with a visibly porous matrix (**Fig 62E**). In contrast, the zeolitized membrane exhibited numerous nanosized pores distributed throughout its highly porous structure (**Fig 62F**). These nanoscale pores, attributed to zeolite crystals, provide a substantial advantage in desalination applications by enhancing salt rejection and water flux efficiency

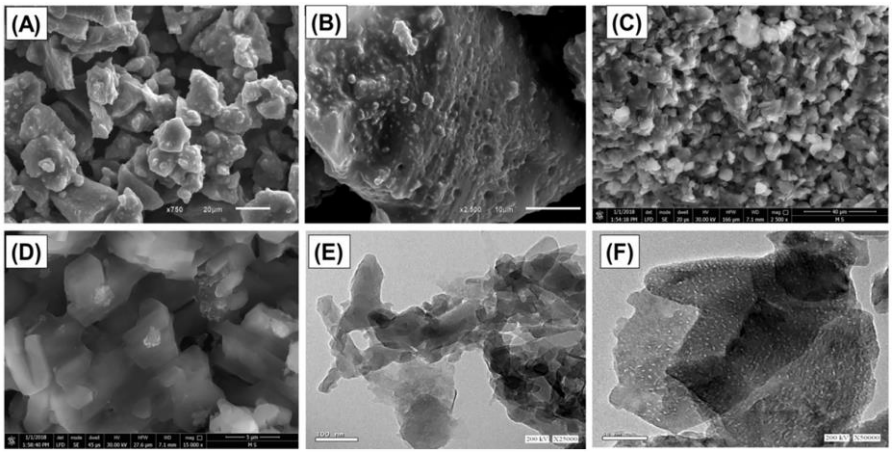

Figure 62. (A) SEM image showing the D/K geopolymer substrate, (B) SEM image illustrating the oriented pores within the D/K geopolymer, (C) SEM image of the Z/GP membrane highlighting its crystalline morphology, (D) SEM image depicting the porous matrix structure of the Z/GP membrane, (E) HRTEM image of the D/K geopolymer revealing its agglomerated particles and porous matrix, and (F) HRTEM image of the Z/GP membrane emphasizing its nanostructured porous material.

a) FT-IR Analysis

The FT-IR spectra of the D/K geopolymer and the zeolitized membrane are illustrated in Fig 63. The spectrum for the D/K geopolymer revealed the presence of –OH (3220–3385 cm^{-1} and 1636 cm^{-1}) and H-O-H (1502 cm^{-1}) groups, likely associated with water molecules trapped within its porous matrix or adsorbed onto the material surface [142] (Fig 63A). Bands corresponding to Si-O-Si and Si-O-Al vibrations were observed at 985.7 cm^{-1} and 602 cm^{-1}, respectively. These positions deviate from those seen in raw kaolinite, indicating the transformation of kaolinite into an amorphous aluminosilicate gel. This structural alteration arises from the condensation of SiO_4 and AlO_4 tetrahedral units during geopolymer formation[143].

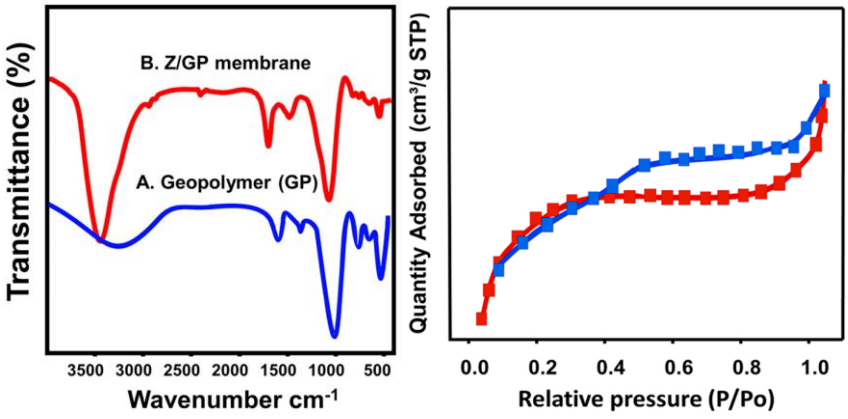

Figure 63. The FT-IR spectra of the synthetic D/K geopolymer (A), and the studied Z/GP membrane and The N_2 adsorption/desorption isotherm curve of the synthetic Z/ GP membrane.

The FT-IR spectrum of the zeolitized membrane closely resembled that of synthetic zeolites reported in the literature (Fig 63B). Bands at 3452 cm^{-1} and 1435 cm^{-1} correspond to hydroxyl groups and coordinated water within the zeolite structure. Additionally, key features include T-O bending vibrations of TO_4 tetrahedra (T = Si or Al), Si-O-Al vibrations, and O-T-O vibrations, observed at

1016 cm^{-1}, 400 cm^{-1}, and 800 cm^{-1}, respectively (Fig 63B). Notably, bands at 469 cm^{-1}, 537 cm^{-1}, and 673 cm^{-1} confirm the presence of FAU-type zeolite (Zeolite-X) and LTA-type zeolite (Zeolite-A). Furthermore, a band at 740 cm^{-1} is characteristic of both FAU and GIS-type zeolite (Zeolite-P)[144]. These findings substantiate the successful synthesis of zeolitized material with a well-defined crystalline structure suitable for desalination applications.

d) Microstructural and Mechanical Properties

The surface area of the synthetic Z/GP membranes was evaluated using the N_2 adsorption/desorption isotherm curve (Fig 63). The surface areas for the GP and Z/GP membranes were found to be 89.2 m^2/g and 106 m^2/g, respectively (Table 8). The increased surface area of the Z/GP membrane is attributed to the incorporation of diatomite and the enhanced porous matrix, contributing to the formation of zeolite phases with microporous structures. This improvement is further reflected in the smaller average pore diameter of the Z/GP membrane (4.2 nm), compared to the GP substrate (11.6 nm) (Table 8). Additionally, the Z/GP membrane exhibited promising mechanical properties with compressive and flexural strengths of 22 MPa and 3.6 MPa, respectively, highlighting its suitability for practical applications.

Table 8. The microstructural properties of the synthetic D/K geopolymer and Z/GP membrane, along with their raw materials, are presented in this table.

Microstructural properties			
	Specific surface area	Total pore volume	Average pore size
Kaolinite	10 m2/g	0.072 cm3/g	43.2 nm
Diatomite	117.7 m2/g	0.032 cm3/g	5.14 nm
Geopolymer	89.4 m2/g	0.039 cm3/g	11.6 nm
Z/GP membrane	106 m2/g	0.058 cm3/g	4.2 nm

5.7.2. The desalination performances with different thicknesses

The effect of Z/GP membrane thickness on desalination performance was examined for thicknesses ranging from 1 mm to 5 mm. The desalination temperature was maintained at 75°C (Fig 64A). A noticeable decline in water flux was observed as the thickness increased from 1 mm to 5 mm. Specifically, the water flux values were 8.34 $kg/m^2/h$, 7.63 $kg/m^2/h$, 7.05 $kg/m^2/h$, 5.72 $kg/m^2/h$, and 3.63 $kg/m^2/h$ for thicknesses of 1 mm, 2 mm, 3 mm, 4 mm, and 5 mm, respectively (Fig 64A).

Meanwhile, the salt rejection percentage significantly improved with increasing membrane thickness, rising from approximately 95.8% to 99.8% (Fig 64A). The increase in thickness enhances the resistance to water molecule permeation through the porous structures of the zeolite phases and the geopolymer substrate, leading to reduced water flux. However, this also boosts the salt rejection efficiency. For balancing high-water flux and efficient salt rejection, a membrane thickness of 3 mm was preferred, achieving a salt rejection of 99.5% and a water flux of 7.05 $kg/m^2/h$ at 75°C. Thus, a membrane thickness of 3 mm was established for subsequent desalination tests.

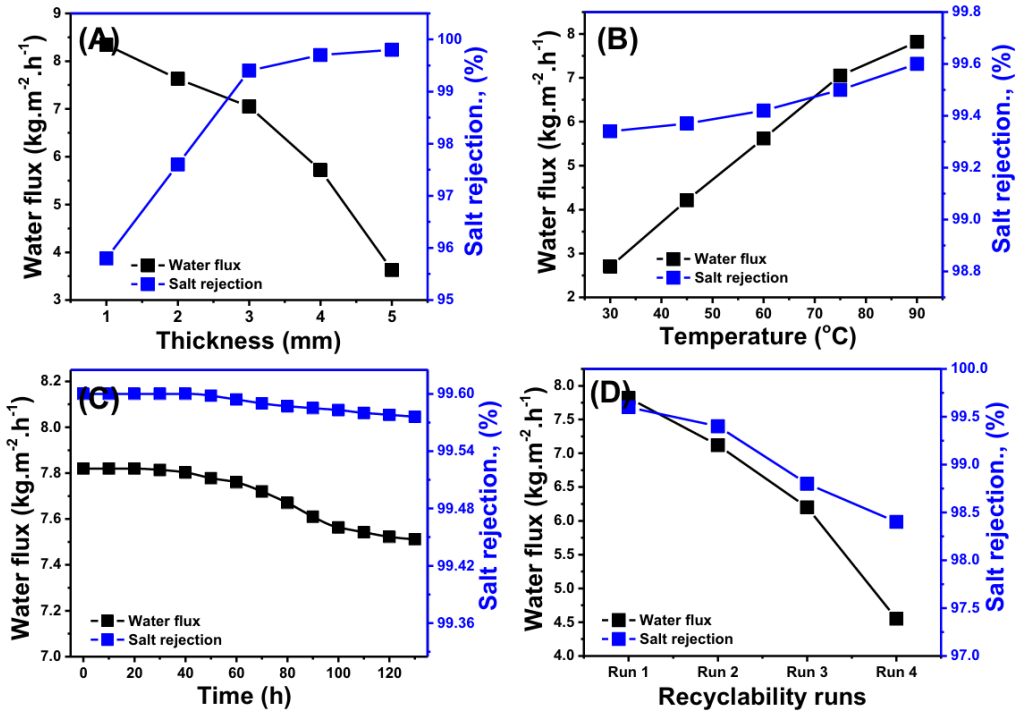

Figure 64. (A) Shows the influence of Z/GP membrane thickness on desalination performance, (B) the impact of feed temperature on the performance of the membrane, (C) the stability of the Z/GP membrane during a 130-hour desalination process, and (D) the recyclability of the prepared Z/GP membrane for reuse in desalination processes of Siwa brackish groundwater.

5.7.3. The desalination performances at different temperatures

The impact of temperature on the performance of the Z/GP membrane in terms of water flux and salt rejection was evaluated at a constant membrane thickness of 3 mm and the natural concentration of a representative sample (3205 mg/L). As the temperature rose from 30°C to 90°C, the water flux significantly increased from 2.65 kg/m²/h to 7.82 kg/m²/h (Fig 64B). Conversely, the salt rejection percentage remained consistently high, exceeding 99% across all temperature ranges (Fig 64B). The observed increase in water flux at higher temperatures is attributed to the enhanced driving forces, facilitating the penetration of water molecules through the membrane pores. Additionally, the stabilization in salt rejection percentage at varying temperatures highlights the effectiveness of the size-exclusion mechanism during desalination, ensuring high efficiency even under elevated temperatures[145].

5.7.4. Reusability of Z/GP Membrane

The reusability of the Z/GP membrane was tested through four cycles of desalination at 3 mm thickness and 90°C temperature (Fig 64D). Membrane regeneration involved backwashing with freshwater and acidic washing with diluted HCl (0.02 M), followed by rinsing. Despite slight reductions in water flux and salt rejection percentages over successive runs, significant recyclability was demonstrated, with values of 7.82 $kg.m^2.h^{-1}$ (run 1), 7.12 $kg.m^2.h^{-1}$ (run 2), 6.2 $kg.m^2.h^{-1}$ (run 3), and 4.55 $kg.m^2.h^{-1}$ (run 4) for water flux, and 99.6%, 99.4%, 98.8%, and 98.4% for salt rejection percentages, respectively. The reduction in performance across reusing runs was attributed to the

continuous blockage of membrane pores with salts and the accumulation of exchangeable ions within the zeolite structure.

5.7.5. The Activation Energy of the Water Permeation Process

The activation energy (Ea) for water permeation through the Z/GP membrane was estimated using the Arrhenius relationship (**Eq 67**). The obtained value is 18.9 kJ/mol, which signifies a positive activation energy, indicating that the water permeation occurs via an activated diffusion mechanism. This results in a substantial increase in water flux with elevated temperatures in the feed water. The equation used is:

$$J_i = A_i \, exp(-EP, i \, / \, RT) \qquad (67)$$

The presented symbols in the equations are Ji, Ai, EP, R, and T refer to the permeate flux of the Z/GP membrane, pre-exponential factor, the activation energy of the diffusion processes, and the sorption heat, the gas constant, and the absolute temperature, respectively. The achieved water flux values are higher than those reported for other zeolite membranes in the literature, which can be attributed to the presence of dominant zeolite phases like Zeolite-X (FAU), known for its higher hydrophilicity and larger pore diameter compared to other phases[146].

5.7.6. The Suggested Mechanism

The rejection of salts from Siwa brackish groundwater using the Z/GP membrane is explained through a model proposed by He [147]. The desalination mechanism of the Z/GP membrane involves a combination of size exclusion, charge exclusion, and adsorption processes. Initially, metal ions such as sodium ions, which carry positive charges, are adsorbed by the negatively charged sites of the zeolite phases and the geopolymer substrate under experimental conditions. This adsorption transforms the membrane surface into a positively charged layer, facilitating the selective rejection of negatively charged ions[148]. The positively charged surface further accelerates the movement of hydrated anions towards the non-zeolitic pores of the geopolymer matrix while impeding the mobility of hydrated cations. This synergistic operation of size exclusion (blocking larger ions) and charge exclusion (repelling similarly charged ions) enhances the membrane's salt rejection efficiency[147]. Additionally, as ions diffuse into the membrane, they are adsorbed onto the surfaces of zeolite phases or into their internal pores, establishing a stable adsorption equilibrium within the polymeric pores. This process prevents further ion entry due to concentration polarization effects. Increasing the thickness of the Z/GP membrane reduces the influence of non-zeolitic pores and defects, strengthening the size exclusion mechanism and resulting in improved salt rejection rates during desalination tests[147]. The theoretical model of the membrane, supported by the electric double layer (EDL) theory, further explains the adsorption mechanism. The membrane's symmetric and homogeneous structure, with vertically and horizontally arranged zeolite layers, promotes effective salt ion rejection. The EDL theory highlights the formation of a Stern layer with strong binding forces and a diffuse layer with high electrostatic potential around zeolitic grains, contributing to stable and efficient salt rejection[149].

5.7.7. Water Evaluation After the Desalination Process

The chemical analysis of the feedwater was compared with that of the permeate obtained after the desalination process using the synthetic Z/GP membrane (Table 9). The results indicated a significant reduction in total dissolved salts and key salts bearing cations and anions. These levels closely align with international and national standards for both drinking water and irrigation water. This outcome underscores the effectiveness of the synthetic Z/GP membrane as a low-cost, inorganic solution for desalinating brackish groundwater in Siwa Oasis.

Table 9. The chemical analysis of the water feed and the permeate water after the desalination experiments in the presence of Z/GP membrane.

Ion concentration					
Parameters (mg/L)	input	output	% salt removal	Egyptian. Standard	WHO
TDS	3205	12.8	99.6	1200	1000
Mg	113.5	0.56	99.5	150	125
Ca	175.6	0.7	99.6	200	200
Na	874	4.4	99.6	200	200
SO4	276	0.6	99.8	250	250
Cl	1630	5	99.7	500	250
HCO3	182	0.3	99.8	-	350
CO3	16.3	-	100	-	-
K	46	-	100	-	12

The comprehensive findings from this study demonstrate the significant potential of the Z/GP membrane in desalination processes, highlighting its innovation, efficiency, and feasibility for practical applications. The evaluation of membrane thickness reveals a balance between water flux and salt rejection, with a 3 mm thickness achieving optimal performance (99.5% salt rejection and a water flux of 7.05 kg/m².h). Furthermore, the impact of temperature on desalination efficiency underscores the membrane's versatility, as water flux increased significantly from 2.65 kg/m².h to 7.82 kg/m².h with elevated temperatures, while maintaining high salt rejection rates above 99%. The stability of the membrane during extended operation for 130 hours showed minimal changes in both water flux and salt rejection, demonstrating its durability and reliability over prolonged use. Additionally, the reusability experiments highlight the membrane's recyclability, maintaining acceptable salt rejection rates and water flux even after four reuse cycles. The activation energy analysis further supports the mechanism of water permeation through the Z/GP membrane, showing a positive activation energy of 18.9 KJ/mol, which is associated with activated diffusion. The proposed desalination mechanism, involving size exclusion, mesoporous adsorption, and electrostatic repulsion, aligns with theoretical models and enhances the removal of salts from brackish groundwater. Based on the recommendations from the mixing models mentioned earlier, integrating the TCA and NSSA on the ground surface with the support of an inorganic membrane such as the Z/GP membrane emerges as an effective solution to prevent groundwater salinization and avoid soil salinization. This approach ensures sustainable management of non-rechargeable aquifers, optimizing the use of brackish water while protecting agricultural lands and maintaining water quality. Ultimately, these findings underscore the Z/GP membrane's innovative capacity to provide a

cost-effective, durable, and efficient solution for desalination, making it a feasible option for treating brackish water in arid regions like Siwa Oasis.

6. New scientific results

6.1.Thesis of the research

Following the established workflow for the application of the above-exposed methods on the constructed database of Siwa Oasis, the new scientific results could be summarized in 7 theses as follows;

Thesis 1: Aquifer Characterization and Structure Controlling Aquifer System

This thesis establishes and validates a novel, cost-effective workflow for the detailed characterization of complex, multi-layered aquifer systems in data-scarce arid regions. By integrating advanced machine learning with traditional geophysical and hydrogeological data, this study provides an unprecedentedly clear and quantitative 3D visualization of the subsurface architecture of the Siwa Oasis. The primary scientific contribution is the successful application of an integrated workflow that synergizes Self-Organizing Maps (SOM) and K-means clustering of well-log data (GR, SP, Resistivity) to classify the subsurface hydrostratigraphic facies. This data-driven approach provides a robust and cost-effective alternative to traditional, expensive cutting sample analysis. The resulting classification was then used to construct a high-resolution 3D geological model, visualizing the spatial distribution and continuity of the key aquifer (sandstone facies) and aquitard (shale facies) layers. Furthermore, this study presents a significant methodological advance by integrating high-resolution aeromagnetic and gravity data to map the deep structural framework controlling the aquifer system. By integrating this structural map with the 3D geological model, this work provides a comprehensive understanding of the specific pathways governing groundwater flow and hydraulic connectivity between the deep NSSA and the shallow TCA. The main key findings of thesis 1 could be concluded as follows;

1. Self-Organizing Maps (SOM) and k-means clustering successfully delineated three distinct lithological units within the NSSA (sand layers, shaly sand, and shale) with SOM proving more accurate than k-means for estimating aquifer layer thickness and providing higher-resolution identification of thin layers. This method could be applied incase lack of data from cutting samples or lithological logs.

2. Hydraulic conductivity validation using both Kozeny-Carman and Cooper-Jacob methods showed strong agreement ($R^2 = 0.92$), with the highest values in central Siwa Oasis. The hydraulic conductivity ranged from 1.2 m/d to 6.6 m/d and effective porosity from 0.2 to 0.3 which could be used for groundwater flow modeling.

3. Integrated gravity and magnetic data analysis identified dominant NE-SW, NW-SE, and E-W lineament trends that control groundwater flow dynamics, with fractures in the shallow carbonate aquifer acting as pathways for surface water leakage and faults in the NSSA serving as conduits for upward flow to recharge TCA.

4. 3D gravity inversion modeling revealed that basement depths ranging from 2.5 km to over 4.5 km and the TCA from 360 m to 630 m.

Thesis 2: Soil Salinization Origin and mechanism controlling water chemistry

This thesis provides a comprehensive diagnosis of the escalating soil salinization in Siwa Oasis by pioneering an integrated approach that combines multi-temporal remote sensing, machine learning, and detailed hydrogeochemical analysis. This thesis moves beyond simply identifying salinization to quantitatively linking it to specific land-use changes and elucidating the complex geochemical processes that govern water quality degradation.

The primary new scientific result is the quantitative, time-series evidence linking the expansion of agricultural land with the dramatic growth of hypersaline lakes and subsequent soil salinization. Over a 30-year period (1990-2020), cultivated land increased by 270%, which directly corresponds to a 168% increase in the surface area of salt lakes due to increased agricultural drainage. This study is the first to establish this direct quantitative relationship for Siwa Oasis. The key methodological advance was the application of a Support Vector Machine (SVM) classifier to a consistent set of Landsat imagery, which allowed for objective and repeatable land use/land cover mapping over three decades, a significant improvement over subjective, manual interpretation methods. The main key findings of thesis 2 are as follows;

1. Remote sensing analysis and SVM could predict the rapid increase of hypersaline lakes from 22.6 km² in 1990 to 60.6 km² in 2020 causing soil salinization. Zeitun lake showed no significant increase in the surface area which could give indication of probability of leakage downward to the TCA through the fracture system and increase the groundwater salinization.
2. Hydrochemical evaluation revealed that the NSSA contains freshwater dominated with Mixed Ca-Mg-Cl-SO4, while the TCA and springs are brackish to saline, and lakes are hyper saline water dominated with Na-Cl and Ca-Mg-SO4 facies.
3. The main mechanism controlling water chemistry are calcite, dolomite, halite, gypsum dissolution, silicate weathering and ion exchange and evaporation.
4. Geochemical modeling using PHREEQC identified mineral supersaturation conditions for montmorillonite, calcite, dolomite, and clay minerals that reduce soil permeability and increase waterlogging.

Thesis 3: Groundwater Recharge Source and Salinity Origin

This thesis provides a definitive identification of the recharge sources and salinity origins in the Siwa Oasis aquifer system by employing combination of stable isotope analysis (δ^2H, $\delta^{18}O$), advanced

statistical techniques (PCA, K-means), and inverse NETPATH mixing models. This thesis moves beyond qualitative descriptions to deliver a quantitative assessment of the complex mixing processes that govern the oasis's water quality.

The primary new scientific result is the quantitative confirmation of a dual-source mixing model for the TCA. By using stable isotopes as tracers, this study proves that the TCA's water is a mixture of upward leakage from the fresh NSSA and downward intrusion from the hypersaline surface lakes. A key methodological advance was the use of PCA to reduce the dimensionality of the complex hydrochemical dataset, followed by K-means clustering to objectively group water samples into three distinct groups. This allowed for the precise selection of representative end-members (NSSA and Salt Lake water) and mixed samples (TCA water) for the mixing model, a significant improvement over subjective, manual selection. The model subsequently quantified the contribution of each source to the TCA's salinity, a critical new finding for management. The main key findings of thesis 3 are as follow;

1. Stable isotope analysis revealed that both the NSSA and TCA contain paleo-meteoric water with $\delta^{18}O$ values ranging from -10.71 to -8.57‰ for NSSA and -10.62 to -8.45‰ for TCA, while salt lakes showed highly enriched values (-7.09 to -0.85‰) due to intense evaporation.
2. PCA identified four key components explaining 75.07% of total variance, with PC1 (40.5%) representing overall **mineralization and salinity**, PC2 (15%) indicating recharge sources and **evaporation effects**, PC3 (11.9%) reflecting trace metal concentrations from **geological formations**, and PC4 (7.64%) showing human-induced contamination from **agricultural activities.**
3. K-means clustering analysis successfully identified three distinct hydrochemical clusters with average electrical conductivity values of 7,000 µS/cm, 10,000 µS/cm, and 2,500 µS/cm, effectively distinguishing between different water sources and mixing processes affecting groundwater quality.
4. NETPATH mixing model quantified that hypersaline lakes contribute 0.6-4% to TCA salinity through downward seepage with the highest contribution from Zeitun lake, while NSSA provides 63-87% freshwater contribution through upward flow, with strong model calibration (R^2 = 88%) confirming that despite small percentages, the extremely high TDS of salt lakes (130,992-153,589 mg/L) significantly impacts groundwater quality.

Thesis 4: Residence Time Estimation and Recharge Location of the TCA from NSSA

This thesis provides a quantitative and spatially explicit understanding of the recharge dynamics and groundwater residence times in the Siwa Oasis aquifer system. By pioneering the combined application of multiple isotopic tracers (including δ^2H, $\delta^{18}O$, $^{87}Sr/^{86}Sr$, ^{13}C and ^{14}C) with a dual-model approach (Faure and NETPATH inverse mixing models), this thesis moves beyond qualitative inference to deliver precise, quantitative estimates of inter-aquifer recharge and its structural controls.

This work provides definitive confirmation for the long-held hypothesis that faults and fractures act as the primary conduits for vertical recharge from the NSSA to the TCA and leakage of salt lake's water to the shallow TCA and fractures. The main findings of this thesis are as follow;

1. Multi-isotopic tracer analysis using $\delta^{2}H$, $\delta^{18}O$, ^{13}C, ^{14}C, and $^{87}Sr/^{86}Sr$ revealed distinct spatial patterns with NSSA showing uniform Sr concentrations (0.04-0.28 mg/L) and $^{87}Sr/^{86}Sr$ ratios ranging from 0.709-0.715, while TCA exhibited highly variable Sr concentrations (1.074-10.1 mg/L) with minimal $^{87}Sr/^{86}Sr$ variation (0.708-0.709), indicating different water-rock interaction processes.
2. The Faure mixing model successfully quantified NSSA contributions to TCA recharge, demonstrating 80-90% NSSA input in low-salinity areas (1000-2000 mg/L) along fault planes, 50-80% in intermediate zones (2000-5000 mg/L), and minimal contributions (0-40%) in high-salinity northern regions (5000-9000 mg/L) near salt lakes.
3. NETPATH inverse mixing model validation showed excellent agreement with the Faure model ($R^2 = 0.96$), confirming NSSA contributions ranging from ~90% in southeastern fault zones to ~52% in northern high-salinity areas, with geochemical processes including calcite/dolomite precipitation in NSSA-dominated regions and halite/gypsum dissolution in evaporative zones.
4. Groundwater age correction using radiocarbon dating revealed significant temporal variations with TCA ages ranging from 640-13,551 years and NSSA ages from 4,296-14,184 years, showing a clear spatial trend of decreasing age from southeast to north, with youngest ages near Siwa Lake indicating active mixing and recharge processes. The relationship between $^{87}Sr/^{86}Sr$ ratios and groundwater age demonstrated that older groundwater (>10,000 years) concentrated near fault systems preserves paleowater from the African Humid Period, while younger northern waters reflect mixing with surface sources (salt lakes), confirming that structural features control both recharge pathways and preservation of ancient groundwater signatures.
5. The findings also provide a generalizable insight for water management in multi-layered aquifer systems: protecting the integrity of deep, pristine aquifers requires not only managing direct abstraction but also understanding and managing the structural pathways that connect them to shallower, more vulnerable aquifers. This has significant implications for the placement of new wells and the development of sustainable abstraction strategies in arid regions globally.

Thesis 5. Numerical flow model using backward particle tracking

This research presents the first fully integrated, three-dimensional numerical flow model of the Siwa Oasis, providing a powerful tool for predicting the long-term impacts of groundwater abstraction and for validating the conceptual hydrogeological model. By coupling the NSSA and TCA and explicitly incorporating major fault and fracture systems, this model offers unprecedented predictive

capabilities and a clear visualization of the complex flow dynamics. The key methodological advance was the use of reverse particle tracking to visually and quantitatively validate the recharge pathways inferred from the geochemical and isotopic data. This is the first model for Siwa Oasis to use this technique, providing direct visual evidence of upward leakage from the NSSA to the TCA along fault planes and, crucially, downward leakage from the surface salt lakes. The primary new scientific result is the quantitative prediction of a catastrophic hydraulic gradient reversal between the TCA and the NSSA within 150-200 years under current abstraction rates. This finding elevates the issue from a problem of water scarcity to a potential ecological and humanitarian crisis, as it would lead to the permanent contamination of the region's only freshwater source. The main key findings of this thesis are as follow;

1. Groundwater numerical flow modeling using FEFLOW demonstrated critical drawdown patterns from 1960-2025, showing dramatic water level decline from 175m to 75m above sea level in western areas and slower decline from 142m to 128m in eastern regions, with future predictions indicating water levels will drop to 30-70m by 2100 under current extraction rates of 330,000 m^3/day.
2. Spring discharge monitoring showed significant decline from 3,900 m^3/d in 1960 to 3,000 m^3/d in 2025, with projections indicating further reduction to 2,400 m^3/d by 2100, directly correlating with decreasing pressure heads and threatening natural water resources for agriculture and tourism.
3. Reverse particle tracking analysis provided definitive validation of NSSA to TCA recharge mechanisms, with all 24 particles released from each TCA tracing back to the NSSA along distinct fault and fracture pathways, confirming that structural features serve as primary conduits for upward groundwater flow between aquifer systems. The pathlines reaches the salt lakes confirming the leakage downward of salt lakes.
4. The modeling results identified a critical threshold scenario where NSSA may cease recharging TCA within 150-200 years under current extraction rates, potentially reversing flow dynamics and causing saline TCA water to contaminate the freshwater NSSA, representing an existential threat to Siwa Oasis's water security and requiring immediate sustainable management interventions.

Thesis 6: Water Quality and Health Risk Assessment of Potential Toxic Elements

This thesis pioneers a comprehensive framework for assessing the suitability of water resources for human consumption and quantifying the associated health risks in the Siwa Oasis. By integrating a novel Integrated Weighted Water Quality Index (IWQI) with advanced machine learning (FFBP-NN) and probabilistic risk assessment (Monte Carlo simulation), this study moves beyond deterministic water quality standards to provide a nuanced, risk-based evaluation of water safety.

The integrated water quality assessment based on the IWQI revealed a clear spatial distinction in groundwater quality across the Siwa Oasis aquifer system. Nearly half of the water samples were

classified as extremely poor for drinking purposes, with the TCA showing widespread deterioration due to salinity increases from water–rock interactions, excessive groundwater abstraction, and return flow from agricultural drainage. In contrast, the deep NSSA generally contained good-quality fresh water, particularly toward the eastern part of the study area, where confined conditions provided protection from salinization and contamination. These findings underscore the vulnerability of the TCA to anthropogenic pressures and hydrogeological processes, while highlighting the relatively better preservation of water quality within the NSSA.

The application of the FFBP-NN prediction model demonstrated excellent performance, with regression coefficients consistently exceeding 0.95 across training, validation, and testing phases. The optimized model, relying on a reduced set of 12 parameters, was able to predict IWQI values with high accuracy and robustness, eliminating the need for exhaustive and costly measurements such as Ca^{2+} and Mg^{2+}. This confirms the model's capacity to capture the complex nonlinear relationships between hydrochemical variables and water quality indices. By accurately reproducing the observed IWQI distribution across both the NSSA and TCA, the model provided a reliable and cost-effective tool for large-scale water quality monitoring and management.

Overall, this study highlights two important outcomes: (i) the groundwater quality in Siwa Oasis is highly variable, with significant risks associated with over-exploitation and salinization of the TCA, and (ii) advanced machine learning approaches, such as FFBP-NN, offer powerful predictive capabilities that can complement traditional monitoring. These insights are crucial for guiding sustainable groundwater management strategies in arid regions, ensuring safe drinking water supplies while supporting agricultural productivity.

The health risk assessment of toxic metals in Siwa Oasis groundwater highlights a serious threat to public health, particularly for children. Non-carcinogenic risk analysis revealed that oral ingestion poses a far greater hazard than dermal exposure, with cadmium (Cd), chromium (Cr), and lead (Pb) consistently exceeding the safety threshold (HQ > 1) in most samples. Children were disproportionately affected, with more than 75% of sampling sites exceeding the acceptable hazard index (HI) for oral exposure, compared to adults who were less vulnerable but still at significant risk. Dermal exposure risks were generally low for adults but remained concerning for children, especially for Cd and Cr, underscoring the heightened vulnerability of younger populations to toxic metal contamination.

Carcinogenic risk assessment further confirmed the severity of the situation, with Cd, Cr, and Pb contributing to elevated cancer risk ($CR > 1\times10^{-4}$) in nearly all samples. Children again showed markedly higher susceptibility compared to adults, both for oral and dermal pathways. These findings emphasize the long-term health implications of chronic exposure to contaminated water, particularly in regions where groundwater is the sole source for drinking and irrigation.

Monte Carlo simulations strengthened the reliability of these conclusions by accounting for variability and uncertainty in exposure parameters. The probabilistic models consistently identified

Cd, Cr, and Pb as the dominant contributors to both non-carcinogenic and carcinogenic risks, confirming their role as priority contaminants requiring urgent mitigation. The simulations also demonstrated that predicted risk values closely matched calculated indices, validating the robustness of the approach for future risk assessment applications.

Thesis 7: Desalination of Brackish Water from the TCA Using Innovative Natural Material

This research presents a groundbreaking solution to the challenge of brackish water desalination by developing, synthesizing, and validating a novel, low-cost, and eco-friendly zeolite/geopolymer (Z/GP) membrane. By utilizing abundant, natural raw materials (kaolinite and diatomite), this study offers a practical and sustainable technological intervention to mitigate water scarcity and soil salinization in arid regions.

The primary new scientific result is the successful synthesis and exceptional performance of the Z/GP membrane, which achieved a salt rejection rate of over 99.8% and a water flux of up to 8.34 kg/m²/h. This demonstrates, for the first time, that a membrane derived from low-cost, natural geopolymers can achieve performance comparable to or exceeding that of more expensive, conventional polymer-based membranes. The key methodological advance was the hydrothermal conversion of a diatomite/kaolin geopolymer substrate into a multi-phase zeolite membrane (containing Zeolite-A, Zeolite-X, Sodalite, and Zeolite-P). This innovative synthesis process resulted in a highly porous, nanostructured material with a large surface area (106 m²/g) and optimal pore size (4.2 nm), which are the key factors behind its high desalination efficiency.

This work provides a powerful, practical solution to the problems identified in the preceding chapters. While previous sections quantified the extent of water quality degradation, this thesis provides a tangible technological solution. The study quantitatively clarifies the optimal operating parameters for the membrane, demonstrating that a thickness of 3 mm and a temperature of 75°C provide the best balance between high water flux (7.05 kg/m²/h) and near-perfect salt rejection (99.5%). Furthermore, the research provides quantitative evidence of the membrane's durability and reusability, showing stable performance over 130 hours of continuous operation and successful regeneration over multiple cycles, confirming its suitability for real-world applications.

The Z/GP membrane developed in this thesis is not just a solution for Siwa Oasis; it represents a paradigm shift in desalination technology for arid and developing regions worldwide. The use of locally sourced, inexpensive raw materials makes this technology highly accessible and economically viable for communities that cannot afford conventional, energy intensive desalination plants. The synthesis method is straightforward and scalable, offering a transferable blueprint for establishing local manufacturing of desalination membranes in other water-stressed countries. This research, therefore, provides a generalizable and sustainable pathway to water security, empowering communities to treat their own brackish water resources and break the cycle of water scarcity and soil salinization.

6.2.Practical applicability

The findings of this study provide critical insights for sustainable water management, particularly in arid regions like the Siwa Oasis, where understanding the complex interactions influencing water chemistry is essential for long-term resource conservation. Based on the results, the following scientifically-backed recommendations are proposed to optimize the quality, quantity, and sustainability of both water resources and soil fertility (Fig 65):

a) Dilution of groundwater salinity through mixing freshwater from the NSSA with brackish water from the TCA on the ground surface using a piped system

b) Desalination of the mixed water to the acceptable level of irrigation water to avoid further soil salinization.

c) Application of subsurface drip irrigation instead of flood irrigation to avoid further increase in the surface area of the salt lakes and protect the limited water resources.

d) Construct a drilling canal to connect the four major salt lakes and discharge their water into an artificial lake lined with impermeable material in the eastern part of Zeitun Lake. This would prevent hypersaline water from seeping into the TCA, reduce the salinity and surface area of hypersaline lakes, and create opportunities for economic and ecological benefits. The artificial lake could be divided into a fish pond and an evaporation pond, supporting aquatic life and salt production.

e) Implement a drainage system with cement-covered drains and perforated pipes to remove waterlogged soil and discharge it into the main lakes and drains.

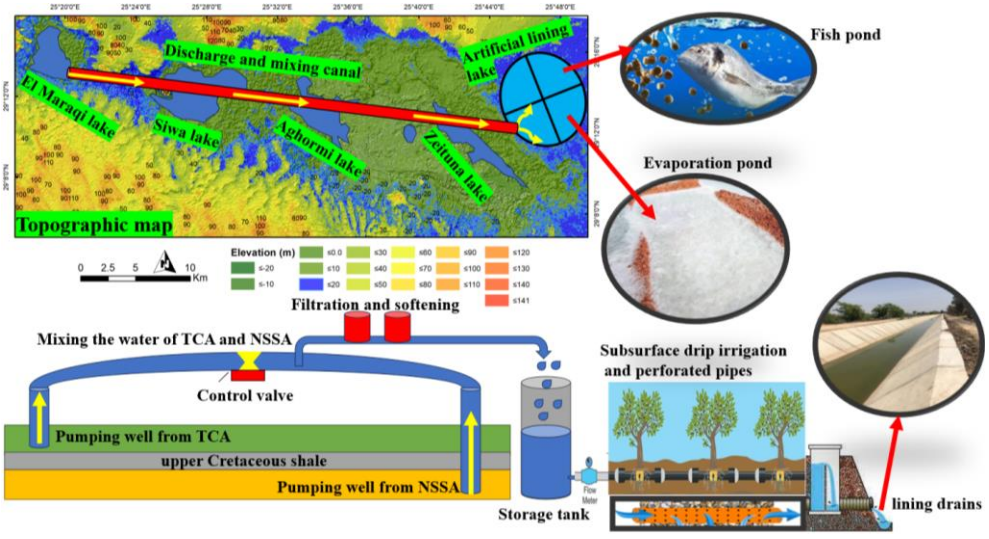

Figure 65. Schematic diagram of the recommended solutions in Siwa Oasis for sustainable development.

7. Conclusions

This PhD thesis has undertaken a comprehensive, multi-disciplinary investigation of the Siwa Oasis hydrogeological system by integrating a wide array of advanced methodologies and diverse data sources. The research framework was designed to build a holistic understanding of the oasis's water resources, from their geological structure to their chemical composition and long-term sustainability.

To achieve this, the study synergistically employed geophysical data (well logs, gravity, magnetics) with machine learning algorithms (SOM, K-means) to construct a high-resolution 3D geological model. Multi-temporal remote sensing data (Landsat) was analyzed using Support Vector Machines (SVM) to quantify land-use change and its environmental impacts. A suite of geochemical and isotopic tracers (δ^2H, $\delta^{18}O$, ^{13}C, ^{14}C, $^{87}Sr/^{86}Sr$) were analyzed and interpreted using advanced statistical techniques (PCA, K-means) and inverse mixing models (NETPATH, Faure) to delineate recharge sources and quantify mixing processes. These empirical findings were then integrated into a predictive numerical flow model (FEFLOW) to simulate long-term aquifer behavior. Finally, the research developed and applied a novel IWQI, a probabilistic health risk assessment using Monte Carlo simulation, and synthesized an innovative zeolite/geopolymer membrane for desalination. The overarching aim of this integrated approach was to move beyond a descriptive analysis and to create a quantitative, predictive, and scientifically robust foundation for the sustainable management of groundwater in this critical arid ecosystem.

The application of this integrated methodology yielded seven key sets of findings. First, the 3D geological model revealed the precise subsurface architecture and identified the fault systems that control the hydraulic connectivity between the deep NSSA and the shallow TCA. The SOM proved to be a highly effective and accurate method for delineating lithological units from well-log data, outperforming K-means in estimating the thickness of critical sand layers. The hydraulic properties of these units were validated, revealing hydraulic conductivity values ranging from 1.2 to 6.6 m/d, which are essential inputs for flow modeling. Furthermore, the analysis of gravity and magnetic data identified the dominant NE-SW, NW-SE, and E-W structural trends that control the groundwater flow system, confirming that deep faults in the NSSA act as conduits for upward recharge to TCA, while shallow fractures facilitate surface leakage. Finally, 3D gravity inversion provided a clear picture of the basin's architecture, mapping the basement depth from 2.5 to over 4.5 km.

Second, the study provided quantitative proof linking the 270% expansion of agriculture over 30 years to a 168% increase in the area of hypersaline lakes, identifying this as the primary driver of soil and water salinization. Zeitun lake showed no significant increase in the surface area which could give indication of probability of leakage downward to the TCA through the fracture system and increase the groundwater salinization. Hydrochemical evaluation revealed that the NSSA contains freshwater dominated with Mixed Ca-Mg-Cl-SO4, while the TCA and springs are brackish to saline, and lakes are hyper saline water dominated with Na-Cl and Ca-Mg-SO4 facies. The main mechanism controlling water chemistry are calcite, dolomite, halite, gypsum dissolution, silicate weathering and ion exchange and evaporation. Geochemical modeling using PHREEQC identified mineral supersaturation conditions for montmorillonite, calcite, dolomite, and clay minerals that reduce soil permeability and increase waterlogging.

Third, the research confirmed a dual-source mixing model for the TCA, quantifying the respective contributions of upward leakage from the fresh NSSA and downward seepage from the saline lakes.

Stable isotope analysis revealed that both the NSSA and TCA contain paleo-meteoric water with depleted $\delta^{18}O$ values, while salt lakes showed highly enriched values due to intense evaporation. NETPATH mixing model quantified that hypersaline lakes contribute 0.6-4% to TCA salinity through downward seepage with the highest contribution from Zeitun lake, while NSSA provides 63-87% freshwater contribution through upward flow.

Fourth, by combining multiple isotopic tracers, the study estimated the residence time of the groundwater and validated the fault-controlled recharge pathways. The Faure mixing model successfully quantified NSSA contributions to TCA recharge, demonstrating 80-90% NSSA input in low-salinity areas (1000-2000 mg/L) along fault planes, 50-80% in intermediate zones (2000-5000 mg/L), and minimal contributions (0-40%) in high-salinity northern regions (5000-9000 mg/L) near salt lakes. Groundwater age correction using radiocarbon dating revealed significant temporal variations with TCA ages ranging from 640-13,551 years and NSSA ages from 4,296-14,184 years, showing a clear spatial trend of decreasing age from southeast to north, with youngest ages near Siwa Lake indicating active mixing and recharge processes. The relationship between $^{87}Sr/^{86}Sr$ ratios and groundwater age demonstrated that older groundwater (>10,000 years) concentrated near fault systems preserves paleowater from the African Humid Period, while younger northern waters reflect mixing with surface sources (salt lakes), confirming that structural features control both recharge pathways and preservation of ancient groundwater signatures.

Fifth, the numerical flow model demonstrated critical drawdown patterns from 1960-2025, showing dramatic water level decline from 175m to 75m in western areas and slower decline from 142m to 128m in eastern regions, with future predictions indicating water levels will drop to 30-70m by 2100 under current extraction rates of 330,000 m^3/day. Reverse particle tracking analysis provided definitive validation of NSSA to TCA recharge mechanisms along distinct fault and fracture pathways confirming the findings of mixing models. The pathlines reaches the salt lakes confirming the leakage downward of salt lakes to the TCA.

Sixth, The IWQI identified areas with extremely poor water quality, particularly in the TCA, due to high salinity. FFBP-NN effectively predicted water quality with high accuracy, reducing the need for extensive testing of many parameters. The health risk assessment highlighted significant non-carcinogenic and carcinogenic risks, especially for children, from exposure to cadmium, chromium, and lead, underscoring the need for targeted mitigation strategies and improved water management practices. Finally, this study developed a geopolymer-based zeolite membrane from natural kaolinite and diatomite for desalination of the brackish water of the TCA after mixing with NSSA. The membrane showed impressive salt rejection (99.5%) and high-water flux (7.05 kg/m^2/h) at 75°C, with excellent thermal stability. The study also demonstrated the membrane's durability, maintaining high performance over multiple reuse cycles. This innovative desalination approach provides a sustainable solution for groundwater salinization in arid regions, offering an eco-friendly, cost-effective method for improving water quality in the Siwa Oasis and similar areas.

8. References

1. Elsheikh, A.E.; Mohallel, S.A.; Ezzeldin, H.A.; Ammawy, M.A.E.; Lateif, R.M.A. Hydrogeological and Hydrogeochemical Insights on the Salinization of the Shallow Groundwater Aquifer in Siwa Oasis – Western Desert – Egypt. *Scientific African* **2023**, *20*, e01742, doi:10.1016/j.sciaf.2023.e01742.
2. Shevah, Y. Challenges and Solutions to Water Problems in the Middle East. In *Chemistry and Water*; Elsevier, 2017; pp. 207–258 ISBN 978-0-12-809330-6.
3. Shevah, Y. Water Resources, Water Scarcity Challenges, and Perspectives. In *ACS Symposium Series*; Ahuja, S., De Andrade, J.B., Dionysiou, D.D., Hristovski, K.D., Loganathan, B.G., Eds.; American Chemical Society: Washington, DC, 2015; Vol. 1206, pp. 185–219 ISBN 978-0-8412-3106-1.
4. Sikka, A.K.; Islam, A.; Rao, K.V. Climate-Smart Land and Water Management for Sustainable Agriculture. *Irrigation and Drainage* **2018**, *67*, 72–81, doi:10.1002/ird.2162.
5. Hamdy Eid, M.; Szűcs, P.; Kovács, A. Problems Threatening Sustainability in Siwa Oasis and Recommendations for Understanding the Sources of Water Quality Deterioration. *Geosciences and Engineering* **2022**, *10*, 138–153, doi:10.33030/geosciences.2022.15.138.
6. Abd El Moniem, A. Overview of Water Resources and Requirements in Egypt; the Factors Controlling Its Management and Development. *Journal of Environmental Studies* **2009**, *2*, 82–97, doi:10.21608/jesj.2009.183681.
7. Eid, M.H.; Eissa, M.; Mohamed, E.A.; Ramadan, H.S.; Czuppon, G.; Kovács, A.; Szűcs, P. Application of Stable Isotopes, Mixing Models, and K-Means Cluster Analysis to Detect Recharge and Salinity Origins in Siwa Oasis, Egypt. *Groundwater for Sustainable Development* **2024**, *25*, 101124, doi:10.1016/j.gsd.2024.101124.
8. Eid, M.H.; Shebl, A.; Eissa, M.; Mohamed, E.A.; Fahil, A.S.; Ramadan, H.S.; Abukhadra, M.R.; El-Sherbeeny, A.M.; Kovacs, A.; Szűcs, P. Comprehensive Approach Integrating Remote Sensing, Machine Learning, and Physicochemical Parameters to Detect Hydrodynamic Conditions and Groundwater Quality Deterioration in Non-Rechargeable Aquifer Systems. *Heliyon* **2024**, *10*, e32992, doi:10.1016/j.heliyon.2024.e32992.
9. Misak, R.F.; Abdel Baki, A.A.; El-Hakim, M.S. On the Causes and Control of the Waterlogging Phenomenon, Siwa Oasis, Northern Western Desert, Egypt. *Journal of Arid Environments* **1997**, *37*, 23–32, doi:10.1006/jare.1997.0252.
10. Abdulaziz, A.M.; Faid, A.M. Evaluation of the Groundwater Resources Potential of Siwa Oasis Using Three-Dimensional Multilayer Groundwater Flow Model, Mersa Matruh Governorate, Egypt. *Arab J Geosci* **2015**, *8*, 659–675, doi:10.1007/s12517-013-1199-4.
11. Arnous, M.O.; Green, D.R. Monitoring and Assessing Waterlogged and Salt-Affected Areas in the Eastern Nile Delta Region, Egypt, Using Remotely Sensed Multi-Temporal Data and GIS. *J Coast Conserv* **2015**, *19*, 369–391, doi:10.1007/s11852-015-0397-5.
12. Poole, G.C.; Stanford, J.A.; Running, S.W.; Frissell, C.A. Multiscale Geomorphic Drivers of Groundwater Flow Paths: Subsurface Hydrologic Dynamics and Hyporheic Habitat Diversity. *Journal of the North American Benthological Society* **2006**, *25*, 288–303, doi:10.1899/0887-3593(2006)25[288:MGDOGF]2.0.CO;2.
13. Flores, Y.G.; Eid, M.H.; Szűcs, P.; Szőcs, T.; Fancsik, T.; Szanyi, J.; Kovács, B.; Markos, G.; Újlaki, P.; Tóth, P.; et al. Integration of Geological, Geochemical Modelling and Hydrodynamic Condition for Understanding the Geometry and Flow Pattern of the Aquifer System, Southern Nyírség–Hajdúság, Hungary. *Water* **2023**, *15*, 2888, doi:10.3390/w15162888.
14. Binley, A.; Hubbard, S.S.; Huisman, J.A.; Revil, A.; Robinson, D.A.; Singha, K.; Slater, L.D. The Emergence of Hydrogeophysics for Improved Understanding of Subsurface Processes over Multiple Scales. *Water Resources Research* **2015**, *51*, 3837–3866, doi:10.1002/2015WR017016.

15. Rahman, A.T.M.S.; Kono, Y.; Hosono, T. Self-Organizing Map Improves Understanding on the Hydrochemical Processes in Aquifer Systems. *Science of The Total Environment* **2022**, *846*, 157281, doi:10.1016/j.scitotenv.2022.157281.
16. Ali, A.; Sheng-Chang, C. Characterization of Well Logs Using K-Mean Cluster Analysis. *J Petrol Explor Prod Technol* **2020**, *10*, 2245–2256, doi:10.1007/s13202-020-00895-4.
17. Chang, H.-C.; Kopaska-Merkel, D.C.; Chen, H.-C. Identification of Lithofacies Using Kohonen Self-Organizing Maps. *Computers & Geosciences* **2002**, *28*, 223–229, doi:10.1016/S0098-3004(01)00067-X.
18. Abraham, E.M.; Alile, O.M. Modelling Subsurface Geologic Structures at the Ikogosi Geothermal Field, Southwestern Nigeria, Using Gravity, Magnetics and Seismic Interferometry Techniques. *Journal of Geophysics and Engineering* **2019**, *16*, 729–741, doi:10.1093/jge/gxz034.
19. Eid, M.H.; Tamma, A.A.; Saeed, O.; Székács, A.; Abukhadra, M.R.; El-Sherbeeny, A.M.; Bence, C.; Mikita, V.; Kovács, A.; Szűcs, P. Advanced Approach Combines Integrated Weight Water Quality Index and Potential Toxic Elements for Environmental and Health Risk Assessment Supported by Simulation Technique in Oued Souf, Algeria. *Sci Rep* **2024**, *14*, 17805, doi:10.1038/s41598-024-68854-1.
20. Eid, M.H.; Mikita, V.; Eissa, M.; Ramadan, H.S.; Mohamed, E.A.; Abukhadra, M.R.; El-Sherbeeny, A.M.; Kovács, A.; Szűcs, P. An Advanced Approach for Drinking Water Quality Indexing and Health Risk Assessment Supported by Machine Learning Modelling in Siwa Oasis, Egypt. *Journal of Hydrology: Regional Studies* **2024**, *56*, 101967, doi:10.1016/j.ejrh.2024.101967.
21. Gaagai, A.; Aouissi, H.; Bencedira, S.; Hinge, G.; Athamena, A.; Heddam, S.; Gad, M.; Elsherbiny, O.; Elsayed, S.; Eid, M.; et al. Application of Water Quality Indices, Machine Learning Approaches, and GIS to Identify Groundwater Quality for Irrigation Purposes: A Case Study of Sahara Aquifer, Doucen Plain, Algeria. *Water* **2023**, *15*, 289, doi:10.3390/w15020289.
22. Saeed, O.; Székács, A.; Jordán, G.; Mörtl, M.; Abukhadra, M.R.; El-Sherbeeny, A.M.; Szűcs, P.; Eid, M.H. Assessing Surface Water Quality in Hungary's Danube Basin Using Geochemical Modeling, Multivariate Analysis, Irrigation Indices, and Monte Carlo Simulation. *Sci Rep* **2024**, *14*, 18639, doi:10.1038/s41598-024-69312-8.
23. Salem, S.; Gaagai, A.; Ben Slimene, I.; Moussa, A.; Zouari, K.; Yadav, K.; Eid, M.; Abukhadra, M.; El-Sherbeeny, A.; Gad, M.; et al. Applying Multivariate Analysis and Machine Learning Approaches to Evaluating Groundwater Quality on the Kairouan Plain, Tunisia. *Water* **2023**, *15*, 3495, doi:10.3390/w15193495.
24. Eid, M.H.; Awad, M.; Mohamed, E.A.; Nassar, T.; Abukhadra, M.R.; El-Sherbeeny, A.M.; Kovács, A.; Szűcs, P. Comprehensive Approach Integrating Water Quality Index and Toxic Element Analysis for Environmental and Health Risk Assessment Enhanced by Simulation Techniques. *Environ Geochem Health* **2024**, *46*, 409, doi:10.1007/s10653-024-02182-1.
25. Ata, A.A.E.-S.M.; Aly, M.H.; Hussein, H.; Eid, M.H.; Abukhadra, M.R.; El-Sherbeeny, A.M.; Bellucci, S.; Gad, M. Hydrogeochemical Characteristics and Air Quality Risks Associated with Gold Mining Operations in Egypt Using Geochemical Modeling and Risk Indices. *Heliyon* **2024**, *10*, e31086, doi:10.1016/j.heliyon.2024.e31086.
26. Eid, M.H.; Eissa, M.; Mohamed, E.A.; Ramadan, H.S.; Tamás, M.; Kovács, A.; Szűcs, P. New Approach into Human Health Risk Assessment Associated with Heavy Metals in Surface Water and Groundwater Using Monte Carlo Method. *Sci Rep* **2024**, *14*, 1008, doi:10.1038/s41598-023-50000-y.
27. Abukhadra, M.R.; Eid, M.H.; El-Meligy, M.A.; Sharaf, M.; Soliman, A.T. Insight into Chitosan/Mesoporous Silica Nanocomposites as Eco-Friendly Adsorbent for Enhanced Retention of U (VI) and Sr (II) from Aqueous Solutions and Real Water. *International Journal of Biological Macromolecules* **2021**, *173*, 435–444, doi:10.1016/j.ijbiomac.2021.01.136.
28. Cartwright, I.; Cendón, D.; Currell, M.; Meredith, K. A Review of Radioactive Isotopes and Other Residence Time Tracers in Understanding Groundwater Recharge: Possibilities,

Challenges, and Limitations. *Journal of Hydrology* **2017**, *555*, 797–811, doi:10.1016/j.jhydrol.2017.10.053.
29. Eid, M.H.; Pinjung, Z.; Mikita, V.; Bence, C.; Szűcs, P. A Novel Integration of Self-Organizing Maps and NETPATH Inverse Modeling to Trace Uranium and Toxic Metal Contamination Risks in West Mecsek, Hungary. *Journal of Hazardous Materials* **2025**, *496*, 139291, doi:10.1016/j.jhazmat.2025.139291.
30. Gad, M.; Gaagai, A.; Eid, M.H.; Szűcs, P.; Hussein, H.; Elsherbiny, O.; Elsayed, S.; Khalifa, M.M.; Moghanm, F.S.; Moustapha, M.E.; et al. Groundwater Quality and Health Risk Assessment Using Indexing Approaches, Multivariate Statistical Analysis, Artificial Neural Networks, and GIS Techniques in El Kharga Oasis, Egypt. *Water* **2023**, *15*, 1216, doi:10.3390/w15061216.
31. Eid, M.H.; Mikita, V.; Eissa, M.; Ramadan, H.S.; Mohamed, E.A.; Abukhadra, M.R.; El-Sherbeeny, A.M.; Bellucci, S.; Kovács, A.; Szűcs, P. Monte Carlo Simulation and PMF Model for Assessing Human Health Risks Associated with Heavy Metals in Groundwater: A Case Study of the Nubian Aquifer, Siwa Depression, Egypt. *Front. Earth Sci.* **2024**, *12*, 1431635, doi:10.3389/feart.2024.1431635.
32. Saeed, O.; Székács, A.; Jordán, G.; Mörtl, M.; Abukhadra, M.R.; Eid, M.H. Investigating the Impacts of Heavy Metal(Loid)s on Ecology and Human Health in the Lower Basin of Hungary's Danube River: A Python and Monte Carlo Simulation-Based Study. *Environ Geochem Health* **2023**, *45*, 9757–9784, doi:10.1007/s10653-023-01769-4.
33. Gad, M.; Gaagai, A.; Agrama, A.A.; El-Fiqy, W.F.M.; Eid, M.H.; Szűcs, P.; Elsayed, S.; Elsherbiny, O.; Khadr, M.; Abukhadra, M.R.; et al. Comprehensive Evaluation and Prediction of Groundwater Quality and Risk Indices Using Quantitative Approaches, Multivariate Analysis, and Machine Learning Models: An Exploratory Study. *Heliyon* **2024**, *10*, e36606, doi:10.1016/j.heliyon.2024.e36606.
34. Lee, K.P.; Arnot, T.C.; Mattia, D. A Review of Reverse Osmosis Membrane Materials for Desalination—Development to Date and Future Potential. *Journal of Membrane Science* **2011**, *370*, 1–22, doi:10.1016/j.memsci.2010.12.036.
35. Collins, F.; Rozhkovskaya, A.; Outram, J.G.; Millar, G.J. A Critical Review of Waste Resources, Synthesis, and Applications for Zeolite LTA. *Microporous and Mesoporous Materials* **2020**, *291*, 109667, doi:10.1016/j.micromeso.2019.109667.
36. Abdel-Fattah, Z.A.; Kora, M.A.; Ayyad, S.N. Facies Architecture and Depositional Development of Middle Miocene Carbonate Strata at Siwa Oasis, Northwestern Egypt. *Facies* **2013**, *59*, 505–528, doi:10.1007/s10347-012-0332-2.
37. Eldosouky, A.M.; Eleraki, M.; Mansour, A.; Saada, S.A.; Zamzam, S. Geological Controls of Mineralization Occurrences in the Egyptian Eastern Desert Using Advanced Integration of Remote Sensing and Magnetic Data. *Sci Rep* **2024**, *14*, 16700, doi:10.1038/s41598-024-66924-y.
38. Khalifa, M.A.; Zaky, A.S.; Jovane, L.; El-Hewy, A.M.; Zahran, E.; Kasem, A.M. The Middle Miocene Microfacies, Cyclicity, and Depositional History: Implications on the Marmarica Formation at the Siwa Oasis, Western Desert (Egypt). *Minerals* **2024**, *14*, 73, doi:10.3390/min14010073.
39. Said, R. *The Geology of Egypt*; Routledge, 2017; ISBN 1-351-41042-3.
40. Elnazer, A.A.; Salman, S.A.; Mohamed, Y.M.A.; Stafford, J.; Davies, P.; El Nazer, H.A. Siwa Oasis Groundwater Quality: Factors Controlling Spatial and Temporal Changes. *Environ Monit Assess* **2023**, *195*, 61, doi:10.1007/s10661-022-10646-z.
41. Masoud, A.; Koike, K. Tectonic Architecture through Landsat-7 ETM+/SRTM DEM-Derived Lineaments and Relationship to the Hydrogeologic Setting in Siwa Region, NW Egypt. *Journal of African Earth Sciences* **2006**, *45*, 467–477, doi:10.1016/j.jafrearsci.2006.04.005.
42. Moghazy, N.H.; Kaluarachchi, J.J. Assessment of Groundwater Resources in Siwa Oasis, Western Desert, Egypt. *Alexandria Engineering Journal* **2020**, *59*, 149–163, doi:10.1016/j.aej.2019.12.018.

43. Yousef, A.F. Impact of Human Activities on Groundwater Depletion and Quality Deterioration in the Northwestern Shelf of Nubian Sandstone and Fractured Carbonate Aquifer Systems. **2010**.
44. Abdel-Gawad, A.M.; El Abd, E.A.; Gedamy, Y.R. Geological Characteristics of Shallow Groundwater Aquifer and Its Relation to Hydrochemical Features and Bacteriological Pollutants in Siwa Oasis, Egypt. *International Journal of Environment* **2020**, *9*, 117–147.
45. Shata, A.A. Hydrogeology of the Great Nubian Sandstone Basin, Egypt. *QJEGH* **1982**, *15*, 127–133, doi:10.1144/GSL.QJEG.1982.015.02.04.
46. Hassan, I.; Kalin, R.M.; White, C.J.; Aladejana, J.A. Hydrostratigraphy and Hydraulic Characterisation of Shallow Coastal Aquifers, Niger Delta Basin: A Strategy for Groundwater Resource Management. *Geosciences* **2019**, *9*, 470, doi:10.3390/geosciences9110470.
47. Kohonen, T. Self-Organized Formation of Topologically Correct Feature Maps. *Biol. Cybern.* **1982**, *43*, 59–69, doi:10.1007/BF00337288.
48. Saputelli, L.; Celma, R.; Boyd, D.; Shebl, H.; Gomes, J.; Bahrini, F.; Escorcia, A.; Pandey, Y. Deriving Permeability and Reservoir Rock Typing Supported with Self-Organized Maps SOM and Artificial Neural Networks ANN - Optimal Workflow for Enabling Core-Log Integration. In Proceedings of the Day 2 Wed, September 18, 2019; SPE: Abu Dhabi, UAE, September 17 2019; p. D021S015R001.
49. Vesanto, J.; Alhoniemi, E. Clustering of the Self-Organizing Map. *IEEE Trans. Neural Netw.* **2000**, *11*, 586–600, doi:10.1109/72.846731.
50. Archie, G.E. The Electrical Resistivity Log as an Aid in Determining Some Reservoir Characteristics. *Transactions of the AIME* **1942**, *146*, 54–62, doi:10.2118/942054-G.
51. Ammar, A.I. Integration of Resistivity, Neutron, and Density Logs for Detecting, Identifying, and Calculating of Groundwater over-Pressuring Phenomenon at Siwa Oasis Depression, Egypt. *Arab J Geosci* **2022**, *15*, 1558, doi:10.1007/s12517-022-10815-x.
52. Larionov, E.A. ON THE NUMBER OF FIXED POINTS OF A LINEAR-FRACTIONAL TRANSFORMATION OF AN OPERATOR BALL ONTO ITSELF. *Math. USSR Sb.* **1969**, *7*, 195–204, doi:10.1070/SM1969v007n02ABEH001084.
53. Kozeny, J. Ueber Kapillare Leitung Des Wassers Im Boden. *Sitzungsberichte der Akademie der Wissenschaften in Wien* **1927**, *136*, 271.
54. Carman, P.C. Fluid Flow through Granular Beds: Transactions of the Institute of Chemical Engineers (London), v. 15. **1937**.
55. Bear, J. *Dynamics of Fluids in Porous Media*; Courier Corporation, 2013; ISBN 0-486-13180-7.
56. Batu, V. *Aquifer Hydraulics: A Comprehensive Guide to Hydrogeologic Data Analysis*; John Wiley & Sons, 1998; ISBN 0-471-18502-7.
57. Chapuis, R.P.; Aubertin, M. *Predicting the Coefficient of Permeability of Soils Using the Kozeny-Carman Equation*; École polytechnique de Montréal Montréal, 2003;
58. Khalil, M.A.; Temraz, M.G.; Joeckel, R.M.; Elnaggar, O.M.; Abuseda, H.H. Estimating Hydraulic Conductivity from Reservoir Resistivity Logs, Northern Western Desert, Egypt. *Pure Appl. Geophys.* **2022**, *179*, 4489–4501, doi:10.1007/s00024-022-03178-7.
59. Cooper; Jacob A Generalized Graphical Method for Evaluating Formation Constants and Summarizing Well-field History. *Eos Trans. AGU* **1946**, *27*, 526–534, doi:10.1029/TR027i004p00526.
60. Ghoneim, E.; Healey, C.; Hemida, M.; Shebl, A.; Fahil, A. Integration of Geophysical and Geospatial Techniques to Evaluate Geothermal Energy at Siwa Oasis, Western Desert, Egypt. *Remote Sensing* **2023**, *15*, 5094, doi:10.3390/rs15215094.
61. Ibraheem, I.M.; El-Husseiny, A.A.; Othman, A.A. Structural and Mineral Exploration Study at the Transition Zone between the North and the Central Eastern Desert, Egypt, Using Airborne Magnetic and Gamma-Ray Spectrometric Data. *Geocarto International* **2022**, *37*, 13098–13126, doi:10.1080/10106049.2022.2076915.
62. Hosseini, S.A.; Keshavarz Faraj Khah, N.; Kianoush, P.; Afzal, P.; Shakiba, S.; Jamshidi, E. Boundaries Determination in Potential Field Anomaly Utilizing Analytical Signal Filtering and

Its Vertical Derivative in Qeshm Island SE Iran. *Results in Geophysical Sciences* **2023**, *14*, 100053, doi:10.1016/j.ringps.2023.100053.
63. Majeed, H.; Al-Banna, A. The Main Lineament Trends of Central Iraq, Depending on the THD of Residual Gravity and Magnetic Maps Obtained from Four Upward Continuation Levels. *IGJ* **2024**, *57*, 201–213, doi:10.46717/igj.57.1C.14ms-2024-3-26.
64. Halidou Amadou, A.; El Azzab, D.; Chaouni, A.A. CONTRIBUTION OF AEROGRAVITY DATA INTERPRETATION TO THE STUDY OF THE DEEP STRUCTURE OF AGADEM PETROLEUM BLOCK (NIGER). *Geodesy and cartography* **2023**, *49*, 157–165, doi:10.3846/gac.2023.17299.
65. Clotilde, O.A.M.L.; Tabod, T.C.; Séverin, N.; Victor, K.J.; Pierre, T.K.A. Delineation of Lineaments in South Cameroon (Central Africa) Using Gravity Data. *OJG* **2013**, *03*, 331–339, doi:10.4236/ojg.2013.35038.
66. Jacobsen, B.H. A Case for Upward Continuation as a Standard Separation Filter for Potential-field Maps. *GEOPHYSICS* **1987**, *52*, 1138–1148, doi:10.1190/1.1442378.
67. El Hossary, M.F.M. Investigating the Development Challenges to Siwa Oasis, Northwestern Desert, Egypt. *NY Sci J* **2013**, *6*, 55–61.
68. Kumar, U.; Pal, S.K.; Sahoo, S.D.; Narayan, S.; Saurabh; Mondal, S.; Ganguli, S.S. Lineament Mapping over Sir Creek Offshore and Its Surroundings Using High Resolution EGM2008 Gravity Data: An Integrated Derivative Approach. *Journal of the Geological Society of India* **2018**, *91*, 671–678, doi:10.1007/s12594-018-0922-x.
69. Liu, J.; Wang, X.; Suo, Y.; Li, S.; Zhou, J. A Robust High-Resolution Potential-Field Edge Detection Filter with Its Application in the Indo-China Peninsula. *Tectonophysics* **2023**, *868*, 230109, doi:10.1016/j.tecto.2023.230109.
70. Embaby, A.; Youssef, Y.M.; Abu El-Magd, S.A. Delineation of Lineaments for Groundwater Prospecting in Hard Rocks: Inferences from Remote Sensing and Geophysical Data. *Environ Earth Sci* **2024**, *83*, 62, doi:10.1007/s12665-023-11389-x.
71. Clarke, G.K.C. OPTIMUM SECOND-DERIVATIVE AND DOWNWARD-CONTINUATION FILTERS. *GEOPHYSICS* **1969**, *34*, 424–437, doi:10.1190/1.1440020.
72. Núñez-Demarco, P.; Bonilla, A.; Sánchez-Bettucci, L.; Prezzi, C. Potential-Field Filters for Gravity and Magnetic Interpretation: A Review. *Surv Geophys* **2023**, *44*, 603–664, doi:10.1007/s10712-022-09752-x.
73. *The Utility of Regional Gravity and Magnetic Anomaly Maps*; Hinze, W.J., Ed.; Society of Exploration Geophysicists, 1985; ISBN 978-1-56080-272-3.
74. Nabighian, M.N. THE ANALYTIC SIGNAL OF TWO-DIMENSIONAL MAGNETIC BODIES WITH POLYGONAL CROSS-SECTION: ITS PROPERTIES AND USE FOR AUTOMATED ANOMALY INTERPRETATION. *GEOPHYSICS* **1972**, *37*, 507–517, doi:10.1190/1.1440276.
75. Miller, H.G.; Singh, V. Potential Field Tilt—a New Concept for Location of Potential Field Sources. *Journal of Applied Geophysics* **1994**, *32*, 213–217, doi:10.1016/0926-9851(94)90022-1.
76. Verduzco, B.; Fairhead, J.D.; Green, C.M.; MacKenzie, C. New Insights into Magnetic Derivatives for Structural Mapping. *The Leading Edge* **2004**, *23*, 116–119, doi:10.1190/1.1651454.
77. Ferreira, F.J.F.; De Souza, J.; De B. E S. Bongiolo, A.; De Castro, L.G. Enhancement of the Total Horizontal Gradient of Magnetic Anomalies Using the Tilt Angle. *GEOPHYSICS* **2013**, *78*, J33–J41, doi:10.1190/geo2011-0441.1.
78. Wang, C.-Y.; Rui, F.; Zhengsheng, Y.; Xingjue, S. Gravity Anomaly and Density Structure of the San Andreas Fault Zone. *PAGEOPH* **1986**, *124*, 127–140, doi:10.1007/BF00875722.
79. Pham, L.T.; Oksum, E.; Dolmaz, M.N. GRV_D_inv: A Graphical User Interface for 3D Forward and Inverse Modeling of Gravity Data. *GZh* **2021**, *43*, 181–193, doi:10.24028/gzh.0203-3100.v43i1.2021.225546.
80. Shin, Y.H.; Choi, K.S.; Xu, H. Three-Dimensional Forward and Inverse Models for Gravity Fields Based on the Fast Fourier Transform. *Computers & Geosciences* **2006**, *32*, 727–738, doi:10.1016/j.cageo.2005.10.002.

81. Oldenburg, D.W. THE INVERSION AND INTERPRETATION OF GRAVITY ANOMALIES. *GEOPHYSICS* **1974**, *39*, 526–536, doi:10.1190/1.1440444.
82. Soliman, M.R.H. REVEALING AND INTERPRETING OF SUBSURFACE TECTONIC PATTERN OF THE AREA NORTH OF SIWA OASIS, WESTERN DESERT, EGYPT, USING BOUGUER GRAVITY DATA. *Journal of Egyptian Geophysical Society* **2016**, *14*, 17–28, doi:10.21608/jegs.2016.385648.
83. Petropoulos, G.P.; Kalaitzidis, C.; Prasad Vadrevu, K. Support Vector Machines and Object-Based Classification for Obtaining Land-Use/Cover Cartography from Hyperion Hyperspectral Imagery. *Computers & Geosciences* **2012**, *41*, 99–107, doi:10.1016/j.cageo.2011.08.019.
84. Shebl, A.; Abdelaziz, M.I.; Ghazala, H.; Araffa, S.A.S.; Abdellatif, M.; Csámer, Á. Multi-Criteria Ground Water Potentiality Mapping Utilizing Remote Sensing and Geophysical Data: A Case Study within Sinai Peninsula, Egypt. *The Egyptian Journal of Remote Sensing and Space Sciences* **2022**, *25*, 765–778, doi:10.1016/j.ejrs.2022.07.002.
85. Ding, X.; Liu, J.; Yang, F.; Cao, J. Random Radial Basis Function Kernel-Based Support Vector Machine. *Journal of the Franklin Institute* **2021**, *358*, 10121–10140, doi:10.1016/j.jfranklin.2021.10.005.
86. Parkhurst, D.L.; Appelo, C.A.J. User's Guide to PHREEQC (Version 2): A Computer Program for Speciation, Batch-Reaction, One-Dimensional Transport, and Inverse Geochemical Calculations. *Water-resources investigations report* **1999**, *99*, 312.
87. Piper, A.M. A Graphic Procedure in the Geochemical Interpretation of Water-Analyses. *Trans. AGU* **1944**, *25*, 914, doi:10.1029/TR025i006p00914.
88. Durov, S.A. Natural Waters and Graphic Representation of Their Composition. In Proceedings of the Dokl Akad Nauk SSSR; 1948; Vol. 59, pp. 87–90.
89. Gibbs, R.J. Mechanisms Controlling World Water Chemistry. *Science* **1970**, *170*, 1088–1090, doi:10.1126/science.170.3962.1088.
90. Czuppon, G.; Demény, A.; Leél-Őssy, S.; Óvari, M.; Molnár, M.; Stieber, J.; Kiss, K.; Kármán, K.; Surányi, G.; Haszpra, L. Cave Monitoring in the Béke and Baradla Caves (Northeastern Hungary): Implications for the Conditions for the Formation Cave Carbonates. *IJS* **2018**, *47*, 13–28, doi:10.5038/1827-806X.47.1.2110.
91. Xu, Q.; Ding, C.; Liu, J.; Luo, B. PCA-Guided Search for K-Means. *Pattern Recognition Letters* **2015**, *54*, 50–55, doi:10.1016/j.patrec.2014.11.017.
92. Kuo, R.J.; Wang, H.S.; Hu, T.-L.; Chou, S.H. Application of Ant K-Means on Clustering Analysis. *Computers & Mathematics with Applications* **2005**, *50*, 1709–1724, doi:10.1016/j.camwa.2005.05.009.
93. Szabó, N.P.; Braun, B.A.; Abdelrahman, M.M.G.; Dobróka, M. Improved Well Logs Clustering Algorithm for Shale Gas Identification and Formation Evaluation. *Acta Geod Geophys* **2021**, *56*, 711–729, doi:10.1007/s40328-021-00358-0.
94. Eissa, M.A. Application of Multi-Isotopes and Geochemical Modeling for Delineating Recharge and Salinization Sources in Dahab Basin Aquifers (South Sinai, Egypt). *Hydrology* **2018**, *5*, 41, doi:10.3390/hydrology5030041.
95. Faure, G. Principles of Isotope Geology. **1977**.
96. Gillon, M.; Barbecot, F.; Gibert, E.; Corcho Alvarado, J.A.; Marlin, C.; Massault, M. Open to Closed System Transition Traced through the TDIC Isotopic Signature at the Aquifer Recharge Stage, Implications for Groundwater 14C Dating. *Geochimica et Cosmochimica Acta* **2009**, *73*, 6488–6501, doi:10.1016/j.gca.2009.07.032.
97. Wang, W.; Zhang, G.; Liu, C. Using Environmental Isotopes to Evaluate the Renewable Capacity of a Typical Karst Groundwater System in Northern China. *Environ Earth Sci* **2018**, *77*, 257, doi:10.1007/s12665-018-7425-3.
98. Fontes, J.; Garnier, J. Determination of the Initial^{14} C Activity of the Total Dissolved Carbon: A Review of the Existing Models and a New Approach. *Water Resources Research* **1979**, *15*, 399–413, doi:10.1029/WR015i002p00399.
99. Clark, I.D.; Fritz, P. *Environmental Isotopes in Hydrogeology*; 0 ed.; CRC Press, 2013; ISBN 978-0-429-06957-4.

100. Tamers, M.A. Radiocarbon Ages of Groundwater in an Arid Zone Unconfined Aquifer. In *Geophysical Monograph Series*; Stout, G.E., Ed.; American Geophysical Union: Washington, D. C., 2013; pp. 143–152 ISBN 978-1-118-66886-3.
101. Boaretto, E.; Thorling, L.; Sveinbjörnsdóttir, Á.E.; Yechieli, Y.; Heinemeier, J. Study of the Effect of Fossil Organic Carbon on^{14} C in Groundwater from Hvinningdal, Denmark. *Radiocarbon* **1997**, *40*, 915–920, doi:10.1017/S0033822200018889.
102. Vogel, J.C. 14C Dating of Groundwater. *Isotope hydrology* **1970**, 225–234.
103. Mook, W.G. The Dissolution-Exchange Model for Dating Groundwater with 14 C. In *Interpretation of environmental isotope and hydrochemical data in groundwater hydrology*; 1976.
104. Appelo, C.A.J.; Postma, D. Geochemistry, Groundwater and Pollution (p. 536). *Rotterdam: Balkema* **1993**.
105. Plummer; Glynn *Isotope Methods for Dating Old Groundwater*; Publication / Division of Scientific and Technical Information, International Atomic Energy Agency; International Atomic Energy Agency: Vienna, 2013; ISBN 978-92-0-137210-9.
106. Han, L.F.; Plummer, L.N. A Review of Single-Sample-Based Models and Other Approaches for Radiocarbon Dating of Dissolved Inorganic Carbon in Groundwater. *Earth-Science Reviews* **2016**, *152*, 119–142, doi:10.1016/j.earscirev.2015.11.004.
107. Gonfiantini, R.; Zuppi, G.M. Carbon Isotope Exchange Rate of DIC in Karst Groundwater. *Chemical Geology* **2003**, *197*, 319–336, doi:10.1016/S0009-2541(02)00402-3.
108. Al- Asad, H.; Moniruzzaman, Md.; Sarker, A.K.; Quaiyum Bhuiyan, Md.A.; Ahsan, Md.A. Hydrogeochemical Evaluation, Groundwater Contamination and Associated Health Risk in Southern Tangail, Bangladesh. *Chemosphere* **2023**, *332*, 138806, doi:10.1016/j.chemosphere.2023.138806.
109. Gao, Y.; Qian, H.; Ren, W.; Wang, H.; Liu, F.; Yang, F. Hydrogeochemical Characterization and Quality Assessment of Groundwater Based on Integrated-Weight Water Quality Index in a Concentrated Urban Area. *Journal of Cleaner Production* **2020**, *260*, 121006, doi:10.1016/j.jclepro.2020.121006.
110. Adimalla, N. Application of the Entropy Weighted Water Quality Index (EWQI) and the Pollution Index of Groundwater (PIG) to Assess Groundwater Quality for Drinking Purposes: A Case Study in a Rural Area of Telangana State, India. *Arch Environ Contam Toxicol* **2021**, *80*, 31–40, doi:10.1007/s00244-020-00800-4.
111. WHO, W.H. Guidelines for Drinking-Water Quality: First Addendum to the Fourth Edition. **2017**.
112. Tian, Y.; Jiang, Y.; Liu, Q.; Dong, M.; Xu, D.; Liu, Y.; Xu, X. Using a Water Quality Index to Assess the Water Quality of the Upper and Middle Streams of the Luanhe River, Northern China. *Science of The Total Environment* **2019**, *667*, 142–151, doi:10.1016/j.scitotenv.2019.02.356.
113. Thanh Nguyen, T.; Nguyen, T.T.; Nguyen, N.A. Optimal Network Reconfiguration to Reduce Power Loss Using an Initial Searching Point for Continuous Genetic Algorithm. *Complexity* **2020**, *2020*, 1–21, doi:10.1155/2020/2420171.
114. EPA, U. Supplemental Guidance for Developing Soil Screening Levels for Superfund Sites. *United States Environ. Prot. Agency* **2002**, *12*, 1–187.
115. Gehlhaus, M.W.; Gift, J.S.; Hogan, K.A.; Kopylev, L.; Schlosser, P.M.; Kadry, A.-R. Approaches to Cancer Assessment in EPA's Integrated Risk Information System. *Toxicology and Applied Pharmacology* **2011**, *254*, 170–180, doi:10.1016/j.taap.2010.10.019.
116. Papa, E.; Medri, V.; Amari, S.; Manaud, J.; Benito, P.; Vaccari, A.; Landi, E. Zeolite-Geopolymer Composite Materials: Production and Characterization. *Journal of Cleaner Production* **2018**, *171*, 76–84, doi:10.1016/j.jclepro.2017.09.270.
117. Szabó, N.P.; Kilik, R.; Dobróka, M. Robust Reservoir Identification by Multi-Well Cluster Analysis of Wireline Logging Data. *Heliyon* **2023**, *9*, e15957, doi:10.1016/j.heliyon.2023.e15957.

118. Hasan, M.M.U.; Hasan, T.; Shahidi, R.; James, L.; Peters, D.; Gosine, R. Lithofacies Identification from Wire-Line Logs Using an Unsupervised Data Clustering Algorithm. *Energies* **2023**, *16*, 8116, doi:10.3390/en16248116.
119. Luo, X.; Sun, J.; Zhang, J.; Liu, W. A New Method Based on Multiresolution Graph-Based Clustering for Lithofacies Analysis of Well Logging. *Comput Geosci* **2024**, *28*, 491–502, doi:10.1007/s10596-024-10277-y.
120. Misstear, B.D. The Value of Simple Equilibrium Approximations for Analysing Pumping Test Data. *Hydrogeology Journal* **2001**, *9*, 125.
121. Misstear, B. Some Key Issues in the Design of Water Wells in Unconsolidated and Fractured Rock Aquifers. *AS-ITJGW* **2012**, *1*, doi:10.7343/as-006-12-0013.
122. Rabeh, T. Using 3-D Magnetic Modeling to Evaluate Subsurface Structures of the Siwa Oasis, Western Desert, Egypt. *Sci. China Earth Sci.* **2012**, *55*, 279–289, doi:10.1007/s11430-011-4288-9.
123. Ayers, R.; Westcott, D. *Water Quality for Agriculture. FAO Irrigation and Drainage Paper 29 Rev. 1, Food and Agricultural Organisation of the United Nations*; 1994;
124. Spalding, R.F.; Exner, M.E. Occurrence of Nitrate in Groundwater—A Review. *J of Env Quality* **1993**, *22*, 392–402, doi:10.2134/jeq1993.00472425002200030002x.
125. Lasagna, M.; De Luca, D.A.; Franchino, E. The Role of Physical and Biological Processes in Aquifers and Their Importance on Groundwater Vulnerability to Nitrate Pollution. *Environ Earth Sci* **2016**, *75*, 961, doi:10.1007/s12665-016-5768-1.
126. Yousif, M.; Van Geldern, R.; Bubenzer, O. Hydrogeological Investigation of Shallow Aquifers in an Arid Data-Scarce Coastal Region (El Daba'a, Northwestern Egypt). *Hydrogeol J* **2016**, *24*, 159–179, doi:10.1007/s10040-015-1308-4.
127. Xiang, J.; Zhou, J.; Yang, J.; Huang, M.; Feng, W.; Li, Q.; Xue, D.; Zhao, Y.; Zhu, G. Applying Multivariate Statistics for Identification of Groundwater Chemistry and Qualities in the Sugan Lake Basin, Northern Qinghai-Tibet Plateau, China. *J. Mt. Sci.* **2020**, *17*, 448–463, doi:10.1007/s11629-019-5660-z.
128. Nazzal, Y.; Ahmed, I.; Al-Arifi, N.S.N.; Ghrefat, H.; Zaidi, F.K.; El-Waheidi, M.M.; Batayneh, A.; Zumlot, T. A Pragmatic Approach to Study the Groundwater Quality Suitability for Domestic and Agricultural Usage, Saq Aquifer, Northwest of Saudi Arabia. *Environ Monit Assess* **2014**, *186*, 4655–4667, doi:10.1007/s10661-014-3728-3.
129. Xu, N.; Gong, J.; Yang, G. Using Environmental Isotopes along with Major Hydro-Geochemical Compositions to Assess Deep Groundwater Formation and Evolution in Eastern Coastal China. *Journal of Contaminant Hydrology* **2018**, *208*, 1–9, doi:10.1016/j.jconhyd.2017.11.003.
130. Mirzavand, M.; Ghazban, F. Isotopic and Hydrochemical Evidence for the Source and Mechanism of Groundwater Salinization in Kashan Plain Aquifer in Iran. *Environ Sci Pollut Res* **2022**, *29*, 34575–34593, doi:10.1007/s11356-021-17457-8.
131. Craig, H. Isotopic Variations in Meteoric Waters. *Science* **1961**, *133*, 1702–1703, doi:10.1126/science.133.3465.1702.
132. Sonntag, C.; Thorweihe, U.; Rudolph, J.; Löhnert, E.P.; Junghans, C.; Münnich, K.O.; Klitzsch, E.; Shazly, E.M.E.; Swailem, F.M. Paleoclimatic Evidence in Apparent^{14} C Ages of Saharian Groundwaters. *Radiocarbon* **1980**, *22*, 871–878, doi:10.1017/S0033822200010262.
133. Zhang, J.; Chen, L.; Hou, X.; Lin, M.; Ren, X.; Li, J.; Zhang, M.; Zheng, X. Multi-Isotopes and Hydrochemistry Combined to Reveal the Major Factors Affecting Carboniferous Groundwater Evolution in the Huaibei Coalfield, North China. *Science of The Total Environment* **2021**, *791*, 148420, doi:10.1016/j.scitotenv.2021.148420.
134. El-Sayed, S.A.; Allam, K.A.; Salama, M.H.; El Begawy, H. Investigation of Chemical and Radiochemical Fingerprints of Water Resources in Siwa Oasis, Western Desert Egypt. *Arab Journal of Nuclear Science and Applications* **2017**, *50*, 158–178.
135. Tawfik, H.A.; Salah, M.K.; Maejima, W.; Armstrong-Altrin, J.S.; Abdel-Hameed, A.T.; El Ghandour, M.M. Petrography and Geochemistry of the Lower Miocene Moghra Sandstones,

Qattara Depression, North Western Desert, Egypt. *Geological Journal* **2018**, *53*, 1938–1953, doi:10.1002/gj.3025.
136. Dansgaard, W. Stable Isotopes in Precipitation. *Tellus A: Dynamic Meteorology and Oceanography* **2012**, *16*, 436, doi:10.3402/tellusa.v16i4.8993.
137. Fritz, P.; Fontes, J.-C. Handbook of Environmental Isotope Geochemistry. V. 2. The Terrestrial Environment, B. **1986**.
138. Sakai, H.; Matsubaya, O. Stable Isotopic Studies of Japanese Geothermal Systems. *Geothermics* **1977**, *5*, 97–124, doi:10.1016/0375-6505(77)90014-1.
139. Vandenschrick, G.; Van Wesemael, B.; Frot, E.; Pulido-Bosch, A.; Molina, L.; Stiévenard, M.; Souchez, R. Using Stable Isotope Analysis (δD–δ18O) to Characterise the Regional Hydrology of the Sierra de Gador, South East Spain. *Journal of Hydrology* **2002**, *265*, 43–55, doi:10.1016/S0022-1694(02)00097-5.
140. Mirzavand, M.; Ghasemieh, H.; Sadatinejad, S.J.; Bagheri, R. An Overview on Source, Mechanism and Investigation Approaches in Groundwater Salinization Studies. *Int. J. Environ. Sci. Technol.* **2020**, *17*, 2463–2476, doi:10.1007/s13762-020-02647-7.
141. Martinez, J.L.; Raiber, M.; Cendón, D.I. Using 3D Geological Modelling and Geochemical Mixing Models to Characterise Alluvial Aquifer Recharge Sources in the Upper Condamine River Catchment, Queensland, Australia. *Science of The Total Environment* **2017**, *574*, 1–18, doi:10.1016/j.scitotenv.2016.09.029.
142. Kljajević, L.M.; Nenadović, S.S.; Nenadović, M.T.; Bundaleski, N.K.; Todorović, B.Ž.; Pavlović, V.B.; Rakočević, Z.Lj. Structural and Chemical Properties of Thermally Treated Geopolymer Samples. *Ceramics International* **2017**, *43*, 6700–6708, doi:10.1016/j.ceramint.2017.02.066.
143. Caballero, L.R.; Paiva, M.D.D.M.; Fairbairn, E.D.M.R.; Toledo Filho, R.D. Thermal, Mechanical and Microstructural Analysis of Metakaolin Based Geopolymers. *Mat. Res.* **2019**, *22*, e20180716, doi:10.1590/1980-5373-mr-2018-0716.
144. Liguori, B.; Aprea, P.; Roviello, G.; Ferone, C. Self-Supporting Zeolites by Geopolymer Gel Conversion (GGC). *Microporous and Mesoporous Materials* **2019**, *286*, 125–132, doi:10.1016/j.micromeso.2019.05.045.
145. Wang, Y.; Rong, H.; Sun, L.; Zhang, P.; Yang, Y.; Jiang, L.; Wu, S.; Zhu, G.; Zou, X. Fabrication and Evaluation of Effective Zeolite Membranes for Water Desalination. *Desalination* **2021**, *504*, 114974, doi:10.1016/j.desal.2021.114974.
146. Qiu, H.; Xu, N.; Kong, L.; Zhang, Y.; Kong, X.; Wang, M.; Tang, X.; Meng, D.; Zhang, Y. Fast Synthesis of Thin Silicalite-1 Zeolite Membranes at Low Temperature. *Journal of Membrane Science* **2020**, *611*, 118361, doi:10.1016/j.memsci.2020.118361.
147. He, Y.; Cui, X.; Liu, X.; Wang, Y.; Zhang, J.; Liu, K. Preparation of Self-Supporting NaA Zeolite Membranes Using Geopolymers. *Journal of Membrane Science* **2013**, *447*, 66–72, doi:10.1016/j.memsci.2013.07.027.
148. Cho, C.H.; Oh, K.Y.; Kim, S.K.; Yeo, J.G.; Sharma, P. Pervaporative Seawater Desalination Using NaA Zeolite Membrane: Mechanisms of High Water Flux and High Salt Rejection. *Journal of Membrane Science* **2011**, *371*, 226–238, doi:10.1016/j.memsci.2011.01.049.
149. Wen, J.; Dong, H.; Zeng, G. Application of Zeolite in Removing Salinity/Sodicity from Wastewater: A Review of Mechanisms, Challenges and Opportunities. *Journal of Cleaner Production* **2018**, *197*, 1435–1446, doi:10.1016/j.jclepro.2018.06.270.

9. Appendix 1 (Supplementary figures)

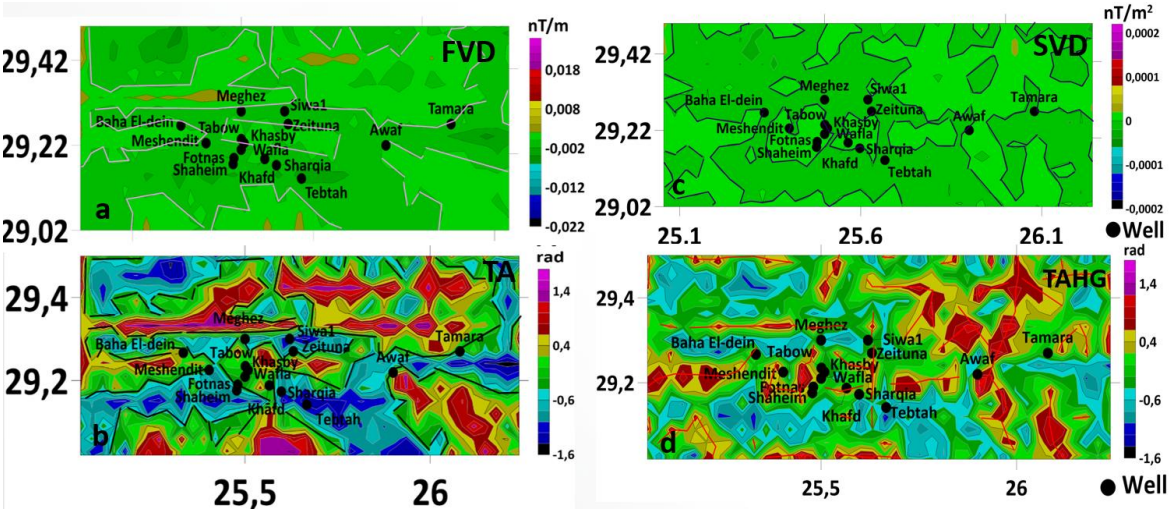

Figure 1s. Lineament extracted from (a) FVD; (b) SVD, (c) TA, and (d) TAHG with edge detection applied on residual 0.5km

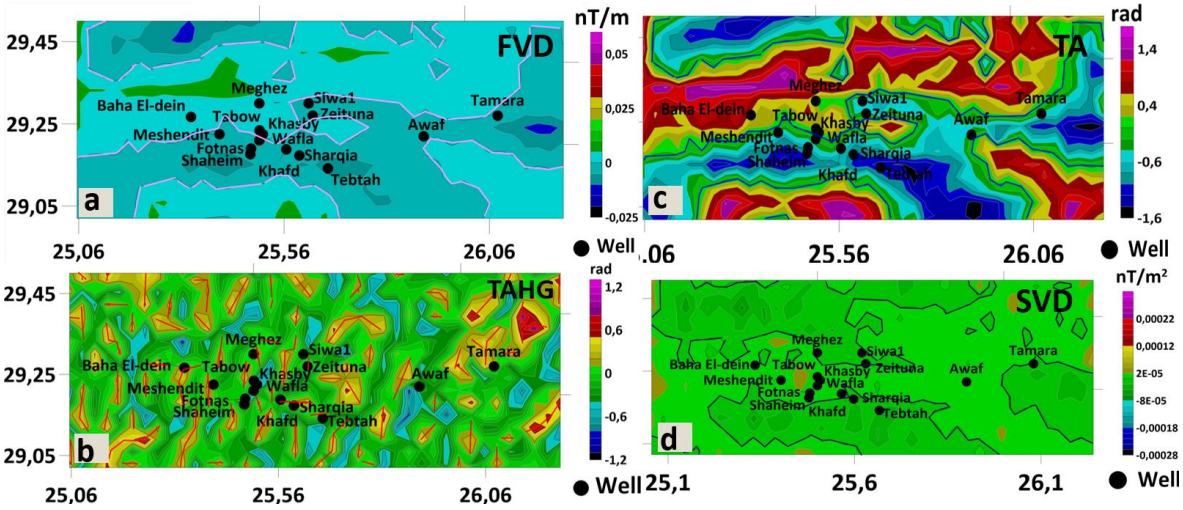

Figure 2s. Lineament extracted from (a) FVD; (b) SVD, (c) TA, and (d) TAHG with edge detection applied on residual 3.5km

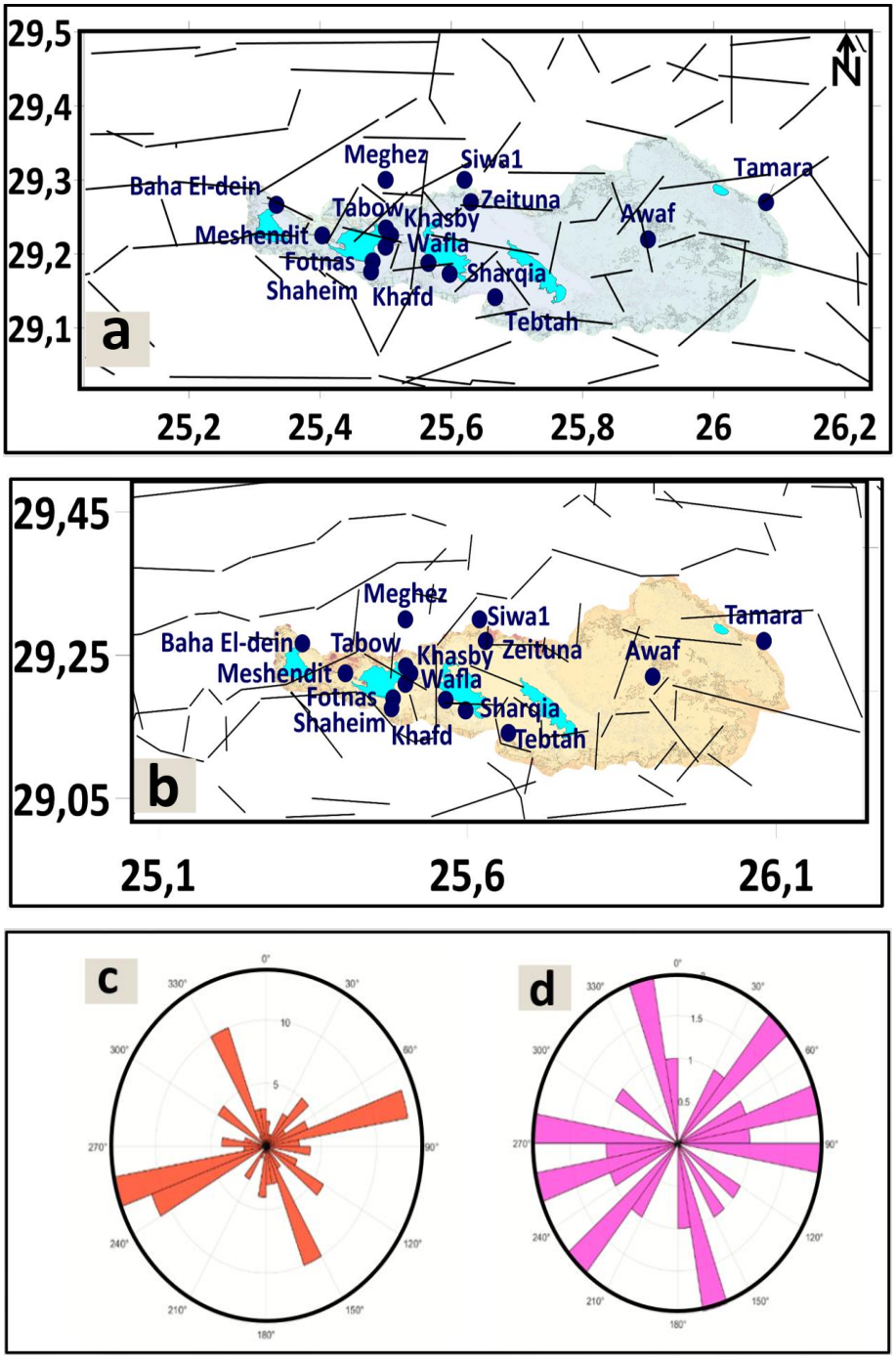

Figure 3s. Combined Lineament map of the gravity and magnetic from different edge filtering techniques with 0.5km (a), 3.5km (b), and the resultant rose diagram showing predominantly NE-SW, NW-SE and E-W trend (c, d).

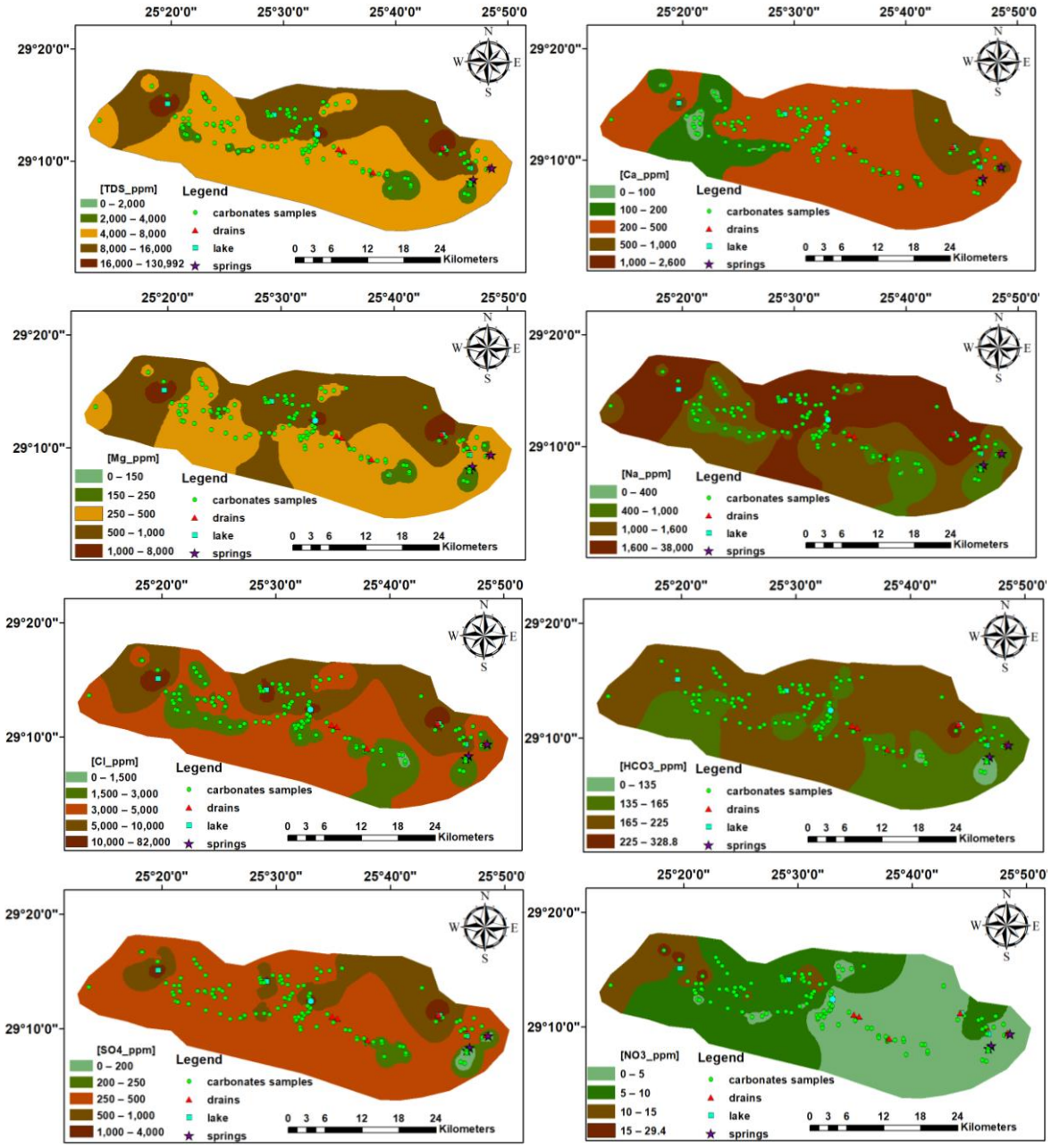

Figure 4s. Distribution maps of physicochemical parameters for the TCA, springs, drains and salt lakes.

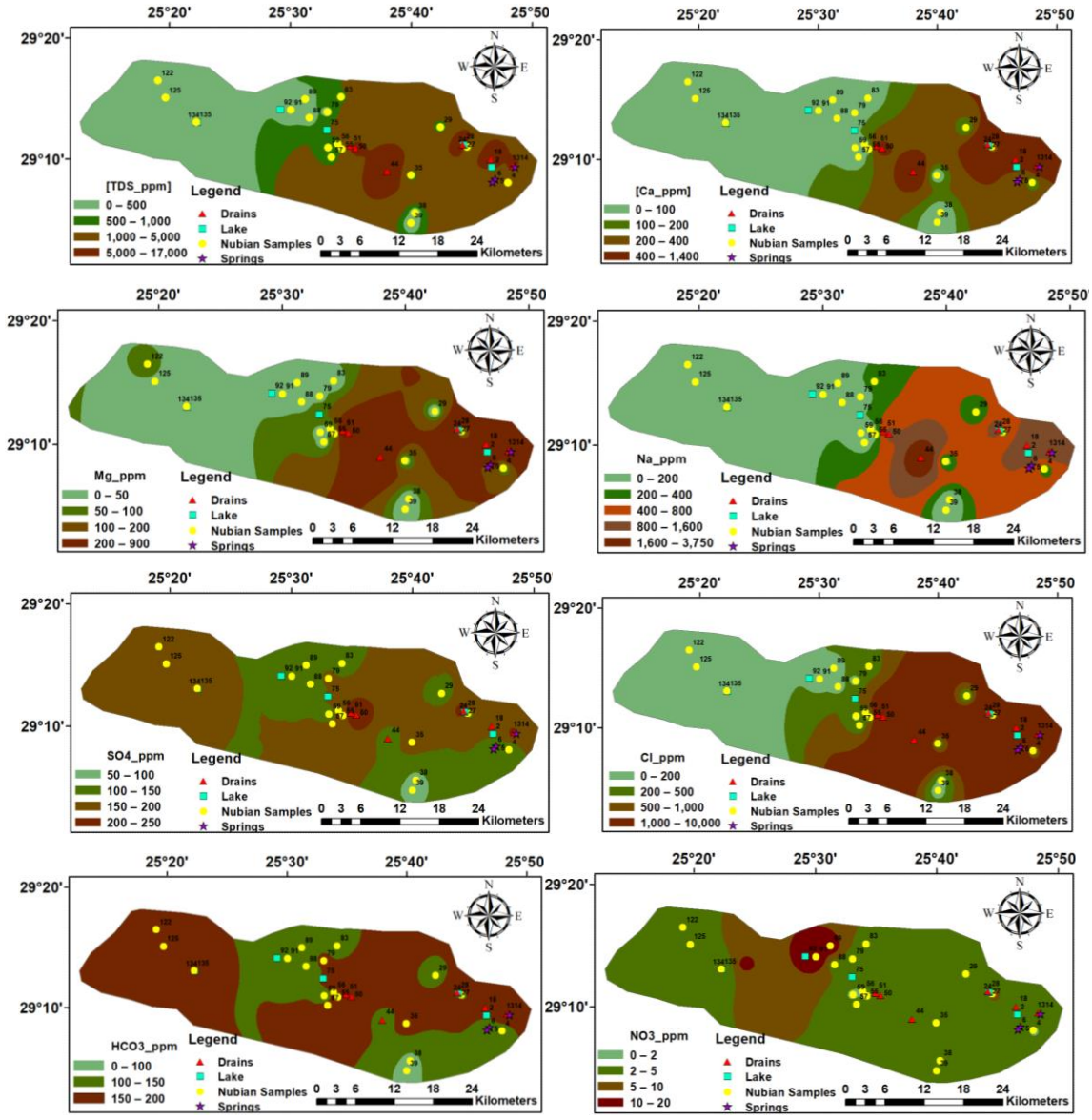

Figure 5s. Distribution maps of physicochemical parameters for the NSSA, springs, and drains

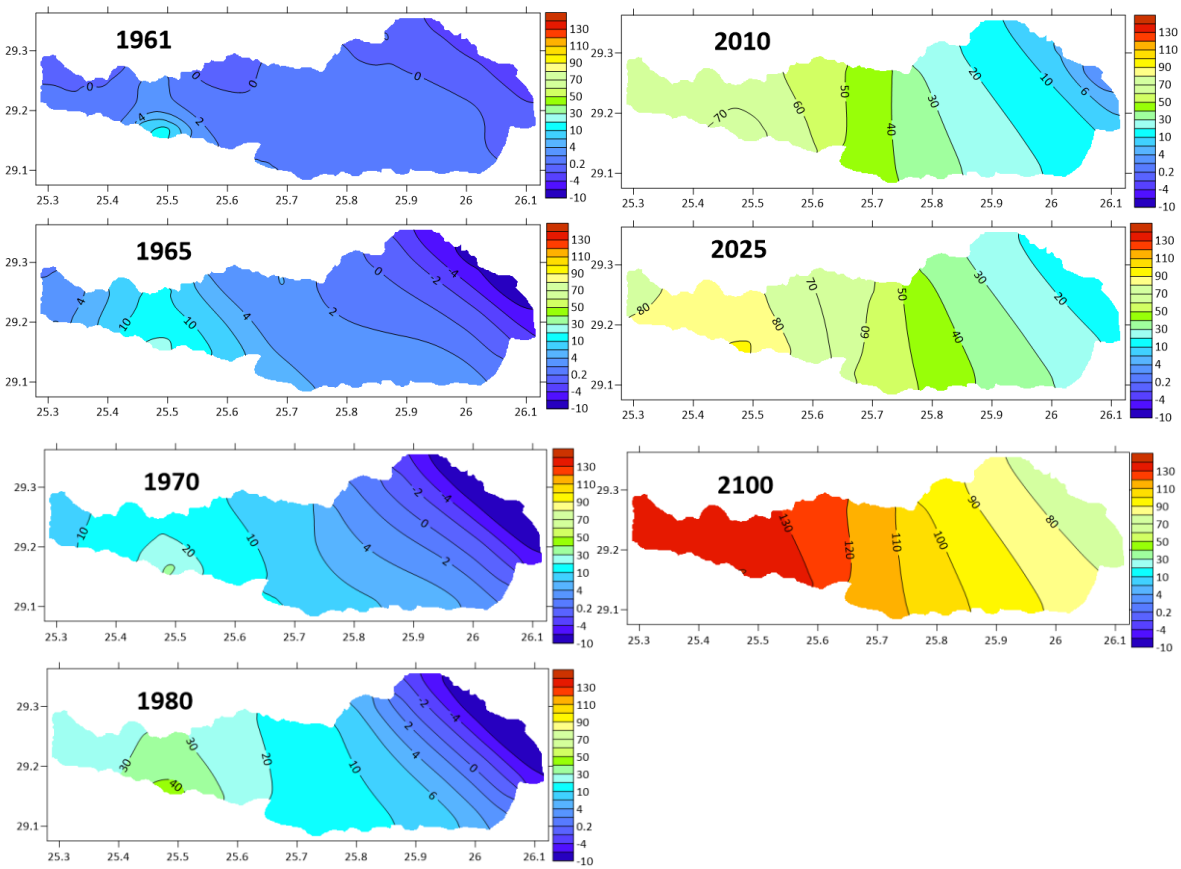

Figure 6s. The drawdown in the piezometric head of the NSSA from 1961 to 2100

10. Appendix 2 (Supplementary tables)

Table 1s Specifications of the utilized images.

Feature	image 1990	image 2000	image 2010	image 2010
Date Acquired	1990/10/19	2000/10/14	2010/10/26	2020/10/05
Satellite		LANDSAT_5		LANDSAT_8
Sensor Identifier		TM		OLI
WRS Path		180		180
WRS Row		040		040
Spatial Resolution (m)		30		30
Wavelength (µm)		Band 1: 0.45–0.52 Band 2: 0.52–0.60 Band 3: 0.63–0.69 Band 4: 0.76–0.90 Band 5: 1.55–1.75 Band 7: 2.08–2.35		Band 1: 0.435–0.451 Band 2: 0.452–0.512 Band 3: 0.533–0.590 Band 4: 0.636–0.673 Band 5: 0.851–0.879 Band 6: 1.566–1.651 Band 7: 2.107–2.294 Band 9: 1.363–1.384

Table 2s Characteristics of training and testing data.

Class	Training data (pixels)	Testing data (pixels)

Sh-W (Shallow water)	207	80
La-W (Lake water)	303	127
Cu-L (cultivated land)	243	83
Mo-Fm (Moghra Formation)	412	169
Ma (Marshes)	226	76
Sa_D (Sand dunes)	468	189

Table 3s Confusion matrices, overall Accuracies, and kappa coefficients (K) for the classified images of 1990, 2000, 2010 and 2020 using SVM.

Table 4s. The descriptive statistics of the measured parameters in all water resources

Sample type	**Intervals**	**pH**	**T°C**	**EC**	**TDS**	**Na**	**K**	**Mg**	**Ca**	**Cl**	**SO_4**	**HCO_3**
NSSA	**Min**	6.4	35.5	268	160	18.4	13.3	2.2	9.8	40.6	1.6	89.6
	Max	8.8	43	642	928	280	23.4	56.4	64.6	174	353.2	185.3
	Mean	8	39.4	396	334	65.3	18.9	17.7	24.7	93.9	48.3	135.7
TCA	**Min**	6.88	17.7	672	466	92	3.5	9	29.7	174	22.5	83.6
	Max	8.7	37.6	24280	17879	4600	83.4	2033	1116	11368	992	328.7
	Mean	7.9	24.8	6617	4603	930	42	350	258	2633.9	321	161
Springs	**Min**	7.6	17.5	1840	1463	200	9.5	113	19.6	725	5	119.6
	Max	8.3	25.1	62000	38295	10000	77.4	2524	1264.8	24360	700	227.2
	Mean	8	22.3	17946	11629	2828	49	724.3	548.6	7093.4	333.9	168.6
Drains	**Min**	7.8	18.8	5350	4023	560	5.1	266.6	104.1	1914	300	125.5
	Max	8.6	21.1	20490	16125	3750	82.8	888.2	1568	9744	1850	274.9
	Mean	8.1	20.2	11305	8585	1692.2	51.2	536.9	692.1	4810.7	807.8	211.8
Lakes	**Min**	7.8	13.5	23250	57216	3455	6.4	1536	1264.8	48430	2344.3	167.3
	Max	8.3	27.1	188800	153589	39500	17.5	1221 6.5	2508.8	94250	5348.7	286.9
	Mean	8.1	19.9	120042	106137	25058	12.4	6654	1906.9	68937.1	3498.6	215.2
sample type		**CO_3**	**NO_3**	**NH_3**	TH	B	Ba	Fe	Mn	Sr	**SiO_2**	Al
NSSA	**Min**	0	1.4	0	63.7	0.06	0.09	0.05	0.04	0.04	11.08	0.003
	Max	11.7	18.2	1.4	265.05	4.4	0.7	27.6	0.9	9.5	74.3	23.91
	Mean	1.9	5.2	0.2	133.9	0.6	0.3	4.3	0.1	0.9	43.1	3.07
TCA	**Min**	0	1.4	0	1715	0.1	0.001	0.003	0.0002	0.008	0.8	0.001
	Max	35.3	29.4	2.1	11160	1.6	2.2	36.2	3.4	12.4	76.2	86.6
	Mean	5.6	6.4	0.5	3884.5	1	0.1	2.3	0.3	4.6	37.1	5.5
Springs	**Min**	0	2.8	0	1674	0.4	0.009	0.029	0.002	1.6	3.3	0.11
	Max	17.6	15.4	2.1	3887.4	0.9	0.65	19.07	3.29	10.0	65.1	0.29
	Mean	10.6	7.6	0.8	2892.3	0.6	0.15	4.02	0.67	5.7	36.6	0.22
Drains	**Min**	0	1.4	0	3255	0.6	0.009	0.005	0.005	3.4	18.4	0.05
	Max	29.4	5.6	1.4	6370	0.7	0.05	2.06	0.05	16.1	74.6	0.26
	Mean	11.	3.7	0.6	4924.9	0.7	0.03	0.49	0.02	8.9	55.5	0.17
Lakes	**Min**	0	1.4	0	23324	7.9	0.02	0.02	0.04	0.06	7.8	0.37
	Max	35.2	4.2	1.4	55664	16.9	0.91	5.2	1.7	30.4	48.8	45.61
	Mean	10	3.2	0.6	38089	11	0.3	1.7	0.5	17	27.9	15.47

Table 5s. The stable isotopes concentrations in all water resources of Siwa Oasis

Sample ID	Aquifer	δ^2H	$\delta^{18}O$	Sample ID	Aquifer	δ^2H	$\delta^{18}O$
1	TCA	-78.44	-9.95	110	TCA	-77.77	-9.82
3	TCA	-77.72	-10.14	117	TCA	-78.06	-10.31
7	TCA	-77.70	-10.26	118	TCA	-78.48	-10.12
8	TCA	-79.24	-10.19	121	TCA	-76.20	-9.81
9	TCA	-78.21	-9.98	123	TCA	-76.90	-9.50
10	TCA	-78.63	-10.22	124	TCA	-79.32	-9.84
11	TCA	-77.58	-9.38	127	TCA	-73.94	-9.69
12	TCA	-76.89	-9.91	128	TCA	-72.38	-8.45
15	TCA	-76.47	-9.93	129	TCA	-78.31	-10.12
16	TCA	-76.64	-9.61	130	TCA	-74.50	-9.86
17	TCA	-65.79	-8.55	131	TCA	-76.78	-9.91
19	TCA	-73.23	-9.41	132	TCA	-78.76	-10.22
20	TCA	-65.63	-8.55	133	TCA	-78.83	-10.62
21	TCA	-66.71	-8.58	139	TCA	-79.65	-10.30
30	TCA	-68.27	-8.79	140	TCA	-78.94	-10.18
31	TCA	-79.38	-10.15	142	TCA	-76.88	-10.27
32	TCA	-79.37	-10.12	144	TCA	-78.14	-10.03
33	TCA	-79.01	-10.22	145	TCA	-80.34	-9.99
34	TCA	-73.70	-8.88	146	TCA	-78.97	-9.89
37	TCA	-78.79	-9.91	147	TCA	-79.52	-9.47
40	TCA	-79.04	-10.35	148	TCA	-77.16	-10.58
41	TCA	-78.51	-10.04	151	TCA	-77.00	-10.56
43	TCA	-78.24	-10.11	152	TCA	-77.23	-9.76
45	TCA	-78.83	-10.10	153	TCA	-76.76	-9.29
46	TCA	-77.31	-9.93	4	NSSA	-79.58	-10.42
47	TCA	-79.05	-10.27	24	NSSA	-66.33	-8.57
48	TCA	-78.66	-10.21	29	NSSA	-79.96	-10.48
49	TCA	-78.10	-10.09	35	NSSA	-80.00	-10.71
52	TCA	-76.69	-10.07	38	NSSA	-79.69	-10.29
53	TCA	-75.76	-9.68	39	NSSA	-79.31	-10.29
54	TCA	-78.17	-10.02	55	NSSA	-79.71	-10.52
58	TCA	-79.23	-10.35	56	NSSA	-79.94	-10.36
60	TCA	-78.94	-10.24	57	NSSA	-79.56	-10.58
61	TCA	-78.92	-10.29	59	NSSA	-79.28	-10.42
62	TCA	-79.04	-10.22	79	NSSA	-79.94	-10.09
63	TCA	-78.97	-10.16	83	NSSA	-79.08	-10.59
65	TCA	-79.47	-10.27	88	NSSA	-80.09	-10.38
66	TCA	-77.21	-9.78	89	NSSA	-79.98	-10.65
68	TCA	-78.59	-10.30	91	NSSA	-80.02	-10.40
69	TCA	-78.30	-10.18	113	NSSA	-79.14	-10.47
70	TCA	-78.90	-10.23	122	NSSA	-79.98	-10.56
72	TCA	-78.05	-10.03	134	NSSA	-80.41	-10.60
73	TCA	-78.40	-10.08	135	NSSA	-79.78	-10.43
77	TCA	-75.22	-9.88	5	Springs	-74.61	-10.06
78	TCA	-73.62	-9.91	6	Springs	-77.92	-10.36
80	TCA	-78.34	-10.27	14	Springs	-73.47	-9.32
81	TCA	-69.49	-8.91	22	Springs	-64.94	-8.35
82	TCA	-69.86	-9.26	23	Springs	-79.73	-10.52
84	TCA	-75.35	-10.17	90	Springs	-63.54	-7.40
85	TCA	-71.18	-9.21	13	Drains	-74.18	-9.02
86	TCA	-72.30	-9.53	18	Drains	-74.61	-9.27
87	TCA	-76.04	-9.95	28	Drains	-69.56	-8.76
93	TCA	-75.53	-9.84	44	Drains	-68.96	-7.62
94	TCA	-73.97	-9.41	50	Drains	-75.62	-9.52
95	TCA	-75.54	-10.02	149	Drains	-73.86	-9.12
96	TCA	-74.93	-9.55	2	Lakes	-61.71	-7.09
101	TCA	-78.21	-10.04	27	Lakes	-30.00	-0.90

104	TCA	-77.31	-9.85	75	Lakes	-29.72	-1.05
108	TCA	-78.10	-10.27	92	Lakes	-32.77	-0.85
109	TCA	-76.69	-9.96	125	Lakes	-43.27	-2.81

Table 6s. Parametric and non-parametric test (ANOVA and Kruskal-Wallis) with reported P-value

Variable	Test	Sum of Squares (sum_sq)	Degrees of Freedom (df)	F-statistic (F)	p-value (PR(>F) or Kruskal-Wallis)
Fe	ANOVA	17.389	2	0.247	0.781
	Kruskal-Wallis	-	-	-	0.035
Mn	ANOVA	0.445	2	0.753	0.473
	Kruskal-Wallis	-	-	-	0.268
SIO_2	ANOVA	2592.65	2	2.141	0.122
	Kruskal-Wallis	-	-	-	0.203
TDS	ANOVA	6.70E+08	2	351.112	3.10E-48
	Kruskal-Wallis	-	-	-	7.50E-22
K^+	ANOVA	20417.34	2	54.436	4.05E-17
	Kruskal-Wallis	-	-	-	6.01E-14
Mg^{2+}	ANOVA	2.96E+06	2	106.496	2.30E-26
	Kruskal-Wallis	-	-	-	1.75E-17
Ca^{2+}	ANOVA	2.11E+06	2	34.586	2.34E-12
	Kruskal-Wallis	-	-	-	6.84E-13
Cl^-	ANOVA	2.34E+08	2	352.123	2.71E-48
	Kruskal-Wallis	-	-	-	7.38E-22
SO_4^{2-}	ANOVA	2.58E+06	2	35.496	1.34E-12
	Kruskal-Wallis	-	-	-	2.13E-12
HCO_3^-	ANOVA	21428.12	2	9.811	0.00012
	Kruskal-Wallis	-	-	-	4.41E-05
NO_3	ANOVA	63.658838	2	1.292	0.278647
	Kruskal-Wallis	-	-	-	0.03
NH_3	ANOVA	2.154	2	3.557	0.031
	Kruskal-Wallis	-	-	-	0.041
d^2H	ANOVA	506.253	2	27.738	1.83E-10
	Kruskal-Wallis	-	-	-	3.60E-12
$d^{18}O$	ANOVA	8.505	2	16.305	6.38E-07
	Kruskal-Wallis	-	-	-	1.06E-08

Table 7s. The saturation index of the investigated minerals from geochemical modelling

SampleID	Anhydrite	Calcite	Dolomite	Gypsum	Halite	Chlorite	Albite	Montmorillonite	Illite
17	-1.23	0.76	1.98	-1.01	-3.81	5.16	-0.3	-0.1	0.31
18	-0.95	1.1	2.33	-0.72	-3.95	9.72	2.42	5.1	5.55
20	-1.8	0.66	1.62	-1.58	-3.79	3.12	-0.14	0.52	0.75
21	-1.11	1.07	2.32	-0.9	-3.83	10.25	2.77	6.08	6.41
22	-1.18	0.41	1.07	-0.96	-3.91	6.09	2.72	6.51	6.6
23	-1.02	1.02	2.41	-0.81	-3.8	10.26	2.38	5.04	5.48
28	-0.19	1.34	2.55	0.04	-3.94	8.21	2.35	5.95	6.22
30	-0.85	1.33	2.87	-0.62	-3.91	11.08	2.12	3.64	4.28
49	-1.35	0.67	1.64	-1.11	-4.02	9.19	3.51	8.13	7.54
50	-1.09	1.41	3.24	-0.85	-3.98	12.29	2.36	4.45	4.44
77	-0.88	0.74	1.93	-0.67	-3.79	4.93	-0.68	-0.49	0
78	-1.22	0.19	1.24	-1.02	-3.82	5.7	0.79	3.65	3.86
81	-1.15	0.15	0.62	-0.91	-3.91	0.74	-2.64	0.41	0.73
82	-1.19	1	2.4	-0.97	-3.68	9.88	1.32	3.68	4.28
85	-1.14	1.14	2.78	-0.92	-4.05	12.15	1.34	3.85	4.62
86	-1.58	0.44	1.83	-1.37	-3.76	8.98	0.91	3.67	4.17
87	-2.02	0.15	1.42	-1.81	-4.13	7.47	0.67	3.99	4.24
93	-1.42	0.63	1.62	-1.21	-3.72	4.33	-0.06	1.52	1.82
94	-0.84	0.6	0.73	-0.62	-3.96	1.35	1.23	5.16	5.06
95	-1.26	0.67	1.87	-1.04	-4.01	7.44	0.78	3.44	3.8
127	-1.39	-2.86	-5.38	-1.17	-3.72	15.14	3.95	9.99	9.73
130	-1.47	0.47	1.75	-1.25	-3.9				
5	-1.73	0.86	1.94	-1.51	-4.28	8.75	1.02	3.96	4.39
6	-3.05	0.68	1.44	-2.81	-4.54	6.29	1.03	4.65	4.99

7	-1.5	0.55	1.32	-1.27	-4.7	5.53	0.4	3.28	3.26
13	-1.36	1.02	2.27	-1.13	-4.09	9.57	3.07	6.46	6.89
14	-1.54	1.22	2.56	-1.31	-4.43	11.73	1.81	4.73	5.22
16	-1.44	0.46	1.3	-1.21	-4.41	7.54	1.74	5.43	5.62
19	-1.38	0.88	2.02	-1.16	-4.08	9.58	1.71	4.37	4.8
37	-1.5	1.19	2.7	-1.28	-4.74	13.3	2.7	5.9	6.45
41	-1.86	0.64	1.53	-1.64	-4.49	8.26	2.38	5.72	6
43	-1.38	1.1	2.44	-1.15	-4.36	12.44	2.87	5.91	6.52
45	-1.47	0.77	1.68	-1.24	-4.45	6.95	1.9	4.48	4.78
48	-1.45	0.71	1.84	-1.24	-4.53	8.39	1.72	4.55	4.84
52	-0.93	0.69	1.59	-0.72	-4.13	4.72	1.06	2.61	2.75
53	-1.09	1.23	2.64	-0.86	-4.46	9.89	2.77	6.68	7
54	-1.34	0.88	2.15	-1.12	-4.54	7.82	1.22	3.12	3.38
60	-1.44	-0.14	0.05	-1.23	-4.73	2.43	2.4	7.88	7.3
66	-1.27	-0.35	-0.33	-1.03	-4.8	-0.72	2.03	7.32	6.66
72	-1.31	0.64	1.65	-1.09	-4.55	6.73	0.53	3.34	3.59
73	-1.53	1.01	2.42	-1.32	-4.56	10.81	0.99	3.34	3.86
80	-1.43	0.6	1.51	-1.21	-4.71	5.81	0.34	3.29	3.43
84	-1.25	1.18	2.76	-1.03	-4.32	11.14	0.55	2.34	3.07
101	-1.61	0.49	1.88	-1.39	-4.12	9.41	0.89	3.91	4.4
104	-1.88	0.48	1.65	-1.67	-4.09	8.6	1.29	4.88	5.21
108	-1.4	0.8	2.09	-1.19	-4.11	8.79	0.9	3.61	3.99
109	-1.43	0.61	1.75	-1.22	-4.33	7.74	1.01	4.43	4.71
110	-1.68	0.46	1.84	-1.46	-4.4	9.34	0.87	3.95	4.44
117	-2.04	-0.01	1.15	-1.81	-4.6	7.56	0.89	4.19	4.59
118	-1.89	0.29	1.92	-1.68	-4.53	11	0.56	2.71	3.43
121	-2.55	-0.13	1.24	-2.32	-4.48	7.79	0.54	3.28	3.78
123	-0.37	-2.71	-5.55	-0.15	-4.73	17.89	2.32	8.03	8.59
129	-1.33	0.53	1.34	-1.12	-4.48	10.53	2.81	8.04	8.19
131	-0.73	-2.56	-5.46	-0.52	-4.11	14.21	3.29	8.89	9.2
140	-1.98	0.11	1.15	-1.75	-4.66	3.56	-1.87	-0.29	0.16
147	-1.96	0.28	1.52	-1.75	-4.73	8.85	0.69	3.87	4.39
149	-1.59	0.17	1.34	-1.36	-4.14	8.11	1.23	4.48	5.02
151	-1.86	0.32	1.63	-1.65	-4.37	8.74	0.39	3.09	3.49
152	-1.63	0.02	0.24	-1.42	-4.22	1.36	0.29	3.11	3.06
153	-1.83	0.39	1.69	-1.61	-4.45	8.42	0.32	2.13	2.72
1	-1.87	0.66	1.44	-1.64	-5.38	6.19	0.43	4.02	4.25
3	-1.75	0.64	1.55	-1.53	-5.17	8.56	0.44	3.39	3.81
4	-2.98	0.7	0.68	-2.85	-7.31	6.52	-0.41	2.92	3.13
8	-1.66	0.65	1.36	-1.43	-5.24	8.33	2.09	6.02	6.15
9	-1.71	0.74	1.67	-1.49	-5.16	8.79	1.62	5.28	5.56
10	-1.52	0.44	0.97	-1.3	-5.16	5.55	1.4	5.39	5.36
11	-1.5	0.74	1.55	-1.28	-4.93	8.13	1.71	5.79	5.94
12	-1.71	0.99	2.2	-1.5	-4.84	10.8	1.55	4.65	5.08
15	-1.11	1.22	1.2	-0.88	-4.72	4.42	0.98	2.32	2.69
24	-3.27	0.25	0.68	-3.15	-7.13	7.4	-0.04	2.62	2.82
29	-2.21	1.21	2.01	-2.07	-7.36	13.43	0.59	3.73	4.27
31	-1.71	0.51	1.44	-1.48	-5.11	8.43	2.02	5.8	5.9
32	-1.33	1.1	2.39	-1.11	-5.23	12.71	2.29	5.61	6.03
33	-1.4	0.8	1.77	-1.18	-5.03	9.61	2.39	6.21	6.37
34	-1.72	0.83	2.13	-1.5	-4.98	14.86	2.31	4.76	5.66
35	-3.7	0.57	1.79	-3.54	-6.9	12.26	0.34	1.81	2.49
38	-3.23	-0.04	0.2	-3.11	-7.55	5.5	-0.77	1.84	2.03
39	-3.11	-0.04	0.23	-2.96	-7.71	8.13	0.46	4.5	4.64
40	-1.94	0.18	0.45	-1.71	-5.57	5.69	2.56	7.85	7.64
46	-1.41	1.15	2.54	-1.18	-4.96	7.76	-0.15	-0.5	0.14
47	-1.38	0.75	1.69	-1.16	-4.87	6.9	1.51	4.09	4.26
55	-3.11	0.39	1.23	-2.96	-7.48	10.1	0.52	4.44	4.77
56	-3.17	0.18	0.11	-3.04	-7.48	4.53	0.25	4.32	4.25
57	-3.15	0.2	0.66	-3.01	-6.6	6.55	0.68	3.67	3.8
58	-2.53	0.98	1.77	-2.37	-6.41	9.04	0.75	3.05	3.4
59	-3.04	0.36	1.24	-2.89	-7.38	11.24	0.63	3.91	4.31
61	-1.59	0.09	0.59	-1.37	-4.85	4.59	2.47	7.61	7.23
62	-1.53	-0.14	-0.06	-1.3	-4.89	0.03	1.76	6.61	5.98
63	-1.38	0.7	1.69	-1.16	-5.19	9.35	2.43	6.62	6.72
65	-1.24	0.8	1.73	-1.01	-5.05	9.37	2.74	7.17	7.25
68	-1.37	1.22	2.62	-1.15	-5.22	12.98	2.04	4.69	5.25

69	-1.39	0.83	1.98	-1.16	-5.11	10.03	2.4	6.16	6.38
70	-1.36	0.72	1.78	-1.15	-4.91	9.38	2.2	5.8	5.93
79	-3.22	-0.14	0.65	-3.07	-6.79				
83	-1.64	-0.13	-0.81	-1.5	-5.96	-0.03	-0.09	3.2	2.94
88	-3.22	-1.55	-2.37	-3.08	-7.36	-9.18	-3.6	0.15	-0.72
89	-3.19	0.21	0.73	-3.05	-7.29	6.49	-1.38	1.64	1.95
90	-2.48	-0.14	1.02	-2.24	-5.47	5.11	-1.6	1.75	2.25
91	-3.15	-0.87	-1.15	-3	-7.42	-1	-1.54	3.31	2.88
113	-3.99	1.02	2.32	-3.85	-6.49	12.14	-1.65	-0.65	0.33
122	-3.01	0.22	1.55	-2.86	-6.77	10.06	-1.32	1.13	1.81
134	-2.13	0.56	1.2	-1.97	-6.45	11.56	0.56	4.47	4.95
135	-2.25	-2.65	-5.27	-2.08	-6.68	9.7	0.54	6.07	6.28
142	-2.26	0.04	1.25	-2.05	-4.8	7.55	0.2	3.09	3.6
144	-1.87	0.8	2.38	-1.66	-5	11.66	0.3	2.76	3.47
145	-2.08	0.7	2.52	-1.87	-5.11	14.26	0.29	2.03	3.02
146	-2.09	0.74	2.68	-1.88	-4.9	15.08	0.53	2.51	3.48
148	-2.3	-0.01	1.08	-2.08	-4.83	6.23	0.24	3.4	3.68
27	-0.15	1.56	4.44	-0.03	-1.03	21.33	2.02	3.18	3.8
75	-0.2	1.08	3.07	-0.02	-1.46	14.45	2.89	5.62	5.7
92	-0.35	1.42	3.76	-0.18	-1.15	17.29	3.64	5.99	6.37
125	-0.66	-2.95	-5.04	-0.45	-1.7	20.33	4.64	9.04	9.46

Table 8s. the concentration of isotopic tracers used for mixing models and age correction of groundwater.

Sample ID	Sr (mg/L)	^{14}C (pMC)	±1σ (pMC)	$\delta^{13}C$ (‰ VPDB)	$^{87}Sr/^{86}Sr$	±1σ
ES_2	14.9	94.72	0.27	-9.91	0.708319	0.000016
ES_4	0.036	34.98	0.99		0.714266	0.000016
ES_6	2.2	18.31	1.00	-10.26	0.708263	0.000016
ES_10	2.2	21.83	0.94	-12.00	0.708329	0.000016
ES_11	2.2	17.36	1.02	-11.61	0.708274	0.000016
ES_13	10.3	68.48	0.59	-9.74	0.708283	0.000016
ES_14	4.1	20.55	0.96	-7.25	0.708272	0.000015
ES_18	8.4	56.97	0.64	-9.12	0.708241	0.000016
ES_20	10.1	16.48	0.98	-9.57	0.708218	0.000016
ES_22	8.3	18.20	0.94	-8.15	0.708229	0.000016
ES_24	0.033	24.39	1.02		0.713643	0.000016
ES_27	20.5	73.66	0.51	-8.80	0.708243	0.000016
ES_28	14.9	72.27	0.56	-8.95	0.708247	0.000016
ES_29	0.044	19.73	1.19		0.711898	0.000016
ES_30	7.5			-9.09	0.708172	0.000016
ES_32	2.1	21.39	1.04	-8.62	0.708316	0.000016
ES_34	1.4	28.38	1.10	-9.84	0.708544	0.000015
ES_35	0.089	16.13	0.76	-11.44	0.708513	0.000016
ES_38	0.051	28.72	1.39		0.714561	0.000016
ES_40	1.1	20.80	1.00	-10.63	0.708400	0.000016
ES_41	2.0	16.23	0.91	-6.91	0.708293	0.000016
ES_44	10.7			-8.70	0.708399	0.000016
ES_52	5.0	20.79	1.05	-8.89	0.708244	0.000016
ES_56	0.045				0.711857	0.000016
ES_57	0.073	22.16	0.90		0.710653	0.000016
ES_58	0.133	17.73	0.74	-12.13	0.709733	0.000016
ES_75	29.9	77.88	0.44	-7.70	0.708294	0.000016
ES_78	8.1	22.23	0.99	-6.46	0.708244	0.000016
ES_82	8.2	19.96	1.03	-8.41	0.708135	0.000016
ES_83	0.050	61.11	0.65		0.711986	0.000016
ES_85	5.6	24.32	0.89	-6.25	0.708229	0.000016
ES_89	0.046	42.56	1.20		0.713835	0.000017
ES_91	0.028	71.50	1.33		0.711877	0.000016
ES_92	30.2	74.86	0.45	-8.71	0.708297	0.000016
ES_93	6.7	19.59	0.90	-7.94	0.708234	0.000016
ES_95	5.7	16.78	1.00	-9.85	0.708254	0.000016
ES_104	5.8	57.92	0.92	-9.08	0.708239	0.000016

ES_108	5.5	19.18	1.11	-10.12	0.708198	0.000016
ES_113	0.076	67.29	0.47		0.710335	0.000016
ES_117	3.3	17.80	2.89	-10.23	0.708249	0.000016
ES_121	4.1	20.65	0.91	-11.34	0.708226	0.000016
ES_122	0.122	29.89	0.74		0.710013	0.000016
ES_124	3.8	42.51	1.15	-6.45	0.708234	0.000016
ES_125	28.1	73.97	0.34	-8.37	0.708251	0.000016
ES_132	3.4	18.70	0.84	-6.25	0.708235	0.000016
ES_133	4.4	16.69	1.03	-12.12	0.708214	0.000016
ES_135	0.0	33.68	0.67		0.710563	0.000016
ES_139	2.9	15.46	0.93	-10.87	0.708270	0.000016
ES_140	3.2	41.98	1.00	-9.57	0.708250	0.000016
ES_144	2.4	24.12	0.87	-8.78	0.708239	0.000016
ES_147	2.6			-8.49	0.708257	0.000016
ES_152	5.2	40.09	0.97	-7.17	0.708250	0.000016

Table 9s. The results of the NETPATH model, after adjustment for isotopic changes related to the calcite phase, demonstrated a high degree of accuracy in age correction.

Aquifer type	Final Water sample	Isotopic Exchange (calcite)	Isotopic exchange (CO_2)	Computed ^{13}C	Observed ^{13}C	Computed ^{14}C	Observed ^{14}C	Age (year)	EV factor (NETPATH)
TCA	78	1.082		-6.46	-6.46	30.87	22.22	2717	16.35
TCA	20	0.291		-9.57	-9.57	83.76	16.48	13438	1.66
TCA	95	0.336		-9.85	-9.85	68.64	16.77	11647	14.29
TCA	108	0.323		-10.12	-10.12	72.82	19.18	11029	8.36
TCA	133	0.11		-12.12	-12.12	84.15	16.68	13375	21.92
TCA	121	1.35		-11.34	-11.34	43.06	20.65	6076	19.69
TCA	41	1.04		-6.91	-6.91	51.71	16.22	9581	2.85
TCA	140	0.348		-9.57	-9.57	65.9	41.9	3739	14.9
TCA	139	0.196		-10.87	-10.87	79.6	15.45	13551	9.7
TCA	11	0.127		-11.61	-11.61	84.02	17.36	13035	11.93
TCA	34	0.311		-9.84	-9.84	67.21	28.37	7128	9.69
TCA	58	1.09		-12.13	-12.13	66.98	17.73	10988	1.48
TCA	82	0.507		-8.41	-8.41	58.3	19.96	8860	14.12
TCA	93	0.774		-7.94	-7.94	60.53	19.58	9328	3.05
TCA	85	0.799		-6.25	-6.25	35.39	24.32	3102	31.9
TCA	52	0.53		-8.88	-8.89	69.98	20.79	10033	3.17
TCA	104	0.47		-9.07	-9.08	65.01	57.91	955	7.56
TCA	132	0.981		-6.25	-6.25	33.02	18.69	4703	17.67
TCA	17	0.284		-10.23	-10.23	71.61	17.8	11507	15.42
TCA	124	0.462		-6.45	-6.45	45.93	42.5	640	3.03
TCA	144	0.5		-8.78	-8.78	72.4	24.11	9088	2.6
TCA	32	0.513		-8.62	-8.62	73.08	21.38	10158	1.93
TCA	10	0.08		-12	-12	88.07	21.83	11529	8.69
TCA	40	0.2		-10.62	-10.63	81.84	20.8	11324	4.96
spring	14	0.58		-7.25	-7.25	45.88	20.54	6642	21.18
spring	6	0.19		-10.26	-10.26	79.48	18.3	12138	10.49
spring	22	0.705		-8.15	-8.15	72.22	18.19	11396	1.35
NSSA	35	0.031	0.2	-11.44	-11.44	58.97	16.12	10720	1.5
NSSA	89	0.152	0.001	-11.44	-11.44	71.55	42.55	4296	1.75
NSSA	57	0.898	0.001	-11.44	-11.44	72.91	22.16	9845	1.04

NSSA	38	1.26	0.2	-11.44	-11.44	68.64	28.72	7202	2
NSSA	24	0.867		-11.44	-11.44	76.01	24.39	9397	1.67
NSSA	29	1.36		-11.44	-11.44	67.62	19.72	14184	1.35
NSSA	135	0.28	0.2	-11.44	-11.44	86.27	33.68	7775	1.15
Elmaraqi lake	125	0.34		-8.37	-8.37	44.57	73.96	recent	486.67
Siwa lake	92	0.34		-8.71	-8.71	69.36	74.86	recent	14.54
Aghormi lake	75	0.47		-7.7	-7.7	46.78	77.88	recent	72.77
Zeitun lake	27	0.47		-8.8	-8.8	45.63	73.66	recent	86.89

Table 10s: The inputs used for estimation of IWQI

Inputs	unit	Cjp	Sj	Wj
TH	mg/L	0	500	0.037613
NO_3^-	mg/L	0	45	0.114075
HCO_3^-	mg/L	0	200	0.089098
SO_4^{2-}	mg/L	0	400	0.044002
Cl^-	mg/L	0	600	0.041255
Fe	mg/L	0	0.3	0.085954
Mn	mg/L	0	0.1	0.0888
Ca^{2+}	mg/L	0	200	0.060805
Mg^{2+}	mg/L	0	150	0.034634
K^+	mg/L	0	12	0.174978
Na^+	mg/L	0	400	0.04027
EC	µS/cm	0	1500	0.042616
pH		7	7.5	0.105457
TDS	mg/L	0	1000	0.040439

Table 11s. The parameters used for the calculation of HQ, HI, and CR.

HM	Cd	Cr	Cu	Fe	Mn	Ni	Pb	Zn
RfD Oral(mg/kg/day)	0.0005	0.003	0.04	0.7	0.024	0.02	0.0014	0.3
ABS	0.05	0.025	0.3	0.2	0.04	0.04	0.3	0.2
Rfd Dermal (mg/kg/day)	0.000025	0.000075	0.012	0.14	0.00096	0.0008	0.00042	0.06
CSF oral mg/kg/day	6.1	0.5					0.5	
CSF dermal	6100	500					500	
Kp	0.001	0.002	0.001	0.001	0.001	0.0002	0.0001	0.0006
Si	0.003	0.05	3	0.3	0.05	0.07	0.01	1
ET Adult (h/day)	0.58							
ET Child (h/day)	1							
SA Adult (cm^2)	18000							
SA Child (cm^2)	6600							
CF (L/cm^3)	0.001							
IR Adult (L/day)	2.2							
IR Child (L/day)	1.8							
EF (day/year)	350							
ED Adult (year)	70							
ED Child (year)	6							
BW Adult (kg)	70							
BW Child (kg)	15							
AT Adult (day)	25550							
AT Child (day)	2190							

Table 12s. The health risk indices regarding carcinogenic and non-carcinogenic impact

Criteria	Min	Max	Mean	Range	Class	Samples (%)
HI Adult (Oral)	1.6	142	14	<1	Low risk	0 (0 %)
				>1	High risk	133 (100 %)
HI Child (Oral)	6.2	542	53	<1	Low risk	0 (0 %)
				>1	High risk	133 (100 %)
HI Adult (Dermal)	0.07	48	2.6	<1	Low risk	108 (80.6%)
				>1	High risk	26 (19.4 %)
HI Child (Dermal)	0.2	141	8	<1	Low risk	30 (22.4%)
				>1	High risk	103 (77.6%)
CR_{Cd} Adult (Oral)	0.0003	0.03	0.007	$< 1\times 10^{-4}$	Acceptable	30 (22.4%)
				$> 1\times 10^{-4}$	High risk	103 (77.6%)
CR_{Cr} Adult (Oral)	2.26E-05	0.18	0.009	$< 1\times 10^{-4}$	Acceptable	5 (3.7%)
				$> 1\times 10^{-4}$	High risk	128 (96.3%)
CR_{Pb} Adult (Oral)	3.16E-05	0.03	0.005	$< 1\times 10^{-4}$	Acceptable	2 (1.5%)
				$> 1\times 10^{-4}$	High risk	131 (98.5%)
CR_{Cd} Child (Oral)	0.001	0.1	0.03	$< 1\times 10^{-4}$	Acceptable	0 (0 %)
				$> 1\times 10^{-4}$	High risk	133 (100 %)
CR_{Cr} Child (Oral)	8.63E-05	0.7	0.03	$< 1\times 10^{-4}$	Acceptable	2 (1.5%)
				$> 1\times 10^{-4}$	High risk	131 (98.5%)
CR_{Pb} Child (Oral)	0.0001	0.1	0.02	$< 1\times 10^{-4}$	Acceptable	0 (0 %)
				$> 1\times 10^{-4}$	High risk	133 (100 %)
CR_{Cd} Adult (Dermal)	0.002	0.2	0.04	$< 1\times 10^{-4}$	Acceptable	0 (0 %)
				$> 1\times 10^{-4}$	High risk	133 (100 %)
CR_{Cr} Adult (Dermal)	0.0002	1.7	0.08	$< 1\times 10^{-4}$	Acceptable	0 (0 %)
				$> 1\times 10^{-4}$	High risk	133 (100 %)
CR_{Pb} Adult (Dermal)	1.5E-05	0.01	0.002	$< 1\times 10^{-4}$	Acceptable	7 (5.3%)
				$> 1\times 10^{-4}$	High risk	126 (94.7%)
CR_{Cd} Child (Dermal)	0.005	0.5	0.1	$< 1\times 10^{-4}$	Acceptable	0 (0 %)
				$> 1\times 10^{-4}$	High risk	133 (100 %)
CR_{Cr} Child (Dermal)	0.0006	5.2	0.2	$< 1\times 10^{-4}$	Acceptable	0 (0 %)
				$> 1\times 10^{-4}$	High risk	133 (100 %)
CR_{Pb} Child (Dermal)	4.43E-05	0.04	0.007	$< 1\times 10^{-4}$	Acceptable	3 (2.2%)
				$> 1\times 10^{-4}$	High risk	130 (97.8%)